Investigation of Fundamental Mechanical Deformation Mechanisms in Rhenium for the Development of Replacement Alloys

by

Julian Elmar Correa Sabisch

A dissertation submitted in partial satisfaction

of the requirement for the degree of

Doctor of Philosophy

in

Engineering – Materials Science and Engineering

in the

Graduate Division

of the

University of California, Berkeley

Committee in charge:

Professor Andrew M. Minor, Chair
Professor Mark D. Asta
Professor Peter Hosemann

Fall 2017

Investigation of Fundamental Mechanical Deformation Mechanisms in Rhenium for the Development of Replacement Alloys

by

Julian Elmar Correa Sabisch

Abstract

Investigation of Fundamental Mechanical Deformation Mechanisms in Rhenium for the Development of Replacement Alloys

By

Julian Elmar Correa Sabisch

Doctor of Philosophy in Engineering – Materials Science and Engineering

University of California, Berkeley

Professor Andrew M. Minor Chair

A comprehensive study of the microstructural evolution of pure rhenium during *ex-situ* compression, *in-situ* and *ex-situ* tension has been conducted using standard TEM and EBSD metallographic analysis. Little information is available on how the microstructure of pure rhenium effects its more notable properties. Some of the unique properties that make rhenium notable include extreme strength, work hardening rate and ductility, all of which are maintained through an extreme temperature range. The insights gained through this improved understanding of the rhenium microstructure, along with previous simulation work, was used as a model around which a rhenium replacement alloy was developed. Due to the extreme cost of pure Re, ruthenium, tantalum, tungsten, and molybdenum alloys were chosen as the proper system for replacement.

Under compression, slip and dislocation plasticity in rhenium was predominantly active in the low strain regime, with $\{11\bar{2}1\}\langle 11\bar{2}6\rangle$ twinning occurring at all strain amounts and dominating after yield. This is contrary to deformation twins typically being active during the initial low strain regime of twinning dominated metals. It was observed that twins could bypass grain boundaries, as previously reported. In addition, a mechanism of twins "jogging" along the c-axis past twin boundaries was observed using TEM. This mechanism allowed for multiple twin variants to be active within individual grains. Twin "jogging" helps to explain the excellent ductility in rhenium accommodating the lack of dislocation plasticity. Postmortem TEM imaging showed dislocation density steadily increased around the twins, this is likely a result of twin boundaries impeding dislocation slip, confirming observations seen in highly work-hardened tension samples. Additionally, dislocation populated twin boundaries have shown $\{11\bar{2}1\}\langle 11\bar{2}6\rangle$ type twins resist growing in size when surrounded by dislocations, tending instead to form new twins as strain increases.

The use of EBSD has shown that under tension the twin area fraction plateaued after one third of the failure strain was achieved. After twin saturation, all changes to the deformed microstructure was seen as increased interior grain misorientations. Through Schmidt factor analysis, EBSD had shown that prismatic and pyramidal slip activated appreciably only at strain values above half of the failure strain. Conventional TEM investigation has shown that <a> type $\vec{b} = [11\bar{2}0]$ screw dislocations operated on the basal planes in loosely aligned slip bands, no

dislocations were seen operating on the prism planes within the TEM. At failure stresses, <a> type $\vec{b} = [11\bar{2}0]$ basal screw dislocations were again observed in dislocation slip bands. <c+a> type $\vec{b} = [11\bar{2}3]$ pyramidal screw dislocations which formed tangled dislocation nets interfering with <a> type glide were observed. HAADF STEM imaging was used to view the morphology of tension induced $\{11\bar{2}1\}\langle 11\bar{2}6\rangle$ twins. These were more representative of classical twin structures involving well defined twin boundaries surrounding a region of crystal with a single new orientation. This did not represent the $\{11\bar{2}1\}\langle 11\bar{2}6\rangle$ type twins seen in compression which consisted of twin aggregates. This compression-tension asymmetry is likely due to the twin favorability of the microstructure forcing the creation of many more twins during compression. Twin transmission with $\{11\bar{2}1\}\langle 11\bar{2}6\rangle$ changing twin plane between parent and matrix orientations was observed. TEM observations confirmed the observations made using purely EBSD maps with Schmidt factor analysis.

In-situ tensile straining was performed on rhenium both at room temperature and at 920°C. The samples had a texture which suppressed possible $\{11\bar{2}1\}\langle 11\bar{2}6\rangle$ twinning, while exaggerating basal or prismatic dislocation activity. Two main samples were successfully tested, with both confirming the observation that <a> type $\langle 11\bar{2}0\rangle$ basal dislocations were the dominant mechanism during tensile straining. Samples were all tested both at room temperature and elevated temperature in order to find any differences in behavior based on temperature. Dislocation motion was characterized as "jerky", as detailed by Clouet in Ti. The only appreciable effect of raising the temperature to 920°C was slightly increased dislocation density. Dislocation motion was unaffected by this slight temperature rise.

The effects of alloying ruthenium with tungsten, tantalum, and molybdenum were investigated, using powder x-ray diffraction to determine crystal structures. A novel indentation stress-strain method was developed as a method for mechanical property screening, using indents on pure Re and Ru as a basis for comparison. Three chemically complex alloys low-Ru content alloys with HCP structures were characterized using XRD. The Ru 45 - Ta 10 - W 20 - Mo 25 (compositions in wt.%) alloy was shown to be near the solubility limit of the HCP phase, proving to be the composition with the lowest Ru content and having completely HCP single phase after annealing at 1850 °C.

Through initial indentation tests, Ru was seen to be extremely hard and brittle with extensive cracking around the indentation tip. Both Berkovich and spherical indentation was performed on all alloys, with indents in pure Re and Ru used as a basis for comparison Tungsten was shown to provide a consistent improvement to Ru alloy behavior throughout all three alloying systems. In general, low level additions of tantalum were seen to improve the mechanical properties significantly, however significant additions of tantalum generally lead to the formation of additional phases and reduced mechanical response. Molybdenum increased the solubility of all solute elements within the HCP alloys, further improving the mechanical properties of any alloy by reducing Ru content. EBSD scans were performed on all of the alloy systems with compositions near the solubility limit. Indents within the Ru-Ta-W system had the unique $\{11\bar{2}1\}\langle 11\bar{2}6\rangle$ twins seen near the indent tip. The Ru-Mo-W system showed $\{11\bar{2}2\}\langle 11\bar{2}3\rangle$ type twins underneath the indents. Finally, the Ru-Ta-W-Mo system showed $\{10\bar{1}2\}\langle 10\bar{1}1\rangle$ twins beneath the indent surface. All twin variants that were observed when indenting Re were also observed in the various designed chemically complex alloys. The observation of these twins is extremely promising for the future of Re-replacement alloy development.

Table of Contents

List of Figures

Figure 1.7: A summation of work from de Jong and Berne (9) (10). a) Calculated twin boundary energy for the $\{10\bar{1}1\}$ and $\{11\bar{2}1\}$ twin boundaries as a function of atomic number. Tc and Re shows extremely low twin boundary energies for $\{11\bar{2}1\}\langle 11\bar{2}6\rangle$ type twins when compared to all other HCP metals. b) Atomic arrangement of $\{11\bar{2}1\}\langle 11\bar{2}6\rangle$ twin boundary. c) bimodality parameter, s, as a function of distance to twin boundary. d-e) Calculation of stable structure of 4-d and 5-d elements. Not the stable structure changes from BCC to TCP to HCP around 4.6 $\frac{e}{at}$ in the d orbital

Figure 1.8: Top: greyscale inverted dark-field images showing both twins and some martensite within a thin iron disk. Bottom: relation of yield stress and UTS with grain size in industrial TWIP steel shows almost perfect Hall-Petch relationship.

Figure 1.9: Polarized light micrographs of the difference between a) 1:1 perchloric acid to lactic acid solution b) and the superior 2:1 perchloric acid to nitric acid solution. Note the extensive pitting seen in select grains, with properly specular grains also showing the initial stages of pitting along twins. b) Here twins and grain boundaries are readily seen. The sample is very flat and there is no pitting seen in this sample. Color differences are purely relative and only highlight twin/grain boundaries and sample topography.

Figure 1.10: a) Cartoon of the interaction body of electrons in a sample surface and various types of resulting emitted radiation (11). b) Geometry of an EBSD scan with inset diffraction pattern on the EBSD detector. (12)

Figure 1.11: Various methods for detailing the same data taken from the current research detailing the types of data used in EBSD analysis. This data was chosen to be easily interpretable for instruction. a) 0001 Pole Figure. RD and TD is the conventional naming scheme of "Rolling Direction" and "Transverse Direction" defining sample geometry. b) Inverse Pole Figure reducing the full pole figure to the smallest possible symmetry cell. c) Same data in b) shown as a color gradient instead of individual spots. d) Inverse pole figure map along the z direction showing the orientation of the colors in the EBSD map in e).

Figure 1.12: a) Laue condition suitable for $\vec{g} \cdot \vec{b}$ analysis. b) A close two-beam condition that is used for $\vec{g} \cdot \vec{b}$ analysis. c) Off zone axis DP were $\vec{g} \cdot \vec{b}$ analysis was able to be performed. d) DF TEM image of three visible dislocations using reflection condition from c). e) Same dislocations in d) this time being invisible. a-e) taken from Re.

Figure 1.13: Images taken from Oliver-Pharr a-c) and Pathak et al. d-e). a) a typical load displacement curve with relevant values. b) Description of section of a typical indent. c) Simulation of indent pile-up and sink-in. d) Same as for b) but specifically designed for use in indentation stress-strain analysis. e) Effect of different values for indentation strain and contact area in aluminum indentation stress-strain curves. Note large variations based on method. (13)

Figure 2.6: BF and DF TEM images for a large twin seen in the 1% strain sample, a),b) and the 28% strain sample c),d) respectively. DF image d) is taken from the twin reflection to show internal twin structure lacking extensive dislocations. The dislocation density of <a> type screw dislocations is seen to dominate over <c+a> dislocations along the twin boundary. This is most likely due to <a> type dislocations being the dominant dislocation during deformation and collecting at the twin boundary.

Figure 2.7: Two-beam BF and DF images for a large twin seen in the 5% strain sample. BF a),c) and DF b,d) of the (0002) a),b) and $(11\bar{2}0)$ c),d) reflections respectively. The dislocation density of <a> type screw dislocations is seen to dominate over <c+a> dislocations along the twin boundary. This is most likely due to <a> type dislocations being the dominant dislocation during deformation and collecting at the twin boundary.

Figure 2.8: BF and DF images of a twin interception in the 1% strain sample. a) and b) show the intersections of two twins with a) being edge on, and b) having tilted 15°, it should be noted that the edge on twin is only a few atomic planes thick, with no misfit dislocations needed to accommodate its formation. The arrows in a) mark the direction change of the larger twin due to twin-twin interactions. Due to the 15° shift in b) some interior structure of the transmitting twin can be seen. The twin appears to terminate and change planes where the arrows mark. Magnifications of the twin intersection are seen in BF c) and DF d) with inset $[11\bar{2}0]$ DP, allowing for some inspection of the interior twin structure. d) is taken from high order twin spots. The intersections between twins are highlighted with arrows, with the twins often "jogging" along $\vec{g} = (0002)$ or terminating at these intersections, suggesting involvement of basal stacking faults. The rightmost arrow in image c) highlights that the boundary of the larger twin has a step-like structure.

Figure 3.1: Initial IPF map of sample surface orthogonal to the loading direction a). Schmidt factor chart which shows the favorability of $\{11\bar{2}1\}\langle 11\bar{2}6\rangle$ type twins is seen in b), the $\{0002\}\langle 11\bar{2}0\rangle$ slip system in c), the $\{10\bar{1}0\}\langle 1\bar{2}10\rangle$ slip system in d), and $\{10\bar{1}1\}\langle 11\bar{2}3\rangle$ pyramidal slip e). Corresponding texture plots f) and grain size chart of this IPF map in g). This undeformed sample was taken from the larger grip sections of the sample. It can be seen that the bulk of grains have a strongly textured orientation with prismatic $\{10\bar{1}0\}$ and $\{11\bar{2}0\}$ planes along the tensile direction, which is unfavorable for $\{11\bar{2}1\}\langle 11\bar{2}6\rangle$ type twinning, as seen by the Schmidt factors in b). It should be noted that the bulk of grains are between 40-90μm in size, while some rare grains are above 100μm, which can lead to large discrepancies in mechanical response.

Figure 3.2: Mechanical data for selected tensile samples taken, a) stress-strain curves and b) work hardening as a function of strain. Example of before and after images of tests are shown for sample 3, to 1.9% strain, c) and samples 6, to fracture, d). Two grain size charts are seen for sample 4 e), and sample 1 f). Sample 4 has appreciably fewer large grains, with the smaller grains taking a larger portion of the area fraction. This accounts for some discrepancies seen in the yield stress in a). This difference in grain size

distribution is taken as random chance, since all samples are small with a gauge area of $8.55mm^2$.

Figure 3.3: Large area overview EBSD maps for tension samples 1-5. Note as strain increases, the number of twins as a function of area saturates after 3.3% strain, where large grain misorientations take over in accommodating the large amounts of applied strain. Misorientation bands can be seen starting at 3.3% strain as well, where they appear to saturate after fracture, causing the internal structure of many larger grains appearing striped in color.

Figure 3.4: Overview EBSD map of sample 1, after fracture a). Local misorientation profile is seen in b), with corresponding Schmidt Factor maps for $\{11\bar{2}1\}\langle 11\bar{2}6\rangle$ type twins seen in c), the $\{0002\}\langle 11\bar{2}0\rangle$ slip system in d), $\{10\bar{1}0\}\langle 1\bar{2}10\rangle$ slip system in e), and the $\{10\bar{1}1\}\langle 11\bar{2}3\rangle$ slip system in f). Note that the obviously twinned grains, marked with white triangles, do not necessarily have the highest Schmidt factors for the $\{11\bar{2}1\}\langle 11\bar{2}6\rangle$ twin system, but contain high basal dislocation activity. Large amounts of pyramidal slip activity is marked with the black arrow. The black triangle marks heavily twinned grains which are more favorable for pyramidal slip.

Figure 3.5: Overview for EBSD IPF maps and local grain misorientation maps for sample 3, 1.9% strain, sample 5, 5.7% total strain, and sample 1, after fracture. These samples were chosen because there was a roughly 4% strain increase between steps. Black triangles mark basal slip favorable grains, and white triangles mark prismatic slip favorability. Note that as the amount of strain increases regularly, the total misorientation profile also steadily increases and contains many more 5° misorientation saturation points. The grains with heavily saturated 5° tend to be highly twinning as well as showing more basal slip band formation.

Figure 3.6: Close up EBSD map of sample 1 (after fracture) a) with correlating local internal grain misorientation map b), and the Schmidt Factor maps for $\{11\bar{2}1\}\langle 11\bar{2}6\rangle$ type twins is seen in c), the $\{0002\}\langle 11\bar{2}0\rangle$ slip system in d) $\{10\bar{1}0\}\langle 1\bar{2}10\rangle$ slip system in e), and the $\{10\bar{1}1\}\langle 11\bar{2}3\rangle$ slip system in e) Black triangles mark basal slip favorability, while white triangles mark prismatic slip favorability.

Figure 3.7: Comparison of high magnification EBSD IPF maps and misorientation maps for a strain progression. The average amount of twinning within twin favorable grains has not increased substantially between the IPF maps in a) and c), this indicates that twinning saturates at relatively low strains. Dislocation plasticity then becomes a dominating factor after the initial twin formation, as seen through the large differences in local average grain misorientation in b,d). The red circles in the IPF map of a results from surface contamination. Triangles mark notable grains.

Figure 3.8: Overview of microstructures seen using conventional TEM 2-beam Dark-field imaging (top) and conventional HAADF STEM imaging (bottom). STEM imaging has removed all dynamical contrast seen in the TEM images (such as thickness fringes in the 1.9% strain image) making images much more interpretable.

Figure 3.9: "G dot B" analysis for a dislocation slip band in sample 5, 3.3% strain, viewed in a JEOL 2011 microscope, using a 200kv accelerating voltage. Images were all taken using a strong 2-beam Bragg condition from a $\langle 11\bar{2}3\rangle$ zone axis with the BF images (left) generally showing less dislocation contrast than the DF two beam condition (right). Using the DF images, the $(1\bar{1}01)$ and $(\bar{1}10\bar{1})$ were seen to be invisible, such that $\vec{g}\cdot\vec{b}=0$, and $\vec{b}=[11\bar{2}0]$ screw dislocations.

Figure 3.10: "G dot B" analysis for a large dislocation network within sample 1. The images were taken in a JEOL 3010 microscope, using a 300kv accelerating voltage. Large black arrows show immobile <c+a> dislocations, with white arrows showing the basal <a> type dislocation slip bands.

Figure 3.11: DF images along three unique zones of a single area within sample 1. Diffraction patterns and crystal orientation show <a> type dislocations (white triangles) lie on basal planes and <c+a> type dislocations (black arrows) lie on pyramidal planes. (14)

Figure 3.12: Close up view of twin transmission in samples 5, 3.3% strain using HAADF STEM at 300 kV. Note that the lateral twin causes a small misorientation (as seen by the inset diffraction pattern) of roughly 5° between the top and bottom of the image. The orientation difference between the middle twin and the main near $[10\bar{1}0]$ orientation is 68°, resulting in the closest possible orientation the $(11\bar{2}1)$ twin commonly prevalent in Re.

Figure 3.13: Twin structures seen using STEM imaging. Unlike twins seen formed during compressive loading of rhenium, twins formed under tension have a much more classical structure involving twin boundaries with a re-oriented crystal in between the boundaries. The twinned region contains roughly similar densities of dislocations as the surrounding matrix.

Figure 3.14: STEM images taken from sample 5, 3.3% strain. The large twins have an interior boundary from which secondary twins appear to grow. Here dislocation density is relatively low, when compared to Figure 3.13, but twin density is much higher.

Figure 3.15: Large twinned region showing many branching twins from sample 5, 3.3% total strain. Here the cause of the twin branching or direction change is not apparent. With the such complex twinning structures the TEM thin disks showing two-dimensional slice of a more complex macroscopic three-dimensional object does not fully describe the twin morphology.

Figure 4.7: Summary of "g dot b" analysis for the mobile dislocations observed in sample 2. The BF image a) and DP b) show the unusual $\langle 5\bar{1}\bar{4}3\rangle$ zone used to index as well as the dislocations marked with triangles. c-f) is the series of diffraction conditions used to characterize the dislocations as $\vec{b} = \langle 11\bar{2}0\rangle$ type screw dislocations. When the dislocations are invisible $\vec{g} \cdot \vec{b} = 0$.

Figure 4.8: Still frames taken from a room temperature *in-situ* video of the dislocation motion of sample 2, using an $(0\bar{1}11)$ DF condition which best showed the dislocation contrast. Frames a and b) show one dislocation appearing into frame from out of frame and stopping. Fames b-c) show the front dislocation quickly move then stop, with the trailing dislocations in d) and e) slowly crawling over a few seconds. Overall, the motion of these dislocations contained parts "jerky" motion and parts smooth flow.

Figure 4.9: Comparison of TEM images a,c) and diffraction patterns with simulated diffraction patterns b,d) with corresponding crystal orientations for samples 1 a,b) and 2 c,d) (14). When lining up the slip band directions (white arrows) for sample 1 in a) we can see that the three fold symmetry of the slip bands is a match. The dislocation in the bottom left is bowing such that the forms a half loop on the basal plane. For sample 2 as there is only 1 direction of slip (white arrow) in c), the alignment is less ideal. However again the best match for operative plane of <a> type dislocations is the basal plane.

Figure 4.10: Formation and destruction of dislocations in sample 1 at 920 °C. The video was taken near failure of the sample with frames a-c) taken sequentially over a few seconds, as such dislocation motion was largely limited at temperature in sample 1. Despite the difficulty in interpreting the contrast seen here, one dislocation leaves through the sample marked in a) and c). Another dislocation appears in b) from the sample surface in the location marked by the arrows.

Figure 4.11: Final TEM images of sample 1 after 30 minutes testing at 920 °C. There is an appreciable development of a film at the coastline of the sample, with the interior of the sample containing many cracks, ostensibly the film penetrating within the sample and causing catastrophic mechanical failure. As the nominal sample temperature is 920 °C this film should not consist of Re_2O_7, as that oxide sublimates at 362 °C and would not be visible after forming. Further investigation was not performed on what the film was, as it was not in the scope of this work.

Figure 4.12: Still frames taken from a elevated temperature (920 °C) *in-situ* video of the dislocation motion of sample 2. The time is sequentially over a few seconds from a-c); the arrows show locations of small dislocation translations. The dislocations are more closely bundled here than in any other dislocation video. This is likely due to the sample geometry of this foil as well as the test being well developed, having much tie to generate additional dislocations. Other than the apparent increase dislocation

density seen in this sample, no effects have been noticed through increasing the temperature of the sample.

Figure 5.1: The binary phase diagrams of a) the Ru-Ta system and b) the Ru-W system and Ru-Mo system c) (15). Note the solubility of Ta into Ru is ~20 at% and the W and Mo binaries are almost identical with 40 at% solubility. d) Initial Ru-Ta-W ternary phase diagram and e) improved Ru-Ta-W phase diagram after initial alloys were investigated. (16) Where the Re-equivalent line intercepts the HCP single phase region was the initial investigation regime for alloy development.

Figure 5.2: Comparison of load displacement curve for a Berkovich tip and for a spherical tip with enlarged images showing the individual data points of the curve. Note the sharp change in load-displacement response for the spherical tip after the initial loading, resulting in a "knee" of the graph. This results from the indentation procedure's transition from purely elastic loading to elastic-plastic deformation. As the Berkovich tip is sharp, plastic deformation occurs immediately during the initial indentation, and no elastic-plastic transition occurs. Also note the different shape of the collected data. The spherical indentation data uses the CSM method applying an oscillation to the load, clearly notable in the shape of the data.

Figure 5.3: Geometry of D8-Discover XRD. Frames are at angles of 15,25,35,45° sequentially for both θ_1 and θ_2 allowing for a total 2θ range from 15° to 105°. The frames are then stitched together and integrated in order to form a standard intensity vs 2θ plot. Through the use of the area detector larger grained polycrystalline samples can be used, with the spots showing. However, this can lead to lower intensity for low-symmetry orientations.

Figure 5.4: Optical micrographs showing the progression of the visible microstructure after annealing at a) 1600°C, b) 1700°C and c) 1850°C for 8 hours. Note the greatly increased size of the individual ligaments of the intermixing phases by the final anneal. Each subsequent anneal showed increase in ligament size.

Figure 5.5: XRD spectra for Series 2 of Ru-Ta-W alloys probing the single-phase solubility limit of Ta and W into HCP Ru as well as the Series 3 alloys 3-1, 3-2 and 3-3, all containing single phase HCP structures. Series 3 alloys did not show any oxide spots as they were investigated immediately after casting with no anneal step. No secondary phase appears as the compositions change with any alloy. With the addition of Mo and W there is a much larger shift in the lattice spacing than with pure Ta and W. Note that Series 3 was not annealed, and as such the samples are not affected with any WO_2 peaks. The missing peaks in alloy 2-5 are due to the randomized nature of the individual grains inside each ingot.

Figure 5.6: XRD spectra for samples containing 2-phase alloys. For both types the second phase was identified as a Tetragonal structure P42/mnm, with the primary phase being the same HCP structures seen in Figure 5.5. Here only the peaks for the Tetragonal phase are indexed. It can be seen that the Series 1 alloys have much more secondary phase

oriented out of plane. d) Re-oriented matrix-twin crystal relationship to view the matrix along a $\langle 10\bar{1}0\rangle$ direction to best see the resulting twinning plane, to be given as $\{\bar{2}\bar{3}55\}$. The unique index of this plane is due to dislocation plasticity that has caused small misorientations moving the twin plane from the ideal orientation of $\{11\bar{2}1\}\langle 11\bar{2}6\rangle$.

Figure 5.18: Two EBSD maps of alloy 3-2 (top) and alloy 3-4 (bottom). Surface quality for EBSD acquisition was poor, however glancing angle FIB milling was used in order to remove the unindexable top layer of the samples. Alloy 3-2 shows $\{11\bar{2}2\}\langle 11\bar{2}3\rangle$ type twining, and alloy 3-4 shows $\{10\bar{1}2\}\langle 10\bar{1}1\rangle$ type twinning as active twin planes for these two orientations.

List of Tables

Acknowledgements

I would like the thank the many people who helped me accomplish with the work done in this manuscript.

Foremost in shaping this work, I must thank my advisor Andrew M. “Andy” Minor. I spent nearly my whole time at Berkeley being advised by Andy, and I don’t think I could ask for a better advisor. Having provided the funding and guidance needed to finish this work, as well as many insights into academia as a whole, I can’t think of a better graduate school experience than my own.

I would be greatly remiss in not acknowledging the advice of my brother Dr. Andrew T.C. Sabisch. Without his kind words during the difficult periods during the work I might not have been able to continue.

I would like to thank my many colleges in the minor group and the materials science department; Dr. Rohini Sankaran, Tom Pekin, Max Poschmann, Nathan Velez. Foremost among my colleagues in terms of impact on this work is Rohini. Without our many long discussions about research, I don’t think I would be able to contextualize and think about research the way I do. Tom and Max have been a prominent factor during this PhD work. Their excellent academic input on subject matter of any complexity without judgment was invaluable. Additionally, they were both consistently a motivating factor to improve myself both physically and mentally during my PhD thesis.

I would like to thank Professors Bill Morris, Mark Asta and Daryl Chzran for their intellectual contributions during the weekly Ti-Re meetings held for ONR funding. The discussions lead to new experimental directions while researching rhenium that would have taken much longer to realize without their input.

The post-doctoral researchers Dr. Burak Ozdol, and Professor Josh Kacher were greatly helpful during the rhenium work. Josh for paving the way in front of me with his own post-doctoral research and Re. Burak for always cleaning up after my jet-polishing, as well as being available to teach me when I needed help.

Without the help of James Wu and Phil Yanoscik I would never have been able to shape and cast my alloys. Many thanks to them for their help, taking interest in the project and fast work.

I would be remis in forgetting to acknowledge Dr. Professor Erica T. Lilleodden, and the many graduate students and colleagues from the Helmholtz-Zentrum Geesthacht für Material und Eisenforschung (HZG). The time I spent at HZG and the lessons I learned from Erica were invaluable to my development as a scientist and I am exceedingly grateful.

Finally, I must gratefully acknowledge funding from the US Office of Naval Research under Grant No. N00014-11-1-0886. Portions of this work were performed as a user project at the Molecular Foundry at Lawrence Berkeley National Laboratory, which is supported by the U.S. Department of Energy under Contract # DE-AC02-05CH11231.

Chapter 1

Background Knowledge

One of the most interesting metals within the HCP crystals family, while not the most used, is pure rhenium. Rhenium is mainly used as a platinum-rhenium reforming catalyst, hydrogenation and fine chemicals for hydrocracking, and as x-ray tubes and targets. However one of its key uses is as a structural metal is as ballistic combustion chambers and nozzles (17), mainly for space and rocketry applications, due to its extremely high melting temperature (3180 ºC), high work hardening rate, great ductility, creep resistance, and high temperature tensile strength (18) (19) (20). Rhenium is the only refractory metal to have an HCP crystal structure, and also has no known ductile to brittle transition temperature. Additionally, the effect of rhenium as an alloying element in a large number of refractory metals will significantly reduce the ductile to brittle transition temperatures of the resulting alloys (21) (22). Unfortunately, rhenium is extremely rare and costly (currently above approximately of 32,000$\frac{\$}{kg}$ for metal powder (23), further increased by the need for iridium coating to prevent oxidation at elevated temperatures (17)) limiting its use to the most sensitive applications and restricting the body of research previously conducted to a few select studies (20). As such, the goal of this work will be to understand the fundamental deformation mechanisms present in rhenium, in order to produce cost effective replacement alloys consisting of high-entropy transition metal alloys.

Among the structural metals, the hexagonal close-packed (HCP) crystal structure is relatively uncommon, only occurring under normal conditions in the widely used pure elements in cobalt, magnesium, titanium, and zirconium (24). General properties vary significantly among the HCP metals, however in general all HCP metals rely on deformation twinning when accommodating strain within macroscopic polycrystalline specimen. This is due to the lack of sufficient slip modes required for isotropic deformation (24) (1) (2). Understanding the interactions between twinning and dislocation slip during deformation of any HCP system is important in understanding deformation behaviors in HCP metals. In order to understand these mechanisms, transmission electron microscopy (TEM) and electron backscatter diffraction (EBSD) will be used in conjunction with systematic experimental setups, to be described in later chapters. This allows for in-situ and post-mortem investigation of the microstructural changes from the micron to nano-scales. With the observations gained through electron microscopy and the associated mechanical data, it is possible to determine the intrinsic deformation mechanisms that determine the macroscopic behavior of rhenium under tension and compression in order to give proper context to the behaviors of Re-replacement alloys.

The methods that will be used in order to probe the microstructure of rhenium will include, spherical and Berkovich nanoindentation, uniaxial compression and tension tests of large samples, and in-situ TEM straining of thin rhenium foils. Nanoindentation is of great use in alloy development, since it allows for site specific investigation of the mechanical properties at the nanoscale. Previous work done has shown that when using non-axisymmetric indentation tips the relationship between indentation and crystal orientation can greatly affect the indentation measurement even for crystals largely seen as isotropic, such as copper (25) (26). While the increase in prevalence of nanoindentation has allowed for a large throughput of mechanical data, the quality of the data in highly deformation twinning materials, due to the interplay between

indentation head anisotropy and changes in twinning behavior. As such the axi-symmetric indentation method was chosen to be used as a comparative method, with full knowledge of the difficulties that deformation twinning produces in indentation mechanical responses. The more classically known tests of macroscopic tension and compression were chosen since they allow for direct insights into the microstructures involved in producing the observed macroscopic mechanical behaviors.

1.1. Interest in Mechanical Properties of Rhenium

While there has been extensive work on magnesium, titanium and other HCP alloys in everything from alloying effects, macro-scale extrusion textures, and microscale pillar deformation, there has been very few experimental electron microscopy studies of rhenium. The most notable study involves only using EBSD without any in-situ TEM deformation (4). The reasons for this are multiple, however due to its rarity (rhenium is third most rare element present in the earth's crust, resulting in prices at the time of writing of over 18,000$ per pound (23)) the industrial driving force behind large scale implementation of rhenium metal applications has been limited (27) (28) (29). A fundamental understanding of the basic mechanisms is required for rhenium in order to be able to find replacement alloys that could later be used in large scale industrial applications for aerospace and beyond.

a lattice constant (nm)	0.2761
$\frac{c}{a}$ ratio	1.615
Melting Temperature	3180 ºC
Tensile Strength	1050-2700 MPa
Slip Systems	Primary: $\{0002\}\langle 11\bar{2}0\rangle$ Secondary: $\{10\bar{1}0\}\langle 11\bar{2}0\rangle$ Additional: $\{10\bar{1}1\}\langle 11\bar{2}3\rangle$
Twinning Systems	Primary: $\{11\bar{2}1\}\langle 11\bar{2}6\rangle$ Secondary: $\{10\bar{1}2\}\langle 10\bar{1}2\rangle$ Additional: $\{11\bar{2}2\}\langle 11\bar{2}3\rangle$
Hardness (Knoop Hardness)	135-825 HK
Modulus	460 GPa in Tension
Strain Hardening Exponent	0.353

Table 1.1: List of relevant properties of rhenium (18) (20) (24) (4) (5) (7)

1.1.1. The HCP Crystal Structure

The HCP crystal structure is described by three lattice vectors a_1, a_2, and a_3, where $|a_1| = |a_2| \neq |a_3|$. The angle α between a_1 and a_2 is 120º and both a_1 and a_2 are orthogonal to a_3 as seen in

Figure 1.1a) (30). In order to avoid confusion when describing HCP systems a 4 index Miller-Bravais notation is used to label directions and planes, such that (hkil) correspond the intercepts of the plane with the crystal, and i is given by Equation 1 (31). The use of four-index-notation is important for clarity in HCP systems. When using 3 index notation it is not readily apparent that the directions $[110]$ and $[1\bar{2}0]$ are equivalent (24) (31) (3). However, using Miller-Bravais notation it is easily seen that the $[11\bar{2}0]$ and $[1\bar{2}10]$ directions are equivalent. Equation 1 can be replaced with the notation used for directions within HCP crystals, <uvtw> instead of {hkil}, however it is important to note that in HCP crystals the normal of a {hkil} plane is not necessarily the same numbers in terms of <u v t w>. This is a result of the fact that $\alpha = 120^{o}$ and $|a_1| \neq |a_3|$, the main characteristics of HCP crystals. The plane normal vectors of (hkil) are given by $\left[h\ k\ i\ \ \frac{3}{2}\left(\frac{a}{c}\right)^2 l\right]$ (31). However, this is not the case for vectors only involving the a_1 or a_3 vectors, i.e. $(1\bar{2}10)$ plane is normal to $[1\bar{2}10]$, and the (0002) plane is normal to the [0002] direction. Additionally, it is not immediately obvious which vectors lie within a given plane, e.g. the $(1\bar{2}11)$ plane does not contain the $\langle 1\bar{2}11\rangle$ family of directions, instead it contains the $\langle 1\bar{2}16\rangle$ family of directions. The zonal equation for HCP crystals, shown in Equation 2, states that the four-index dot product must equal zero for the direction to lie within a plane.

$$h + k + i = 0 \tag{1}$$

$$0 = \frac{(hkil)[uvtw]}{a^2} = hu + kv + it + lw \tag{2}$$

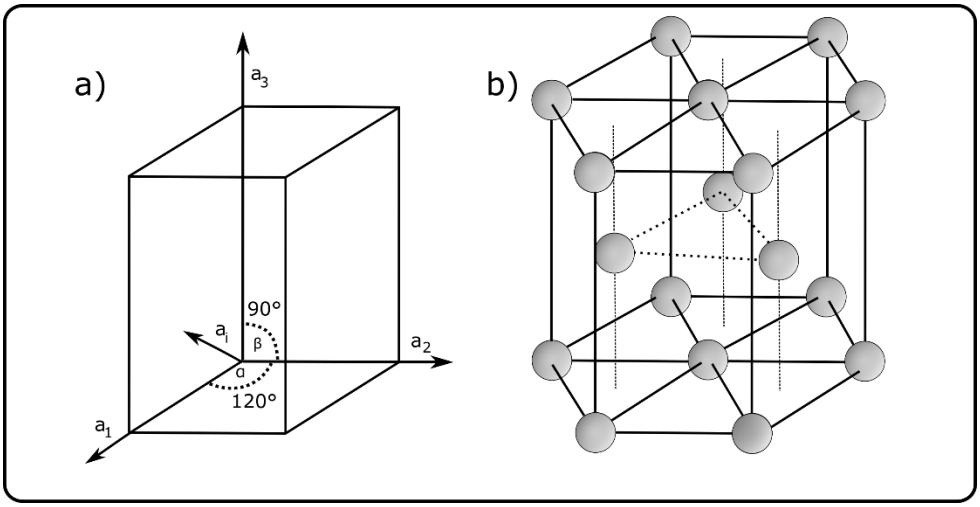

Figure 1.1: a) Drawing of the base unit vectors that constitute the HCP unit cell. b) Full HCP crystal populated by atoms.

The difference between the indexes of planes and their normal vectors in HCP crystals is due to this fact that the a_1 vector has a different magnitude than a_3. Typically, the two lattice constants are referred to the a-lattice constant for a_1 and a_2 and c-lattice constant for a_3. By looking at Figure 1.1b), it can be seen what the HCP system looks like populated with 2 atoms per unit cell, one at the $(0,0,0,0)$ position and one $\left(\frac{a}{3}, \frac{2a}{3}, -a, \frac{c}{2}\right)$, resulting in ABAB type stacking. This reffers to the different basal planes, the hexagonal planes consisting of only a_1 and

a_2 vectors (from now on simply a vectors), stacked upon each other in a regularly repeating stacking pattern where the atoms in the basal plane sits exactly above the one from two planes previous along the a_3 direction (henceforth known as the c direction). Other systems also exhibit an ABC type stacking, but this is generally seen in stacks of the {111} planes in face-centered cubic crystals.

One of the most important parameters detailing the crystal properties of HCP cells is the $\frac{c}{a}$ ratio. This ratio can range wildly from 1.886 of cadmium to 1.581 of beryllium (24) and can have significant effect on the resolved shear stress for various deformation modes seen within HCP crystals. For an ideal HCP system the $\frac{c}{a}$ ratio is $\sqrt{\frac{8}{3}} = 1.633$, this results from taking the crystal seen in Figure 1.1b) and requiring all the atoms to be identical in size and touching when possible. The result is in two close packed directions, namely the $[1\bar{2}10]$, along the basal plane, and $[1\bar{2}13]$ directions, of a <c + a> character. A bit of simple geometry, left as a potential excercise for the reader, gives the result: $\frac{c}{a} = 1.633$. For $\frac{c}{a}$ ratios above the ideal 1.633 each atom's nearest neighbors are within the basal plane, with the atom planes above and below, located at $\frac{c}{2}$, further away than the in basal plane atoms. Both rhenium and ruthenium (which will form the base metal for alloy development in Chapter 5) have a $\frac{c}{a}$ ratios under 1.633 which makes the out of basal plane atoms nearest neighbors. The next chapter will detail the deformation slip systems which are relevant in HCP systems with $\frac{c}{a}$ ratios below 1.633.

1.1.2. Deformation Slip in HCP Metals

The anisotropy of an HCP crystal informs the slip modes that are prevalent during deformation due to the limited number of slip systems available for deformation, consequently this also increases the importance of twinning, as the twinned crystal can then be in a slip-favorable orientation (32). This makes understanding the texture of the crystal and which slip systems can activate given an orientation (33). In most HCP metals, either prism slip (as is the case for titanium) or basal slip (in the case of magnesium) will be dominant (4) (34). However, for rhenium basal, prism and pyramidal slip has been observed (7) making understanding the conditions for which each type of present dislocation operates important for understanding deformation in rhenium in general. Currently there have been no studies as to the dislocation structures present in Re.

Much work has gone into describing the different dislocation structures in HCP metals. Read and Frank and Nicolas have proposed models, which have been since repeatedly vindicated, for the dislocations structures in HCP metals as early as the 1950s (35) (36). The most important Burgers vectors for perfect dislocations in HCP metals are the $\frac{1}{3}\langle 1\bar{2}10\rangle$ basal plane dislocation followed by the $\frac{1}{3}\langle 1\bar{2}13\rangle$ <c + a> type dislocation operating on the pyramidal $\{10\bar{1}1\}$ planes. While there can also be the <0001> type perfect dislocation as well as the $\frac{1}{3}\langle 20\bar{2}3\rangle$ and $\frac{1}{3}\langle 10\bar{1}0\rangle$ type imperfect dislocations, these are more commonly used to form partial dislocation to comprise one of the other two, such as in Equation 3. As an example, the most commonly seen dislocations in magnesium are $\vec{b} = \frac{1}{3}\langle 1\bar{2}10\rangle$ dislocations operating along the basal (0002) planes, with <c+a> type slip only being largely active at elevated temperature (34).

$$\frac{1}{3}\langle 1\bar{2}10\rangle = \frac{1}{3}\langle 1\bar{1}00\rangle + \frac{1}{3}\langle 0\bar{1}10\rangle \quad (3)$$

$$\frac{1}{3}\langle 1\bar{2}13\rangle = \frac{1}{3}\langle 1\bar{2}10\rangle + \langle 0001\rangle \quad (4)$$

As a result of these different dislocation types, the common slip planes are the $\{0002\}$ basal plane with $\vec{b} = \frac{1}{3}\langle 1\bar{2}10\rangle$ or the $\{11\bar{2}0\}$ prismatic plane, again with $\vec{b} = \frac{1}{3}\langle 1\bar{2}10\rangle$. For deformation along the c-axis the active slip plane is the $\{10\bar{1}1\}$ pyramidal I plane with the operative dislocation $\vec{b} = \frac{1}{3}\langle 1\bar{2}13\rangle$. Dislocations also have screw and edge character (diagrams of each type are readily available on any crystal defects book (24)), the operative difference between the two types of dislocations is that screw dislocations are active on many planes simultaneously, while edge dislocations only interact along a single plane. Screw type dislocations have Burgers vectors parallel to the line directions, while edge dislocations have orthogonal Burgers vectors and line directions. Besides the difference in stress states surrounding both dislocation types, the two types move through the crystal differently. The edge types must "jog" when changing planes, essentially a dislocation changes its Burgers vector in order to change planes, allowing it to operate on different plane for a short segment, before coming back to its initial plane. This mechanism is important when edge dislocations encounter obstacles that impede their continued glide along their current plane. Screw dislocations are not required to jog in order to move around obstacles. In most crystals, dislocations observed are often a combination of screw and edge character. Regardless of dislocation type, the method for determining what type of dislocation is present in a TEM metal foil remains the same.

1.1.3. Twinning Modes in HCP Metals

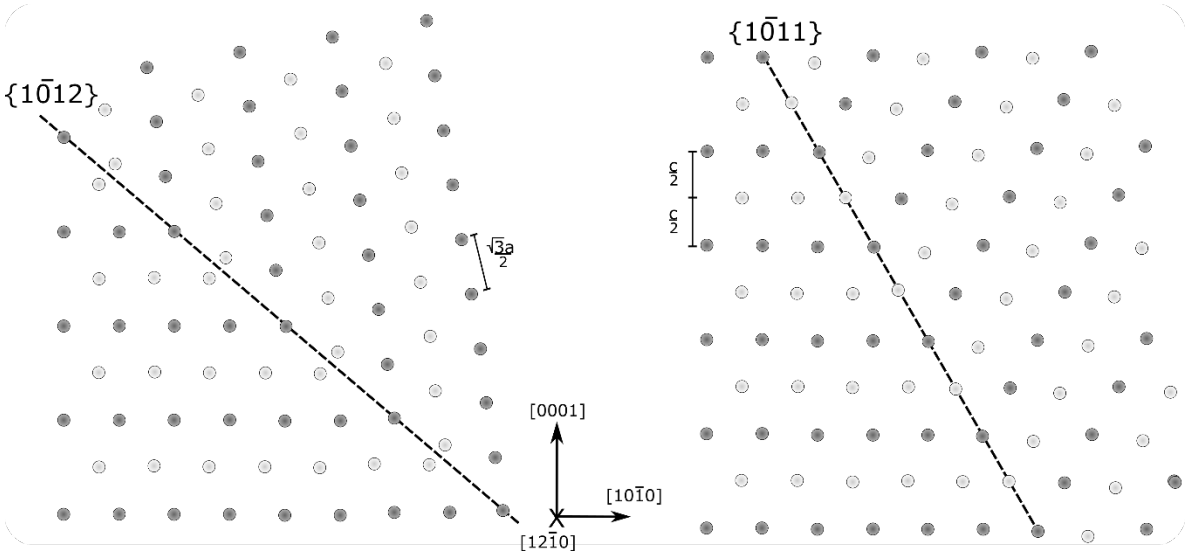

Figure 1.2: Projection of the $\langle 11\bar{2}0\rangle$ plane that show the $\{10\bar{1}2\}\langle 10\bar{1}1\rangle$ and $\{10\bar{1}1\}\langle 10\bar{1}2\rangle$ type twins respectively, with dark circles being atoms in the basal plane of the $\{11\bar{2}0\}$ plane and light circles atoms out of the $\{11\bar{2}0\}$ plane. Within the Mg they are known as the "tension" and "compression" twins due to their occurrence under uniaxial tension and compression along the c-axis. In rhenium only the $\{10\bar{1}2\}\langle 10\bar{1}1\rangle$ is seen,

as well as in all other HCP metals. Here the c a ratio used was ideal: $\frac{c}{a} = 1.633$, close to that of Re at 1.615 (1) (2) (3).

In crystallography, a crystal is said to be twinned when two subsets of the crystal lattice are oriented relative to each other by a crystallographic symmetry operation (24). While this behavior can be seen during the initial growth of a material, such as five-fold rotational twins that can be grown in gold nano-islands (30), the main relevance twinning form to this work is that of deformation twinning in structural metals. Deformation twinning occurs when one portion of a crystal undergoes shear to reorient itself in order to relieve a certain amount of applied strain (37). Different twin types have differing strain magnitudes, which depend on the $\frac{c}{a}$ ratio and as a result differ for each HCP crystal. The most common type of twin, the $\{10\bar{1}2\}\langle 10\bar{1}1\rangle$ twin is seen in all HCP metals and generally can only accommodate a low amount of strain, anywhere from 12% to 17% strain in tension along the c-axis (38). The formation of a $\{10\bar{1}2\}\langle 10\bar{1}1\rangle$ twin relieves 12.9% strain in tension along the c-axis in Re. A simple shuffle, or small atom displacements around the initial shear direction, is required in order for twin formation to be completed. A cross-sectional diagram with the optic axis along the $\langle 11\bar{2}0\rangle$ direction, in Figure 1.2, shows the atom arrangements along a $\{10\bar{1}2\}\langle 10\bar{1}1\rangle$ and $\{10\bar{1}1\}\langle 10\bar{1}2\rangle$ twin boundary.

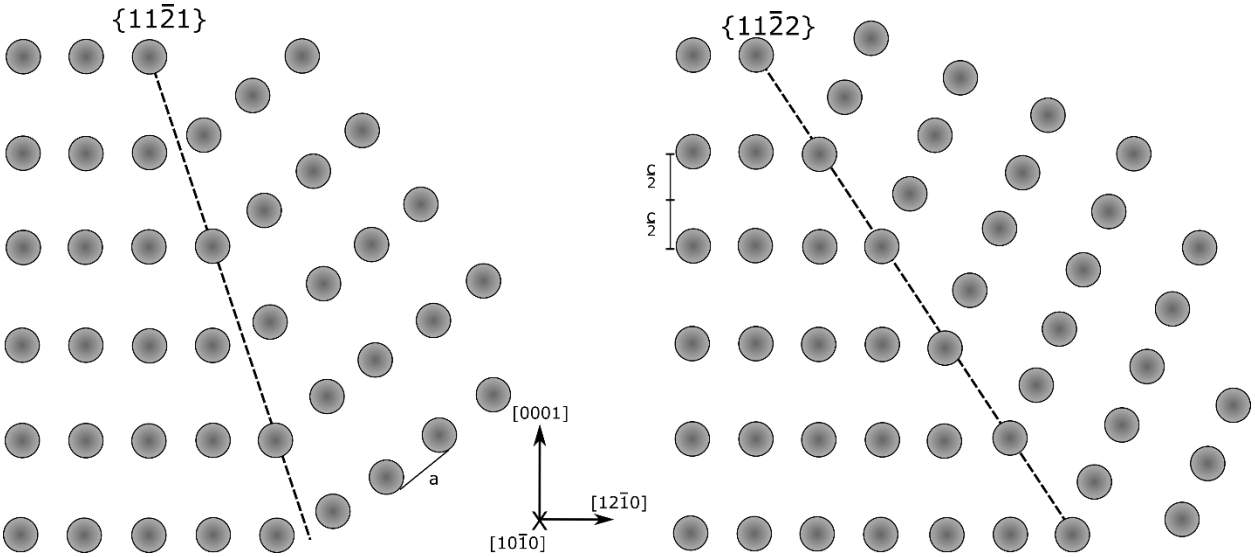

Figure 1.3: Projection of the $\{10\bar{1}0\}$ plane that shows the $\{11\bar{2}1\}\langle 11\bar{2}6\rangle$ and $\{11\bar{2}2\}\langle 12\bar{2}3\rangle$ type twins respectively, with dark circles being atoms in the basal plane of the $\{10\bar{1}0\}$ plane. The $\{11\bar{2}0\}$ twin is most common twin in Re (4) (5) (6). Again the $\frac{c}{a}$ ratio used was ideal: $\sqrt{\frac{8}{3}} = 1.633$, close to that of Re at 1.616.

One noteworthy twin feature among HCP metals is the prolific formation of $\{11\bar{2}1\}\langle 11\bar{2}6\rangle$ type twins in rhenium. As this is the dominant twin formed during any deformation in rhenium, understanding the orientations that will produce such a twin is very important to fully contextualizing the way in which rhenium deforms. Much like the $\{10\bar{1}2\}\langle 10\bar{1}1\rangle$ twin, formation of a $\{11\bar{2}1\}\langle 11\bar{2}6\rangle$ type twin produces an 61.9% expansion along the c-axis in

tension. This is an abnormally large amount of strain for an individual twin to accommodate and as such properly oriented grains do not need to fully twin in order to accommodate normal strain values. An additional twin somewhat commonly seen in Re is the $\{11\bar{2}2\}\langle 11\bar{2}3\rangle$ type twin, however it has been widely reported that during most deformation the $\{11\bar{2}1\}\langle 11\bar{2}6\rangle$ type twin makes up over 95% of the total twin types present in deformation (4). Figure 1.3 shows how the shearing of the crystals affect the atomic planes at the twin boundary for both $\{11\bar{2}1\}\langle 11\bar{2}6\rangle$ and $\{11\bar{2}2\}\langle 11\bar{2}3\rangle$ type twins. To best view the change in crystal orientation caused by the $\{11\bar{2}1\}$ and $\{11\bar{2}2\}$ twins, the crystal should be oriented such that the $\langle 10\bar{1}0\rangle$ direction lies parallel to the optic axis.

1.2. Rhenium as a Structural Material

Rhenium is found in the environment mixed together with molybdenum and various other ores as the ReS_2 sulphide or Re_2O_7 oxide (39). Rhenium has many uses as a high temperature structural material, as was briefly discussed previously, however its industrial uses mainly consist of reagents for oxidation catalysts as well as filament coatings in electronics and electrical equipment. (40)The toxicity of rhenium in the human body is thought to be very low, with medical studies showing that ^{188}Re is an effective radiopharmaceutical that upon regular ingestion, leading to a marked decrease in patient bone cancer pain with minimal toxicity (27). With what research is available on the toxicity of rhenium in its pure form, it is relatively safe to conclude that contact with rhenium during research or industrial work will not lead to detrimental health effects, rendering incidental exposure inert.

Working with elemental rhenium metal is difficult as it will readily form an oxide of Re_2O_7 above roughly 350°C. This oxide melts at 297°C and will sublimate at 362°C (8). Due to this oxide, rhenium experiences extensive hot-shortness, as the grain boundaries are quickly infiltrated by oxide. Rhenium can be hot worked within an inert argon or hydrogen-argon environment and is extremely formable during cold working (8). Luckily rhenium does not experience any hydrogen embrittlement and does not form a carbide, making its use for combustion chambers only oxygen sensitive (8). What few studies have been performed on the toxicity of Re_2O_7 has concluded that the white oxide, like the pure metal, is also non-toxic to humans (18) (20). However due to the lack of knowledge on Re oxide's effect in humans, experiments in this work at elevated temperatures were limited to in-situ high-vacuum environments.

1.2.1. Mechanical Properties of Rhenium

The extent of work on pure rhenium has been largely limited by its rarity and resulting high cost, lack of industrial applications, and relative recent discovery; first being isolated in 1928 from metallic ores. The main body of work into the general bulk mechanical properties has been sporadic since the 1950's and 60's when the first investigations were performed, save for a few niche studies (5) (7) (8) (41). Churchman (1960) investigated the work hardening and deformation mechanisms present in polycrystalline rhenium of different grain sizes using optical microscopy slip trace analysis and x-ray diffraction (XRD) in order to determine the operating deformation mechanisms (7). The results showed that slip was dominated by basal (0001) and pyramidal $(10\bar{1}1)$ slip with prismatic slip $(10\bar{1}0)$ occurring only secondarily, slip traces seen in Figure 1.4a). The relevant twin variants seen during uniaxial tension was dominated by

$(11\bar{2}1)$ type twins with $(11\bar{2}2)$ and $(10\bar{1}2)$ type rarely seen. Strain hardening rate and yield stress was shown to be proportional with grain size, smaller grains would yield at lower stresses with lower work hardening rates, Figure 1.4c) (7).

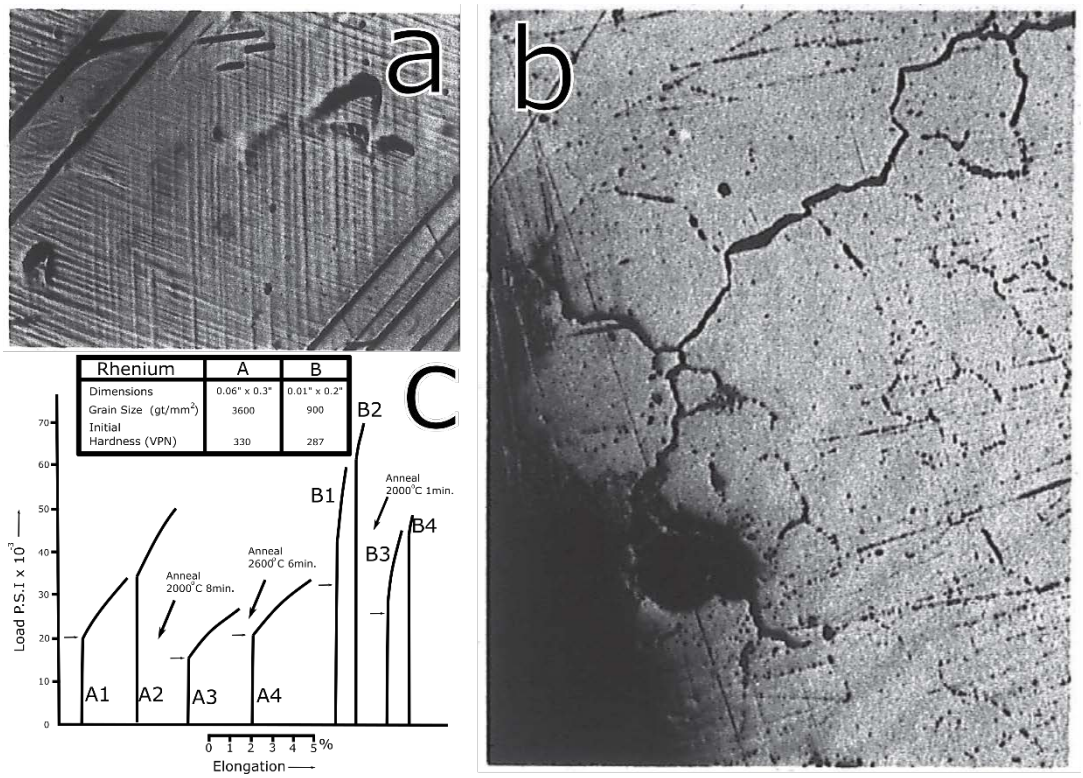

Figure 1.4: Work from Churchman describing the deformation behavior of rhenium at room temperature (7). a) Optical micrograph of $(10\bar{1}1)$ and (0002) slip bounded by twins. b) Optical micrograph extensive intergranular cracking in tension samples. This is commonly caused by hot-shorting and Re_2O_7 forming along grain boundaries (8). c) Reproduction of stress strain curves of different sample dimensions under tension. Quick anneals above 2000 °C have shown to greatly reduce the yield strength between loading segments. The validity of the mechanical data remains in question as it is contrary to general behaviors of grain size in material and previous research.

This is opposite of previous work by Sims, that has shown inducing smaller grain sizes through cold working and annealing rhenium would increase the yield strength (8). This discrepancy has been attributed by Churchman to be due to some unknown sample texture, methodological discrepancy or chemical imperfections collected from casting or annealing. While all these reasons are possible, Figure 1.4b) shows the large amount of intergranular cracking in tension samples. As previously stated by Sims, hot shorting and intergranular failure was a large problem in hot working and heat-treating Re. As such the discrepancies between these works is most likely due to imperfections in the annealing process that was used by Churchman. Besides reporting slip and twin mechanisms, which seem to be perfectly well founded, Churchman concluded his study by postulating that the high strain hardening rate seen in rhenium is due to intersecting prismatic slip dislocations, not due to impurities in his samples.

This does not address the fact that basal slip was more dominant than prism slip, and it does not address the role the high amount of deformation twinning plays in the high work hardening rate.

Later works on processing of CVD rhenium used in the creation of rocket propulsion chambers showed that the properties of rhenium remain extremely favorable over a large range of temperatures (18) (28). As rhenium has such a high melting temperature, these studies provide ample motivation for the use of rhenium in high temperature applications. These studies also investigated the possibilities of casting Re powder with a variety of other metals, such as tungsten and molybdenum. Due to the high melting temperatures and desperate properties, it was shown that it is indeed possible to cast various alloys and process them into useful shapes. As it stands much of the processing, alloying, and deformational microstructure work involving rhenium is very rudimentary when compared to other more widely used HCP metals, such as titanium or magnesium (42) (43) (44).

Another study using TEM imaging in conjunction with mechanical property discussion of rhenium used more advanced imaging techniques with diffraction pattern simulation to determine twinning response of deformed samples. The study by Peter et al. used conventional TEM imaging (Figure 1.5a), high resolution TEM using a JEOL 4000 EX microscope at 4MeV (Figure 1.5b) and diffraction analysis (Figure 1.5c-d) on the heavily deformed microstructure. The samples investigated were created through intermittent steps of cold rolling and annealing, with samples having been reduced by anywhere from 15% to 50%. The study showed that the dominant twin mode exclusively seen after deformation was the $\{11\bar{2}1\}\langle 11\bar{2}6\rangle$ from a 5% strained sheet of rhenium (6). The diffraction analysis showing $\{11\bar{2}1\}\langle 11\bar{2}6\rangle$ twin reflections overlaid over the matrix reflections is very nice work for comparison, as is the high-resolution imaging showing the $\{11\bar{2}1\}\langle 11\bar{2}6\rangle$ twin boundary.

However, much like in the report by Churchman, the experimental methodology performed by Peter is suspect. In order to make an electron transparent disk, dimple grinding in conjunction with ion milling was used by Peter, a method most commonly used for brittle, non-conductive samples not suitable for electro-polishing (45). The use of dimple grinding in ductile metallic samples should be avoided when necessary due to extensive induced deformation in ductile materials. Since it was reported as an acceptable experimental procedure, samples using dimple grinding and ion milling were created during the initial sample preparation for this work in order to determine the undeformed microstructure, seen Figure 1.5e. All samples using this method provided extensively twinned samples regardless of any other twin structure seen in initial EBSD or optical microscopy using traditional metallographic techniques (mechanical polishing with soft cloths or electropolishing with strong acids). As such it has been determined that dimple grinding rhenium specimens for TEM sample preparation induces too much deformation and is not valid for traditional TEM characterization. A full discussion of proper TEM sample preparation will be provided in the experimental section of this manuscript.

The latest in studies detailing the ways in which twinning accommodates strain in rhenium was performed by Kacher et al., showing that the $\{11\bar{2}1\}\langle 11\bar{2}6\rangle$ is indeed vital for deformation in Re, making up more than 95% of all twins observed in macroscopic compression samples (4). There were additional twins of the $\{11\bar{2}2\}\langle 11\bar{2}3\rangle$ and $\{10\bar{1}2\}\langle 10\bar{1}1\rangle$ types, but these were uncommon enough to only have a negligible effect on the overall deformation behavior. The main criterion used for evaluation of the propensity of twins to pass through the twin boundary was the *m*' value. Where *m*' is given in Equation 5.

$$m' = \cos(\kappa)\cos(\psi) \tag{5}$$

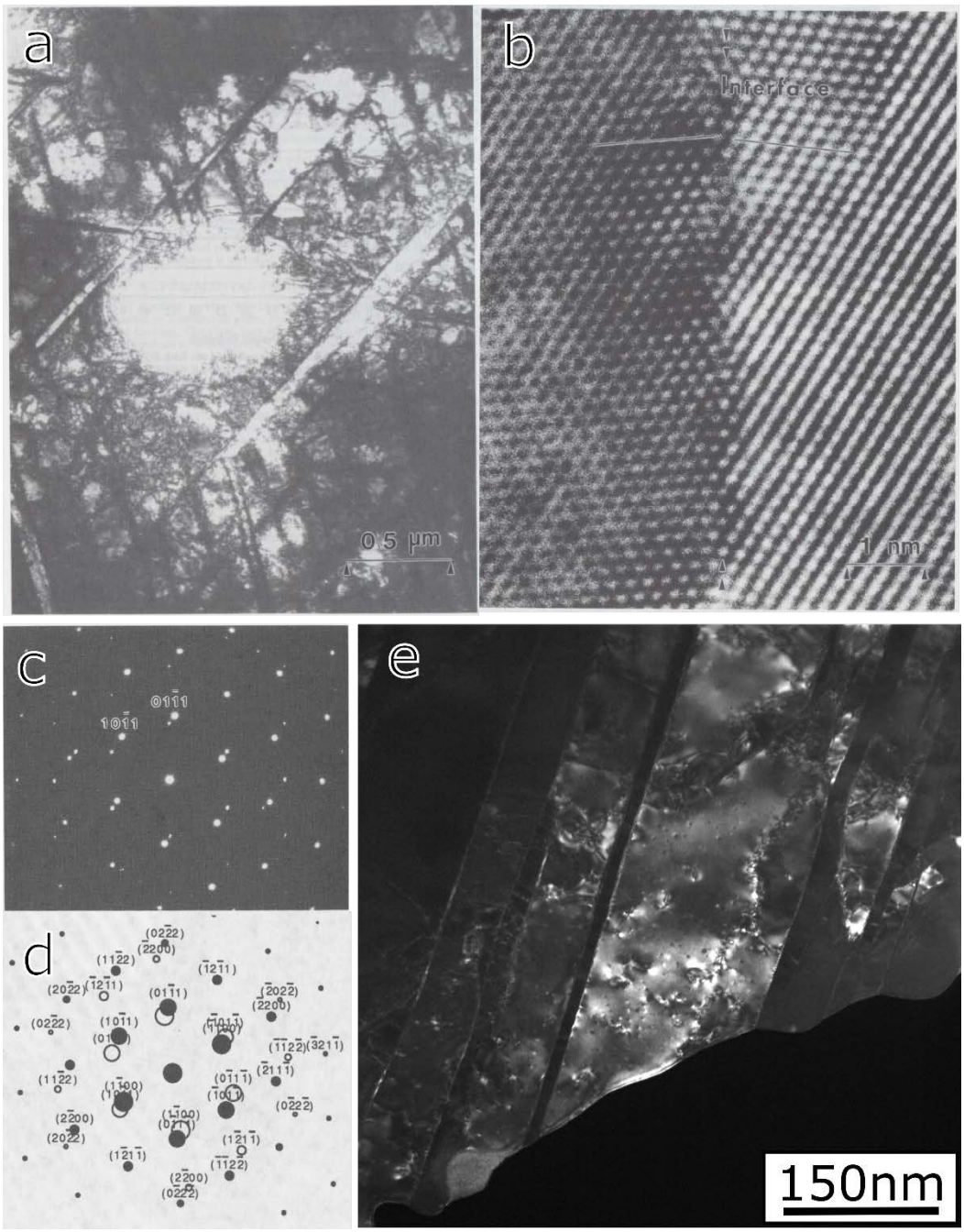

Figure 1.5: Relevant TEM work reproduced from Peter et al. (6) a-d). a) Re diffraction pattern along a $\langle 11\bar{2}3 \rangle$ zone axis showing twinning spots confirmed by the simulation in b). c) Low magnification image of electron transparent region clearly showing large twinned regions. d) High resolution scanning transmission electron microscope image showing the $\{11\bar{2}1\}\langle 11\bar{2}6 \rangle$ twin boundary. e) Nominally undeformed sample created for this study using sample preparation method from Peter et al. to look at an initial nominally undeformed microstructure. The number of long thin deformation twins and plastic deformation was not seen when preparing samples with jet-polishing.

Where κ is the angle between slip plane normal of the incoming dislocation system and the twin plane normal. The ψ angle is that between the shear and Burgers vectors of the two systems on either side of a grain boundary (46). This value has long been used as a reference for the propensity of twinning propagation in other metals such as Ti and Mg (47). However here it was shown that a high value of *m*' was not enough to ensure twin transmission, the associated values of cos(κ) and cos(ψ) have to also be suitably aligned, with the alignment of shear vectors was crucially important. The main result was that if grain boundary misorientation was lower than 25° the impinging twin could most easily transmit through the boundary.

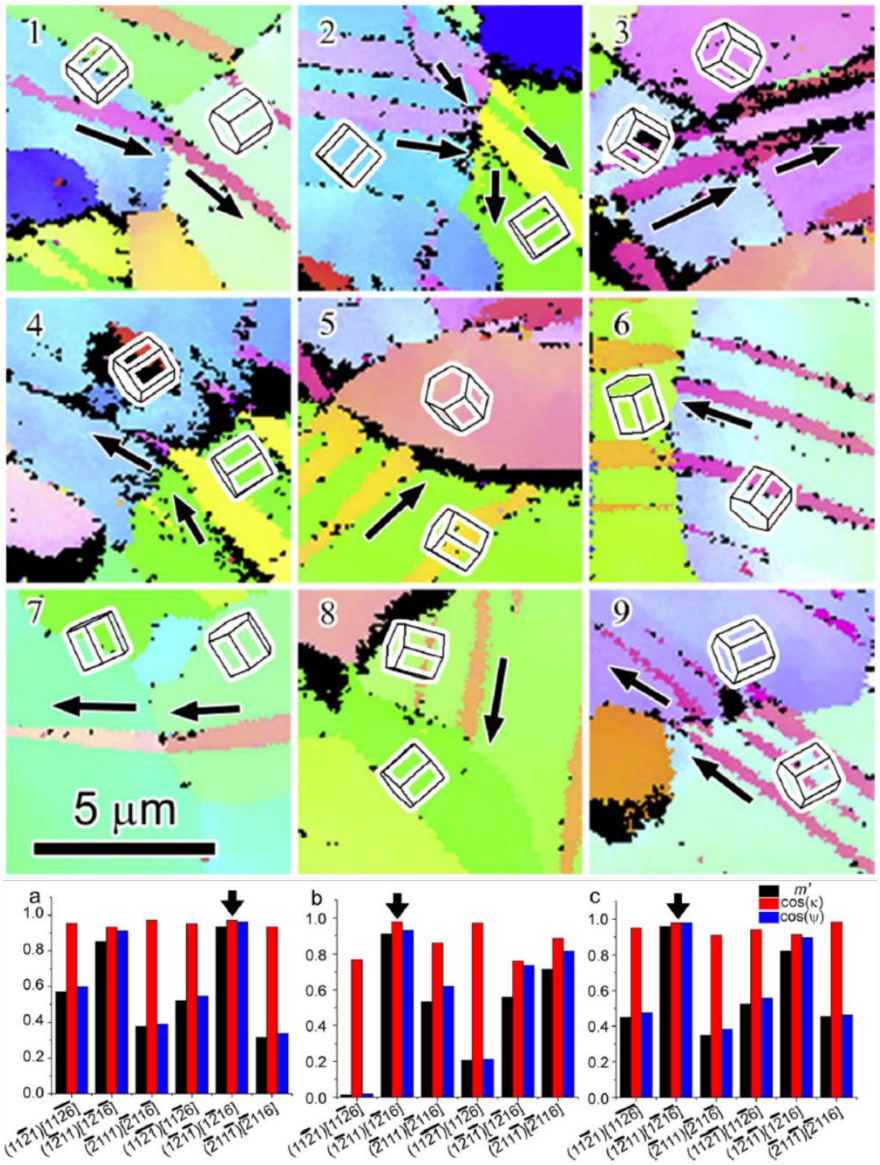

Figure 1.6: Work from Kacher showing twin transmission behavior between Re grains. (4) 1-9) Large selection of Re grains showing orientation relationship between twins transmitting through and arresting at grain boundaries. a-c) *m*', cos(κ), and cos(ψ) values of twins on the emission side of the grain boundary for emitted twins in a) IPF map 1, b) IPF map 2, and c) IPF map 7. The black arrow marks the combination of factors that has allowed twin transmission.

To summarize the most important information that is known about rhenium from the literature (excluding results based on suspect methodologies from different studies), it is unusual for a structural metal to show such extensive deformation twinning accommodating the strain for strains as large as 5%. In the case of rhenium, this is not unexpected, due to the large amount of strain accommodation possible of $\{11\bar{2}1\}\langle 11\bar{2}6\rangle$ twins, accommodating up to a magnitude of 61.9% total tensile strain along the c-axis (5). While Sims concluded in his study that rhenium has the highest work hardening rate of any known metal, this paper was published in 1955 with advancements in metallurgy providing a few new metals classes that closely mimic the natural properties of rhenium. Additionally, a full realization of the role dislocations play in accommodating strain within in the rhenium microstructure also remains to be described.

1.2.2. High-Manganese TWIP Steels as a Reference Material

Some insights into the mechanisms producing such high work hardening rates and ductility in Re can be found in a the class of steels known as TWIP (twinning induced plasticity) and TRIP (transformation induced plasticity) steels. Both TWIP steels and TRIP steels operate with the same fundamental strengthening mechanism, which results in an excellent balance between flow stress and high ductility (50). Application of stress to a TWIP or TRIP steel results in a dynamic strain aging process, which changes the microstructure during deformation both enhancing ductility and work hardening response (54). The general evolution of microstructure as a function of strain in TWIP steels involves deformation twinning and dislocation glide activating in competition to deform the crystal.

The name TWIP steels comes from the fact that TWIP steels extensively twin during deformation, allowing for extremely high ductility while still providing ample barriers to dislocation motion in the form of twin boundaries, resulting in very high initial work hardening which lowers as the strain increases (50) (51). These steels are a set of body-centered cubic (BCC) steels defined by having high manganese content, with additional solutes changing their deformation behavior in significant ways. There is also a class of high manganese steels known as TRIP steels that precipitate austenitic platelets within the microstructure during deformation, greatly increasing the work hardening of these materials by forming barriers for dislocation motion. While TWIP and TRIP steels operate using different mechanisms, the favorable properties come from the formation of barriers for dislocation motion.

The purpose of understanding either TWIP steels or TRIP steels is in service of better understanding the deformation seen in rhenium, as such the usefulness of understanding TRIP steels is negatable as no phase transformations have been observed in pure rhenium. In order to form a TWIP steel, TRIP effects must be suppressed, which can be done above a very specific weight percentage composition of Mn and C (51). As above this boundary line austenite is the stable phase, not allowing for the precipitation of austenite within a pearlite matrix (52). Equation 4, taken from Schumann et al., gives the minimum Mn content per C required to stay fully within the austenitic phase field (52).

$$wt.\%\, Mn = -20\, wt.\%\, C + 32 \tag{6}$$

This loose boundary is the basis for the minimum solute elements required to TWIP steel, while the maximum weight percentage of carbon is roughly 1.2% and Mn is between 30 wt.% and 35 wt.% (50). Having higher weight percentages of carbon leads to the precipitation of

cementite (a carbon rich phase common in high carbon steels) within austenitic regions. The phase boundary of the Fe-Mn binary lies within the maximum of 35% Mn (53). While this provides the basis for what constitutes a TWIP steel, many TWIP steels have TRIP processes included, as well as having a host of other solute constituents including vanadium, niobium, titanium, etc. While this work with alloy constituents as well as recrystallization microstructure and temperatures are all very fine interesting work, again the emphasis for studying this material is to provide comparison to the deformation mechanisms inherent in pure rhenium. As such, the body of research into the deformation response of TWIP steel along with the microstructural response to deformation will be shown.

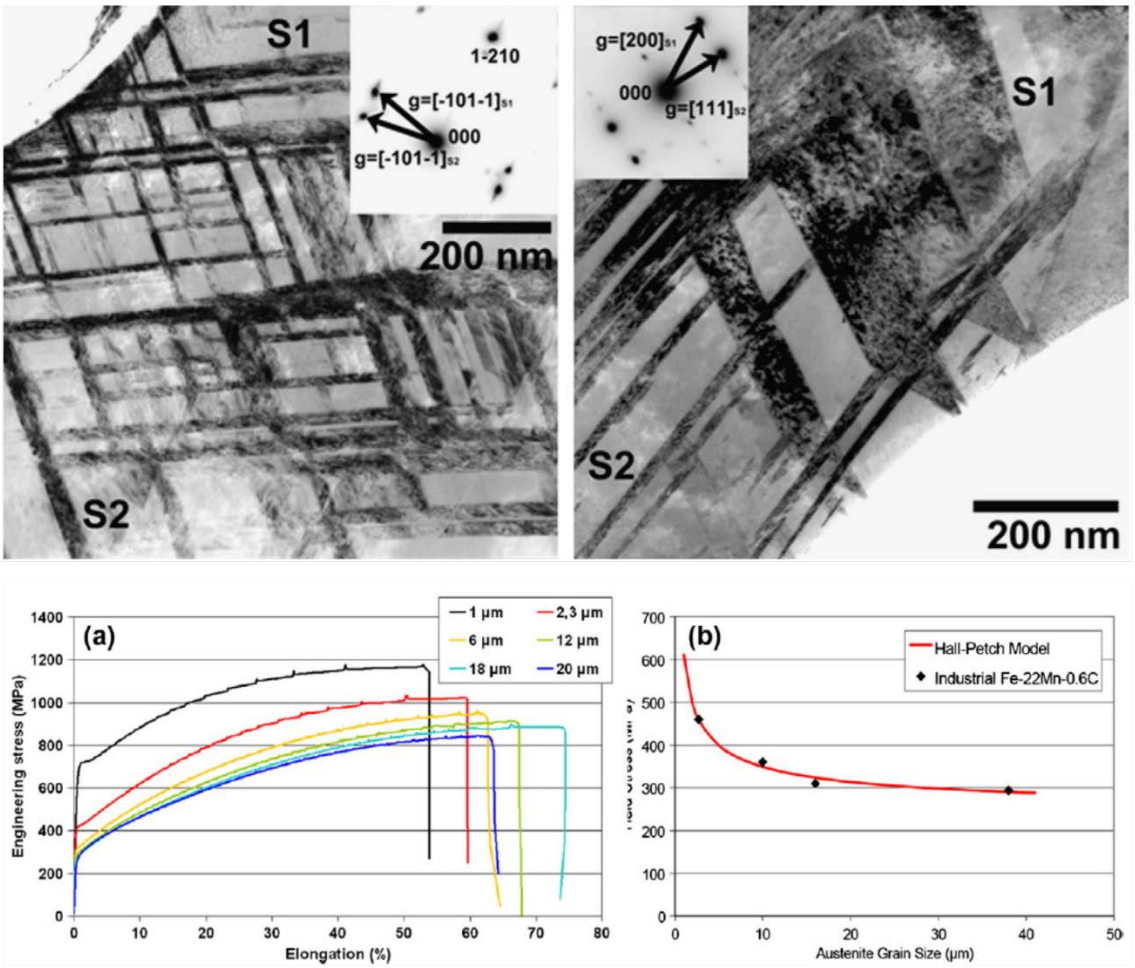

Figure 1.8: Top: greyscale inverted dark-field images showing both twins and some martensite within a thin iron disk. Bottom: relation of yield stress and UTS with grain size in industrial TWIP steel shows almost perfect Hall-Petch relationship (50).

As more twin boundaries are formed, there are many more barrier for dislocation motion, resulting in a high work hardening rate. The formation of twins in low stacking fault face-centered cubic (FCC) materials has long been described as a collection glide of intrinsic $\frac{a}{6}\langle 112\rangle$ Shockley partial dislocations on the {111} twinning fault (37) (50). As such the crystallography is well understood and not entirely relevant to understanding $\{11\bar{2}1\}\langle 11\bar{2}6\rangle$ in HCP rhenium.

However, the knowledge that lowering the stacking fault energy results in twinning in FCC metals and that the high work hardening and ductility is an interplay between microstructural changes and dislocation motion can be used as a bases for understanding the mechanisms in Re that lead to high work hardening rates and ductility.

1.2.3. Computational Studies on Pure Re

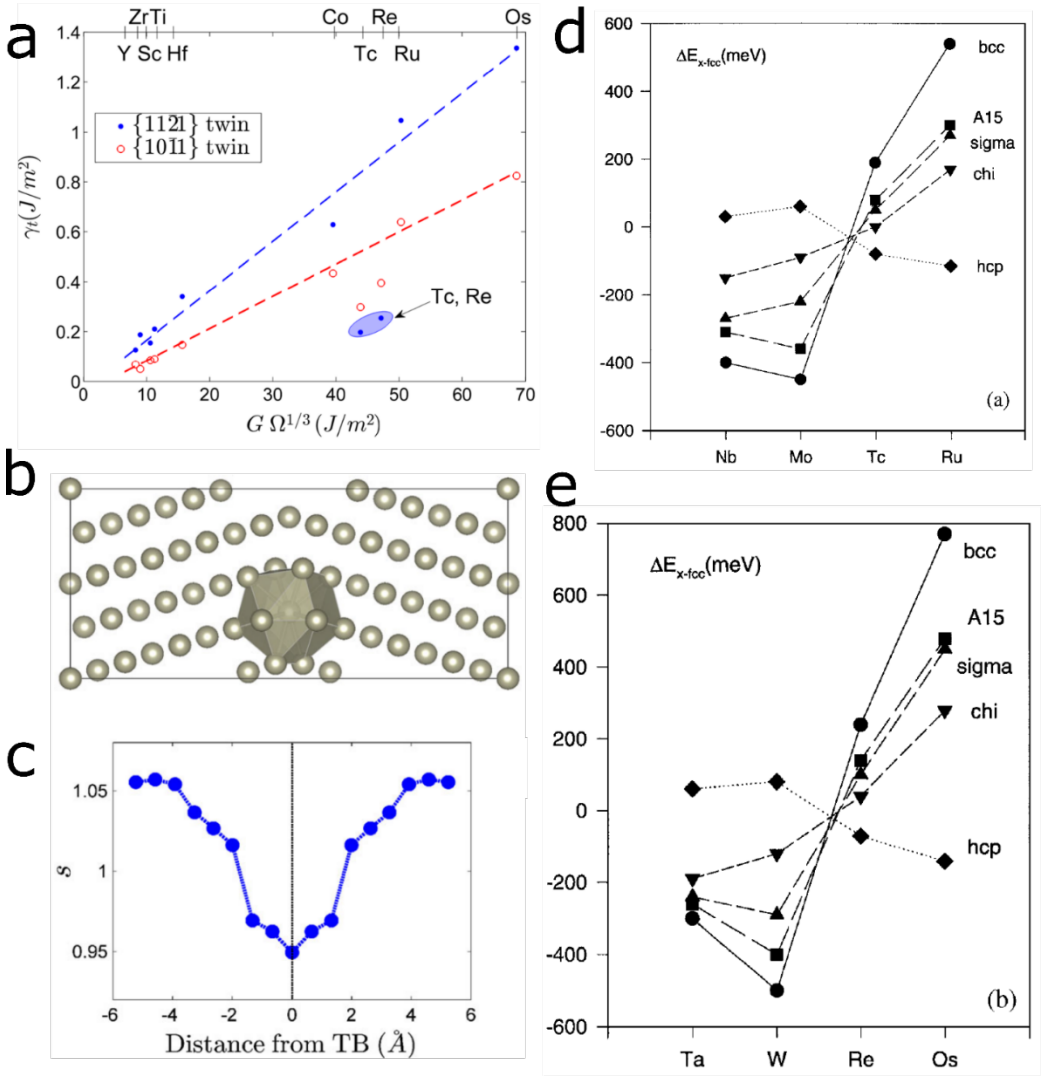

Figure 1.7: A summation of work from de Jong and Berne (9) (10). a) Calculated twin boundary energy for the {10$\bar{1}$1} and {11$\bar{2}$1} twin boundaries as a function of atomic number. Tc and Re shows extremely low twin boundary energies for {11$\bar{2}$1}⟨11$\bar{2}$6⟩ type twins when compared to all other HCP metals. b) Atomic arrangement of {11$\bar{2}$1}⟨11$\bar{2}$6⟩ twin boundary. c) bimodality parameter, s, as a function of distance to twin boundary. d-e) Calculation of stable structure of 4-d and 5-d elements. Not the stable structure changes from BCC to TCP to HCP around 4.6 $\frac{e}{at}$ in the d orbital.

While the extent of experimental studies on rhenium is lacking due to the cost and scarcity of the metal, it is often involved in computational work of other HCP or transition metals since it has such unique materials properties. Many of the studies involve tangential work that is subsequently applied to Re in order to have a broader impact for the work, without the initial project goal involving better understanding of Re primarily (48). Even though Mg, Ti and Zr are the primary discussion point of Yin et al., information can be gleaned from the calculation of different stacking fault energies in Re and dislocation core structure. Most notable from the work is that the basal stacking fault energy in Re is nearly an order of magnitude lower than that of any other stacking faults in Re, which may help explain the unique twin transmission displacements along the c-axis direction as seen by Kacher (4). Work completed in this dissertation will detail that the c-axis "jog" during twin transmission is present at all length scales, and is fundamental to the process of twin transmission in rhenium.

Other studies performed on understanding the twin boundary energies and atomic configurations along the unique $\{11\bar{2}1\}\langle 11\bar{2}6\rangle$ twin boundary present in Tc and Re showed that the $\{11\bar{2}1\}\langle 11\bar{2}6\rangle$ twin has an anomalously low twin boundary energy, when compared to any other refractory metal (49) (9). In conjunction with this, the $\{11\bar{2}1\}\langle 11\bar{2}6\rangle$ twin boundary was shown to form a distorted icosahedron structure, which is analogous to the tetrahedrally close packed (TCP) structure, seen in transition metal intermetallic compounds and in Figure 1.7. The well-known structures included in the TCP structural family are the σ, χ, and A15 Frank-Kasper structures, all of which have been shown to occur in transition metals and alloys with valence electron per atom ratios, $\frac{e}{at}$ (essentially the extent of d-band filling) between that of pure Re and W (10). Due to this unique twin boundary structure and additional density of states calculations made by de Jong, in Figure 1.7, it was determined that the d-band filling is the operative electronic structure consideration needed in order to create the unique twin boundary seen in pure Re and Re-W alloys (9). As such, a main goal of the alloy development work involves finding an chemically complex (also known as multi-component) or high entropy alloy that results in an HCP single-phase alloy with the d-band filling in between Re and W. This is an exceedingly difficult task, because of the very energetically favorable σ, χ, and A15 phases present in intermetallics formed in all of the refractory metal alloy binaries, limiting the composition at which single phase HCP solid solutions can be produced.

1.3. Experimental Techniques

In order to get an understanding of the mechanisms which cause the mechanical response seen in rhenium, many advanced (and some less advanced) imaging, microscopy, and mechanical testing techniques will be used. The vast majority of data collected (both in data size and amount collected) will be through the use of some type of electron microscope. Since a full description of the physics underlying electron microscopy could take up the bulk of this work (as the multiple textbooks and papers referenced can attest), the explanations of experimental techniques will overlook a more rigorous description of the mathematics and physics involved. The descriptions here will opt instead to briefly describe how the data is collected, and what information is required in order to adequately interpret and contextualize the collected data. Alternatively, all of the sample preparation methods and mechanical testing methods will be fully detailed in this manuscript, because (unlike for the physics of electron microscopy) a truly rigorous representation of the creation of test specimens is often overlooked in most published works, as the scientific merit is secondary when compared to collected data. Of utmost

importunate for the sample preparation for the Re work is the unique jet-polishing technique that was developed during the work. Without this development, large portions of the data collected would have been untenable. This chapter will be used as a reference in later parts of this thesis in order to describe the relevant information needed to understand and analyze the data collected. This is convenient as most of the sample preparation techniques for electron microscopy are the same throughout this work, regardless of how the sample was mechanically tested**.**

1.3.1. Optical Microscopy and Digital Image Correlation

Optical microscopy is the oldest observation technique material's scientists have had for understanding and characterizing the microstructures of materials. As such it is often overlooked and replaced with more advanced techniques, such as the plethora of electron microscope based techniques described in later sections. However, it is important to use optical microscopy in determination of sample quality and also strain state before a sample ever reaches a vacuum sealed electron microscope chamber. To this end, a Dino-Lite II brand digital USB Microscope was used to film the deformation during all macroscopic deformation. In order to provide contrast on the metallic surface, a speckled pattern of powdered printer ink was applied to the sample surface. Other methods of applying a speckle pattern include spray paint as well as creative uses of glue and alumina polishing powder. The method that gives best contrast depends entirely on the sample geometry and luster of the metal tested. In the case of Re, the dark color of the metal (much akin to tungsten) a bright pattern upon the darker metal provided best contrast.

Multiple feely available DIC software are available for use, with both "Shift" and "NCorr" having been tried used in this work. Shift is a quick but relatively basic Java based program that is stand alone, while NCorr is a Matlab based program that requires many of the expensive Matlab toolbox plugins in order to use, and having much of the code database out of date. The use of the software is simple and the software runs more quickly on systems with poor system specs than either NCorr or Shift. A full accounting of the software use and features should be left to the user manual (55). The output of the software contains strain measurements for each frame of the video, making aligning the 10-fps strain information (based on the initial video framerate) with the 10 Hz load-displacement data trivial. A comparison between the DIC-corrected stress-strain curves and the stress-strain curves calculated from the data output from the MTS Criterion system can be seen in Figure 2.1. While the difference here for Re is significant, for much softer metals (e.g. magnesium or titanium) the difference becomes negligible.

1.3.2. Metallographic Preparation, EDM, and Electropolishing Rhenium

In order to achieve the best sample surface for microstructure characterization multiple mechanical preparation methods were tried. This included dimple grinding followed by argon ion milling, as initially reported in Peter et al., with the subsequent microstructure showing heavily deformed structures despite a nominally undeformed initial microstructure. As such, many other chemical etching processes were tried in order to be able to produce a sufficiently polished surface while using a batch process involving chemical etching. While the use of many etchants prescribed in literature was untenable (such as using molten iron at 1600°C (56), or HF solutions due to safety concerns), there were sufficient alternative methods that a proper

electropolishing solution was eventually found. Among the failed etchants used without any electrical bias were: 70% lye (NaOH), 70% perchloric acid ($HClO_4$), 60% nitric acid (HNO_3), a 1:1 mixture of 70% perchloric and 60% nitric, and 70% sulfuric acid (H_2SO_4). None of the proscribed etchants from the Handbook of Metals Etchants that were tried sufficiently etched any rhenium samples after an hour of exposure with stirring.

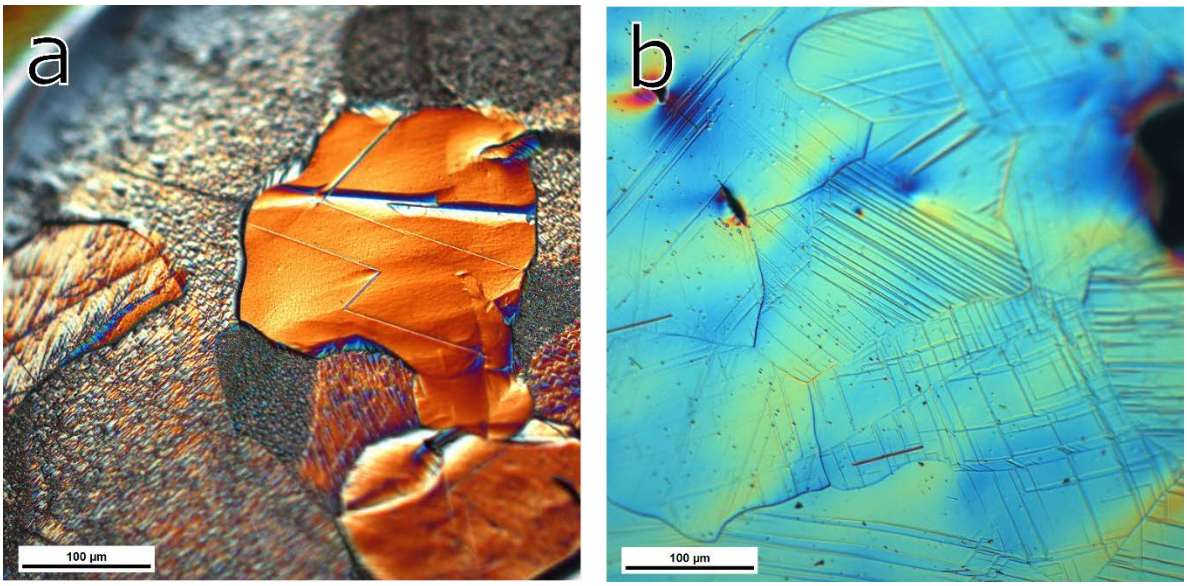

Figure 1.9: Polarized light micrographs, taken with a Leica DM 2500M, of the difference between a) 1:1 perchloric acid to lactic acid solution b) and the superior 2:1 perchloric acid to nitric acid solution. Note the extensive pitting seen in select grains, with properly specular grains also showing the initial stages of pitting along twins. b) Here twins and grain boundaries are readily seen. The sample is relatively flat and there is no pitting seen in this sample. Color differences are purely relative and only highlight twin/grain boundaries and sample topography.

Electropolishing was successful in producing electron transparent and metallographically excellent samples. Among the tried solutions were various solutions of pure perchloric acid, pure nitric acid, nitric acid with lactic acid, and sulfuric acid. A solution of 1:1 70% perchloric acid and 70% Lactic acid, 20% total acid, in a bath of methanol containing 50ml of 2-buytoxyethanol was used with an applied voltage of 85-100 V at -40 °C. A high quality surface was only produced from certain orientations, dependent on applied voltage.. The high end of the voltage regime will pit some orientations, and the lower end will form faceted structures in other orientations, as seen in Figure 1.9a). With the quality of sample produced, perchloric acid with lactic acid was abandoned in favor of a nitric acid and perchloric acid solution.

The best electropolishing solution developed was a 100ml perchloric acid, 50ml of nitric acid, 50ml 2-buytoxyethanol, with a balance of 1:1 ethanol and methanol finishing the solution. The baths used for jet polishing are nominally 500ml in total volume. The best polish will be achieved if the surface of the bath is as close to the sample as possible, necessitating less methanol and ethanol to be added to the total solution in order to achieve the proper volume. To meet this end, roughly only 110ml of ethanol and methanol each were added to the solution perchloric and nitric acid bath. As such this is a very highly acidic solution of 25% total acid, once taking the 70% initial concentrations of the acids into account. A voltage of 50 V is

nominally acceptable for the initial polishing steps, however as more samples are made the solution becomes more reactive, resulting in a need to lower the voltage to between 42 V and 47 V. Failing to do so will result in heavy pitting and unusable samples. The main downside of using a perchloric acid solution mixed with nitric acid is that one must account for the difficulties in using both. Perchloric acid must be used in a washable perchloric acid fume hood, as perchloric acid vapor condenses into crystals that are explosive when shocked (56). Nitric acid can also become highly reactive until finally exploding when it is mixed with any alcohols at room temperature, and as such keeping the electropolishing solution cold and neutralizing the solution after polishing has finished is of great importance (56).

Mechanical polishing was accomplished (both for some select rhenium samples and for all refractory metal alloys) using standard silicon carbide grinding paper starting at a low grit of 500, increasing incrementally to 800, 1200, 2400 and finally 4000 grit paper. Steps were increased when all scratches on the surface were aligned in the same direction, after changing sanding direction by 90 degrees in order to view the progress of material removal. Blasts of air were used to clear the surface of SiC particulate, then the samples were wiped with ethanol soaked cloth in order to fully remove SiC particles of the previous step. The samples were then polished for up to 12 hours using a Buehler MicroCloth brand polishing cloth with a solution of Buehler MasterMet 2 brand non-crystallizing amorphous colloidal silica suspension. This solution works well when light pressure is applied to the sample and the cloth is kept relatively dry after the solution has fully permeated the cloth. This method has worked very well on the refractory metal alloys, allowing for optical characterization as well as limited EBSD results.

In order to cut all Re samples and section samples after testing, electric discharge machining (EDM), also known as spark erosion machining, was used. The machining technique of EDM has long been used on conductive samples to make extremely precise cuts in virtually any geometry. The process functions through submersion of the machining target into a dielectric liquid with a large continuous flux, while applying a large electrical bias to the target. The machining tool consists of a continuous feed of wire that is also submerged into the dielectric liquid with an extremely large applied electric field. The dielectric fluid acts twofold: first, it keeps the target piece from overheating, and secondly it acts as an insulator until the wire approaches the target. When the EDM wire approaches close to the target, the fluid dielectrically breads down, causing a large discharge of current, liquifying the surface layer of the target (57). Through a continuous series of such discharge events, complex structures can be machined from the target. However, the nature of the EDM discharge leaves some significant surface damage, up to tens of microns deep depending on the material (58), from the different layers of melted material. While the majority of melted material is flushed away in the continuous fluid flux, a fair amount of liquid target recrystallizes on the surface with some additional contamination gained from the fluid. Luckily, since the recast layer is generally only a few microns thick, it is easily etched away and is of little concern in this Re study.

1.3.3. Scanning Electron Microscopy (SEM) Techniques

Scanning electron microscopy (SEM) and electron backscatter diffraction (EBSD) are extremely powerful techniques that allow for surface investigation of samples from mm scale down to nanometers. The SEM is powerful as the sample chamber can be operated at relatively low pressures, allowing for the chamber to be much larger than in other electron microscopes.

The electron beam itself is also relatively simple, consisting of a conical convergent beam of relatively low energy electrons (ranging between 1kV and 30 kV), resulting in minimal beam damage to samples (11) (12) (59). Images are formed using secondary electrons emitted from a sample's surface, which provides a very easily interpretable greyscale image that forms shadows and other contrast effects based on sample topology. Figure 1.10a) shows the different types of radiation emitted from a sample when creating an image using SEM secondary electron, however other techniques have been developed to take advantage of all the different types of radiation emitted from the sample. The auger electrons and x-rays emitted from the sample are dependent directly on what species of elements are present within the sample and are used to characterize chemical content.

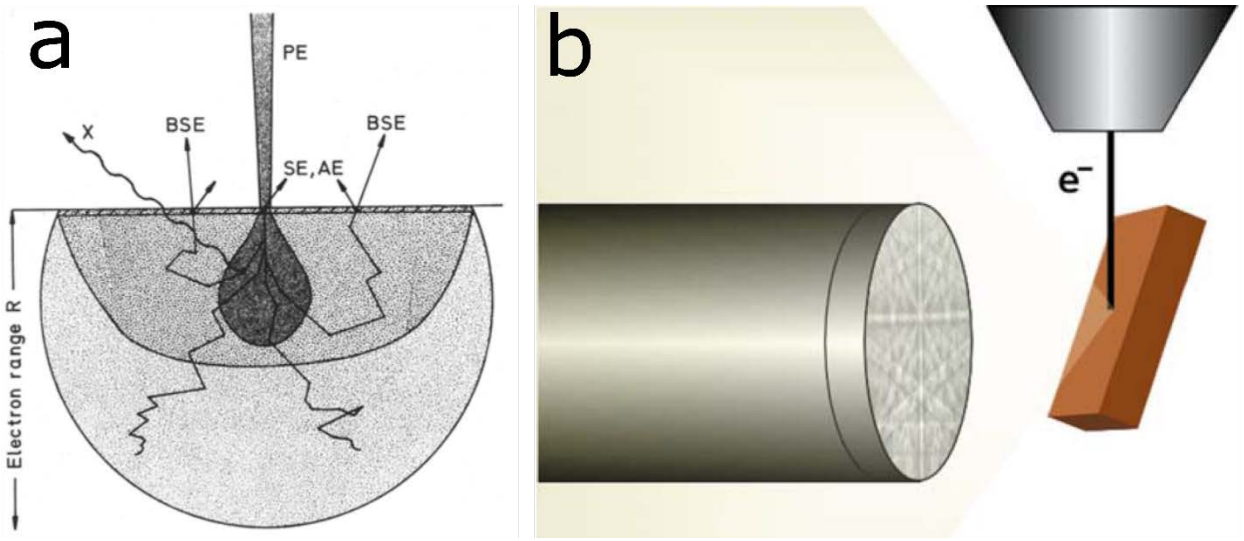

Figure 1.10: a) Cartoon of the interaction body of electrons in a sample surface and various types of resulting emitted radiation (11). b) Geometry of an EBSD scan with inset diffraction pattern on the EBSD detector. (12)

A cursory explanation of how of how EBSD functions is useful for readers completely unacquainted with this work to understand the significance of the results, however to truly understand the phenomenon of EBSD a deeper reading into the underlying physics of diffraction is needed (60). The backscattered electrons are the result of an inelastic scattering event, where the electrons lose energy, followed by an elastic scattering event, where the electrons do not lose energy when interacting with the crystal (11). The backscattering event allows for the electrons to undergo a Bragg reflection, imparting information about the crystal structure and orientation. The resulting electron backscatter pattern (EBSP), also commonly known as a Kikuchi pattern due to its many intersecting Kikuchi bands (seen in Figure 1.10b), is unique for each crystal and orientation and gives reciprocal space information. A pair of Kikuchi bands in an EBSP represents a unique family of planes diffracting the electrons. The spacing between Kikuchi bands is unique to each set of planes and known as the reciprocal lattice vector, $\vec{g}$ vector, where $\vec{g}$ is defined in Equation 4.

$$2d \sin\theta = n\lambda \; ; d = \frac{1}{\vec{g}} \tag{7}$$

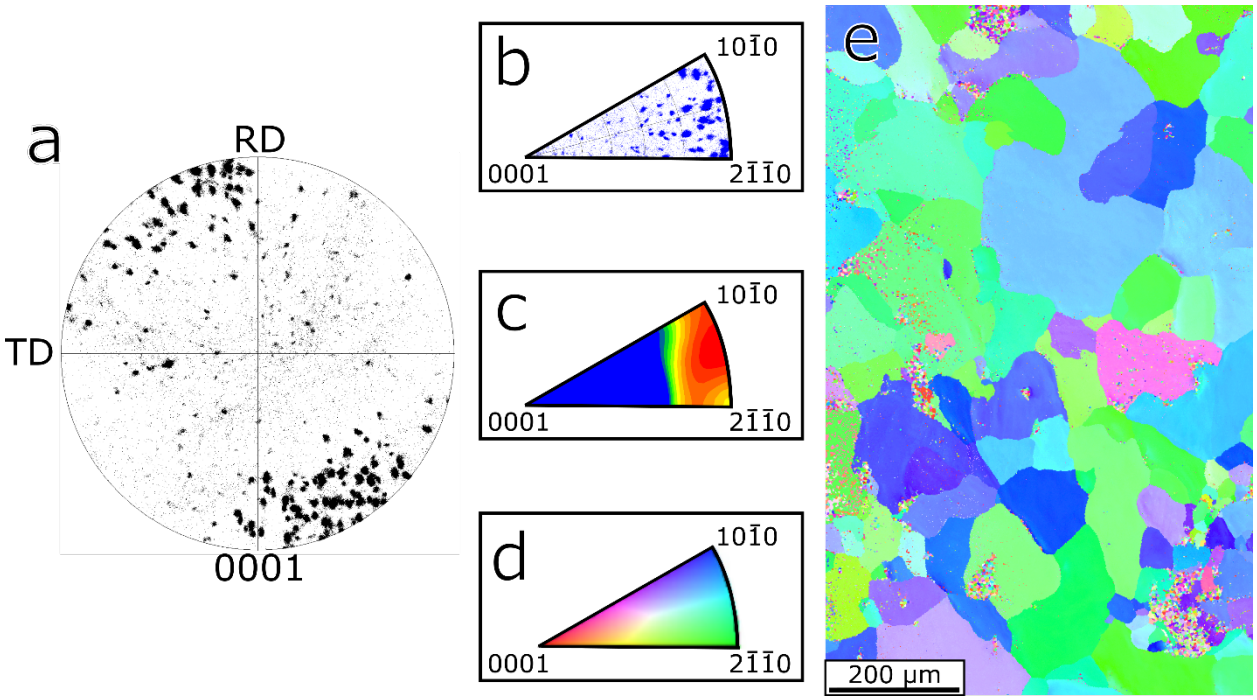

Figure 1.11: Various methods for detailing the same data taken from the current research detailing the types of data used in EBSD analysis. This data was chosen to be easily interpretable for instruction. a) 0001 Pole Figure. RD and TD is the conventional naming scheme of "Rolling Direction" and "Transverse Direction" defining sample geometry. b) Inverse Pole Figure reducing the full pole figure to the smallest possible symmetry cell. c) Same data in b) shown as a color gradient instead of individual spots. d) Inverse pole figure map along the z direction showing the orientation of the colors in the EBSD map in e).

Here θ gives angle between the atomic planes, *d*, and the incoming radiation, with a wavelength of λ (60). All of these values can be solved for individually, but in conjunction they can be used to solve for the orientation of any EBSP. This is due to the fact that Kikuchi bands will intersect together along certain crystal orientations (known as a zone axis), based on the allowable diffraction conditions of each crystal. Solving for crystal orientations then becomes a trivial exercise of matching the observed Kikuchi bands, including lattice spacing and allowed reflections, to a known crystal structure. The orientation of a crystal is often represented as a colorized map with accompanying pole figures and inverse pole figures, as seen in Figure 1.11.

To understand the information given in Figure 1.11, one first must be acquainted with poll figures, a method of representing 3-D crystallographic information in a 2-D diagram. This can be easily found in any crystallography book (24). With that information in hand, one can easily recognize that Figures 1.11a-c) are all representations of the same data (mapped in Figure 1.11e), with Figure 1.11a) showing the whole pole figure where spots in the center of the plot representing a [0001] direction normal with the sample surface. Due to the HCP crystal symmetry having a 6-fold rotation axis around the [0001] zone, if one were to decompose the whole pole figure into the symmetrically identical orientations, one is left with Figure 1.11b), an inverse pole figure (IPF), where Figure 1.11c) is simply a map averaging the occurrence of points in the inverse pole figure. In cubic metals, the IPF angle that gives the lowest symmetry

angle of the crystal will be 45° instead of the 30° shown here. Finally, the last IPF gives the map color shown in Figure 1.11e), where colors represent the orientation out of plane, i.e. an IPF Z map. While EBSPs are a very detailed piece of information one can use to discover anything from sample space group, to the elastic strain on the sample, it is often said that EBSD is the only experimental technique where one routinely throws away all the data. That being said, in this work, as with the overwhelming majority of research involving EBSD, the EBSPs were not saved in this work and the analysis is performed on the collected IPF maps and pole figures.

1.3.4. Transmission Electron Microscopy (TEM)

Transmission electron microscopy (TEM) has been in constant use since the early 1960's at the University of California, Berkeley for the characterization of materials (61). The main strength of this technique is the ability to see nano-scale features which cannot be resolved by any other techniques, this includes dislocation, stacking faults, nanotwins, different precipitates, etc. While this is extremely powerful in understanding localized nanoscale phenomenon, there is always the caveat that what one sees during TEM analysis may not fully represent the macroscopic behavior of the material, but can help garner insights into the fundamental mechanisms responsible for macroscopic behaviors. While it is true that TEM samples are strongly influenced by the enormous surface to volume ratios of the specimen at electron transparency, this is of little effect for ex-situ or in-situ TEM dislocation analysis. While it is true that TEM imaging has a lack of statistical studies and any fatigue or large statistical studies would be prohibitively expensive and time consuming, it is also true that there is no other technique allows for the possibility of imaging dislocations as they deform a crystal with unrivaled clarity. Conventional TEM bright-field (BF) and dark-field (DF) images in conjunction with the crystal's diffraction pattern (DP) are used to analyze the twin morphologies and the character of dislocations in the crystal. The full details of how images and diffraction patterns are formed will not be described here and are best left to the textbooks of Williams and Carter or Fultz and Howe (45) (62). However, it is useful to briefly describe the BF image as being the image formed from those electrons that have not interacted with the sample, and the DF image being the image that comes from diffracted electrons.

The basis of dislocation analysis in TEM foils is known as “G dot B” ($\vec{g} \cdot \vec{b}$) analysis. This is quite simply due to fact that by taking the dot product of a possible dislocation Burgers vector within a TEM image, $\vec{b}$, and the diffraction condition of the image where the dislocation is viewed, $\vec{g}$, one can determine the Burgers vector of the viewed dislocation. In order to make this determination, one has to image a dislocation in a set of different diffraction vectors, and when the dislocation is no longer visible one knows that $\vec{g} \cdot \vec{b} = 0$. The possible Burgers vectors, $\vec{b}$, that can be used in this determination are known from the crystal structure as was detailed in previously, and it should be noted that the dot product can be performed in 4-index Miller-Bravais notation without the need for conversion to conventional 3-index notation (31). Needless to say, for HCP metals the main two possible Burgers vectors are $\vec{b} = \frac{1}{3}\langle 1\bar{2}10\rangle$ and $\vec{b} = \frac{1}{3}\langle 1\bar{2}13\rangle$. The planes each dislocation operates on is determined by tilting the sample to known zone axis and viewing the orientation of the dislocation line relative to the possible operating planes.

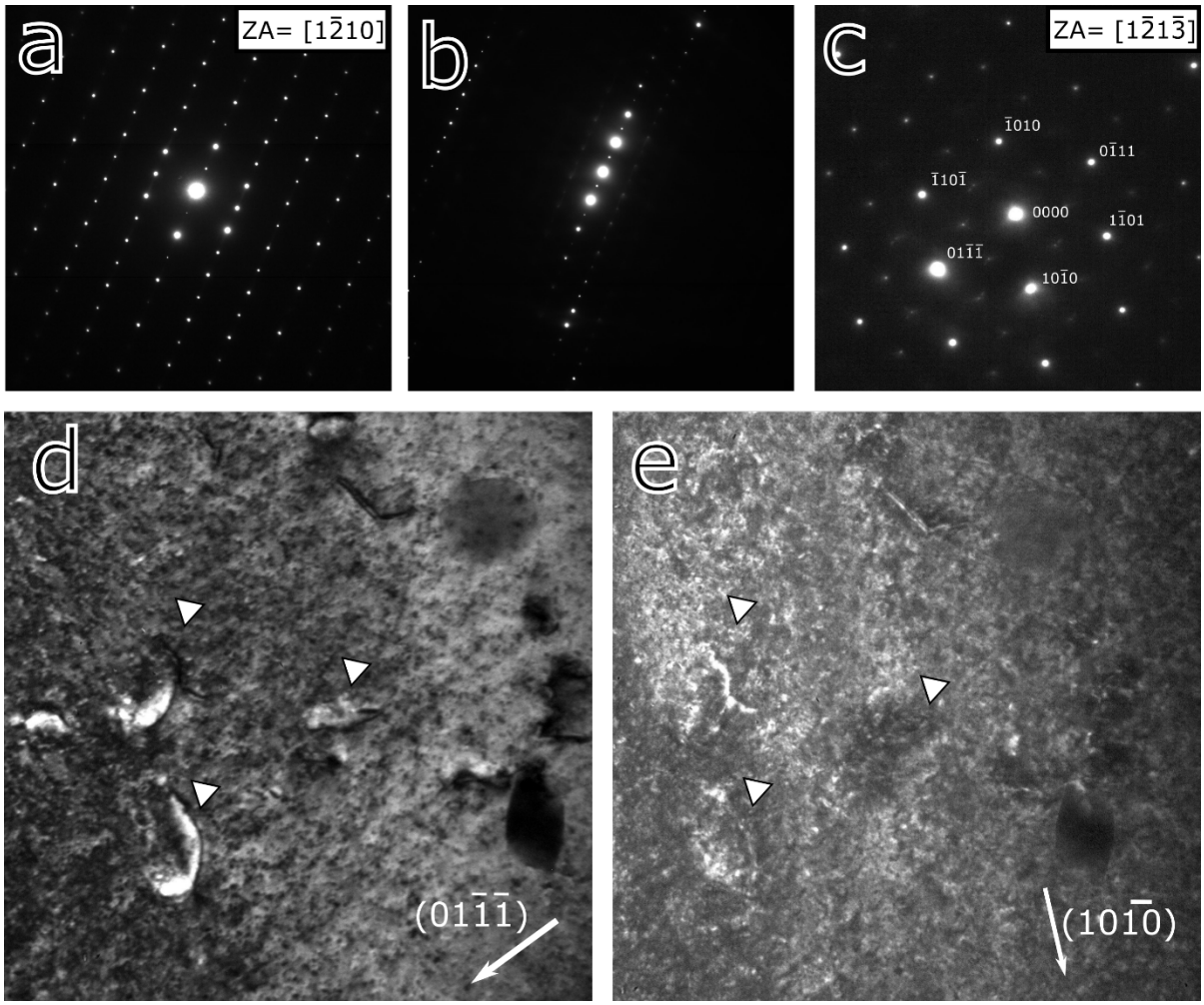

Figure 1.12: a) Laue condition suitable for $\vec{g} \cdot \vec{b}$ analysis. b) A close two-beam condition that is used for $\vec{g} \cdot \vec{b}$ analysis. c) Off zone axis DP were $\vec{g} \cdot \vec{b}$ analysis was able to be performed. d) DF TEM image of three visible dislocations using reflection condition from c). e) Same dislocations in d) this time being invisible. a-e) taken from Re.

Figure 1.12 shows a few diffraction conditions for making a $\vec{g} \cdot \vec{b}$ determination in an HCP crystal. The zone used to easily perform "g dot b" analysis is the $\langle 1\bar{2}13 \rangle$ zone as it allows for determination of both types of dislocations by using all six first order reflections; a detailed table showing all possible combinations of $\vec{g} \cdot \vec{b}$ can be found by Partridge (3). When choosing a reflection condition for $\vec{g} \cdot \vec{b}$ analysis it is important to have an acceptable diffraction condition, either being on a perfect Laue condition, Figure 1.12a) or two-beam condition Figure 1.12b). A two-beam condition is much preferable for $\vec{g} \cdot \vec{b}$ analysis as it allows for the diffracted beam to contain the maximum amount of intensity. For comparison Figure 1.12c) shows an off-zone axis DP, where it was still possible for the $\vec{g} \cdot \vec{b}$ analysis to be performed successfully. It is a common occurrence in metal foils to be slightly bent, or sensitive to local strains due to holes in the foil. This will result in slightly off-axis diffraction patterns when translating around a

sample. Finally, a comparison between DF images showing an "invisible" dislocation, where $\vec{g} \cdot \vec{b} = 0$, and a visible dislocation is seen in Figure 1.12d,e).

Some scanning transmission electron microscopy (STEM) imaging will also be performed in this work. The optics of the STEM imaging technique bear much in common with that of conventional SEM techniques. Instead of collecting the secondary electrons from a sample surface, the image is created from the high voltage transmitted electrons. In fact, new techniques have combined SEM and STEM imaging by incorporating annular dark-field (ADF) or high angle annular dark-field (HAADF) STEM detectors within a conventional SEM while using electron transparent sample (63). For this work, only the HAADF STEM technique will be utilized. There are a few key differences between HAADF STEM imaging and conventional TEM images that should be taken note of. First the HAADF STEM detector is simply a current collector surrounding the transmitted BF beam at very high angles. These very high angles (generally above 3° to avoid Bragg diffraction) are used in order to reduce the effects of diffraction contrast while maximizing the Z-contrast within the images. When the beam is rastered across the sample any electrons scattered at very high angles will be collected on the HAADF detector. When many scattering events happen at a given scan point, the resulting pixel within the STEM image will be bright. As such this technique allows for very easy interpretation, as the nearly all dynamical effects and diffraction interactions between the beam and crystal are removed by using the high angle scattered electrons. A full description of the physics of HAADF stem is left to the reader (45).

1.3.5. Indentation Stress Strain Analysis

Indentation has long been used for material characterization, due to its ease of use, high throughput and site specificity of the test. With the advent of extremely sensitive piezoelectric controllers, new methods of indentation allowed for the characterization of indents on the order of nanometers and micronewtons. The Oliver-Pharr method became the standard method for finding the indentation modulus and hardness of samples at the nano- to micro- scale (13). To quickly summarize, this method involves first finding an area function profile for the indentation tip as a function of depth. This is usually performed by performing indents at increasing depths on a known modulus sample, usually fused silica with an elastic modulus of 72 GPa (13). Knowing the modulus, one can solve Equation 8 for the area constants given the unload stiffness at each depth, and the assumed modulus of the fused silica. Then with the calibrated tip area function one can test whatever material one has in to find the required modulus and hardness from load-displacement data. It should be noted that this method works for any of the common tip geometries (Berkovich, cube corner, spherical or conical). One must be careful when taking the calibrated area for granted, as many materials will either "sink-in" or "pile-up" material surrounding the indentation tip, causing misleading area values, as shown in Figure 1.13c) (64). In order to combat this, optical microscopy in addition to SEM imaging can be used to get a projected area or contact radius measurement which is proper for indentation hardness and modulus measurements.

$$A(h_c) = C_0 h_c^2 + C_1 h_c^1 + C_2 h_c^{\frac{1}{2}} + \cdots + C_8 h_c^{\frac{1}{128}} \quad (8)$$

$$h_c = h_{max} - h_s \; ; \; E_r = \frac{\sqrt{\pi}}{2}\frac{S}{\sqrt{A}} \; ; H = \frac{P_{max}}{A} \quad (9)$$

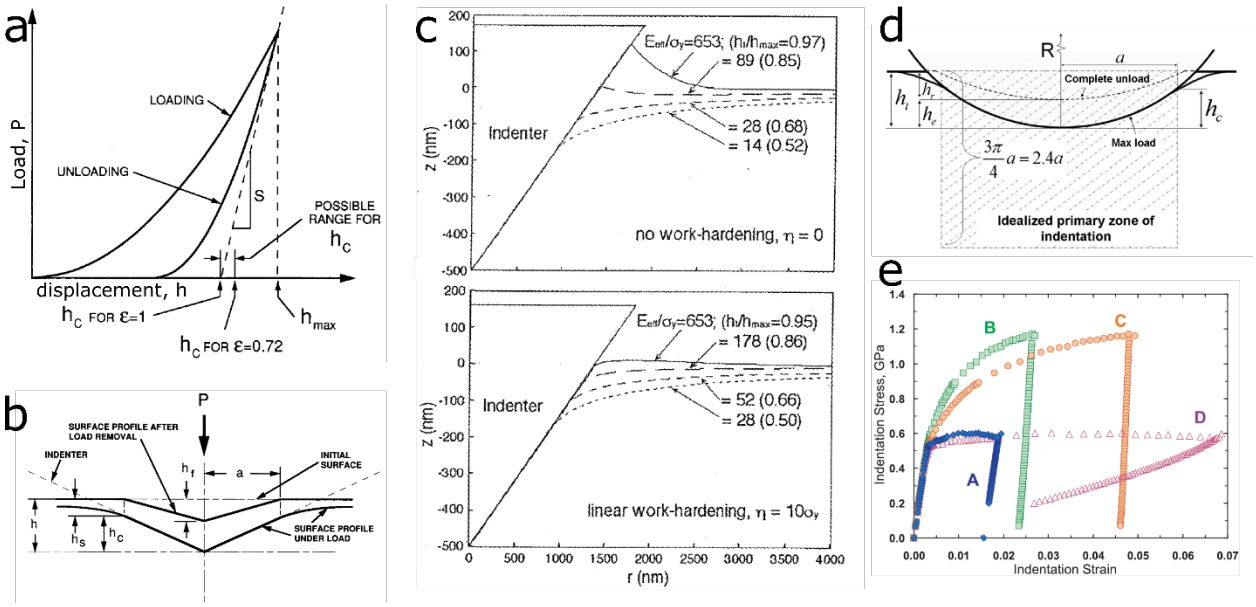

Figure 1.13: Images taken from Oliver-Pharr a-c) and Pathak et al. d-e). a) a typical load displacement curve with relevant values. b) Description of section of a typical indent. c) Simulation of indent pile-up and sink-in. d) Same as for b) but specifically designed for use in indentation stress-strain analysis. e) Effect of different values for indentation strain and contact area in aluminum indentation stress-strain curves. Note large variations based on method. (13)

More recent developments have included adding an oscillating displacement (generally only 2nm total) during indentation, that allows for instantaneous stiffness measurements, often (among other acronyms) referred to as continuous stiffness measurement (CSM) (64). This procedure allows for a much easier method for determining the indentation area function, as the oscillations imposed upon the indentation tip during testing result in a measurement of the system stiffness. While there are problems with this technique inherent to introducing a dynamic displacement profile onto a mechanical test, it allows for the unique ability of having a value for elastic modulus for every corresponding value of indentation depth. It must be noted that pileup and sink-in is not a linear process, requiring measurements of true contact radius/area to be made at multiple displacement maxima if one is to use a true measure of indentation strain derived from CSM. When coupled with a spherical nanoindentation probe, the ability to achieve an indentation stress-strain profile is possible (65) (66). The method for calculating the indentation stress-strain all derives from Hertzian mechanics (67), with a few key assumptions applied based on the geometric interplay of the spherical indentation probe and the sample surface.

From the work of Pathak et al., changing various assumptions can have a large effect on the resulting stress-strain curves. It can be seen that the most important value required for accurate stress-strain curves is the indentation contact radius, *a* (66). The contact radius gives not only the area of contact, which leads to the indentation stress, but also the idealized primary zone of indentation, which is used to describe the indentation strain. Pathak showed that Equations 6, derived from Hertzian mechanics, gives the base method for identifying the contact radius during any point of indentation, with Equations 7 giving the indentation stress and strain (66). Where P is the applied load, R_i is the indenter radius, S is the dynamic stiffness given through use of CSM,

and h_e is the elastic indentation depth, which is approximated as equal to h_c as given in Equation 7.

$$a = \sqrt{2h_eR_i - h_e^2} \; ; \; h_e \approx \; h_c = \; h_t - \frac{4}{3}\frac{P}{S} \tag{10}$$

$$\sigma_{ind} = \frac{P}{\pi a^2} \; ; \; \varepsilon_{ind} = \frac{4}{3\pi}\frac{h_e}{a} \; \approx \; \frac{h_c}{2.4\,a} \tag{11}$$

As well defined and powerful as this indentation stress-strain method is, there are many difficulties with how one will actually calculate the indentation strain and contact area from a set of indentation data (65). This is well detailed by Pathak, concluding that one must be skeptical when looking at data from this method. Invariably during testing, pop-in events (large displacement bursts in the load-displacement or stress-strain curves) will occur. These pop-ins can all result from cracking around the indenter tip or plasticity events such as twinning or dislocation plasticity, or even phase transformations of material under the indenter (68). With so many different types of effects that can cause anomalies in the indentation curve, it can be quite difficult to analyze indentation data, even though the acquisition is relatively easy. However, due to the ability for site-specific very localized testing and well-understood stress state under spherical tips, nanoindentation with indentation stress strain data is very useful for comparative studies between samples having very heterogeneous local microstructures. As such it will be used later in this work during the development of chemically complex qausi-high-entropy refractory metal alloys that show two phase regions with very different properties.

Chapter 2

Microstructural Evolution of Re using Compression

Uniaxial compression testing has long been used in order to understand the mechanical response of materials. Some of the earliest procedures involving a systematic methodology for describing the materials properties of metals in terms of stress-strain go as far back as the early 1940's (69). The current standard in mechanical testing to determine material's properties has become the uniaxial tension test, due to the ability to determine ductility, necking, work hardening rates, elastic modulus, creep properties, etc. Compression tests still provide many benefits as an experimental technique when one understands the limitations of the data one can collect. In terms of testing Re and Re replacement alloys the main benefit of compression testing is the lowered cost of sample manufacturing. Since there is no grip section required as in tension samples, much material is saved per test. Tension test samples can have upwards of 70% of the total volume of material dedicated to non-data viable material. While in compression samples, since the whole sample is compressed, with no need for a grip section, the maximal amount of material is saved for microscopic investigation later.

The drawbacks of compression testing are inherent to the sample geometry and the effects of compressing a material that are constrained by two incoming platens. First of the characteristic deformation behaviors seen in compression samples is buckling. Buckling is defined as a failure of the sample due to inelastic or inelastic instability along the column length, resulting in non-axiality of loading. (70) While there are three distinct ways this can occur, all buckling involves a bending of the column with fixed end-points, resulting in an applied load non-representative of materials strength. It should be noted, that the stress required for buckling is inversely proportional to the square of the column length. As such, in order to avoid buckling, it has been recommended that high strength materials (such as rhenium) should be tested with a gauge length of between 1.5-2x the diameter of the cylindrical specimen.

The other main characteristic deformation mode seen in compression samples is known as barreling. As the name would suggest, barreling is the restriction of the sample end regions due to high contact friction, resulting in nonuniform transverse deformation in the middle of the gauge section (70). The resulting shape looks very much like a barrel used for aging wine or beer, hence the name. Due to fixing the end regions of the sample as well as the nonuniform transverse deformation seen in barreling, nothing can be said about the work hardening behavior of the sample. It can be readily seen in the samples tested in this work, or in any other work involving compression, have nonuniform cross sections during uniaxial deformation, leading to an unknown true stress in the gauge. To compound upon this, the end regions are constrained, containing a much smaller cross-sectional area, and a higher resulting stress (generally near to that given by the engineering stress taken from the initial area). However, despite these detrimental intrinsic behaviors of compression testing, the high absolute strains that one can achieve with compressive strain allow for a microstructural investigation that is not possible using tension.

2.1. Experimental Procedure of Macroscopic Compression

Material was purchased from Rhenium Alloys Inc. in the form of a 3mm diameter 20.3 cm long annealed rod. Pure rhenium powder was pressed into a 6.4cm square bar and sintered at 2350 °C. 12 rolling passes follow by 3 swaging passes with intermittent 1650 °C heat treatments were performed. The resulting Re rod was straightened and ground to 3mm diameter with a final 1650 °C anneal. The annealing steps must be performed in vacuum or under argon to temperatures exceeding the roughly 1600 °C recrystallization point (18) (8). The resulting rod was taken and cut using EDM into 6mm segments. As previously mentioned, some concern was placed on the effects of the EDM process inducing a melt layer and large thermal shocks, however as reported previously reported (41) (71), rhenium is essentially immune to thermal shock. Conventional mechanical diamond saw cutting methods were tried on initial test samples, however extensive damage was seen after surface polishing. The damage seen from mechanical cutting is unsurprising when considering the report from Kacher (4) showing that twins can easily transmit through grain boundaries. Thus, any mechanical cutting of rhenium should have a much larger effect on sample microstructure than thermal induced shocks. As a result of this initial sample formation testing, all subsequent samples, for all future studies, were cut using EDM to stop any possible damage inducement from sample creation. Additionally, due to its precision, the sectioning of post-deformation samples was also prepared using EDM, where the final thickness of 3mm disk sections could be as low as 75μm thickness. Even if the recast layer is as thick as 20 μm thick as seen in tool steels (72) (which is unlikely due to the unique properties of Re), any electropolishing performed on the sample will remove the damage layer leaving pristine Re metal with no mechanically induced deformation.

2.1.1. Methodology of Compression Testing

Compression samples were polished on each end to 1200 grit SiC sandpaper in order to remove the damage layer induced from EDM on the surfaces touching the platens. Great care was taken to ensure that polishing the end surfaces resulted in planarity orthogonal to the loading direction, as to not include contact between compression platens and sample surface. Any deviation from orthogonality with loading direction, or incline of the end surface will result in anomalies appearing in the load displacement data due to the fact that only a portion of the assumed initial area is under load. Loading was performed on an MTS Criterion Universal Test System with a strain rate of 0.005 mm/s. For accurate strain readings the compression sample surfaces were speckled with ink to provide contrast as fiducial markers. The fiducial markers are used in conjunction with DIC software detailed previously [*Optical Microscopy and Digital Image Correlation*]. DIC software was especially important on low strain segments, as the load frame stiffness became a large factor during initial loading, as well as for maximum strains tried, as the platens would become dented by the large stresses incurred on the sample ends.

In total 10 samples were tested at a variety of maximum strains, numbered from 1-10. The initial tests were performed before errors involving load-frame compliance and sample surfaces denting the platens were noticed, however since the principal variable used in determination of a microstructural evolution map for Re is the ruminant plastic strain, measuring the final length of the samples with unknown stress-strain curves will supply sufficient information. Two of the sample tests, numbers 1 and 3, were also removed from the microstructural map due to having

been placed on areas where the platens were already dented, resulting in faulty load data as the sample was non-uniformly loaded. Additionally, tests 4 and 5 were performed to less than 1% total strain, resulting in a microstructural morphology that was not differentiable from the initial conditions of the annealed rod, as seen through EBSD. For the final analysis, the main tests used to describe the microstructural evolution were Tests 2,6, and 7 which were strained to a maximum plastic strain of 28%, 5%, and 1% respectively. Tests 8,9 and 10 were performed with the aid of DIC imaging, to a maximal strain of 25%, 12% and 8% respectively. As the raw load displacement curves were in excellent alignment, seen Figure 2.1, and that the end strain values were known for all tests, the use of the DIC specimens to represent the typical behavior of all compression tests was deemed valid.

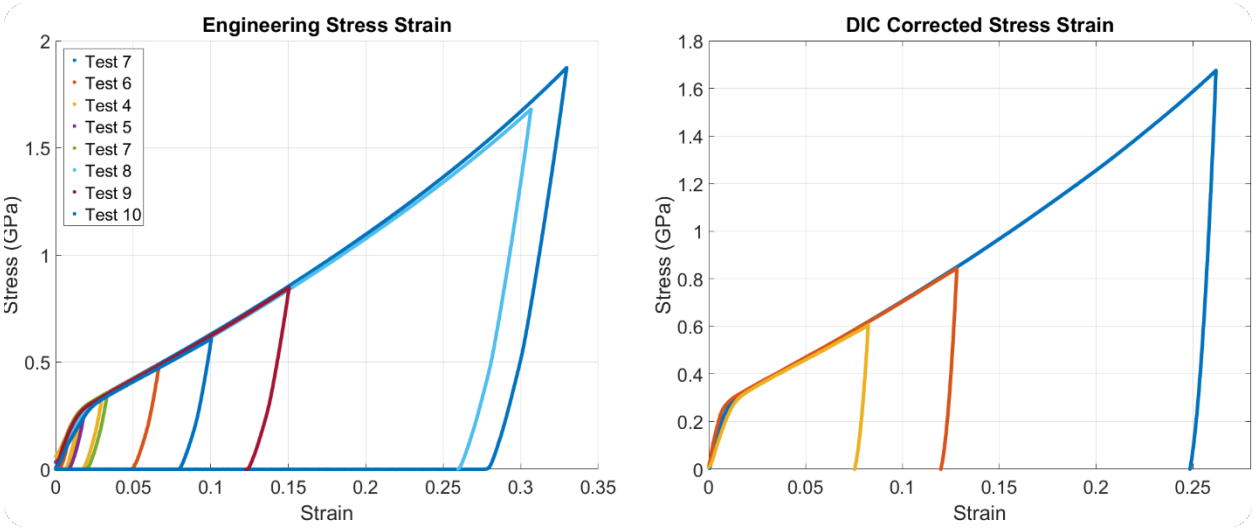

Figure 2.1: Comparison of all tests that were properly performed, having no anomalies due to platen roughness or other anomalies, to tests done with DIC. Notice the raw load displacement data perfectly aligns for all tests, and that the DIC corrected data holds the same trend. The difference in modulus for the two methods is a factor of 3.

After testing, samples were sectioned to a disk thickness of 150-200μm using EDM, as previously discussed. Care was taken to make sure that the disks sectioned for inspection were taken from the center of the sample (especially for high strain samples) due to the barreling present in compression and the constraint on the sample surfaces. The samples were jet-polished, as previously described, using a perchloric and nitric acid solution with an applied voltage of 50 V. With the large strain samples, the cross-sectional area increased to such an extent that it was possible for a single section to be jet-polished twice to achieve a larger area of inspection. For each test and for the undeformed samples, post-jet-polished samples were inspected in TEM and EBSD microscopes in order to gain a correlative insight into how features at the nanoscale influence features at the mesoscale and how the total microstructure determines the mechanical response. Weak beam DF imaging (WBDF) as well as strong 2-beam conditions were used to characterize and image dislocations present at twin interfaces and in the general crystal. For WBDF imaging, $(11\bar{2}0)$ reflections were used to view <a> type and <c+a> type dislocations, while (0002) reflections were used to view <c> type and <c+a>. If dislocations were visible in both conditions they were immediately known to be <c+a> type. However, only imaging dislocations in a single orientation is not perfectly indicative of either <a> type or <c>

type dislocations due to the three different Burgers vectors that <a> type and <c+a> type dislocations can take.

2.2. Microstructure as a Function of Compressive Strain in Rhenium

For all macroscopic tests involving twinning induced plasticity, it is very important to have an understanding of the sample texture in order to determine the likelihood and effect of the predominant twin mode. For Re, the dominant twinning mode is the $\{11\bar{2}1\}\langle 11\bar{2}6\rangle$ type tension twin. Crystallographically, $\{11\bar{2}1\}\langle 11\bar{2}6\rangle$ type twins can accommodate up to 0.619 plastic strain along the c-axis in tension (24) (5), the largest amount of strain accommodation for any type of HCP twin. However, this type of twin only operates as an expansion along the c-axis, making their effectiveness for strain accommodation entirely orientation dependent. Knowing this, it can be predicted based on the strong initial texture of the compression samples, Figure 2.2 a,b), that samples will be strongly twinned. However, the extent of dislocation slip present entirely depends on the character of available dislocations. Figure 2.2a) shows that the compression samples have almost exclusively $\{11\bar{2}0\}$ or $\{10\bar{1}0\}$ planes oriented parallel with the compression axis, making them very $\{11\bar{2}1\}\langle 11\bar{2}6\rangle$ twin favorable and basal slip unfavorable. It should be noted that while the samples were annealed in order to remove microstructural damage from the initial forming process, it was observed that some $\{11\bar{2}1\}\langle 11\bar{2}6\rangle$ twins were still present in the initial microstructure, Figures 2.2 b,c). Dislocation analysis of undeformed samples shows that both <a> type prismatic screw dislocations as well as <c+a> type screw dislocations are present before straining, with <c+a> dislocations always showing a curved structure and <a> type dislocations largely being straight.

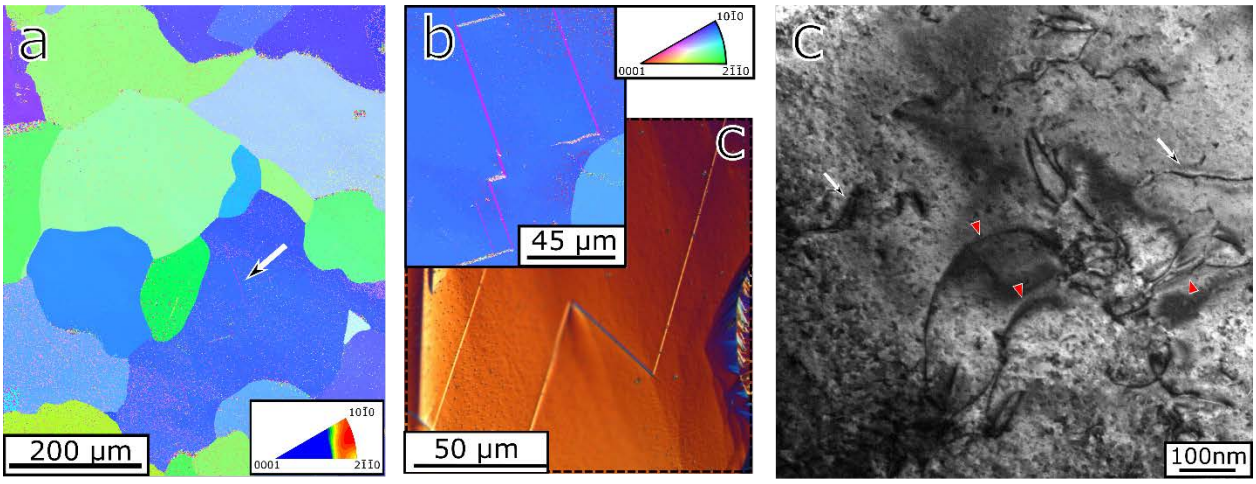

Figure 2.2: Initial inverse pole figure maps (IPF), with inset texture map, of the initial grain structure before compression. (a) The compression axis in a) (and subsequent IPF maps) is normal to the image. It can be seen in c) that for compression samples most all grains are oriented with either $\{11\bar{2}0\}$ or $\{10\bar{1}0\}$ type planes oriented along the compression axis. This is ideal for $\{11\bar{2}1\}\langle 11\bar{2}6\rangle$ twins to accommodate compressive strain by expanding along the in-plane c-axis. b,c) show remnant twins after annealing the sample using EBSD and polarized light microscopy respectively. d) shows

dislocations within a Re sample having both <a> type $\vec{b} = \{11\bar{2}0\}$ (white arrows) and <c+a> $\vec{b} = \{11\bar{2}3\}$ (red triangles) character. All undeformed samples viewed have shown both <a> and <c+a> type dislocations and very few small thin twins that have not managed to recrystallize after processing and annealing.

2.2.1. Ex-Situ Mechanical Compression and Texture Evolution

Samples were compressed to strains of 1%, 5% and 28% to establish the microstructures at characteristic amounts. All samples having nearly the same reproducible stress-strain curves. The average yield strength was seen to be roughly 290 MPa, which is notably lower than what has previously been reported by Kacher et al (4), however samples there contained a much larger portion of twinning "hard" orientations with nearly an order of magnitude smaller average grain size. As twins do not work harden, and yield strength is inversely proportional to grain size in Re (8), this noted discrepancy in stress strain is unsurprising. It was observed (Figure 2.2) that at low strains twinning immediately activates with twins of only a few microns in width crossing entire grains two orders of magnitude greater in width. While not all grains twin, the 1% deformation sample already shows the immediate importance of twinning for strain accommodation. As strain increases twins provide shear across grains and transmit through the grain boundaries if the misorientation between grains is less than ~25º, as reported by Kacher et al (4). One feature seen in Figure 2.2, but not emphasized by Kacher (a mechanism most likely suppressed as grain size decreases), is the ability for twins to bypass other twins within grain interiors, allowing for multiple twin variants to nucleate within a single grain and span the whole grain. This twin transmission mechanism is very prevalent during macroscopic compression as it appears across samples and in every grain where large amounts of twins form. In the 28% strain sample, it becomes increasingly difficult to differentiate grain boundaries as the interiors of grains have twinned to such a degree that grain boundaries and the intersections of twins become closely spaced, resulting in a finely striped twin-matrix structure.

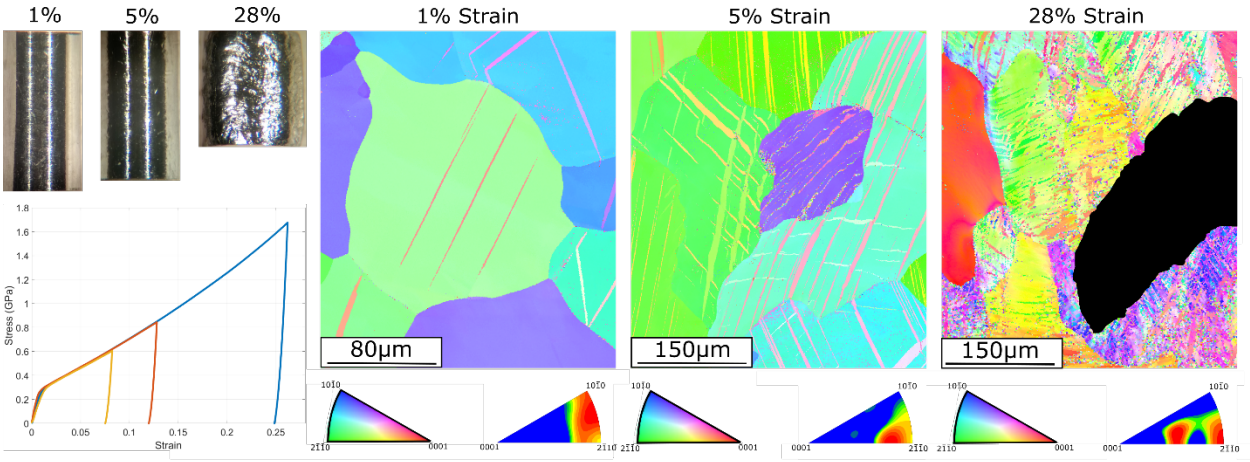

Figure 2.3: Texture evolution of rhenium as a function of final plastic strain. Optical images show a steady and uniform amount of barreling seen at the largest stress states due to the large amount of $\{11\bar{2}1\}\langle 11\bar{2}6\rangle$ twins. Stress strain curves are corrected with DIC to show accurate strain readings that are extremely repeatable. Texture maps (bottom right below EBSD images) show evolution of twining as strain increases.

It should be noted that twinning is not ubiquitous in all grains as the $\{11\bar{2}1\}\langle 11\bar{2}6\rangle$ twin alone is not able to accommodate all strain during uniaxial compression. Figure 2.4e) shows that a grain oriented with the c-axis within ~20º of the compression axis will have no twins either nucleating within it or transmitting from adjacent grains. The interior is quite heavily deformed with large crystal misorientations suggesting that the applied stress is accommodated purely through dislocation slip. It should be noted that the relative intensities of the twinning orientations in texture inverse pole figures (IPFs) (Figure 2.3 bottom right below each IPF map) show that as strain increases the proportion of $\{11\bar{2}1\}\langle 11\bar{2}6\rangle$ twin planes to initial orientation becomes equivalent. This is not surprising as the maximal applied strain sample ended at 28% total strain in the polycrystalline sample. With twins being able to accommodate up to ~60% strain, and with the twin favorability of the initial texture, only approximately half of the mostly twin favorable grains will need to twin in order to reach 28% strain, resulting in the striped twin-matrix structure seen in the EBSD maps.

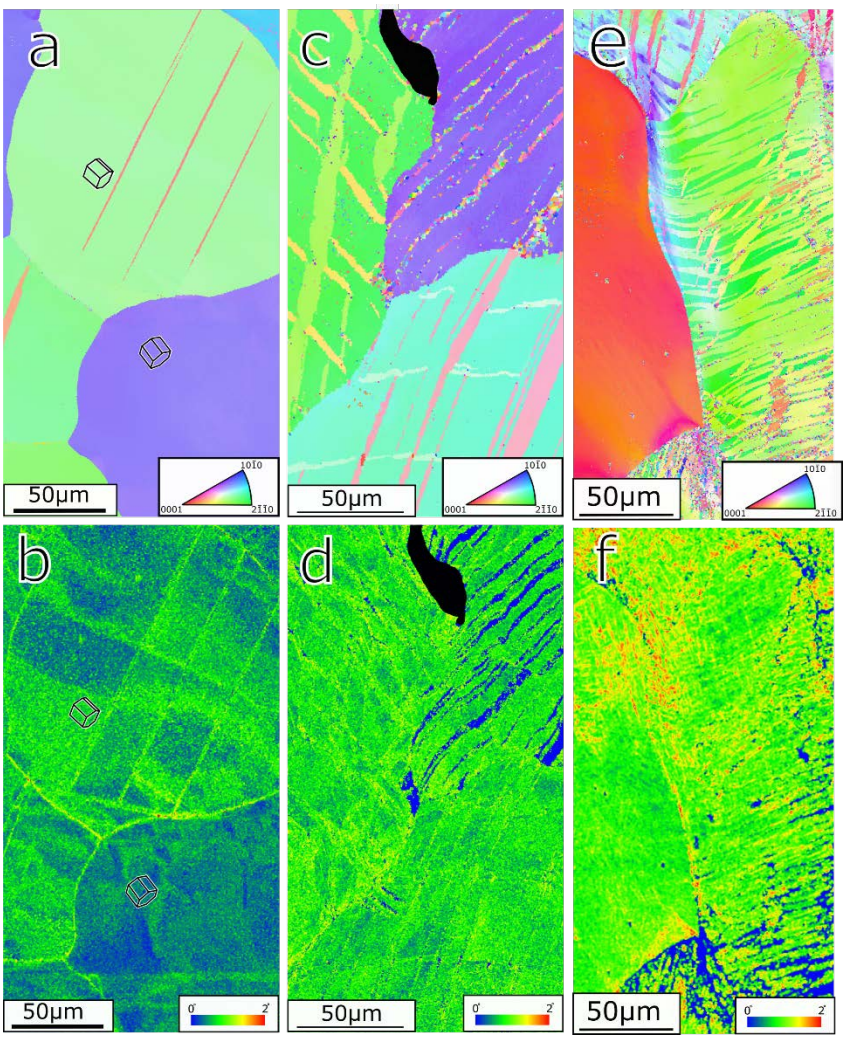

Figure 2.4: Comparisons between IPF maps a,c,e) and internal grain misorientations b,d) for 1% strain sample a,b) 5% strain sample c,d) and 28% strain sample e). The grain misorientation maps in b and d) show the domination of twinning immediately after

straining. It can be seen that the 5% strain sample has a uniform maximum internal local misorientations of 1.5º. Note in b) that slip bands form in grains with and without twins, meaning that dislocation slip is a precursor to twinning in Re. e) shows the change in grain orientation along the dotted line of the slip dominant grain. While in the adjacent grains, aggregating twins dominate the deformation, the basal oriented grain has fully accommodated the 28% strain without initiating or transmitting any twins. Note that extreme misorientations are due to twin boundary interactions.

The extent of dislocation involvement in twin favorable grains seems to be largely relegated to the low strain regime. While twin unfavorable grains show that large amounts of dislocation plasticity will be utilized, grains that allow for deformation twinning have been seen to only have maximal interior grain misorientations up to 1.5º, (Figure 2.4). The saturation of local misorientation at 1.5° is likely due to the resistance toward work hardening of twins. After the initial dislocation motion and twin formation, the required stress to further propagate dislocations increases, resulting in preferential twin nucleation after dislocation plasticity equivalent to a 1.5º misorientation is achieved. Couple this with the fact that with this texture twins can accommodate roughly 60% of all applied strains and the fact that they readily transmit through grain boundaries and other twins, makes the abundance of twinning in Re samples unsurprising. The slip bands that are seen in grain interiors seem to intersect through twin boundaries, and through slip trace analysis they are shown to lie on the prismatic planes and pyramidal planes, as seen Figure 2.4. However, as it will be shown later (and has long been seen in TWIP steels as a hardening mechanism (50)) dislocations collect along twin boundaries and as such this slip band has to have formed before the formation of the twin. While the great ductility of rhenium can be explained by its readiness to twin accompanied by dislocation accommodation for slip unfavorable grains, the extremely high work hardening behavior and creep resistance seen by Churchman (7) cannot be well understood using compression samples, and must be investigated further using uniaxial macroscopic tension.

2.2.2. TEM Analysis of Compression Samples

The extent of slip and twining as a function of strain has been described using EBSD analysis, however the interactions between individual dislocations and twins/twin boundaries needs higher resolution analysis. The evolution of microstructure has already shown a very clear progression, from some dislocation slip, to twinning and dislocation slip, to finally twin saturation. Electron transparent TEM disks were investigated in order to determine the nature of twin-dislocation and twin-twin interactions as a function of strain, and to see how twin and dislocation densities change with increasing deformation. At very low strain amounts twinning was immediately observed, however the twins were generally very thin, some as small as 10 nm wide and having extremely high aspect ratios, or consisting of aggregated twins where many smaller twins have collected to form a larger twinned region. These aggregate twin structures can be seen in Figure 2.5 a,b,d) with Figure 2.6 a,b) also showing bright and dark-field images of a large twin made up of many smaller components.

As strain increases it is common to see larger aggregate twins throughout the sample, with the twins collecting dislocations along its interface and around the twin. As a high density of interface dislocations is not seen at low strains, it can be said that they are not due to a misfit strain requirement of the twin to reside in the matrix, but instead these dislocations are collected

during deformation as the twin grows and dislocations move through the crystal. This is important to note, as it means that dislocation do not aid the formation of deformation twins. While it has been seen using EBSD that some slip bands have transmitted through twins, the majority of dislocations are impeded by twin boundaries and cannot enter the twinned regions. At very large strains, the saturation of dislocations in the matrix becomes apparent and dislocations no longer only cluster around the twin boundaries. At this point, the area fraction of twins starts to approach the aforementioned 50% seen in EBSD, however here with the twins now being multiple microns long and less than 100nm wide. It is also clear that at this small length scale twins can either nucleate from twin boundaries, or are able to pass through existing boundaries, with unique twin intersections showing no particularly common dislocation structure under conventional TEM.

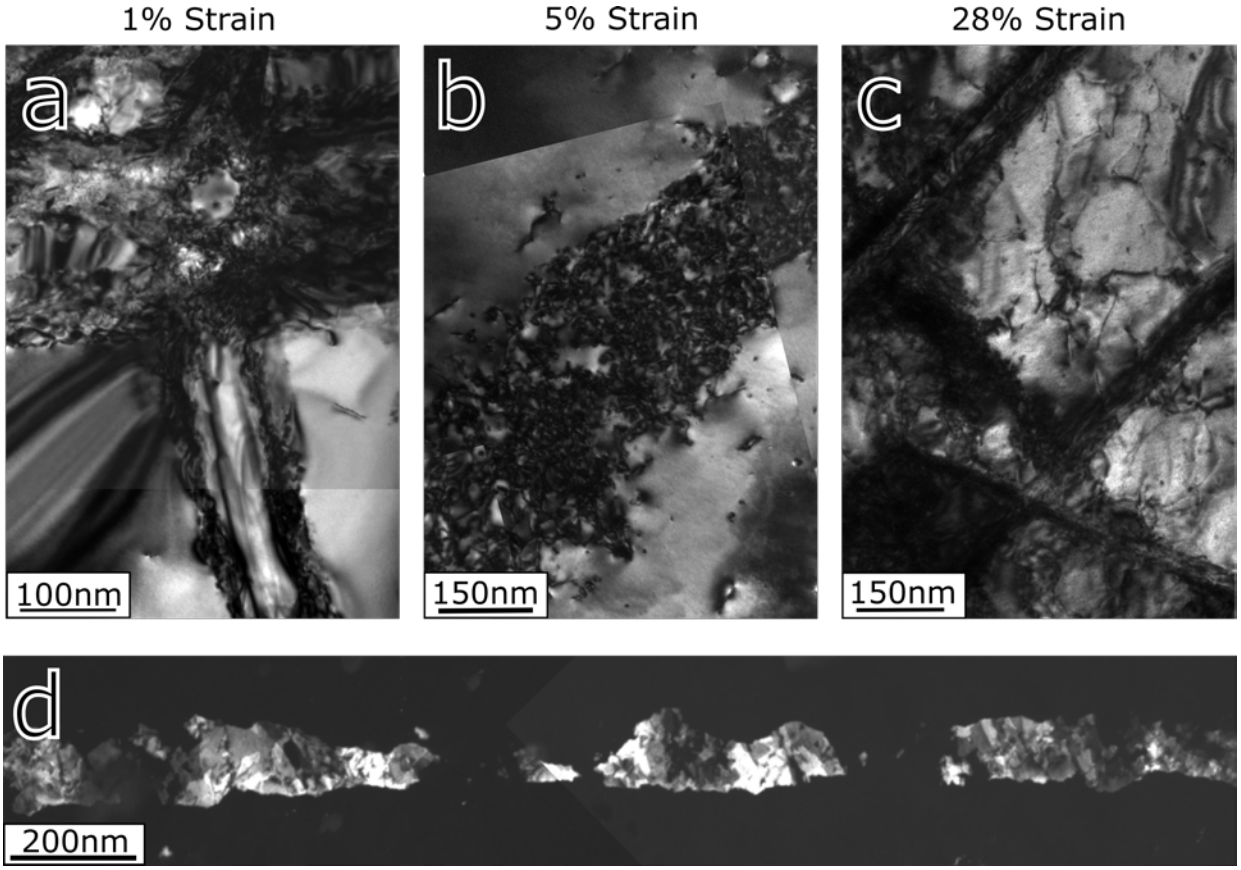

Figure 2.5: Characteristic TEM images showing both twins and dislocations for different absolute strains amounts. It can be seen that the dislocation density both adjacent to twins and in the surrounding matrix increases substantially with applied strain. At the twin intersection in bright-field image a), few dislocations can be seen surrounding the twins, with none being found populating the twin boundary. This changes significantly in b) and c) with the dislocations surrounding the twin being concentrated at the twin/matrix boundary. Bright-field image c) shows extensive twin-twin interactions, including twins transmitting through each other, and a high dislocation density in the matrix, as well as collected at the twin boundaries. d) shows that large twins, over 3 microns, are aggregated of many different smaller twinned sections. This behavior seems to be observed in any twin larger than a few tens of nm thick.

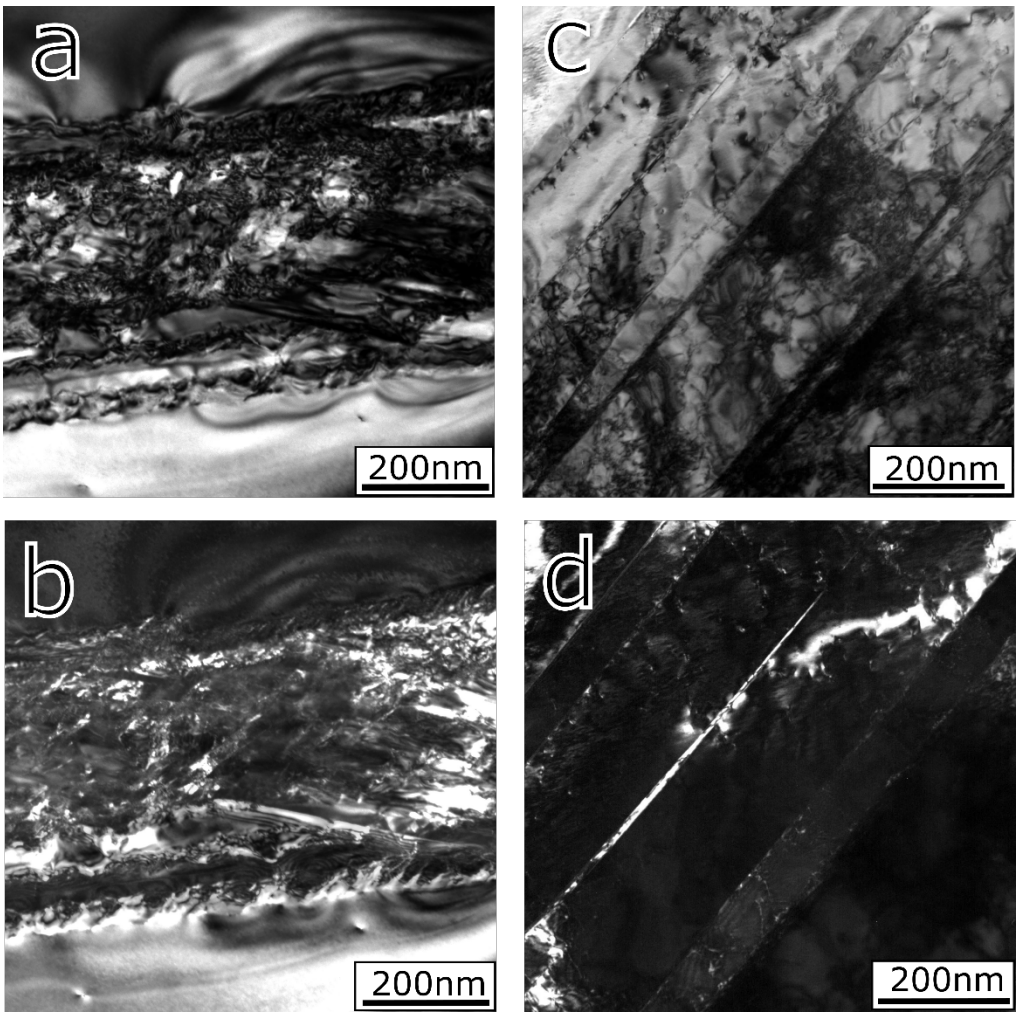

Figure 2.6: BF and DF TEM images for a large twin seen in the 1% strain sample, a),b) and the 28% strain sample c),d) respectively. DF image d) is taken from the twin reflection to show internal twin structure lacking extensive dislocations. The dislocation density of <a> type screw dislocations is seen to dominate over <c+a> dislocations along the twin boundary. This is most likely due to <a> type dislocations being the dominant dislocation during deformation and collecting at the twin boundary.

In order to determine the types of dislocations present at the twin boundary in the matrix, weak beam dark-field images were taken of the matrix surrounding the twins by using two-beam (0002) and $(11\bar{2}0)$ reflection condition in the moderate 5% strain sample. The (0002) condition was used to see the extent of present <c+a> type dislocations along and around the twin boundary. Figure 2.7a,b) show that while there are fairly common <c+a> dislocations near twin boundaries and in samples in general, they are an uncommon occurrence along the twin/matrix interface, located in the matrix. This could be due to a relative lack of mobility when compared to <a> type screw dislocations, reducing the likelihood of finding a <c+a> type dislocations to only occasions where twin boundary forms to intersect the immobile dislocation.

Using the $(11\bar{2}0)$ reflection to view the interfacial <a> type discolorations shows a much higher density both along the matrix boundary and next to the twins. The <a> type dislocations are relatively regularly spaced apart and tend not to lie fully lengthwise along the twin, which suggests that there may be a favorable configuration for dislocations to transmit through the twin boundary. Dislocations accumulating on the boundary between twin and matrix is consistent with the observations by Peter et al. (6), who concluded that dislocation accumulations attributed to the high work hardening of rhenium. As these samples are in compression, the nature of work hardening cannot be completely assessed. The high ductility has been shown to be caused by the prevalence of twinning, with further studies required to investigate the tension-compression asymmetry present in Re and the effects of twin-twin interactions on work hardening.

The intrinsic behavior of twins in rhenium are best seen both at the low strain portion of deformation, where dislocations have not yet populated the twin-matrix interface, and at high strain portions of deformation, where twins and dislocations are forced to interact. Due to the nature of the compression test, very high amounts of strain can be applied without the worry of catastrophic failure after necking, as would be the case with uniaxial tension (70). This allows for the comparison of twin morphologies, and how the interplay between dislocations and twins can cause various structures. The larger twins observed in all samples consist of many sub-twinned regimes, with BF and DF images shown in the 1% strain sample, Figure 2.6a,b). This structure can be explained by the Re twin boundary having an abnormally low twin-boundary energy, as calculated by de Jong (9), and that the $\{11\bar{2}1\}$ twin boundary is exceedingly stable, with a structure analogous to tetrahedrally close-packed. With this combination, one would expect that the propagation of twin boundaries would be harder than the formation of new boundaries, making groups of much smaller twins easier than forming one large twin with a mobile boundary.

At the largest of strains the spacing of the second thin type of twin has been shown to be very regular, with large amounts of dislocations evenly saturating the space in between (Figure 2.6c,d). Since it was observed that dislocations cluster at twin boundaries, and that twin boundaries do not allow for the transmission of dislocations, it should be noted that these thin twin stripes are likely formed evenly to avoid dislocation/twin-boundary interactions. If these twins had been formed before the saturation of dislocations in the matrix, any dislocations moving through the crystal to accommodate the applied strain will be clustered at the boundaries. However, since no dislocations are seen clustering in the matrix next to the twin boundary, as in Figure 2.7, these late deformation twins are formed after the saturation of dislocations in the matrix, showing that dislocations act as barrier to twin boundary propagation.

Twin intersections were imaged for all samples, however the low strained samples allow for easier imaging without contrast interference from dislocations. In Figure 2.8 two twins were observed, the first roughly 65nm wide and through the thickness of the foil labeled as 1, the other less than 5nm thick labeled as 2. In order to determine that the twins were indeed intersecting and not bypassing each other out of plane, a tilt series was performed in order to view the twin from multiple angles and view as clean an intersection as possible, the most salient images seen in Figure 2.8. Figure 2.8a) shows an edge on overview twin intersection with Figure 2.8b) showing the same overview tilted by 15º along a tilt axis nearly orthogonal to the Twin 1 boundary. It can be seen that Twin 2 not only "jogs" 38nm along the Twin 1 boundary along the $\vec{g} = (0002)$ direction (as shown by the diffraction pattern (DP)), the interception points between the twins cause twin 1 to kink at both intersection points as well. It has been reported previously that the calculated stacking fault energy of basal type stacking faults are the lowest in rhenium,

up to an order of magnitude lower than some stacking faults in other orientations (48). As has been seen in Figure 2.8c,d), the aggregate nature of twins along with a very low stacking fault energy of the basal planes are the likely cause of this ability for the twins to jog. As Twin 2 is nearly atomically thin, there are almost no defects within it that can explain its change of direction. However, its interaction with the aggregated Twin 1 contains multiple intersections where the propagation of the twin can be halted and the internal aggregate structure of Twin 1 can act as a guide and nucleation point for the new jogged twin to travel past the boundary.

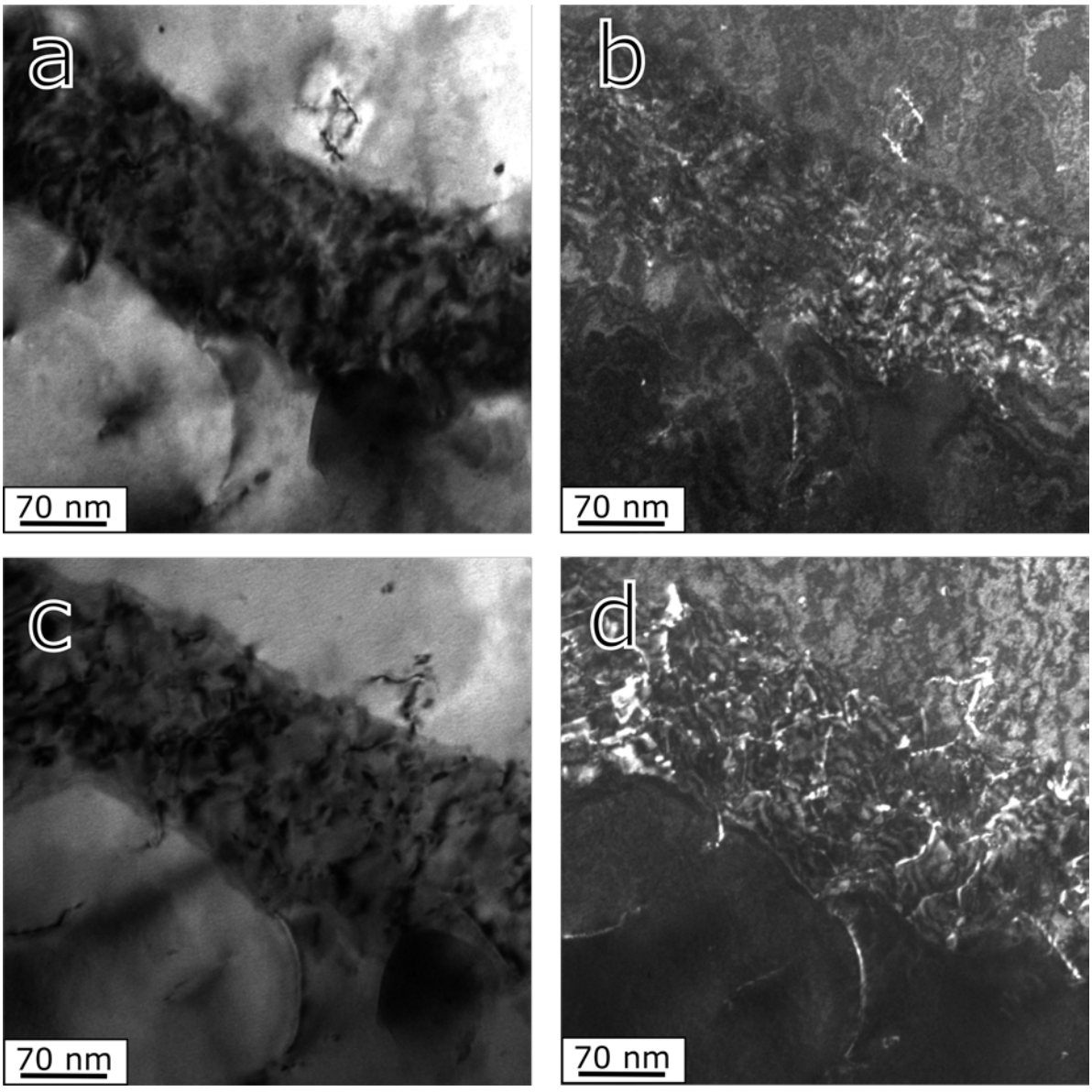

Figure 2.7: Two-beam BF and DF images for a large twin seen in the 5% strain sample. BF a),c) and DF b,d) of the (0002) a),b) and $(11\bar{2}0)$ c),d) reflections respectively. The dislocation density of <a> type screw dislocations is seen to dominate over <c+a> dislocations along the twin boundary. This is most likely due to <a> type dislocations being the dominant dislocation during deformation and collecting at the twin boundary.

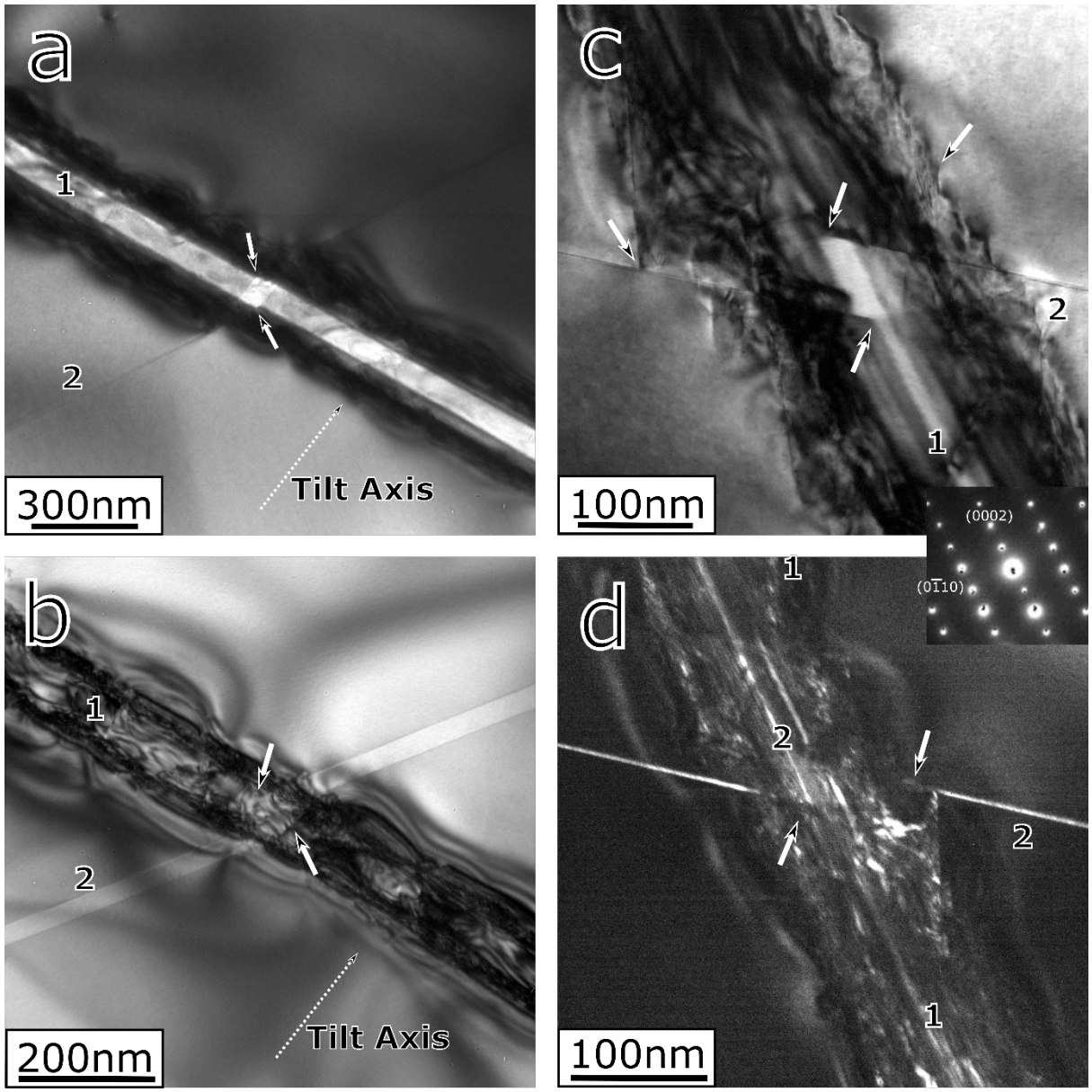

Figure 2.8: BF and DF images of a twin interception in the 1% strain sample. a) and b) show the intersections of two twins with a) being edge on, and b) having tilted 15°, it should be noted that the edge on twin is only a few atomic planes thick, with no misfit dislocations needed to accommodate its formation. The arrows in a) mark the direction change of the larger twin due to twin-twin interactions. Due to the 15° shift in b) some interior structure of the transmitting twin can be seen. The twin appears to terminate and change planes where the arrows mark. Magnifications of the twin intersection are seen in BF c) and DF d) with inset $[11\bar{2}0]$ DP, allowing for some inspection of the interior twin structure. d) is taken from high order twin spots. The intersections between twins are highlighted with arrows, with the twins often "jogging" along $\vec{g} = (0002)$ or terminating at these intersections, suggesting involvement of basal stacking

faults. The rightmost arrow in image c) highlights that the boundary of the larger twin has a step-like structure.

Twin intersections observed in the 1% strain sample (and also in higher strained samples, however with the low strain allows for easier imaging) allow for structural observations without contrast interference from dislocations. Two twins were observed, the first roughly 65nm wide and through the thickness of the foil labeled as 1, the other less than 5nm thick labeled as 2. In order to determine that the twins were indeed intersecting and not bypassing each other out of plane, a tilt series was performed in order to view the twin from multiple angles and view as clean an intersection as possible, the most salient images seen in Figure 2.7. Figure 2.7a) shows an edge on overview twin intersection with Figure 2.7b) showing the same overview tilted by 15º along a tilt axis orthogonal to the Twin 1 boundary. It can be seen that Twin 2 not only "jogs" 38nm along the Twin 1 boundary, the intersection points between the twins cause twin 1 to kink at both intersection points. As has been seen in Figure 2.7c,d), the aggregate nature of twins is the likely cause of this ability for the twins to jog. As Twin 2 is nearly atomically thin, there are almost no defects within it that can explain its change of direction. However, its interaction with the aggregated Twin 1 contains multiple intersections where the propagation of the twin can be halted and the internal aggregate structure of Twin 1 can act as a guide and nucleation point for the new jogged twin to travel past the boundary.

While the interiors twin intersection in Figure 2.8c,d) show much dynamical contrast, some unique features can be recognized. The internal structure of Twin 1 shows similar aggregate structure as in Figure 2.6, with high aspect ratio twins initiating and terminating on facets of the internal microstructure and the Twin 2 intersection. It can also be seen in BF, Figure 2.8c), that the Twin 1 boundary is not perfectly straight, but instead shows a step-like structure with the same orientation of each step as that between Twins 1 and 2. This step structure could be an important determinant of which twins are allowed to transmit through twin boundaries, and which terminate at twin boundaries. Additionally, this provides an explanation as to why twins with a "Z" shape are relatively common within Re (Figure 2.2c). As the aggregate twin boundaries are not necessarily straight, a twin can change its twin plane at any point when it impinges upon an obstacle to its propagation. With the observation of this unique twin structure, future work will focus on the use of atomic resolution scanning transmission electron microscopy (STEM) in order to fully characterize the internal working of twin-twin transmission.

2.3. Conclusions Based on Post-Compression Microscopy

The evolution of the rhenium microstructure during uniaxial compression has been described. Sample texture was shown to be a large determinant of the operative deformation mechanism for all samples tested, with grains having c-axis near parallel to the compression axis showing no twinning. The post-compression microstructure was shown to consist of $\{11\bar{2}1\}\langle 11\bar{2}6\rangle$ twins, with prismatic and some pyramidal slip bands only recognizable during the initial deformation. Slip bands were quickly overshadowed by twinning which by themselves cannot accommodate the large strains applied during compression. However, due to the sample texture and large amount of strain accommodation by $\{11\bar{2}1\}\langle 11\bar{2}6\rangle$ twins, twinning becomes the dominant strain accommodation. The ability for twins to accommodate strain was further improved by the unique propensity for twins in Rhenium to bypass twin and grain boundaries.

This allowed for multiple twin variants to be simultaneously active within individual grains and change their twin plane to overcome obstacles such as other twins.

TEM investigations of the twin structure and dislocation-twin interactions has confirmed the EBSD result of low dislocation activity for all strained samples. Low strain samples showed atomically thin twins and larger twins aggregated from many smaller twins, unpopulated with dislocations. As strain increased, the matrix surrounding twins were populated by <a> type dislocations impeded from transmitting through the twin boundaries, as is common in TWIP steels. As twinning saturated the crystal, twins were seen to be regularly spaced apart without an extensive matrix dislocation population, showing that twins boundaries are not mobile but resulted in new twin formation instead of twin growth. The aggregate twin nature and lack of twin growth at the smallest length scales is explained by high twin boundary stability of $\{11\bar{2}1\}\langle 11\bar{2}6\rangle$ twins coupled with an anomalously low twin boundary energy. Further research is required into the twin transmission mechanisms seen in the large Re grains, using both in-situ and HRTEM techniques. Additionally, the effect of twin boundary stability and dislocation populations along the twin boundaries on the high work hardening requires further investigation in samples deformed in tension.

Chapter 3

Microstructure Evolution of Re in Tension

The microstructural evolution of rhenium has been shown using compression, however the most impressive property is that of the high work hardening rate, highest among any pure metal (and any known metal at the time of discovery (8)). As it has already been shown in the previous chapter how the microstructure of Rhenium is able to accommodate very large strains in compression, an investigation of the effects of how microstructure changes during a tensile test is the logical next step. The use of tension has some key advantages over the use of compression, as well as some drawbacks not seen when using compression samples. As the test is performed using uniaxial tension, the test is much easier to conduct, with the stability of the test increasing as strain increases. While buckling and barreling of the sample is a common occurrence during compression, these effects cannot occur when under tension, allowing for extremely accurate gauge section as well as cross sectional area measurements. This allows for more accurate readings of yield strength, modulus, as well as the ability to easily investigate the work hardening behavior of rhenium. With the same systematic procedure of straining a piece of Re in tension with strain measured using DIC, then imaging the microstructure using both EBSD and TEM techniques, it is possible to correlate the microstructure to the work hardening. Gaining new insights into the mechanisms that make Re the highest work hardening rate pure metal is key for the future development of high temperature structural metals.

With potentially substantial benefits of tension testing based on the inherent characteristics of the test, these include some drawbacks that are not seen in compression testing. The main drawback for rhenium is that the materials and processing costs are much higher for tension samples than compression samples. While for most metals the processing is the costliest part of making a mechanical test sample, in the case of rhenium, material is so expensive that processing and materials costs become commensurate. For example, the price of a single 200mm long x 3mm diameter rhenium rod was $284 in May of 2016 (73). The machining time cost to cut the rod into 6mm long compression samples was roughly an additional 600$ for 15 pieces, making the total roughly $884. In contrast this, fully machined Re dog-bone style samples from Re Alloys Inc. cost $3,472 for 10 pieces (73). This is in large part due to the increased total material costs (roughly 4x more mass) as well as the necessity of having large grip sections from which the samples are pulled. The other main problem, that was exacerbated due to Re being much stronger and tougher than steel, as well as having a very low coefficient of friction compared to other refractory metals (28), was that the grips which held the end tabs took a significant crosshead displacement in order to fully grip the sample. This grip sliding leads to unusual load-displacements curves during the initial deformation of each sample bar. Contrasting this initial instability with the initial stability of Re during compression testing. Despite the drawbacks inherent in the tensile testing methodology, the improved understanding that is possible with the more stable uniaxial tension procedure offsets any complications inherent to the process.

3.1. Experimental Procedure of Macroscopic Tension

The methodology used for the tension samples is much the same as used for the compression sample. Here testing was done under tension with tensile sample geometry and not compressing small rhenium cylinders. The experiment is conducted systematically, as was done with the compression samples, to different characteristic amounts of strain. Multiple samples were deformed to various strain amounts, measuring strain using commercial Vic-2d software to give accurate strain readings. After deforming samples to multiple strains, the samples are sectioned using EDM and then jet-polished using the standard 2:1 nitric:pechloric 35% acid solution in 1:1 ethanol:methanol with 50ml of 2 butoxyethanol. These samples are then able to be scanned using EBSD to understand the meso-scale texture and microstructure inherent at each strain. Jet-polished samples are also electron transparent so conventional TEM and STEM can be used to understand the dislocation and twin structures seen at the smallest scales. With the *in-situ* tension testing done on rhenium in the next chapter and the work shown within this chapter, a full accounting of the unique structures and behaviors of rhenium under tension will be shown.

3.1.1. Initial Structure of Rhenium

As with all of the rhenium tested in this thesis, the samples deformed in this work were purchased from Rhenium Alloys, Inc. A tensile design was supplied to their machinists for the tensile bar geometry. 10 tensile samples were provided for testing, all of which were used to test reproducibility. The samples were cut from a sheet of 2.85mm thick rhenium using wire EDM. The sheet was made using the same process as for the Re rod from the previous chapter, where an ingot of Re that was formed from powder was cold rolled with intermittent 1650°C heat treatments, and a final 1650°C anneal to remove the deformation induced through rolling. An overview scan of the grip section of the tensile samples, Figure 3.1, was taken in order to understand the initial microstructure of the rhenium tension samples. The grip section was chosen from sample 4, as the interior of the grip should be essentially undeformed. Sample 4 was only deformed to 0.4% strain, and the amount of material on the grip was sufficient that there should no plastic deformation within the interior from which the EBSD map was taken. The resulting microstructure of the Re sheet was heavily textured, shown Figure 3.1e), where nearly all of the grains oriented such that prismatic $\{10\bar{1}0\}$ and $\{11\bar{2}0\}$ planes are oriented parallel to the tensile axis. This is a result of the rolling process used to form the initial sheet form which the Re tensile samples were cut, and is same texture for all of the samples tested within this work.

In order to determine the likely active slip systems, a series of Schmidt factor maps are shown in Figure 3.1b-d). It can be seen that the Schmidt factors for the predominant $\{11\bar{2}1\}\langle 11\bar{2}6\rangle$ twins commonly found in rhenium are relatively high, however due to the nature of the texture, these twins will only activate rarely. $\{11\bar{2}1\}\langle 11\bar{2}6\rangle$ twins are capable of giving up to 61% strain in tension along the c-axis. The c-axis for grains with this texture is generally orthogonal to the tensile direction, meaning that these tension twins should not activate. There are exceptions within the microstructure of the high Schmidt factor grains (seen in Figure 3.1b) in red), then they will only twin minimally, as <a> type dislocation plasticity of $\{0002\}\langle 11\bar{2}0\rangle$ is

far more favorable, seen Figure 3.2 c,d). Additionally, as twinning operates as a simple shearing mechanism with a relatively low critical resolved shear stress (5), any twinning favorable grains should show twin formation at relatively low strain amounts. One last notable feature of the initial sample microstructure, it can be seen in the bulk of the grain size distribution for these textured tensile samples lies squarely between the 40-90µm size range, with large grains above 100µm, up to 160µm, showing rarely at the tail end of the distribution. This allows for some randomization of grain sizes in each sample, allowing for the possibility of disparate yield strengths, as having multiple 160µm will aid in reducing the yield strength of the tensile sample while increasing the work hardening rate.

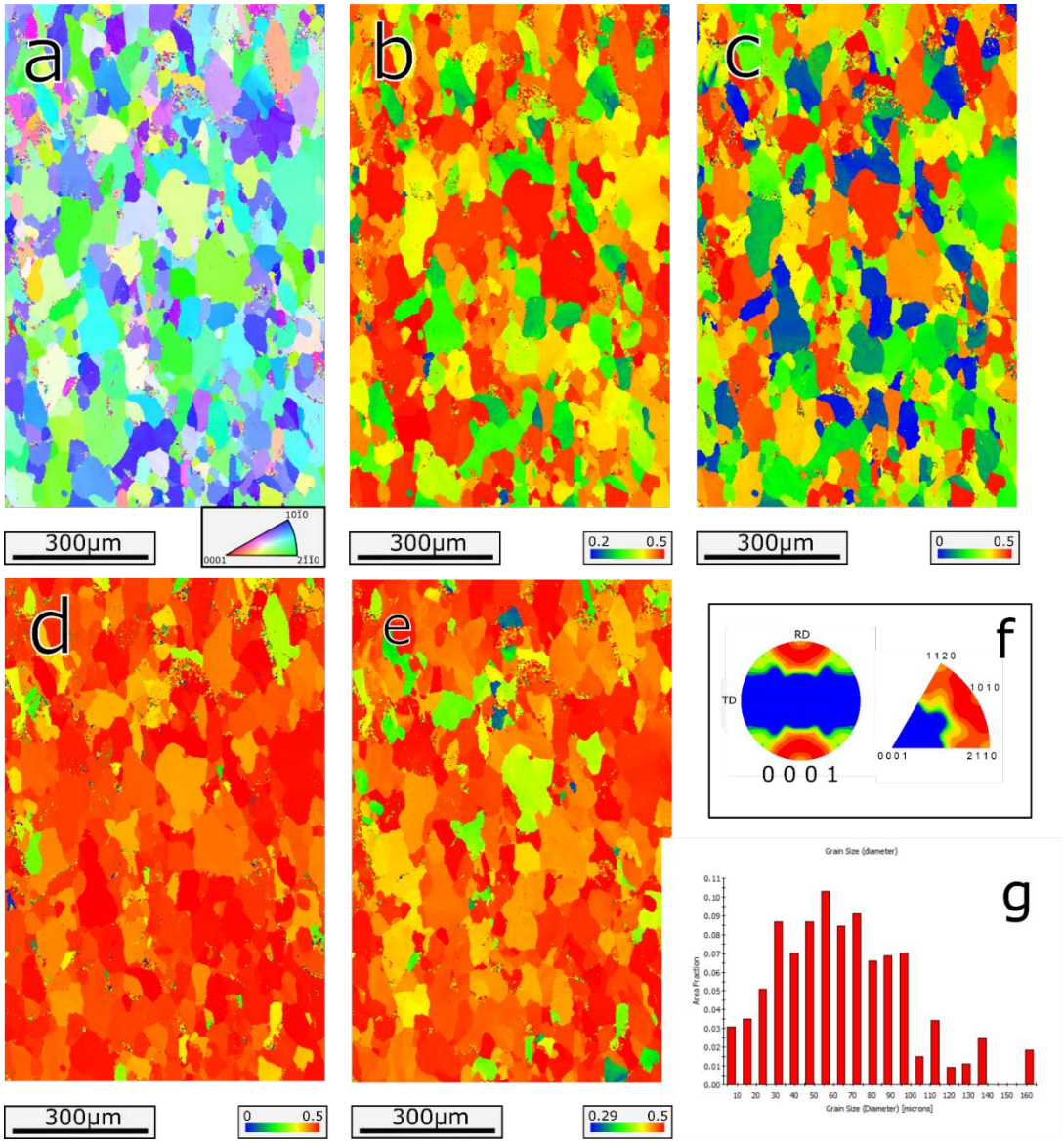

Figure 3.1: Initial IPF map of sample surface orthogonal to the loading direction a). Schmidt factor chart which shows the favorability of $\{11\bar{2}1\}\langle 11\bar{2}6\rangle$ type twins is seen in b), the $\{0002\}\langle 11\bar{2}0\rangle$ slip system in c), the $\{10\bar{1}0\}\langle 1\bar{2}10\rangle$ slip system in d), and $\{10\bar{1}1\}\langle 11\bar{2}3\rangle$ pyramidal slip e). Corresponding texture plots f) and grain size chart of

this IPF map in g). This undeformed sample was taken from the larger grip sections of the sample. It can be seen that the bulk of grains have a strongly textured orientation with prismatic $\{10\bar{1}0\}$ and $\{11\bar{2}0\}$ planes along the tensile direction, which is unfavorable for $\{11\bar{2}1\}\langle 11\bar{2}6\rangle$ type twinning, as seen by the Schmidt factors in b). It should be noted that the bulk of grains are between 40-90μm in size, while some rare grains are above 100μm, which can lead to large discrepancies in mechanical response.

3.1.2. Mechanical Response of Rhenium under Tension

The samples were all tested on an MTS Criterion Universal Test System, and were tested at a strain rate of 0.005 mm/second. Samples were square with an 8.55 mm^2 initial area and had the same initial gauge length of 15mm. The samples all showed some degree of grip slippage, as the high strength and low coefficient of friction of Re did not allow the steel tensile grips to properly attain a hold on to the samples during the initial test segments (74). This was mitigated in later test samples through re-gripping the samples multiple times to assure proper adhesion. Some slipping can be seen as irregularities of the DIC collected strain data near the beginning of the stress-strain curves in Figure 3.2a). All samples, except for samples 1 and 6 which were tested to failure, were deformed to preset strains, then unloaded before sectioning for the microstructural investigation. Sample 6 included an unload and re-load segment to investigate the modulus after grip slippage has ceased, showing the reported value for Re of 450 GPa. The total strain amounts for the samples used for the microscopy investigation are as follows: sample 1 – to fracture, sample 2 – 5.7% strain, sample 3 – 1.9% strain, sample 4 – 0.4% strain, and sample 5 – 3.3% strain. The work hardening curves in Figure 3.2b) also point to the samples having different microstructures. Taking samples 5 and 8 as examples, the significantly different work hardening rates at low strains indicate different microstructures. After sufficient yielding, the work hardening rate reaches a similar value for all samples, regardless initial microstructural differences.

Images of sample 3 and sample 6 can be seen in Figure 3.2c) and d) respectively. The standard speckling of sample 6 using spray paint is preferable for DIC. However, the Sharpie dot method provided sufficient contrast on the sample for the Vic-2D DIC software to provide an accurate reading for each sample. Some small discrepancies in yield stresses can be attributed to the different the grain size distributions among the various samples, as seen in Figure 3.2e) and f). It can be seen that on the high end of the grain size distribution, there are fewer larger grains for sample 4 than for sample 1, which can be a great influence due to the relatively small size of samples. Larger grains within the microstructure would be much softer than the smaller grains, causing a reduction in the yield strength. No other factor observed within the initial microstructures of the samples could account for the yield stress distribution. Differences in sample texture, geometry, and test methodology are virtually nonexistent between samples.

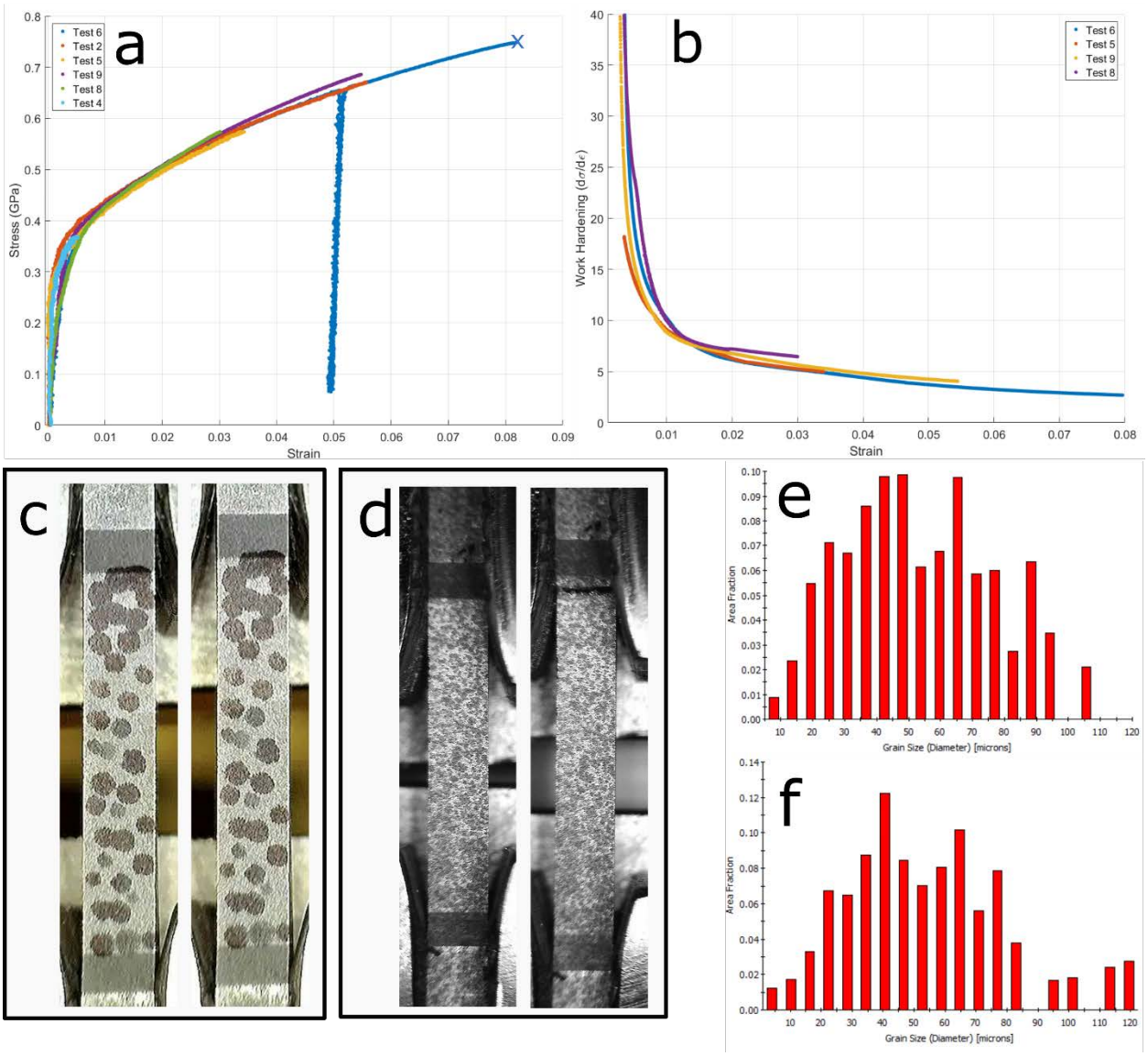

Figure 3.2: Mechanical data for selected tensile samples taken, a) stress-strain curves and b) work hardening as a function of strain. Example of before and after images of tests are shown for sample 3, to 1.9% strain, c) and samples 6, to fracture, d). Two grain size charts are seen for sample 4 e), and sample 1 f). Sample 4 has appreciably fewer large grains, with the smaller grains taking a larger portion of the area fraction. This accounts for some discrepancies seen in the yield stress in a). This difference in grain size distribution is taken as random chance, since all samples are small with a gauge area of 8.55mm^2.

3.2. Microstructural Evolution of Rhenium in Tension

The initial overview of the strain effects on the sample behavior were investigated using EBSD scans of large regions of the sample. The default step size of 750nm was used for the large area overview scans. This allowed for the highest data acquisition throughput, while still

being able to observe which grains had initiated deformation twinning. While the large scans allowed for the acquisition of datasets which showed general trends in the microstructure, finer detailed scans were required in order to view the twinning and dislocation (seen as grain misorientations) interactions in the sample as a function of strain. This allows for insights into the very high work hardening rates seen in Figure 3.2b). TEM micrographs can then be used to understand how the very small twins seen in the EBSD maps interact with individual dislocations to accommodate the applied tensile strain. This multi-scale approach allows for a truly deep understanding into the effect of tensile strain on the microstructure, and the tension compression asymmetry present in Re microstructures.

3.2.1. Microstructural Progression of Rhenium under Tension seen through EBSD

Large area overview EBSD maps, seen in Figure 3.3, were taken of each sample numbered in Figure 3.1, and were used to provide a general progression of microstructure as a function of strain. With an average scan step size of 750nm, it is not possible to observe the smallest twin features common in Re, which can be as small as a few nanometers in width to a few tens of microns. Most grains which have Schmidt factors above 0.4 for $\{11\bar{2}1\}\langle 11\bar{2}6\rangle$ type twins will show signs of twinning, seen Figure 3.4c). For very low strains, immediately after initial yielding, there is little difference between the IPF maps of the annealed samples seen in Figure 3.1a) the IPF maps for 0.4% strain in Figure 3.3. No twins are observed in large grains, with no noticeable color gradients within grains indicating local grain misorientations. With the increase further increase of strain to 1.9%, large twins become visible in the microstructure, in high Schmidt factor grains, with more noticeable color gradients internal to the grains appearing in the majority of these grains. This is likely due to basal dislocation slip, as seen by the coincidence of twinning and the high $\{0002\}\langle 11\bar{2}0\rangle$ basal slip Schmidt factor seen in Figure 3.4d). Once the deformation reaches 3.3% strain, large-scale twinning crossing full widths of grains has become prominent in all the grains which will show large scale twining. It can be seen above this value, the ratio of twined grains relative to untwinned grains observed does not increase appreciably, suggesting that deformation twinning is mainly activated at low strains when orientation allows, with dislocation plasticity accommodating the additional strain after twinning saturates.

To get a more complete understanding of when of each possible deformation mode within a deformed sample is activated, EBSD maps of sample 1 with significant dislocation plasticity and twinning were compared to the Schmidt factors of prominent deformation modes for this texture, seen Figure 3.4. Having Schmidt factors for each orientation only gives insights into the favorability for which orientation to deform, in order to understand the full complete stress state, an understanding of the critical resolved shear stress (CRSS) for each orientation on the sample must be accounted for. It has been observed by Jeffrey et al. (5) that the shear required to form $\{11\bar{2}1\}\langle 11\bar{2}6\rangle$ twins is anomalously lower than in Zr or other HCP metals. Basal slip was also seen to be heavily activated, accompany the $\{11\bar{2}1\}\langle 11\bar{2}6\rangle$ type twins by Jeffrey. This leads to Figure 3.4 which shows an EBSD map of sample 1 (after fracture) with accompanying misorientation map and $\{11\bar{2}1\}\langle 11\bar{2}6\rangle$, $\{0002\}\langle 11\bar{2}0\rangle$, $\{10\bar{1}0\}\langle 1\bar{2}10\rangle$, and $\{10\bar{1}1\}\langle 1\bar{2}13\rangle$ Schmidt factors. While it is less commonly seen in Re, the $\{10\bar{1}0\}$ plane has been observed

forming slip bands in polycrystalline Re by Churchman, and was also the plane along which dislocations were observed in Re compression in the previous Chapter (7).

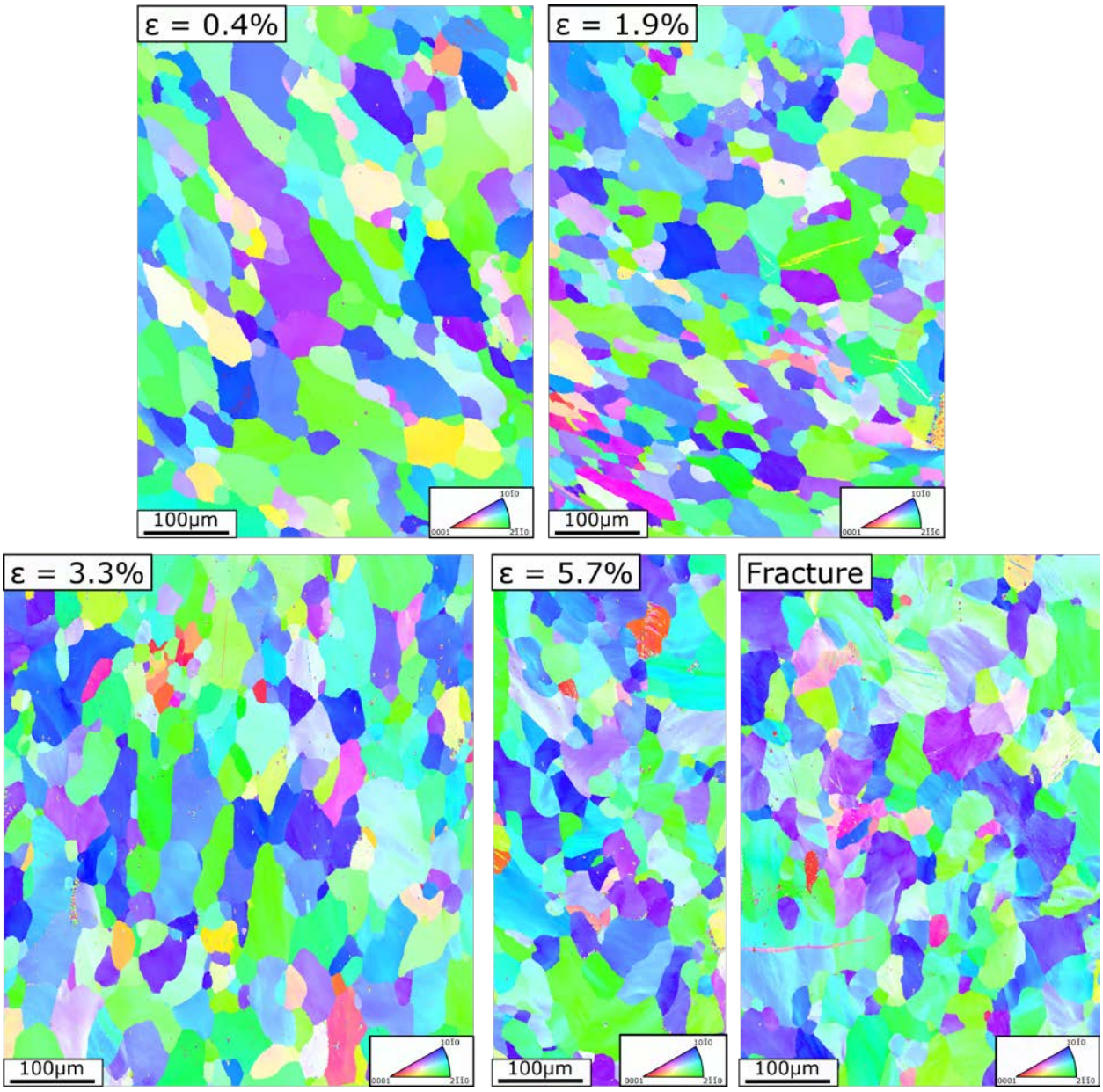

Figure 3.3: Large area overview EBSD maps for tension samples 1-5. Note as strain increases, the number of twins as a function of area saturates after 3.3% strain, where large grain misorientations take over in accommodating the large amounts of applied strain. Misorientation bands can be seen starting at 3.3% strain as well, where they appear to saturate after fracture, causing the internal structure of many larger grains appearing striped in color.

The first thing to note is that for deformation twinning, the color gradient for Schmidt Factor goes from 0.2 to 0.5, and for basal and prismatic slip the gradient goes 0 to 0.5, making any

yellow or green still have a very high Schmidt factor when compared to the two operative slip systems. Pyramidal slip has high Schmidt factor range as well, going from 0.29 to 0.5. It should be noticed immediately that while basal slip has some favorable and unfavorable grains, prism slip almost always has a favorable orientation. From this it can be concluded that the observations by Jeffery that basal slip and $\{11\bar{2}1\}\langle 11\bar{2}6\rangle$ twinning are the dominant mechanisms, otherwise deformation would be far more uniform than it currently appears if prism slip was the dominant slip system. It can be seen from the scans in Figure 3.4, that while most of the large grains with high $\{11\bar{2}1\}\langle 11\bar{2}6\rangle$ Schmidt factors show deformation twins, twins can appear in grains with Schmidt factors lower than 0.4, however it is less common. All grains with high twin Schmidt factors also show high basal Schmidt factors and large amounts of misorientation. This indicates that after twins have formed, basal slip is the operative method for strain accommodation. Significant misorientations are also seen in grains oriented only for pyramidal slip, making the number of active deformation modes in this sample a minimum of three, based on EBSD observations.

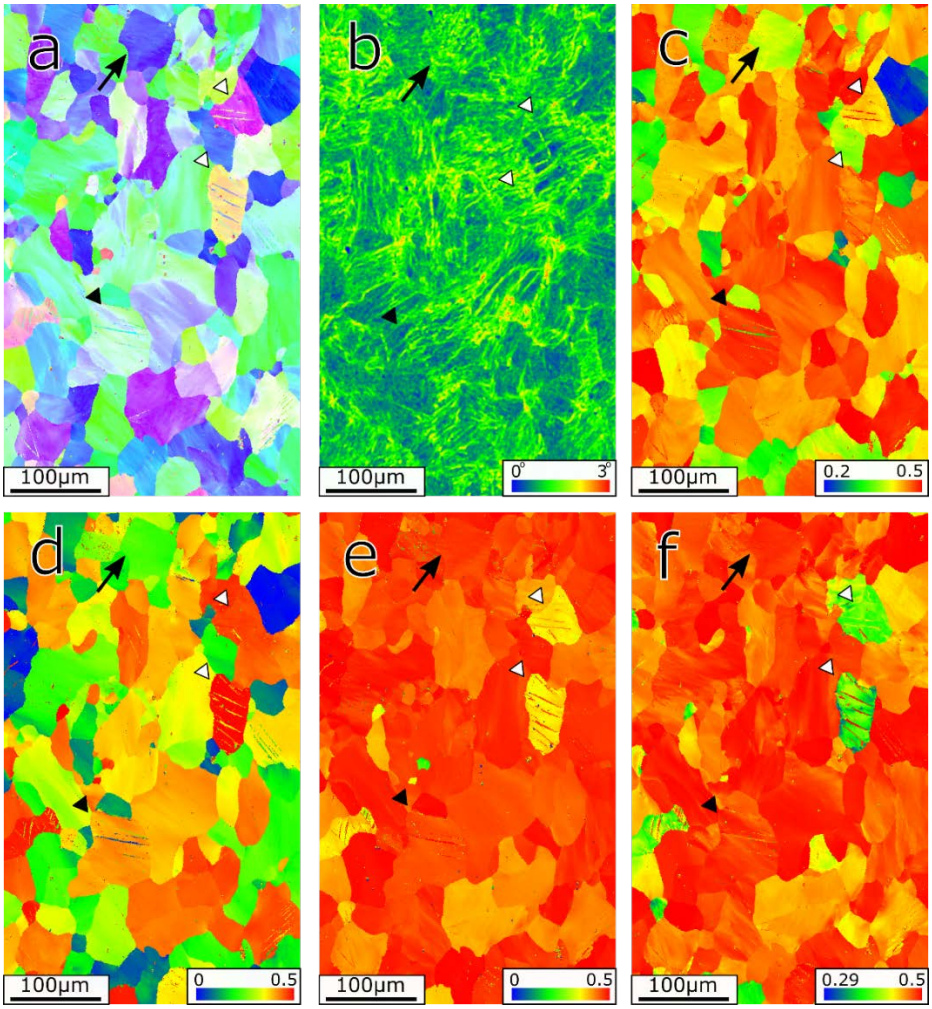

Figure 3.4: Overview EBSD map of sample 1 (after fracture) a). Local misorientation profile is seen in b), with corresponding Schmidt Factor maps for $\{11\bar{2}1\}\langle 11\bar{2}6\rangle$ type twins seen in c), the $\{0002\}\langle 11\bar{2}0\rangle$ slip system in d), $\{10\bar{1}0\}\langle 1\bar{2}10\rangle$ slip system in e), and

the $\{10\bar{1}1\}\langle 11\bar{2}3\rangle$ slip system in f). Note that the obviously twinned grains, marked with white triangles, do not necessarily have the highest Schmidt factors for the $\{11\bar{2}1\}\langle 11\bar{2}6\rangle$ twin system, but contain high basal dislocation activity. Large amounts of pyramidal slip activity is marked with the black arrow. The black triangle marks heavily twinned grains which are more favorable for pyramidal slip.

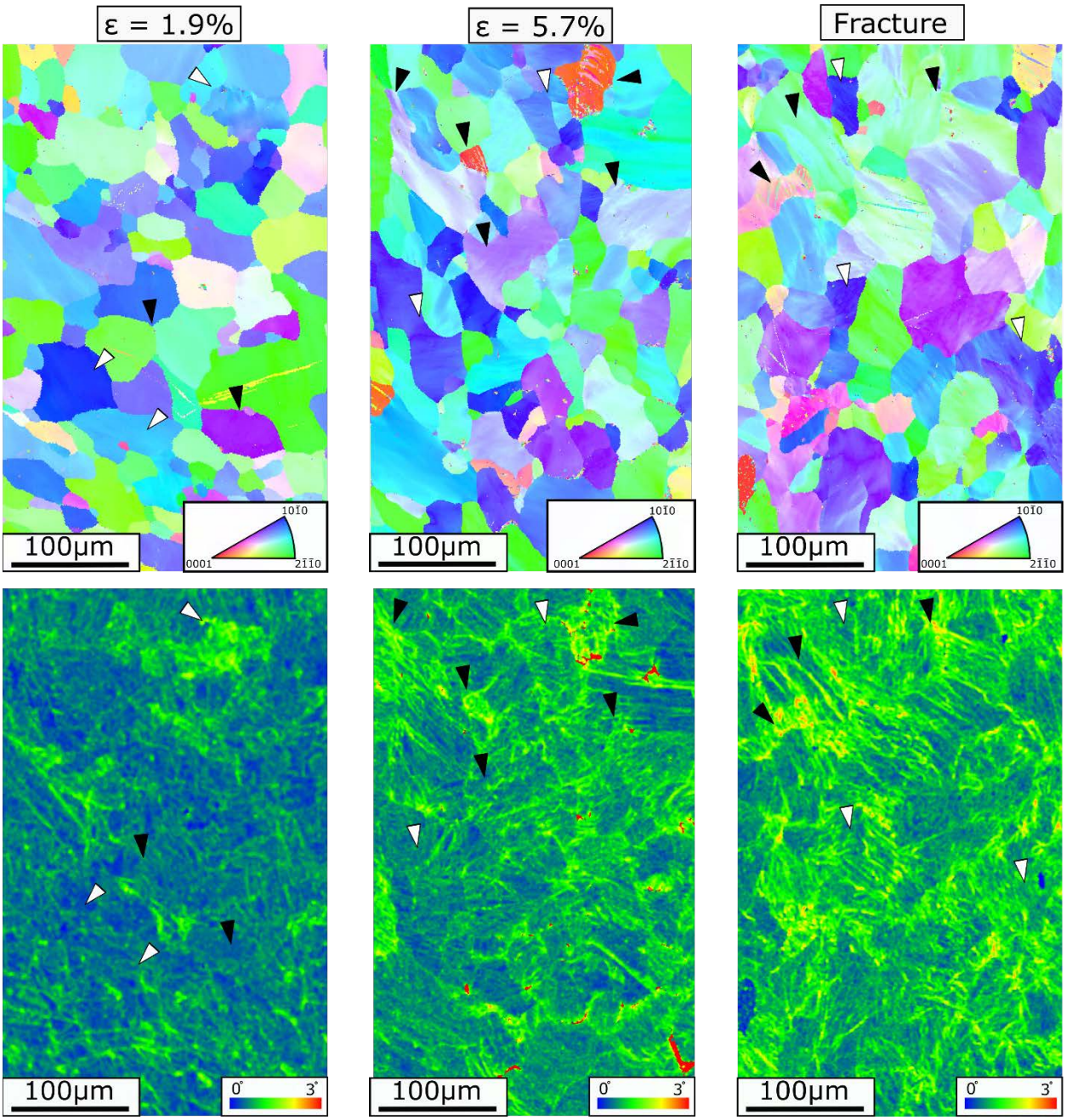

Figure 3.5: Overview for EBSD IPF maps and local grain misorientation maps for sample 3, 1.9% strain, sample 5, 5.7% total strain, and sample 1, after fracture. These samples were chosen because there was a roughly 4% strain increase between steps. Black triangles mark basal slip favorable grains, and white triangles mark prismatic slip

favorability. Note that as the amount of strain increases regularly, the total misorientation profile also steadily increases and contains many more 5° misorientation saturation points. The grains with heavily saturated 5° tend to be highly twinning as well as showing more basal slip band formation.

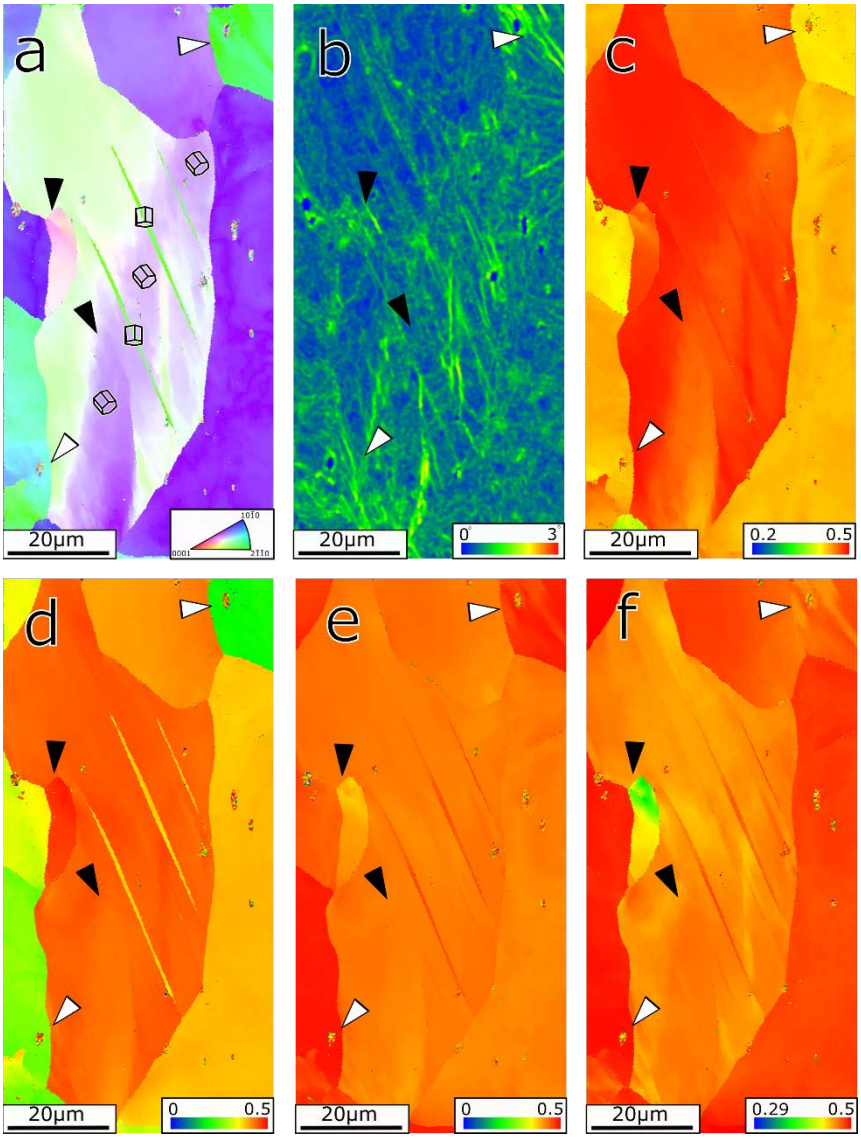

Figure 3.6: Close up EBSD map of sample 1 (after fracture) a) with correlating local internal grain misorientation map b), and the Schmidt Factor maps for $\{11\bar{2}1\}\langle 11\bar{2}6\rangle$ type twins is seen in c), the $\{0002\}\langle 11\bar{2}0\rangle$ slip system in d) $\{10\bar{1}0\}\langle 1\bar{2}10\rangle$ slip system in e), and the $\{10\bar{1}1\}\langle 11\bar{2}3\rangle$ slip system in e) Black triangles mark basal slip favorability, while white triangles mark prismatic slip favorability.

When looking at overall trends of misorientations as a function of strain, Figure 3.5, it can be quickly seen that the overall local misorientation maps have large bands saturated up to high values of 3° as the strain increases to fracture. Additionally, at the low and intermediate strain,

the relative amount of deformation is seen to be lower in pyramidal slip oriented grains (deep blue and purple marked with white arrows). Any grain with noticeable deformation twinning has coupled increased basal slip Schmidt factors and generally has higher local misorientations at low strains. Couple this behavior of basal slip dominating at low strains with the proclivity for deformations twins to all have been formed at strain values of 3% or below, a behavior of dynamically changing deformation modes seems to be the operating mechanism for accommodating deformation in Re. As twinning in the crystal saturates and basal slip occurs in twin grains, basal slip work hardens quickly, allowing for the higher CRSS system of pyramidal slip to begin deforming properly oriented grains. This evolving deformation behavior is the likely cause of the high initial work hardening rates. Initial twins form in easy basal slip grains, causing high work hardening, which allows for the activation of pyramidal slip.

While the 750μm step sized used for the overview scan can acquire adequate measurements of overall structure of Re as a function of strain, detailed maps of each orientation using small step sizes of sub 200nm are required to fully observe any possible small and thin deformation twins within the twinning-unfavorable grains. Figure 3.6 shows a detailed map of sample 1 after fracture, with Schmidt factor maps for the most important deformation systems next to the misorientation maps. Through use of the black (basal slip and twinning favorable grains) and white triangles (pyramidal slip oriented grains) to show grains of note. In the large central grain and the smaller neighboring grain of Figure 3.6a and b), the large misorientation band through the center is highly favorable for basal slip. This misorientation band goes through multiple twins, and crosses along basal planes through many twins. While in compression twinning was seen to impede dislocation motion, the large scale EBSD data shows that dislocations are less affected by twins in tension. It can be seen that both grains perfectly oriented for pyramidal dislocations here have large local misorientations. This series of Schmidt factor maps shows that the basal slip and twinning operate in tandem at the hundreds of nanometer length scale, while pyramidal slip operates largely without any interaction with twins.

Finally, a close look at how dislocation plasticity and twinning interact with each other at different strains, seen in Figure 3.7 where a sub 200nm step size for EBSD acquisition is used. Here it is again observed that the trend for twinning and dislocation plasticity seen in the overview scans of Figure 3.4 is apparent at smaller size scales that include only a handful of grains. Grains marked with black triangles were favorable for basal slip and grains with white triangles are pyramidal slip favored. Here the large contrast between 9.3% strain and 3.8% strain is readily apparent, as is the difference between the misorientation in pyramidal grains when compared to basally oriented grains. Again, it is seen that grains with twins have much more misorientation than those without, meaning that basal slip and twinning operate in unison to deform the crystal. In the 3.4% strain sample, the largest misorientations are surrounding twins, with very little seen in purely pyramidal slip grains. Most importantly, from 3.4% strain to fracture, the relative amounts of twinning within similarly oriented grains has not changed appreciably, only the extent of dislocation plasticity has increased substantially. Further evidence that the high initial work hardening is due to extensive twinning which quickly gets replaced by basal slip followed by pyramidal slip.

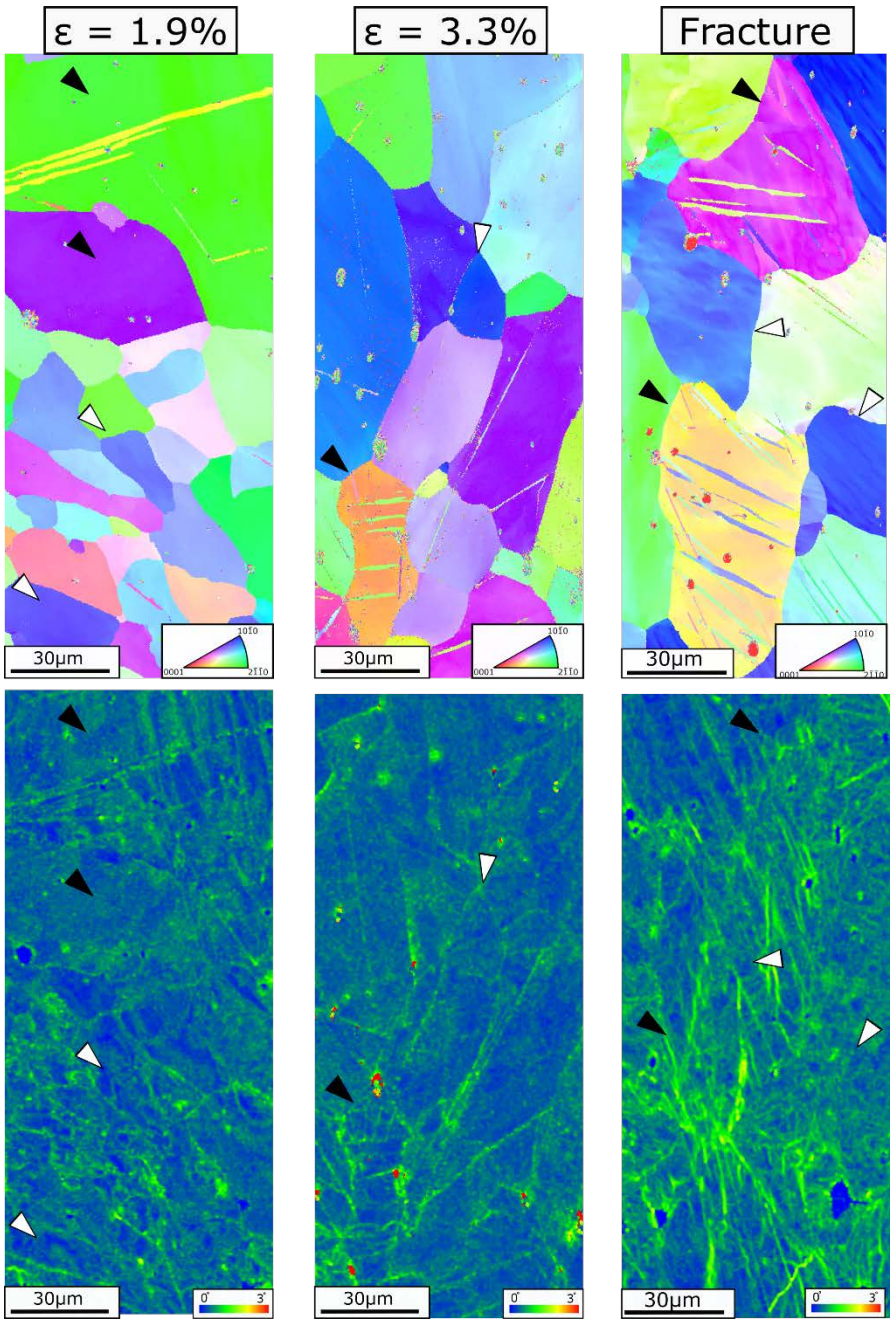

Figure 3.7: Comparison of high magnification EBSD IPF maps and misorientation maps for a strain progression. The average amount of twinning in twin favorable grains has not increased substantially between the IPF maps within a) and c), this indicates that twinning saturates at relatively low strains. Dislocation plasticity then becomes a dominating factor after the initial twin formation, as seen through the large differences in local average grain misorientation in b,d). The red circles in the IPF map of a results from surface contamination. Triangles mark notable grains.

3.2.2. TEM Imaging of Twins and Dislocations in Rhenium

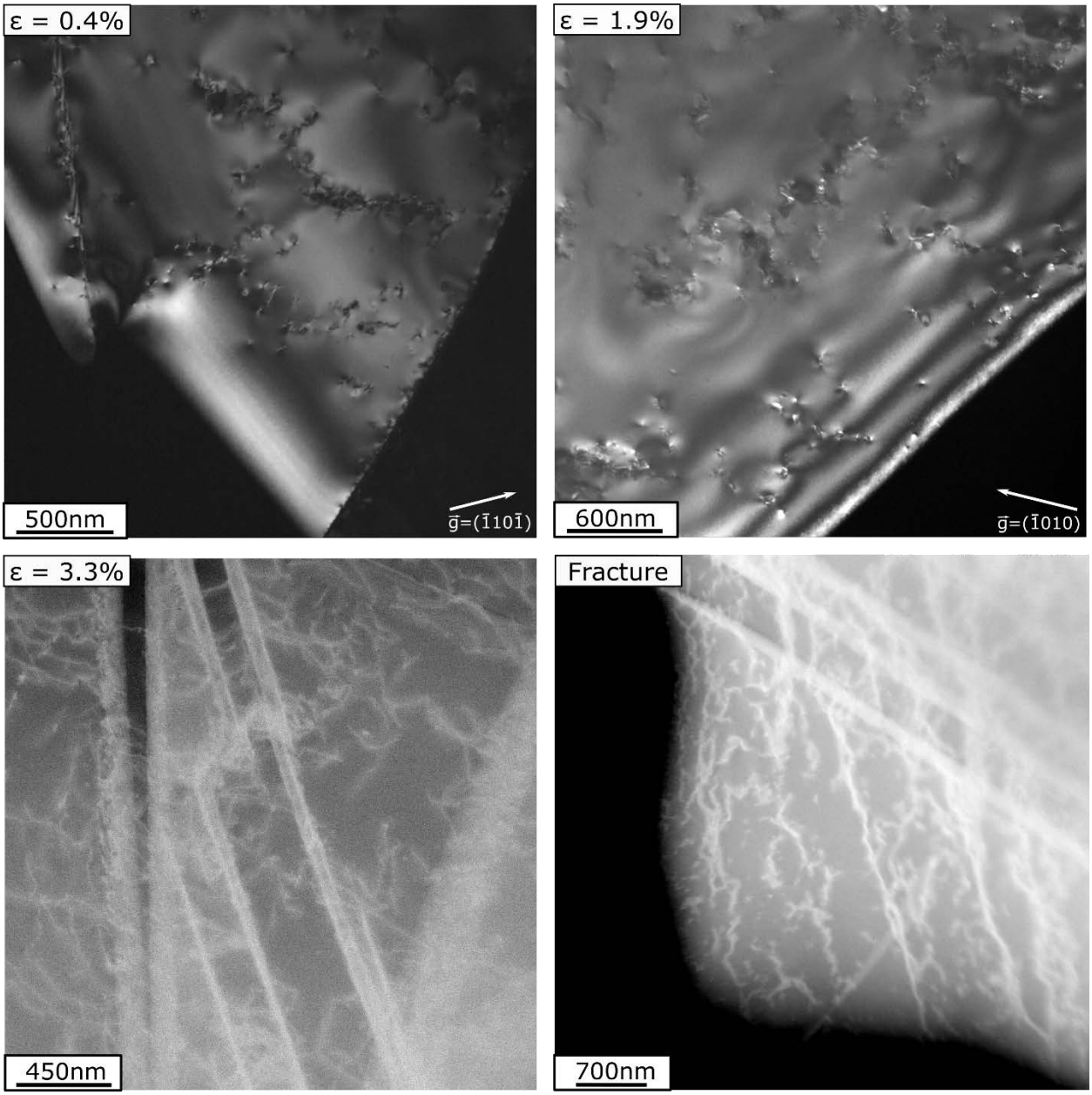

Figure 3.8: Overview of microstructures seen using conventional TEM 2-beam Dark-field imaging (top) and conventional HAADF STEM imaging (bottom). STEM imaging has removed all dynamical contrast seen in the TEM images (such as thickness fringes in the 1.9% strain image) making images much more interpretable.

As it was previously seen in compression Re samples, as well as in the EBSD maps, twins in rhenium can be extremely thin and complex in structure. This requires a multi-length scale analysis that correlates the microstructures and relates observations internal to the microstructure to properties at large length scales. Due to the complexity of twinned structures in Re, TEM analysis gives valuable context for understanding the mechanisms causing strain accommodation within the Re microstructures. For this work conventional TEM imaging was used to determine

the twin structures as well as the dislocation Burgers vectors and habit planes, and HAADF STEM was used to get detailed images of the general microstructural behavior. HAADF STEM was invaluable in imaging the detailed dislocation structures surrounding twins for two main reasons. Firstly, STEM images are easily interpretable, and have more forgiving microscope alignment and image acquisition procedures. Secondly, and more importantly for this work, using a large camera length and convergence angle reduces nearly all of the dynamical contrast induced by phase contrast interactions between the electron beam and the crystal. The resulting images achieved using STEM is essentially pure Z contrast, and here since the only species is Re, the contrast changes linearly with thickness as well as clearly showing any defects within the crystal.

Overview images of the four main strain amounts is seen in Figure 3.8, where the images for 0.4% and 1.9% strain are conventional TEM DF, with the more heavily dislocated 3.3% and after fracture samples taken in STEM. Immediately it can be seen that the thickness fringes in the 1.9% strain sample, an effect of the contrast transfer function interacting with the sample thickness (45) (62), as well as other uninterpretable contrast surrounding twins and dislocations, do not appear in the STEM images. This allows for a large throughput of images to be taken on STEM machines for understanding the general microstructure of the samples. This combined use of STEM images and conventional TEM for microstructural analysis provides the most comprehensive dataset of TEM images of the rhenium microstructure formed under tension.

Immediately when looking at the samples in Figure 3.8 some trends can be seen. Firstly, dislocations orient themselves with respect to each other such that they form long rows of dislocations crossing from twin to twin. Secondly, very long thin twins are seen in the more heavily strained samples, while at low strains, very small twins are much more difficult to observe. The two twin boundaries seen in the 0.4% strain sample is more commonly seen at lower strains, where wider twins have formed. As the strain increases twins tend to form with very high aspect ratios, stretching tens of microns through the crystal, while remaining a few hundred nanometers thick. In terms of dislocation density, it is quite easily seen that the density of dislocations steadily increases, however from the 1.9% strain sample to the 3.3% strain sample the density of twins increases significantly more than between any other steps.

As seen in the low strain overview samples, slip bands containing many dislocations are extremely prevalent in the tension samples. Often these bands span in between twin boundaries, and unlike with the twins seen in compression, dislocation slip bands appear able to pass through the twin boundaries. A full "G dot B" analysis for a dislocation slip band seen within the moderately strained sample 5, 3.3% strain, can be seen in Figure 3.9. Strong two beam conditions were used for each of the first order spots along the $\langle 11\bar{2}3\rangle$ zone axis. This zone axis allows for the determination of both <a> type and <c+a> type dislocations. The invisibility condition here is satisfied when $\vec{g} = (1\bar{1}01)$ and $(\bar{1}10\bar{1})$ making the Burgers vector for the dislocations in this slip band have the vector $\vec{b} = [11\bar{2}0]$. Close observation of the $\vec{g} = (0\bar{1}11)$ BF condition shows largely invisible dislocations, however with the corresponding DF image showing quite noticeable dislocation contrast the overall condition was said to be visible. Additionally, having the clearly invisible $(\bar{1}10\bar{1})$ combined with a $(0\bar{1}11)$ invisibility condition leads to no possible Burgers vectors for this dislocation band. Finally, as the dislocations are

invisible when the $\vec{g} = (1\bar{1}01)$ vector is roughly orthogonal to the dislocation line vector, these dislocations are seen to be screw dislocations.

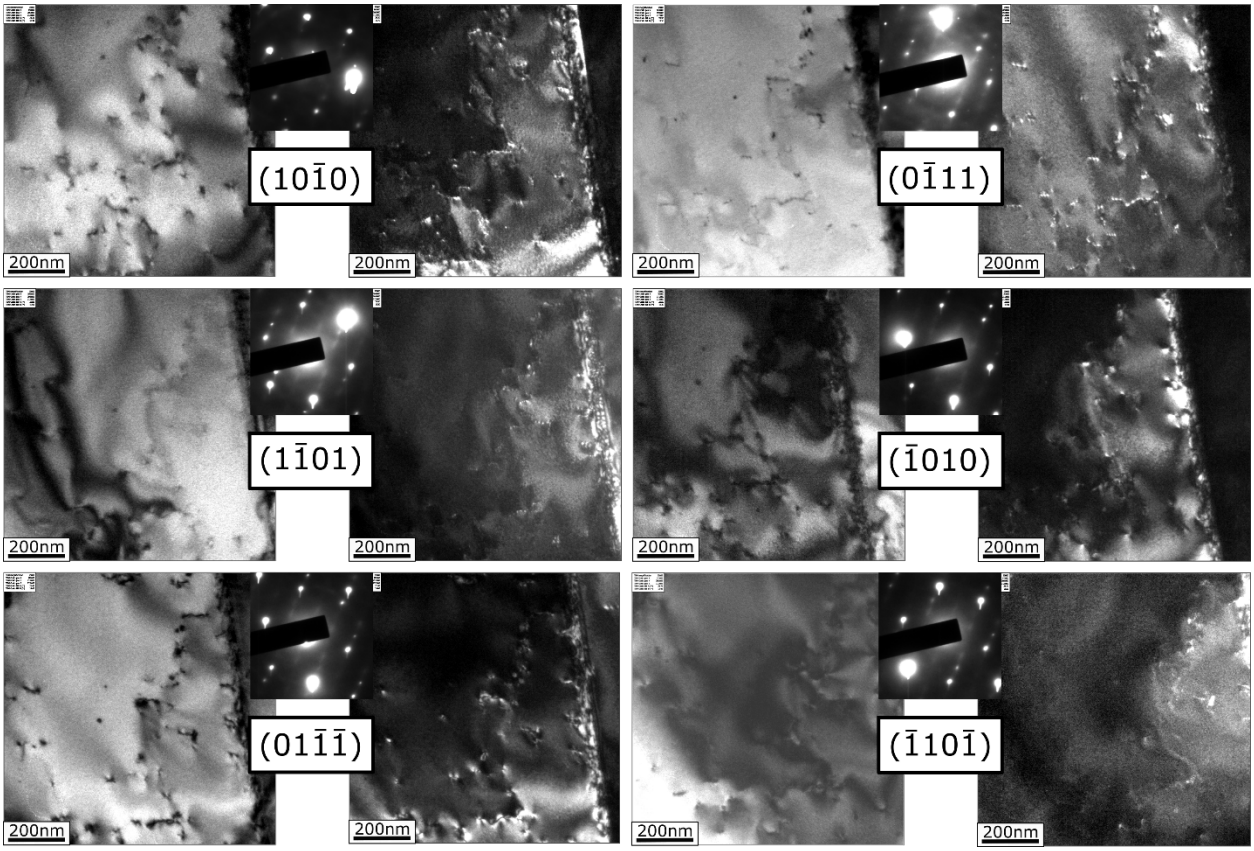

Figure 3.9: "G dot B" analysis for a dislocation slip band in sample 5, 3.3% strain, viewed in a JEOL 2011 microscope, using a 200kv accelerating voltage. Images were all taken using a strong 2-beam Bragg condition from a $\langle 11\bar{2}3 \rangle$ zone axis with the BF images (left) generally showing less dislocation contrast than the DF two beam condition (right). Using the DF images, the $(1\bar{1}01)$ and $(\bar{1}10\bar{1})$ were seen to be invisible, such that $\vec{g} \cdot \vec{b} = 0$, and $\vec{b} = [11\bar{2}0]$ screw dislocations.

These relatively low strain dislocations provide insight into the macroscopic behavior of slip and twinning seen in the EBSD maps. As the dislocations are all loosely aligned, so they should all slip along the same plane, accommodating strain along the same direction. Additionally, sizable twins have already been formed, with the bulk of this dislocation motion happening in between the twin boundaries. This corroborates the conclusions of the EBSD data, showing that twin favorable grains would have basal slip after the formation of twins, based on the Schmidt factor and misorientation maps. The next set of dislocation analysis on sample 1, Figure 3.10 after fracture, shows the interactions of <a> type and <c+a> type dislocations. The series of DF images tilting todifferent known zone axis shows clearly a few sets of <c+a> dislocation networks (black arrows) surrounding slip bands of <a> type dislocations (white triangles).. Through using the tilt series in Figure 3.11, it was determined that the <a> type dislocations operated upon the basal plane, and the <c+a> dislocations are upon the standard pyramidal plane,

as was determined using Schmidt factor analysis with EBSD maps. Within sample 1 (after fracture) just like in sample 5 (3.3% strain), the <a> type dislocations form loosely aligned slip bands of dislocations slipping along the same direction. In this high strain sample however, there are two distinct slip bands oriented roughly 60° apart from each other. This means that when fracture occurs, multiple easy basal slip systems are activated within individual grains, with pyramidal <c+a> dislocations surrounding the basal dislocations. These <c+a> dislocations, that were not visible during the initial low-strain dislocation observations, are likely appearing in such large quantities only when the motion of basal dislocations becomes exceedingly difficult. With the pyramidal dislocations bounding the basal dislocations so precisely, the formation of pyramidal dislocations serves to further impede the motion of basal dislocations, resulting in inability for the sample to adequately accommodate further strain, which leads to failure.

With the observation of multiple active dislocation systems at high strains, STEM imaging of twins within the moderate strain, the 3.3% total strain sample 5, was used to investigate the properties of twin boundaries as well as the interactions they have with the extremely common <a> type dislocations. STEM imaging allows for the removal of the complex phase contrast seen in Figure 3.8, making the imaging of twins much more readily interpretable. The common behavior unique to the $\{11\bar{2}1\}\langle 11\bar{2}6\rangle$ twins seen in rhenium is their ability to transmit through each other. Another key feature which was commonly seen in Re twins under compression in Chapter 2, is the formation of larger twins often comprised of many smaller twins aggregated together. Figure 3.12 shows the structure of a typical $\{11\bar{2}1\}\langle 11\bar{2}6\rangle$ twin formed under tension with a second $\{11\bar{2}1\}\langle 11\bar{2}6\rangle$ twin propagating horizontally through the larger twin.

Two main factors were used when determining the orientation of the twins and matrix in Figure 3.12. First diffraction patterns of the six noticeable regions were taken to determine orientation relationships and the angles between incident and exiting twins was measured within the STEM image, each DP inset within the STEM image of Figure 3.12. Due to the non-standard shape of tension samples (2.85mm x 3mm rectangles) these images are taken using the single tilt FEI TEM holder since this abnormal shape could not fit within the FEI double tilt holder (something which was not an issue within the JEOL double-tilt holders, allowing for "G dot B" analysis). As such, the closest achievable zone for the matrix was near to a $\langle 10\bar{1}0\rangle$ zone, which is an excellent choice as it is the "rotation axis" around which the $\{11\bar{2}1\}\langle 11\bar{2}6\rangle$ twin changes its orientation. The most important thing to note about the twins seen here is that they have the same classical twin morphology seen in other heavily deformation twinned metals, where a distinct twin boundary separates the matrix crystal orientation from the twinned crystal orientation. The interior of the large vertical twin contains a single heavily dislocated region separated by the horizontal twin. Secondly it should be noted that the horizontal twin changes the orientation of the crystal between the top and bottom of the sample by a few degrees. While this does not appear to be a large misorientation it factors into the angles between the various twins not being quite what the misorientation between $\{11\bar{2}1\}\langle 11\bar{2}6\rangle$ twins should be in a perfect Re crystal.

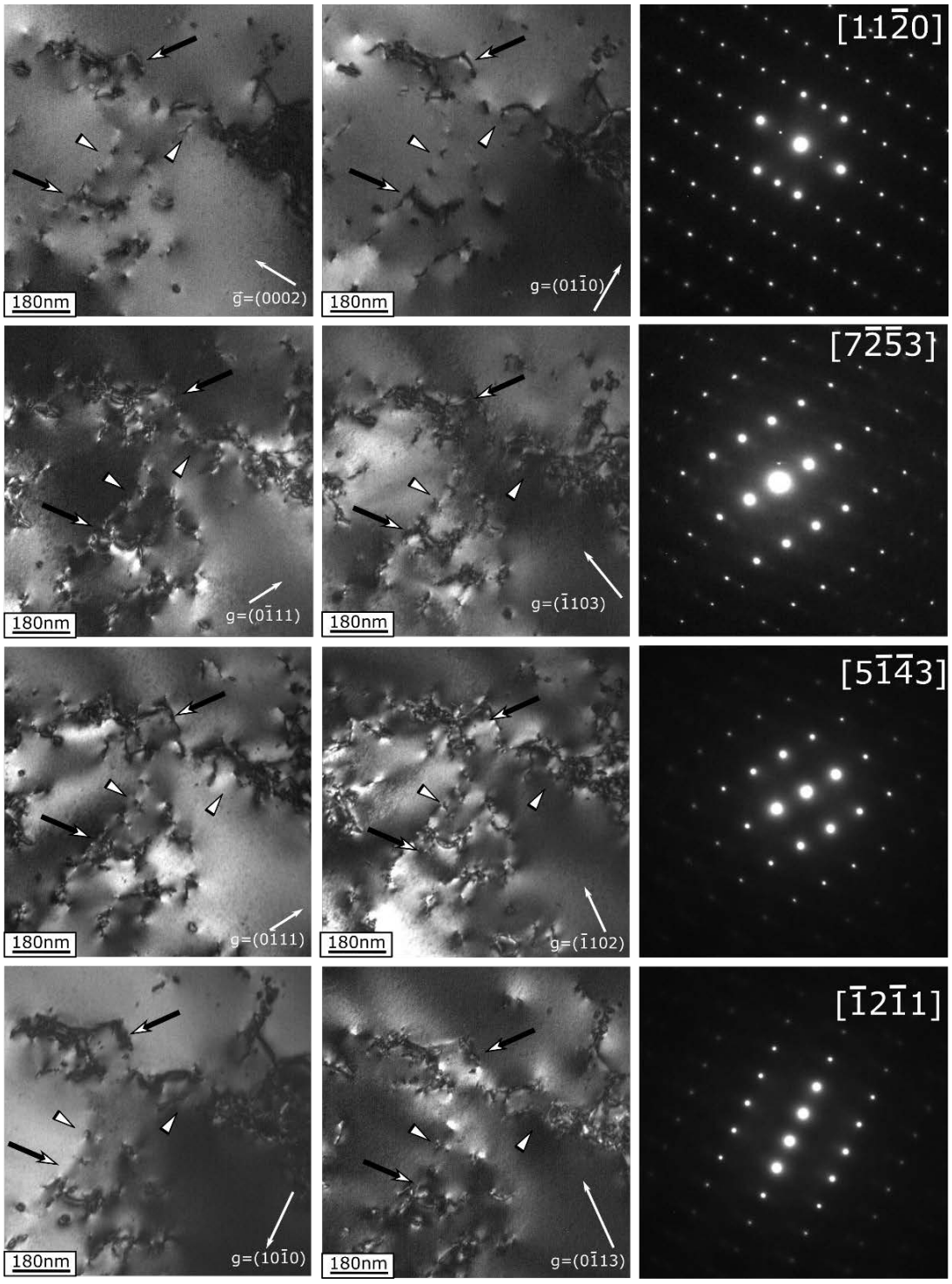

Figure 3.10: "G dot B" analysis for a large dislocation network within sample 1. The images were taken in a JEOL 3010 microscope, using a 300kv accelerating voltage. Large black arrows show immobile <c+a> dislocations, with white arrows showing the basal <a> type dislocation slip bands.

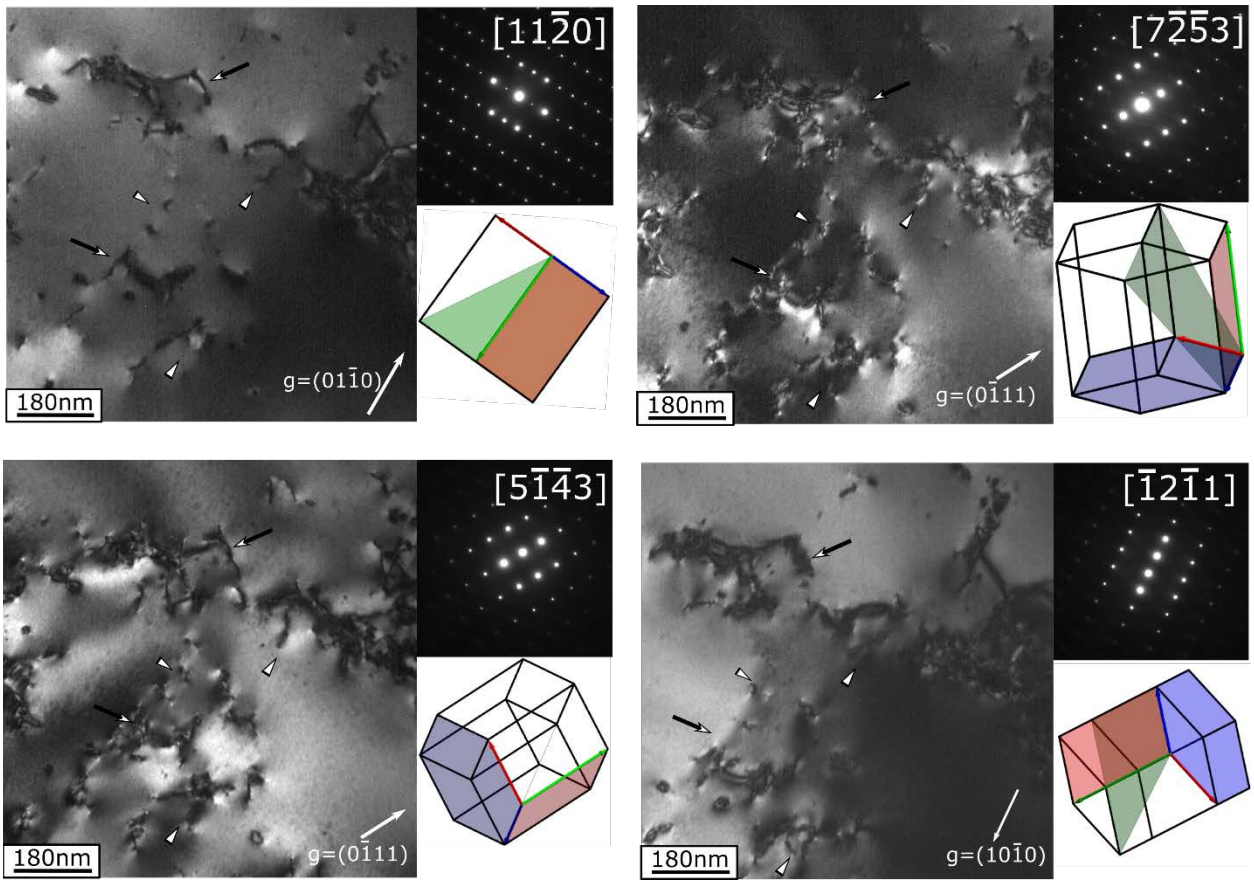

Figure 3.11: DF images along three unique zones of a single area within sample 1. Diffraction patterns and crystal orientation show <a> type dislocations (white triangles) lie on basal planes and <c+a> type dislocations (black arrows) lie on pyramidal planes. (14)

The horizontal twin forms an angle of 68° to the twin boundary seen of the larger vertical twin, this angle is mirrored around the twin boundary twice, allowing for the twin to exit through the twinned region parallel to its initial direction after effectively "jogging" through the crystal along the basal planes. The measured angle of 68° is relevant for two more reasons, firstly it is the misorientation between the $\langle 10\bar{1}0\rangle$ zone axis and the $\langle 7\bar{2}\bar{5}3\rangle$ zone axis. Since there is a few degree misorientation accompanied by the horizontal twin boundary, this 68° misorientation also becomes relevant as the angle between a $[1\bar{2}16]$ and a $[1\bar{2}1\bar{6}]$ direction will result in a roughly 65° for Re. Coupled with the few degree misorientation between the top and bottom diffraction patterns leads to the conclusion that the two twins are both the very common $\{11\bar{2}1\}\langle 11\bar{2}6\rangle$ type twin.

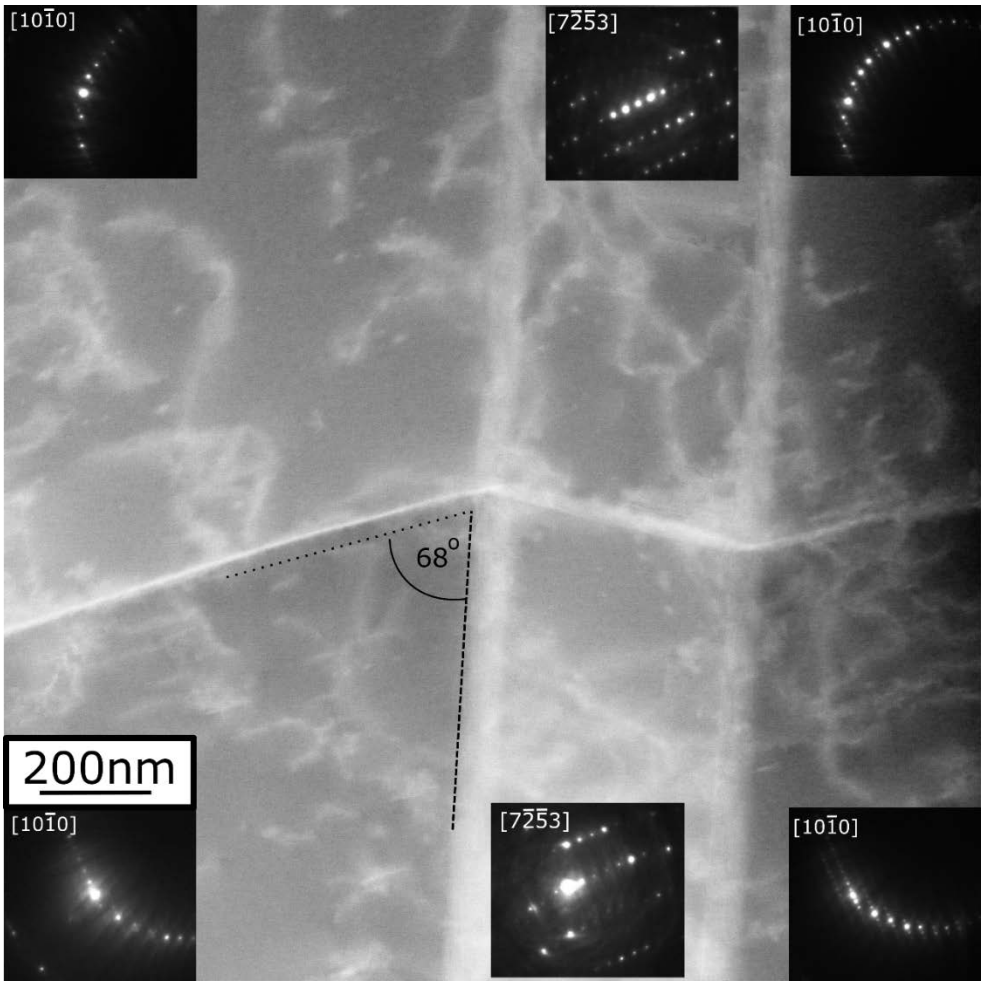

Figure 3.12: Close up view of twin transmission in samples 5, 3.3% strain using HAADF STEM at 300 kV. Note that the lateral twin causes a small misorientation (as seen by the inset diffraction pattern) of roughly 5° between the top and bottom of the image. The orientation difference between the middle twin and the main near $[10\bar{1}0]$ orientation is 68°, resulting in the closest possible orientation the $(11\bar{2}1)$ twin commonly prevalent in Re.

It should be noted that the horizontal twin appears to increase in width substantially in width within the larger vertical twin regime, meaning that the twin plane along which it was formed has changed to occupy the requisite plane within the twinned regime. This twin transmission has been accompanied by an overall "jog" of the twin relative to the basal plane normal, as was seen in the twin transmission of $\{11\bar{2}1\}\langle 11\bar{2}6\rangle$ formed during compression. However here it can be clearly seen (mainly due to the use of contrast free STEM imaging and not conventional TEM) that with simple internal structure of the large vertical twin, transmission through the twin boundary involves a change of twin plane to that of the crystal past the twin boundary, while still maintaining the large misorientation across the twin after transmitting through the twin boundary.

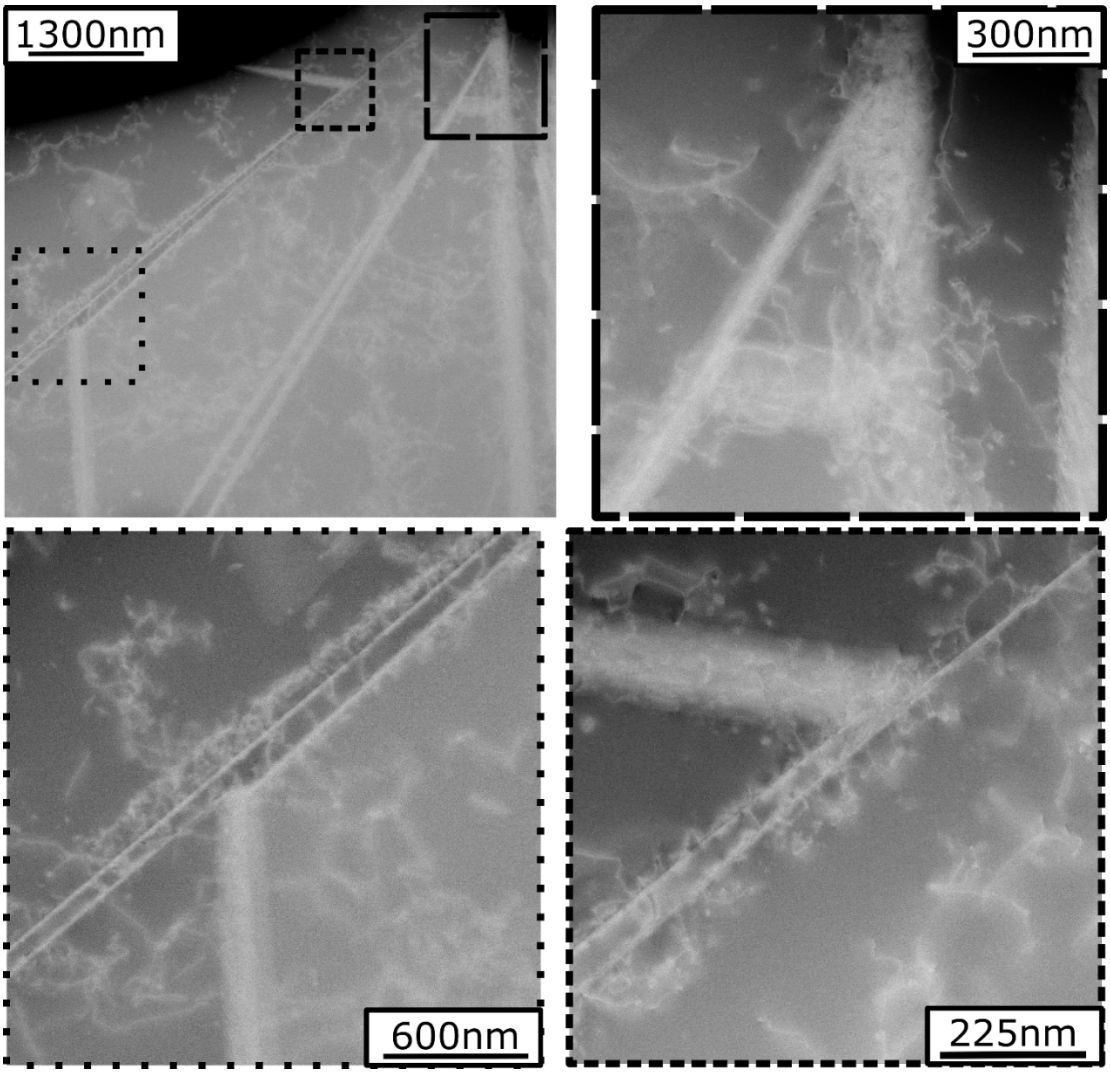

Figure 3.13: Twin structures seen using STEM imaging. Unlike twins seen formed during compressive loading of rhenium, twins formed under tension have a much more classical structure involving twin boundaries with a re-oriented crystal in between the boundaries. The twinned region contains roughly similar densities of dislocations as the surrounding matrix.

Dislocation interactions with the $\{11\bar{2}1\}\langle 11\bar{2}6\rangle$ twins formed in tension are much simpler than during the $\{11\bar{2}1\}\langle 11\bar{2}6\rangle$ compression formed twins. Since the twins formed in compression had such an intricate internal structure it was not surprising that dislocations were not identified within the twins themselves, only populated on the boundaries. It is also unsurprising the difficulty that twins had in transmitting through such complicated compression induced twin boundaries. In Figure 3.13 it can be seen that very long thin twins form much like in the samples of all strain amounts that have been observed. The twins are populated along their lengths with multiple dislocations coming from the twin boundaries, as well as dislocations crossing the interiors of the twins, bridging in between the two twin boundaries. It is also noticeable how twins appear to intersect one another or branch away, forming regions of thicker

and thinner twins, seen Figure 3.13 bottom images. The large nets of dislocations surrounding twins being accompanied by noticeable changes in the directions of the twin boundary, Figure 3.13 top right, can lead to some speculation that the in order for the twins to change their twin plane and their direction, a large dislocation network is present during the nucleation of a new twin from a pre-existing twin. The interactions between dislocations and twins are not conclusively observed with these STEM images, and future work would be needed in order to view the twin formation process *in-situ*.

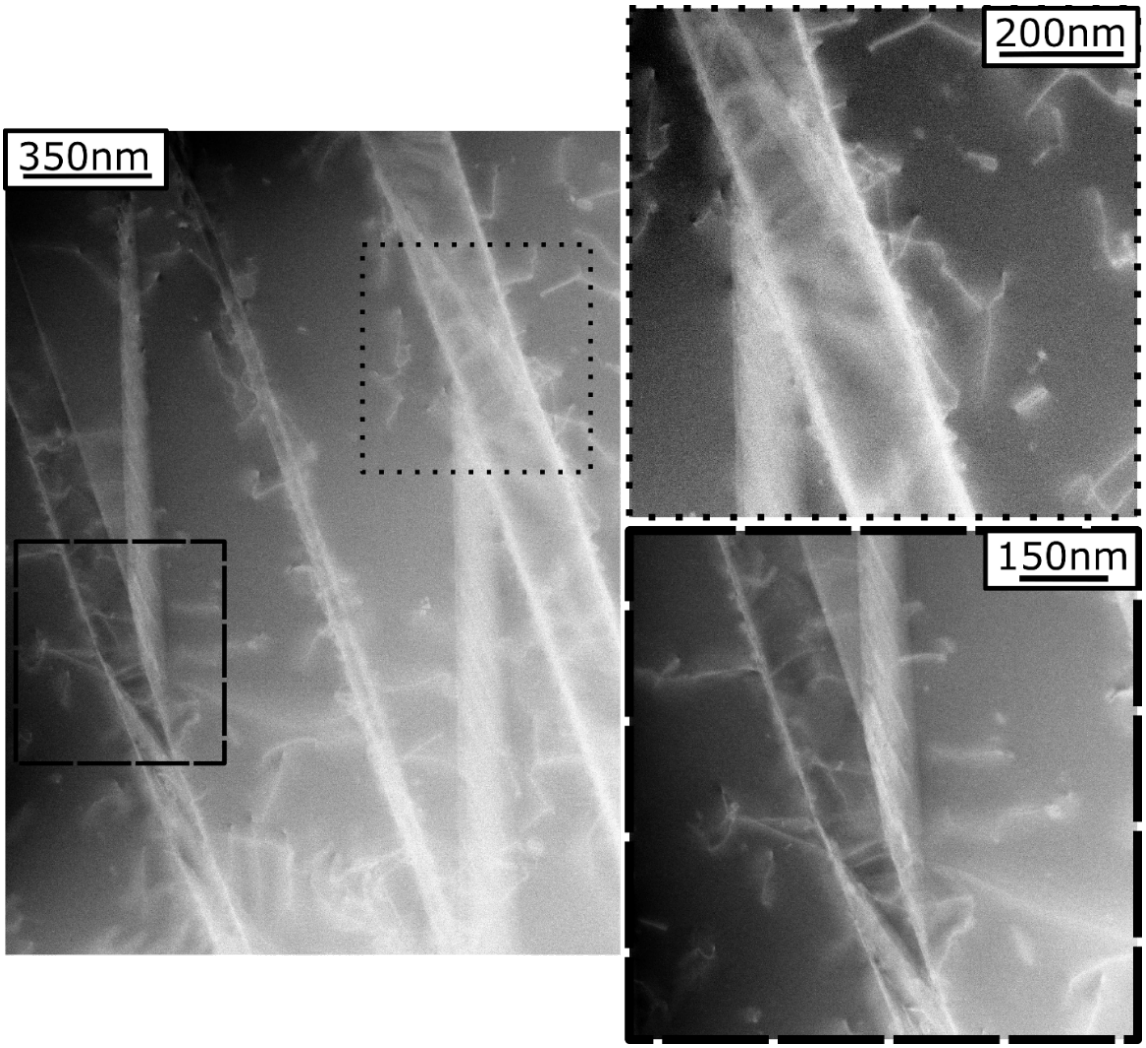

Figure 3.14: STEM images taken from sample 5, 3.3% strain. The large twins have an interior boundary from which secondary twins appear to grow. Here dislocation density is relatively low, when compared to Figure 3.13, but twin density is much higher.

Large bands of heavily dislocated regions are not the only sites from which new twins appear to form. In the secondary area seen in Figure 3.14, multiple long thin twins can be seen branching from the twin boundaries with many dislocations passing between and through the individual twin boundaries. Unlike as in the previous area, Figure 3.13, the dislocation density surrounding the twins is relatively low, and the twin boundaries appear to come from areas

containing a secondary twin boundary lies within the twin. This section of the sample with a much higher twinning density shows that if the relative area of observed twins increases, when compared to Figure 3.13, the dislocation density reduces substantially. This further validates the notion that when it is crystallographically feasible, twinning will be dominant initially followed by basal slip, and then finally by <c+a> pyramidal slip.

To finish the possible twin configurations seen in Tension twinning, Figure 3.15 shows the very complex possibilities of twins within tension samples of Re. In this part of the sample 5 microstructure the unique "z" twinning seen in previous compression samples also appears within the tension sample microstructure. It can also be seen in the magnified larger twins that dislocations are highly active within the in twinned regime, with dislocations clearly being able to cross the interior twin boundary near interior junction of the twin split. With the more conventional twin boundary structure seen in tension induced $\{11\bar{2}1\}\langle 11\bar{2}6\rangle$ twins, it is unsurprising that dislocation transmission through twin boundaries is easily achieved. To this end, future work should involve the developing the understanding of the intricacies of the $\{11\bar{2}1\}\langle 11\bar{2}6\rangle$ twin boundary for twins created in tension, contrasted to compression induced twins, as well as the twin boundary orientations which either allow or disallow the transmission of dislocations.

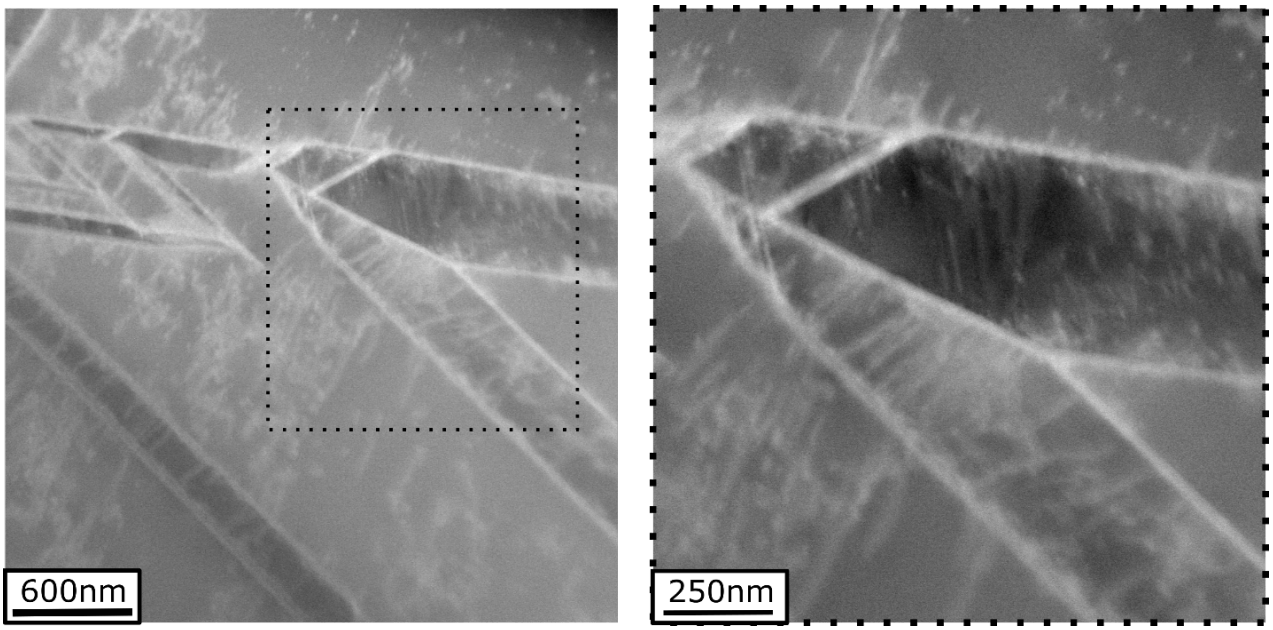

Figure 3.15: Large twinned region showing many branching twins from sample 5, 3.3% total strain. Here the cause of the twin branching or direction change is not apparent. With the such complex twinning structures the TEM thin disks showing two-dimensional slice of a more complex macroscopic three-dimensional object does not fully describe the twin morphology.

3.3. Conclusion Remarks of Macroscopic Tension

Pure annealed rhenium samples were tested in tension in order to understand the interplay between microstructure and the exceptionally high work-hardening behavior seen uniquely in rhenium. Re tension samples were strained to systematically chosen total strain amounts and sectioned in order to understand the microstructure present within each section of the stress-strain profile. Through the use of multiple microscopy techniques, a full description of the typical microstructure progression of Re under tension as a function of strain has been achieved. The use of EBSD has shown that the overall undeformed microstructure had a large grain size distribution, with a very $\{11\bar{2}1\}\langle 11\bar{2}6\rangle$ twin unfavorable texture for loading under tension. This lead to the overall area fraction of twins within the post-deformation microstructure being equivalently saturated above a strain value of one third the fracture strain. From the point of twin saturation and above, all changes to the deformed microstructure using EBSD were seen as increased local misorientations within the grain interiors. Grains showing extensive large twins had large misorientations in between the twins due to basal slip activity, as determined by the Schmidt factor favorably seen in the EBSD maps and later confirmed using TEM imaging. Finally, EBSD had shown that pyramidal slip activated appreciably only when strain increased above half of the failure strain. The high initial rate of twin formation with dislocation slip was tied to the high initial work hardening rate which quickly lowers as twinning saturates.

Conventional TEM "G dot B" analysis was performed to understand the dislocation structures as well as the planes upon which dislocation slip operated. <a> type $\vec{b} = [11\bar{2}0]$ screw dislocations operated on the basal planes in loosely aligned slip bands. Only <a> type dislocations were observed in the TEM at low strains, generally between twin boundaries. At failure, <a> type $\vec{b} = [11\bar{2}0]$ basal screw dislocations were again observed in dislocation slip bands. <c+a> type $\vec{b} = [11\bar{2}3]$ pyramidal screw dislocations, which formed tangled dislocation nets interfering with <a> type glide, were observed at high strains, likely due to much higher CRSS value. HAADF STEM imaging was used in order to view twin boundaries without dynamical contrast as well as dislocations passing through twin boundaries. The morphology of tension induced $\{11\bar{2}1\}\langle 11\bar{2}6\rangle$ twins was more representative of classical twin structures involving well defined twin boundaries surrounding a region of crystal with a single crystallographically related orientation. This did not represent the $\{11\bar{2}1\}\langle 11\bar{2}6\rangle$ type twins seen in compression which consisted of twin aggregates. This compression-tension asymmetry largely due to the twin favorability of the microstructure during compressive loading allowing for the creation of many more twins. Twin transmission with $\{11\bar{2}1\}\langle 11\bar{2}6\rangle$ twins changing twin plane between parent and matrix orientations was observed. Multiple twin systems with twins growing out of twin boundaries were observed, with the TEM and STEM observations confirming the observations made using purely EBSD maps for analysis.

Chapter 4

In-Situ Deformation Analysis of Rhenium

Having seen extensive ex-situ dislocation imaging with dislocation-twin and twin-twin interactions, further understanding can be gained through imaging the formation and motion of dislocations and twin in-situ during straining. While there exist advanced x-ray techniques that can view interior dynamics of crystal structure during deformation of macroscopic samples (75), TEM techniques provide the unique ability to view dislocations (with the possibility of coupling strain mapping using advanced electron detectors (76) (77)) in real time at the highest resolutions while samples are strained. The ability to view the motion of dislocations gives insight into mechanical deformation that is impossible using ex-situ procedures. For instance, if dislocations glide smoothly or glide in a "jerky" manor, this can give insights into the energetics of dislocation core structures and how they operate within crystals (78). Clouet et al. rationalized Zr deforming with very smooth dislocation motion by showing through *Ab initio* modeling that Zr does not have an energy barrier associated with prismatic glide, causing any deformation along the prismatic planes to instantly activate with no noticeable energy barrier between dislocation motion initiation and propagation. Contrast this with the jerky motion of Ti, dislocations in Ti demonstrate an energy barrier between dislocations in a resting lowest energy state, and that of the energy state required for prismatic glide.

The benefits of using in-situ deformation are quite readily apparent with the available data acquired (at a large range of temperatures). The technique does have many drawbacks that, while not overwhelming in their negativity, should be addressed when interpreting any *in-situ* deformation data. As with any nano-scale process, the influences of sample surface area is greatly increased, causing the data that is collected to no be representative of bulk behaviors. With the increased sample surface area nucleation surfaces for dislocation and twins are readily available, possibly suppressing or accentuating certain deformation mechanisms or the formation of precipitates or oxide layers during high temperature tests. Conversely, dislocations are able to easily leave through sample surfaces, which can cause difficulties when looking at the specific behavior of dislocation pile-up effects due to dislocation source starvation (79) (80). The sample stress and strain states are also unknown throughout the *in-situ* foil testing procedure, due to the required geometry used to fit into a Gatan heating-straining TEM holder. This can lead to increased materials and machining costs in order to properly prepare a sample for investigation. Additionally, due to constraints of the geometry of the straining holder, it is only possible to tilt samples along a single axis, making selection of imaging conditions limited and based on random happenstance (due to the unknown nature of producing properly oriented samples on a nano-scale from bulk batch processes). Regardless of the apparent drawbacks, the benefits of in-situ TEM are overwhelming, especially when performed in conjunction with traditional post-mortem characterization techniques.

4.1. Experimental Procedure for In-Situ Deformation

As in the previous pure rhenium experiments, a sample was ordered directly from Rhenium Alloys Inc. to ensure purity and proper processing procedures. The sample was formed from

powder and cold rolled with intermittent heat treatment steps at 1650 °C, with a final 1650 °C anneal to recrystallize twinned grains and remove large scale deformation. The final product took the form of a foil sheet of Re of roughly 600 mm^2 area with a thickness of nominally 100µm, with a total cost of $4,486.35 (81). A microstructure map showing the initial texture of the foil sheet can be seen in Figure 4.1a). As would be expected the sheet is heavily textured, with [0001] direction being oriented normal to the foil, which indicates that basal and prism slip would dominant over twinning during the forming process. This is the same texture as seen in both the Re rod and Re tensile bars in previous chapters, however the EBSD scan direction is orthogonal to that of the macroscopic tests. It should be noted that the grain size is relatively large, roughly 150 µm, with a large distribution of sizes and smaller grains located indicating that recrystallization was an ongoing process. As in all previous mechanical tests, the samples were machined using EDM to provide the correct shape for the TEM holder. An example of the geometry required for the Gatan heating-straining holder tensile bar sample is shown in Figure 4.1b) and the holder itself in is seen in Figure 4.1c). This geometry is standard for all Gatan brand straining TEM holders, regardless of the microscope manufacturer (however the holders are not interchangeable for the microscopes). As with all standard metal foils, the straining bars are electropolished with the 35% acid 2:1 Nitric:Perchloric acid solution used previously until electron transparency. It should be noted that Rhenium has a very high atomic number and thus a very short extinction distance, resulting in difficulties imaging through large sections of material is difficult (62). This also results in large effects of dynamical contrast and phase contrast within TEM micrographs, which can be used to determine if dislocations leave behind steps within the sample surface.

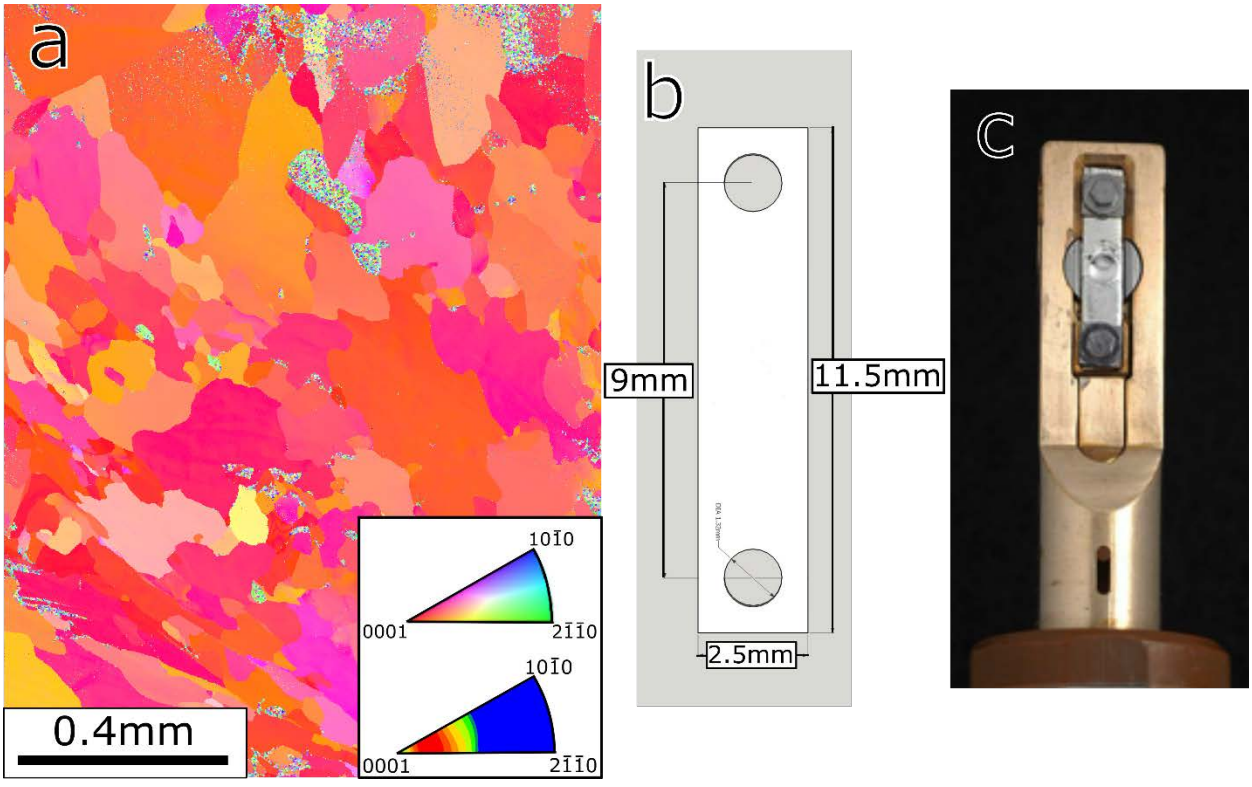

Figure 4.1: a) Initial EBSD pattern with inset IPF and texture maps. b) Required geometry of the Gatan tensile samples. c) Optical image of Gatan Straining holder mounted with a sample

ready for testing. Sample is screwed into position, with a furnace positioned below the electron transparent area used for heating. The holder in c) is designed for use in a JEOL 3010 TEM, however models are available for all commercial TEMs.

4.1.1. Test Method, Sample Pre-Straining, and High Temperature Testing

Once the samples have been prepared, straining the samples is as straightforward a procedure as for macroscopic tensile or compression experiments, however imaging the microstructural changes that result from straining can be exceedingly difficult. The only method for controlling the applied strain is the grip separation of the tensile holder, making the area of most interest for dislocation imaging a matter of intuition. Generally, the region of interested with active dislocations will be along the electron transparent coastline parallel to the strain axis. Straining the sample will result in the elongation of the sample parallel with the viewed coastline, and large translations will accompany any deformation taking place within the sample. Viewing the deformation is the operative the goal of the observation, but deforming the sample can also lead to the sample bending due to the nature of thin samples containing holes. This bending can cause the loss of a diffraction condition suitable for dislocation analysis or imaging of the dislocation in dark-field. Translation of the sample during any applied strain segment can cause the loss of the area of interest from the field of view. The general solution to both of these issues is to strain the sample with intermittent stage translations and gather relevant data of dislocation motion during the relaxation of the dislocations to and equilibrium state after a large straining event.

As the texture for this sample, seen Figure 4.1a), has the basal plans parallel to the straining axis, there are almost no grains that are properly oriented to induce the $\{11\bar{2}1\}\langle 11\bar{2}6\rangle$ type twins. As detailed in previous chapters, this is due to the fact that the twins create a strain along the c-axis of approximately 61.9% in tension, with tensile strains orthogonal to the c-axis producing no impetus for $\{11\bar{2}1\}\langle 11\bar{2}6\rangle$ twins to form. As such, it is expected for in-situ tests to exclusively show a form of deformation slip accommodating all of the strain, with no possibility to observe dislocation-twin interactions in-situ using standard samples. While this would be an issue when studying the effects of twins on dislocation motions *in-situ*, this provides an excellent sample texture to contextualize the distinct dislocation motion seen in the macroscopic tensile samples from Chapter III. One could overcome this texture in order to study the effects of twins on dislocation motion *in-situ*, if samples were created with twins pre-induced. This could be accomplished by pre-bending the samples in the area where jet-polishing was to occur, then straining the samples *in-situ* to see the interactions between twins and dislocations when applying tension.

As rhenium is a used almost exclusively in high temperature applications when used a structural material, in-situ experiments allow for the investigation at elevated temperatures without need for oxidation protections, due to the high vacuum needed for TEM imaging removing most oxygen which can damage the sample. In order to test the high temperature characteristics of dislocations, samples that were shown to have extensive characterizable dislocation motion were heated after the initial straining of the sample was performed and dislocations were observed at elevated temperatures. The necessity of testing a single *in-situ*

sample at room temperature and elevated temperature is due to the nature of the irreproducibility of the in-situ test.

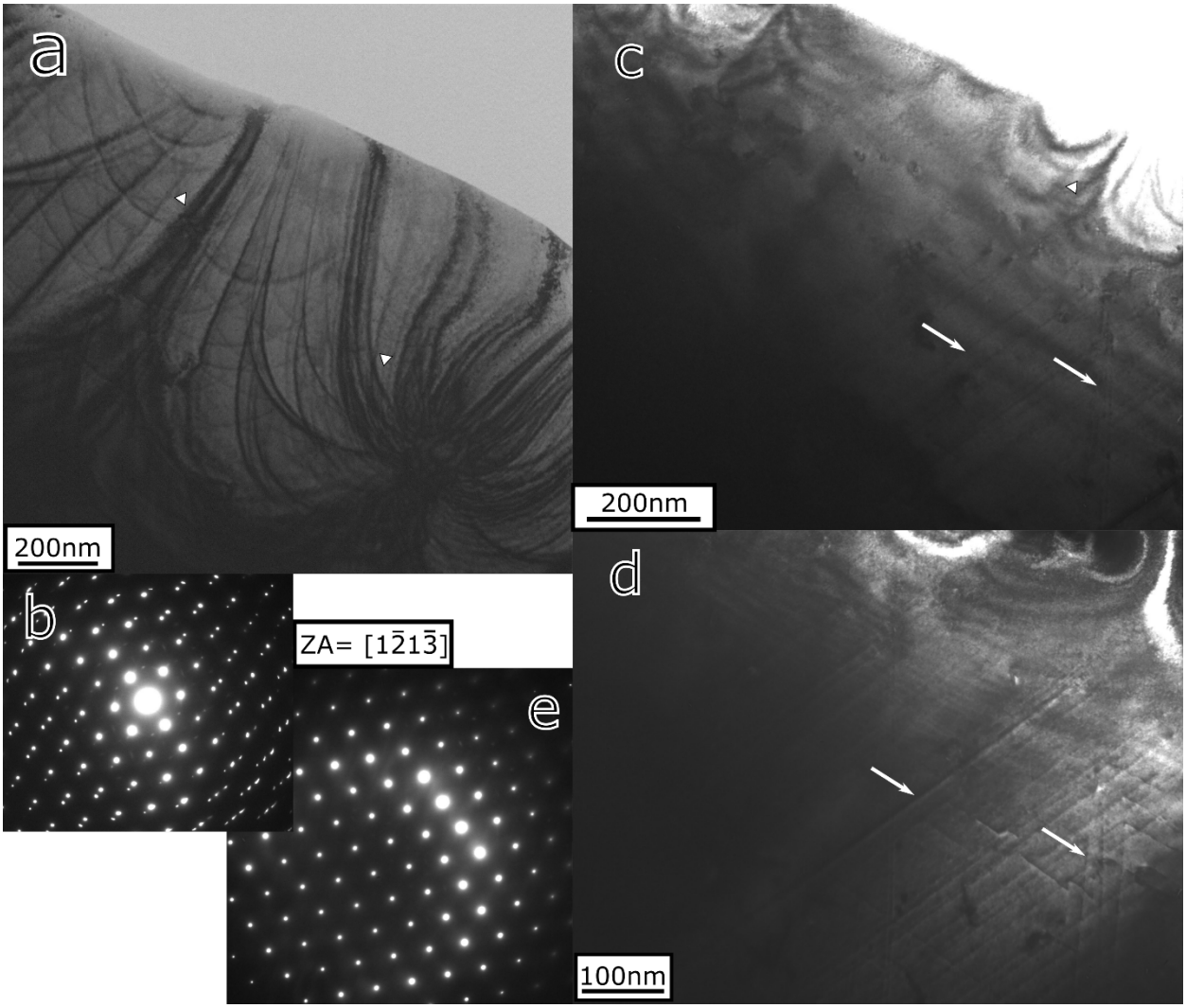

Figure 4.2: Comparison of pre- a,b) and post-c,d,e) initial straining of Re foil sample 1. White triangles mark contrast in the sample due to bend contours, and white arrows mark slip traces. The initial BF image a) and related DP b) show a very bent sample with some twins present in the pre-deformed state. After initial straining c) the BF image shows a sample that is much flatter, with the twin spots completely removed from the diffraction pattern e). Dark-field image of post initial strain area from a,c) contains many slip bands as well as dislocations within the microstructure.

Foil samples, even when heavily textured, all have random grain orientations which result in randomized active slip systems for each individual grain along the coastline. In order to get a direct comparison of deformation behavior between room and elevated temperatures, it is simplest to first characterize dislocation motion at room temperature then heat the same dislocations in order to observe changes due to elevated temperatures. It is also important to

have fully characterized the sample before elevating temperature since the foils have an extremely large surface area resulting in increased oxidation rates with any ambient oxygen that is available in the sample, regardless of the extremely low partial pressure of oxygen within the TEM column. Finally, due to the material and electrical constraints within the TEM sample holder, the maximum temperature that was achieved while testing the Re foil at temperature was 920 °C. While this is extremely high for most metals, in the case of Re it does not yet pass a third of the 3180°C melting temperature, making any appreciable difference in sample behavior minimal, if at all observable.

4.2. Dislocation Motion Observation during *In-Situ* Straining

For the *in-situ* dislocation analysis of Re foils, two samples were produced which yielded interpretable results; the two samples will be referred to as sample 1 and sample 2. It is difficult to determine the region of the sample where dislocation motion will appear during the initial straining of any in-situ tension test, due to the inherent nature of sample geometry. As such, an initial survey of the possible locations for dislocation motion was performed and the sample was tilted to be close to a significant zone axis as possible. The initial pre-straining condition of sample 1 was close to a $[11\bar{2}3]$ zone axis, as well as the results of some initial straining are shown in Figure 4.2a). It can clearly be seen that the initial sample is largely undeformed, showing little to no dislocations within the initial microstructure. The sample is however severely bent, which is seen through the large amount of bend contours in the middle of the sample, making finer determinations of microstructure in the initial pre-strained condition difficult.

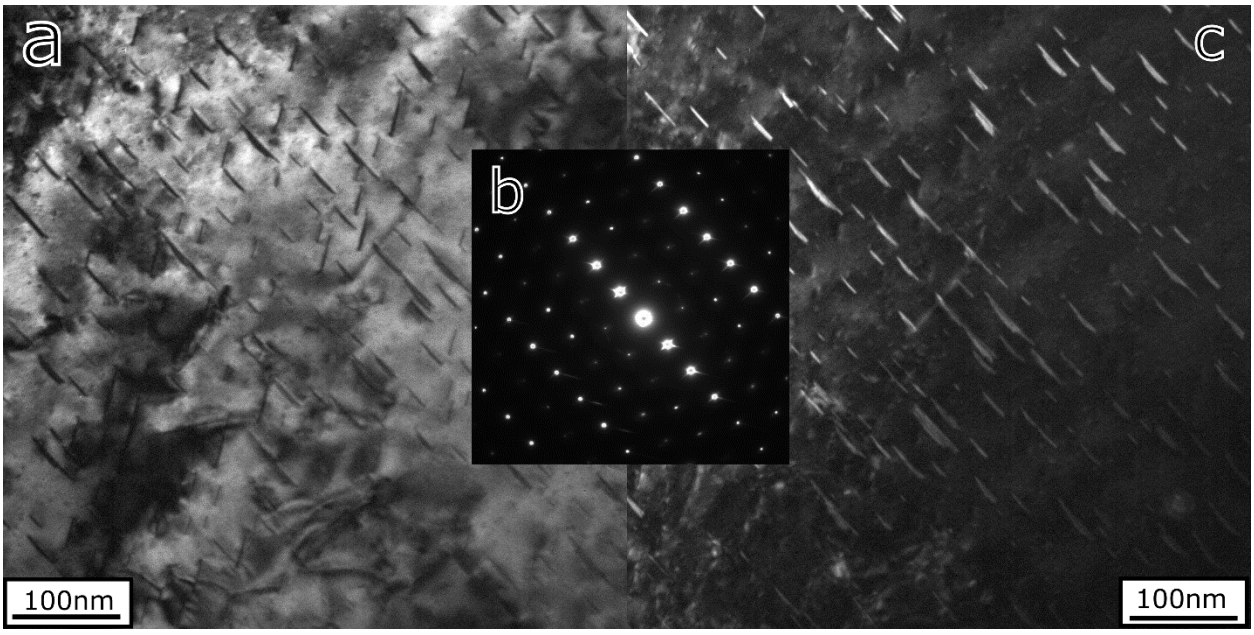

Figure 4.3: Nominally undeformed pure Re sample which contained areas with significant numbers of nano-twins. These twins were never seen during any deformation or in any samples that had appreciable plastic deformation, however they were observed in a

nominally undeformed sample. The diffraction from pattern in b) shows a low symmetry zone where smaller diffraction spots between matrix points are used to produce the DF image in c).

It should be noted that while the DP in Figure 4.2b) shows twinning spots that are representative of $\{11\bar{2}1\}\langle 11\bar{2}6\rangle$ type twins, none are visible in the diffraction pattern of the post initial straining DP, Figure 4.2b). While it is possible that this twin comes from an adjacent grain, the crystal is oriented in such a way that de-twinning of $\{11\bar{2}1\}\langle 11\bar{2}6\rangle$ type twins will accommodate applied tensile strain. Since the texture of the sample, and the general orientation of this crystal, has the c-axis oriented orthogonal to the tensile direction, any detwinning would reorient the twin c-axis to be coincident with the matrix, causing an expansion along the loading direction. While they are not seen in the bright-field images of the sample taken before loading (a result of the large bend contours in the pre-strained sample), it is entirely possible that some nano-scaled twins are smaller than the resolvable features in these images. Figure 4.3 shows the types of twins nano-twins (a few tens of nanometers long while being under 10 nm wide) that can be found within nominally undeformed grains. While these twins are not seen in the initial microstructure, their existence in the undeformed microstructure of swaged and annealed samples indicates a possibility of them being the cause of such a drastic diffraction pattern change seen between Figure 4.2b and e).

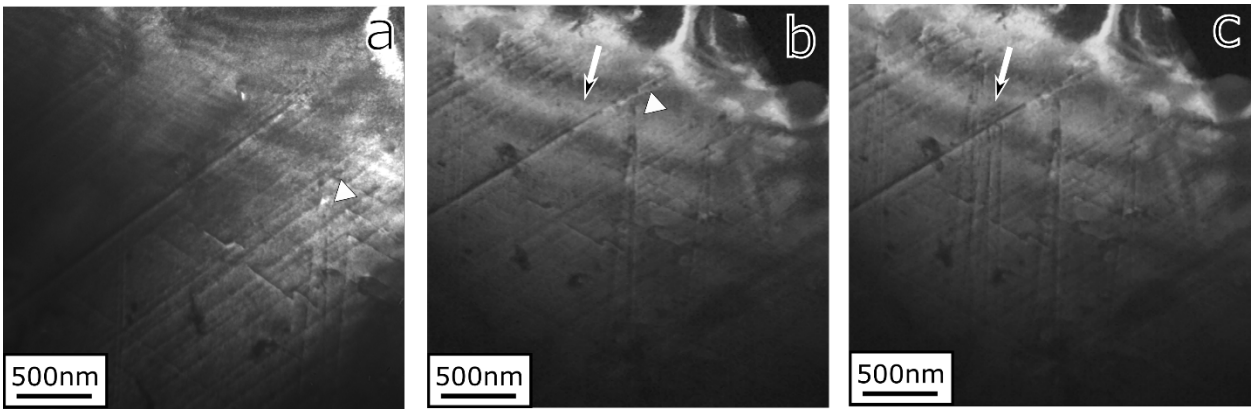

Figure 4.4: Still frames taken from a room temperature *in-situ* video of the dislocation motion of sample 1. The initial dislocation in a) marked by a triangle is much slower and takes a few frames to extent to its resting position seen in b). A second set of dislocations marked by the white arrow transmit through the sample and exit the sample surface in the span of 1 frame as seen in b-c).

The initial straining was stopped once the majority of contrast from the bend contours had disappeared and after the contrast lines were visible in the bottom right of Figure 4.2c). The cause of these contrast lines was not initially clear, however using the phase contrast inherent to the electron beam, it was determined by shifting the electron beam through convergence with the condenser lenses that the fringes bracketing the contrast lines changed. This shows that the contrast visible is due to a slip band based on the interaction with the step created on the sample surface, one Burgers vector in length. This step left within the sample surface provides enough

thickness for phase contrast effects within the electron beam to occur. The alternate hypothesis of the contrast lines being formed from a residual dislocation was thus proven to be incorrect.

Further evidence of these lines being due to slip bands is taken from the *in-situ* deformation videos of sample 1, three frames of which are taken from the video and reproduced in Figure 4.4. The formation of the slip bands through dislocations exiting through the surface can clearly be seen in the progression between Figure 4.4a-c). The slip bands are oriented with respect to each other with three-fold symmetry that is due the crystallography of the basal or prismatic planes upon which these dislocations must lie. After characterization of Burgers vectors of the dislocations within the sample, the exact planes upon which these dislocations lie can be determined using slip trace analysis and simulations that relate the diffraction pattern to the crystal orientation.

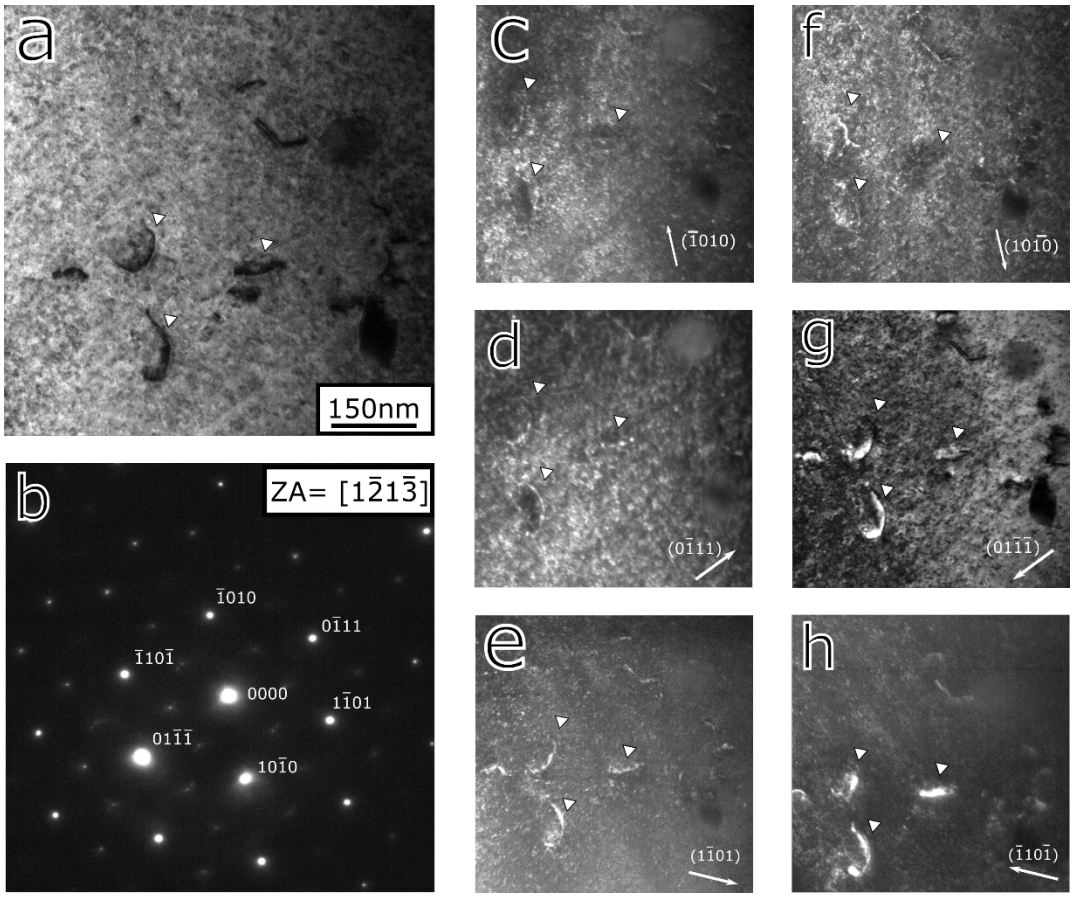

Figure 4.5: Summary of "g dot b" analysis for the mobile dislocations observed in sample 1. The BF image a) and DP b) show the $\langle 11\bar{2}3\rangle$ zone used to index as well as the dislocations marked with triangles. c-f) is the series of diffraction conditions used to characterize the dislocations as $\vec{b} = \langle 11\bar{2}0\rangle$ type screw dislocations. When the dislocations are invisible $\vec{g} \cdot \vec{b} = 0$.

4.2.1. Room Temperature Dislocation Motion of Two Samples

After identifying a thin area with suitable dislocations for *in-situ* dislocation analysis, further straining can be performed to see how dislocation motion evolves with increasing strain. First, a full description of the dislocations must be achieved in order to fully understand the observations made using the *in-situ* tests. Figure 4.5 has the full series of DF images required to fully characterize the dislocations. The zone used is a $\langle 11\bar{2}3\rangle$ zone which allows for characterization of both <a> type dislocations and <c+a> type dislocations, if all of the first order diffraction spots are imaged. It is generally useful during this type of dislocation characterization to tilt the sample to a "two-beam" Bragg condition, as seen in Chapter III during the characterization of dislocations within the tensile specimen. As previously stated, there is only a single tilt-axis available for tilting the sample to a proper zone axis on the straining holder, thus the dark-field images are taken purely with beam tilt from the near Laue condition seen in Figure 4.5b).

The observation that will describe if a dislocation has the Burgers vector parallel to the diffraction condition of the microscope is the invisibility condition of $\vec{g} \cdot \vec{b} = 0$. With the series of DF images seen in Figure 4.5 c-f) it can be difficult to determine which dislocations can be considered "invisible", especially since certain combinations are only partially visible, and dislocations can have mixed character where only a portion of the dislocation is invisible. With sample 1, it is quite easy to see (and the effect is enhanced when comparing each image to the bright-field image in Figure 4.5a) that of the DF diffraction conditions only the dislocations in Figure 4.5c and f) are invisible, satisfying the condition $\vec{g} \cdot \vec{b} = 0$. Immediately, this gives two possible Burgers vectors (and their negative variants), $\vec{b} = [1\bar{2}10]$ and $\vec{b} = [1\bar{2}1\bar{3}]$. However, for the Burgers vector to be $\vec{b} = [1\bar{2}1\bar{3}]$ the dislocations would have to be invisible in the DF images, Figure 4.5d and e), with $\vec{g} = [0\bar{1}11]$ and $\vec{g} = [01\bar{1}\bar{1}]$. As this is not the case, the final Burgers vector determination is $\vec{b} = [1\bar{2}10]$ or $\vec{b} = [\bar{1}2\bar{1}0]$. For a full table, and further details on the required conditions and diffraction intensities when imaging dislocations, the review paper by Partridge et al. covers all the details required for working in HCP systems (3). One last detail on characterizing dislocations is the dislocation is invisible when the diffraction vector $\vec{g}$ and the dislocation line direction are nearly orthogonal, which is only the case for screw dislocations (62). While there is some deviation from perfect orthogonality, the deviation is small enough to conclude that the dislocations are screws, due to the rotation difference between image plane and diffraction plane of the microscope.

With the active dislocations in sample 1 fully characterized, the sample can be further strained in order to image dislocation motion. As stated in the methodology, any straining of the sample will also cause large translations of the viewed area. In order to mitigate this for viewing, a low magnification was used for the dislocation motion videos. The sample stage was also translated during straining in an attempt to counteract the translation of the sample due to the grip separation. Manual stage translations during straining were only partially successful in keeping dislocations in view. The video of dislocation motion from which the stills in Figure 4.6 are taken was edited for contrast in Adobe Premier, as well as using stabilization software in order to keep the active region in view. Finally, most of the dislocation motion was seen after

the strain was applied, during relaxation of the sample, and with the sample translated back into the field of view.

For the initial configuration of dislocations in sample 1, Figure 4.6a), it can be seen that the active dislocations marked with arrows are all spaced relatively close together with an average spacing in between each dislocation of 300nm. The whole series of frames takes place over a span of 15 seconds. Over this timespan, it can be seen that the leading dislocation has moved far out from the others, where it encounters an immobile pinned dislocation and they mutually annihilate. In frames b) and c) of Figure 4.6, the other dislocations continue on the path made by the initial dislocation, however they also do not move with the same velocity as each other. In the video it can be seen that during this relaxation period, dislocations do no flow smoothly, but start and stop in a "semi-jerky" fashion, less than what is described by Clouet in Ti (78). This hints at a lower energy configuration where the dislocations rest on a different plane when immobile than the plane they glide on. However, since this is the third orientation of mobile basal dislocations, as seen by the slip traces, basal dislocation activation should require little energy. Additionally, it seems that dislocations will tend to glide along similar slip bands through the sample even if they do not move at similar paces. Having seen this behavior in a single sample *in-situ*, sample 2 will be investigated to determine how reproducible the observations are within Re.

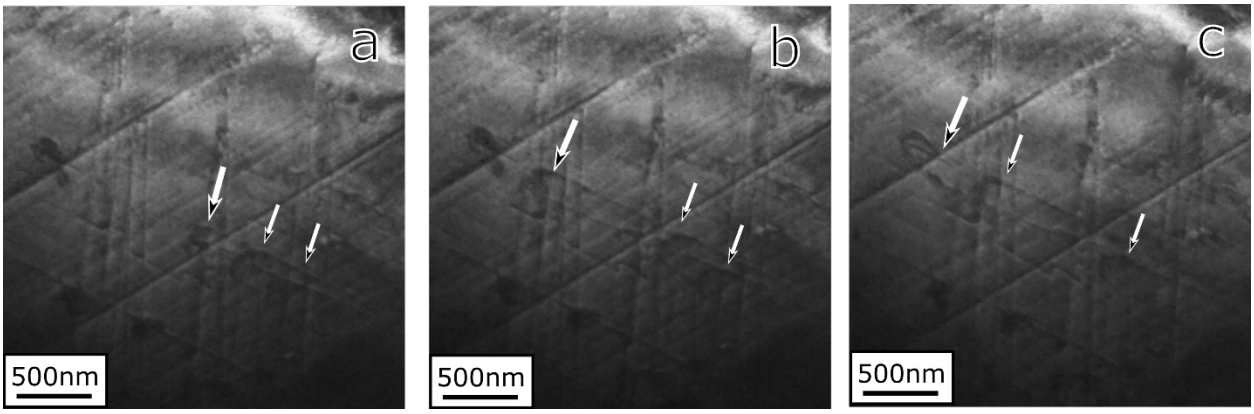

Figure 4.6: Still frames taken from a room temperature *in-situ* video of the dislocation motion of sample 1, using an $(10\bar{1}0)$ DF condition which best showed the dislocation contrast. The leading dislocation in a) annihilates itself by the time it reaches frame c). It can be seen in the progression from a-c) that the dislocations have separated away from each other over the course of travel. This only happens if the dislocations move at disparate rates, with some dislocations moving more swiftly then slowing. The dislocations do follow each other closely, moving along in nearly the same slip band.

Sample 2 was a more difficult sample in characterizing the mobile dislocations, with the closet major zone axis available with the single tilt axis the high order $[5\bar{1}\bar{4}3]$ zone. One peculiar facet with diffraction in Re is the fact that extremely easy for disallowed diffraction conditions to be visible in the diffraction patterns. In Figure 4.7b), the disallowed $(1\bar{2}1\bar{1})$ is equally bright as the allowed $(1\bar{1}0\bar{2})$ and $(10\bar{1}\bar{3})$ diffraction spots. This makes determining the zone of the diffraction more difficult (but with references and tables it is still a simple task),

however dislocation analysis is the same procedure of taking dot products of reflection conditions and the possible Burgers vectors (for HCP crystals generally only $\vec{b} = \langle 11\bar{2}0 \rangle$ and $\vec{b} = \langle 11\bar{2}3 \rangle$).

Again, looking at Figure 4.7c-h), it is much more difficult to determine the invisible dislocations, however close inspection reveals the dislocations in DF images Figure 4.7 d,f,h) however since the $(1\bar{2}1\bar{1})$ reflection is disallowed, we will only consider Figures 4.7d and h). This again necessitates a Burgers vector (negatives of these vectors excluded) of $\vec{b} = [1\bar{2}10]$, since the <c+a> type dislocation, $\vec{b} = [1\bar{2}1\bar{3}]$, cannot equal zero when a dot product is performed with the $(10\bar{1}\bar{3})$ reflection. Including the disallowed reflection would produce a result where none of the possible dislocations would provide a consistent answer. Finally, for the dislocation analysis, it can be seen that when the $\vec{g}$ vector is orthogonal with the line vector of the dislocation the dislocation becomes invisible, making these dislocations <a> type screw dislocations. While sample 2 does not have the three-fold slip banding that is apparent in sample 1, the dislocations are of the same character as in sample 1, and as such the general behavior should be directly relatable between the two samples.

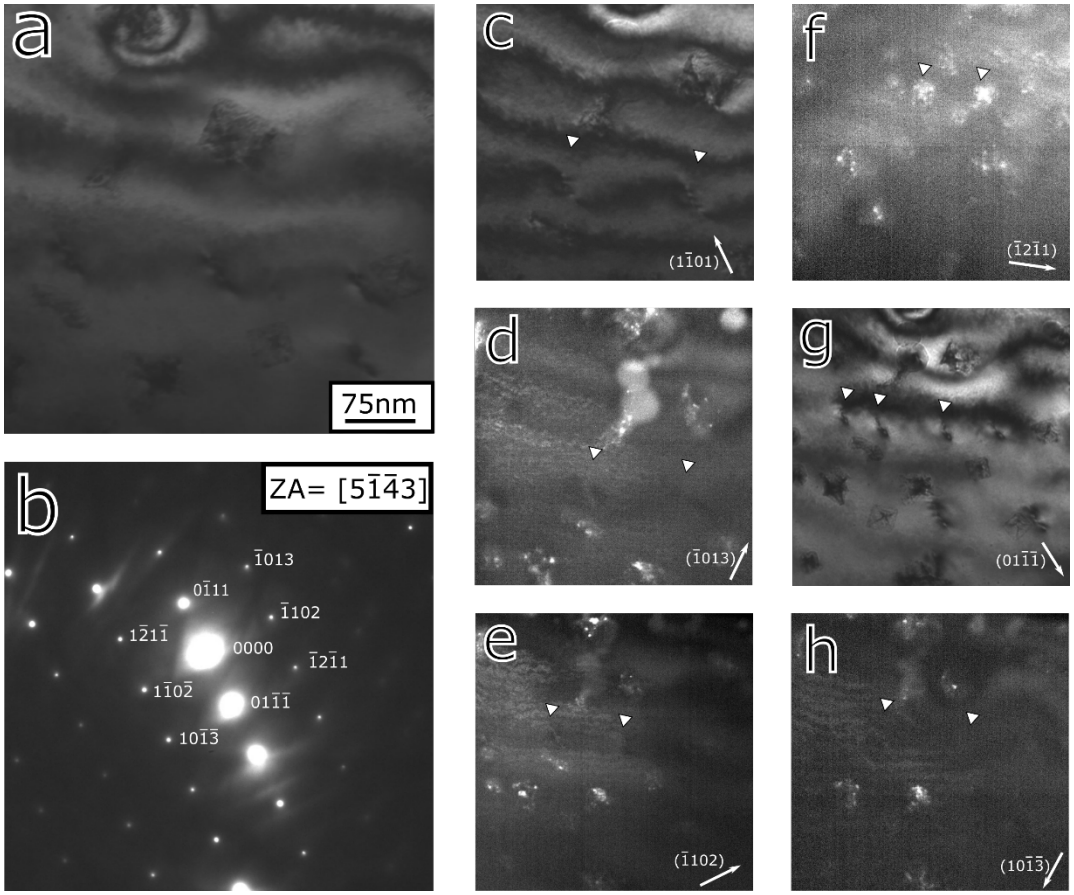

Figure 4.7: Summary of "g dot b" analysis for the mobile dislocations observed in sample 2. The BF image a) and DP b) show the unusual $\langle 5\bar{1}\bar{4}3 \rangle$ zone used to index as well as the dislocations marked with triangles. c-f) is the series of diffraction conditions used to

characterize the dislocations as $\vec{b} = \langle 11\bar{2}0 \rangle$ type screw dislocations. When the dislocations are invisible $\vec{g} \cdot \vec{b} = 0$.

As with the video in sample 1, the dislocation motion video for sample 2 required much stabilization and post processing. A series of frames from sample 2 in a $(0\bar{1}1\bar{1})$ DF imaging condition are seen in Figure 4.8a-e). Much like in sample 1, dislocations are seen to be irregularly spaced. Here the dislocation spacing is much larger than what was seen in sample 1. This is to be expected as the total number of dislocations is much lower, likely due to the fact that this region was observed to be active earlier within the strain history than the region of interest in sample 1. Despite this lower dislocation density, the overall behavior of dislocations has not changed, with different dislocations moving at different speeds with different total distances traveled. The dislocations shown in Figure 4.8 d,e) are seen to be very slow, while the leading dislocation travels a large distance and stops between Figure 4.8 b) and c). Additionally, the distances that dislocations jumped in their "jerky" motion was much larger than in sample 1, likely due to the abundance of previously formed slip bands as well as sample 1 having a much longer deformation history.

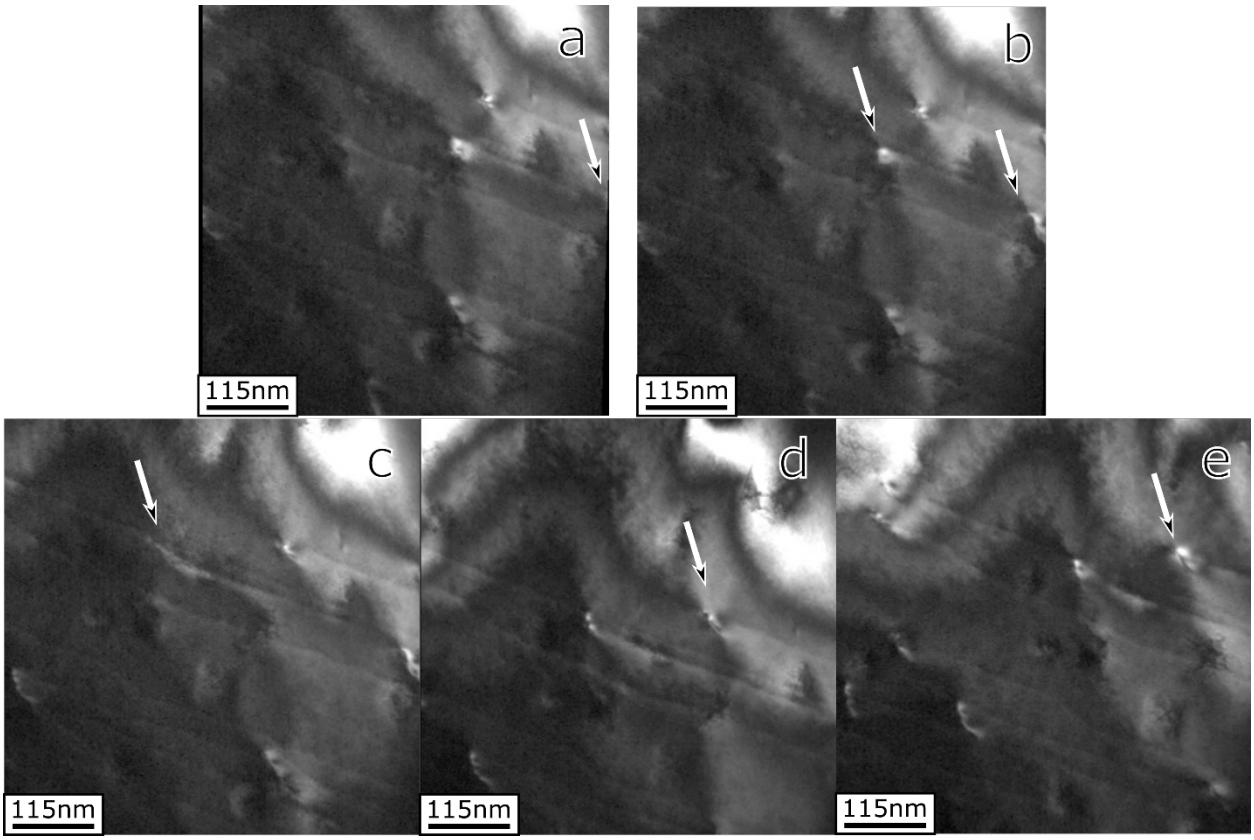

Figure 4.8: Still frames taken from a room temperature *in-situ* video of the dislocation motion of sample 2, using an $(0\bar{1}11)$ DF condition which best showed the dislocation contrast. Frames a and b) show one dislocation appearing into frame from out of frame and stopping. Fames b-c) show the front dislocation quickly move then stop, with the

trailing dislocations in d) and e) slowly crawling over a few seconds. Overall, the motion of these dislocations contained parts “jerky” motion and parts smooth flow.

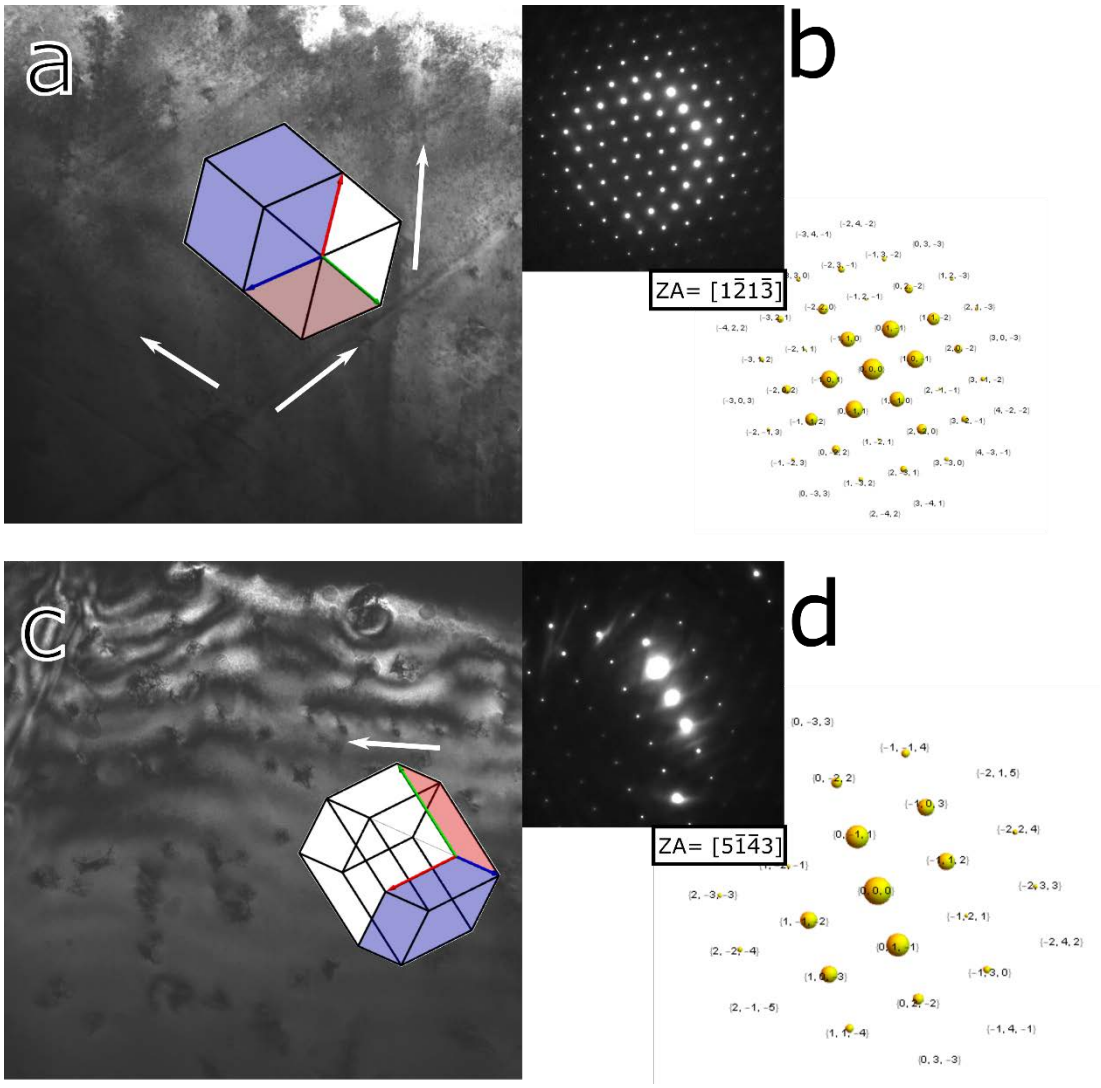

Figure 4.9: Comparison of TEM images a,c) and diffraction patterns with simulated diffraction patterns b,d) with corresponding crystal orientations for samples 1 a,b) and 2 c,d) (14). When lining up the slip band directions (white arrows) for sample 1 in a) we can see that the three fold symmetry of the slip bands is a match. The dislocation in the bottom left is bowing such that the forms a half loop on the basal plane. For sample 2 as there is only 1 direction of slip (white arrow) in c), the alignment is less ideal. However again the best match for operative plane of <a> type dislocations is the basal plane.

One remaining question that has not yet been answered with the observations between the two samples is which plane the dislocations are active upon. In order to determine an operating plane upon which the dislocation glides, in general a series of images at different well-defined tilt conditions are taken to investigate the dislocation line relationship to the crystal. Since this cannot be done with the limited amount of tilt available with the *in-situ* sample holder, the

crystallography of the dislocation lines as well as the crystal orientation must be used to determine the operating plane. This leads to the use of simulation program that creates a simulated diffraction pattern based on the material and zone one chooses, with a corresponding crystal orientation (coding care of Max Poschmann). Figure 4.9 has real space structures as well as diffraction patterns for samples 1 and 2. Through looking at sample 1, seen Figure 4.9a), we can relate the slip band direction (white arrows) to the three-fold symmetry of the crustal structure. A noticeable dislocation half loop can be seen in the bottom right of Figure 4.9a), which looks extremely similar to basal dislocation loops seen in Mg (82). With this crystal orientation, the bowing of the dislocation looks similar to dislocations expanding upton their operative basal planes, where prismatic dislocations would appear as straight lines from this orientation. This makes the most likely habit plane candidate for these dislocations the basal plane.

4.2.2. Observations during Elevated Temperature Dislocation Motion

With the aim of investigating the mechanical properties of rhenium guided by the high temperature properties of this unique metal, each *in-situ* sample provides an opportunity for the direct comparison of dislocations at room temperature and high temperature. The effect of temperature is immediately seen when operating the sample holder within the TEM, as large thermal expansions translate the sample during the initial heating. The test cannot take place until the stage stabilizes to a thermal equilibrium, which can take a significant amount of the total possible experimental time. Once thermal equilibrium is reached, the sample is strained in the same manner as before. Sample 1 did not yield many interpretable results except for the images taken from a video near the sample failure, seen in Figure 4.10. A large network of dislocations, higher in density than what was seen for the room temperature sample, is seen interacting with each other near the sample surface. The leading dislocation from Figure 4.10a) eventually manages to interact with a dislocation in Figure 4.10c) annihilating each other. In the interim, the appearance of a dislocation between frames Figure 4.10a) and b) can be seen marked by the arrow in Figure 4.10b). This dislocation is immobile. It was created at temperature in view of the electron beam, something that was not observed in the room temperature samples. For sample 1, no other dislocation observations were made at temperature. While sample 1 had room temperature dislocation much more easily interpretable, the high temperature dislocation motion was lacking. The formation of dislocations does help when interpreting the high dislocation density seen in sample 2.

Sample 1 was kept at temperature for an extended period of time, roughly 30 minutes at 920°C. While the TEM column containing the sample generally has an extremely low ambient pressure with little oxygen, when raising the temperature to regimes where the sample would heavily oxidize, any oxygen contained within the chamber will react with the sample. After over 30 minutes within the TEM column at a temperature of 920°C the sample formed an unidentified film, seen Figure 4.11. While oxygen is the most common element reacting with Re to form the Re_2O_7 oxide, this cannot be the compound that is formed in Figure 4.11, as Re_2O_7 sublimates at 362°C. This would leave a question as to what compound has formed a film on sample 1, especially since Re is not known to form any hydride or carbide the other common contaminants

within the TEM column. With the large number of possible oxidation states of Re, one possible explanation of the film is the formation of another oxide due to the low oxygen concentration such as, Re_2O_5, ReO_2 or Re_2O_3 (83). However, as this study involving Re is focused on the mechanical properties, and not the low oxygen concentration high surface area *in-situ* oxidation properties of Re, the identity of this unknown compound was not investigated. The point of showing this unknown film formation, Figure 4.11, is that any *in-situ* experiments are also limited in length due to the reactivity and formation of Re-based compounds.

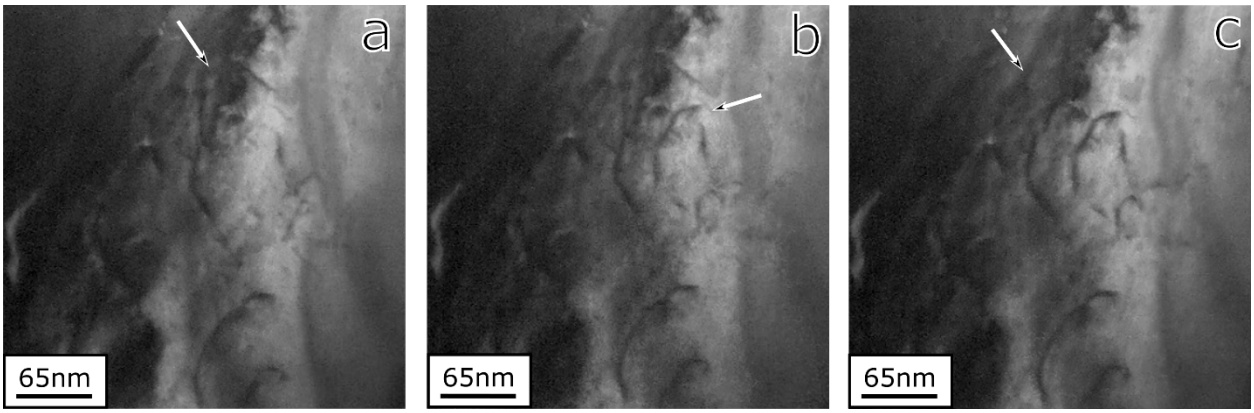

Figure 4.10: Formation and destruction of dislocations in sample 1 at 920 °C. The video was taken near failure of the sample with frames a-c) taken sequentially over a few seconds, as such dislocation motion was largely limited at temperature in sample 1. Despite the difficulty in interpreting the contrast seen here, one dislocation leaves through the sample marked in a) and c). Another dislocation appears in b) from the sample surface in the location marked by the arrows.

Finally, the results of high temperature in-situ testing of sample 2 gives the most insights into the effects of temperature on the dislocation motion of basal <a> type dislocations in Re. Again, it must be reiterated that the temperature changes increase the temperature to less than one third of the melting temperature of rhenium. With this relatively low temperature increase, large behavior changes should not be anticipated. Still frames that detail the motion at temperature of Re dislocations can be seen in Figure 4.12a-c). While the still frames leave much to be desired in describing dislocation motion, the arrow mark the position of large motions between the frames. Much of what was seen in the room temperature motion of the dislocations, they move in the same "semi-jerky" way as was seen in the room temperature tests. This amount of thermal energy increase has not appreciably changed the energy barriers associated with the initiation of dislocation motion. The dislocations form loosely aligned slip bands that are coincident with the direction of strain. However, the only discernable difference seen between these dislocations and the room temperature straining is the number of active dislocations, and the size of the motion bursts. At 920°C there are far more dislocations activated during deformation, and the dislocations start and stop in a smoother manner. In order to see appreciable differences at temperature, the sample must be tested at well over 1000°C, something that is beyond the capabilities of the *in-situ* holder.

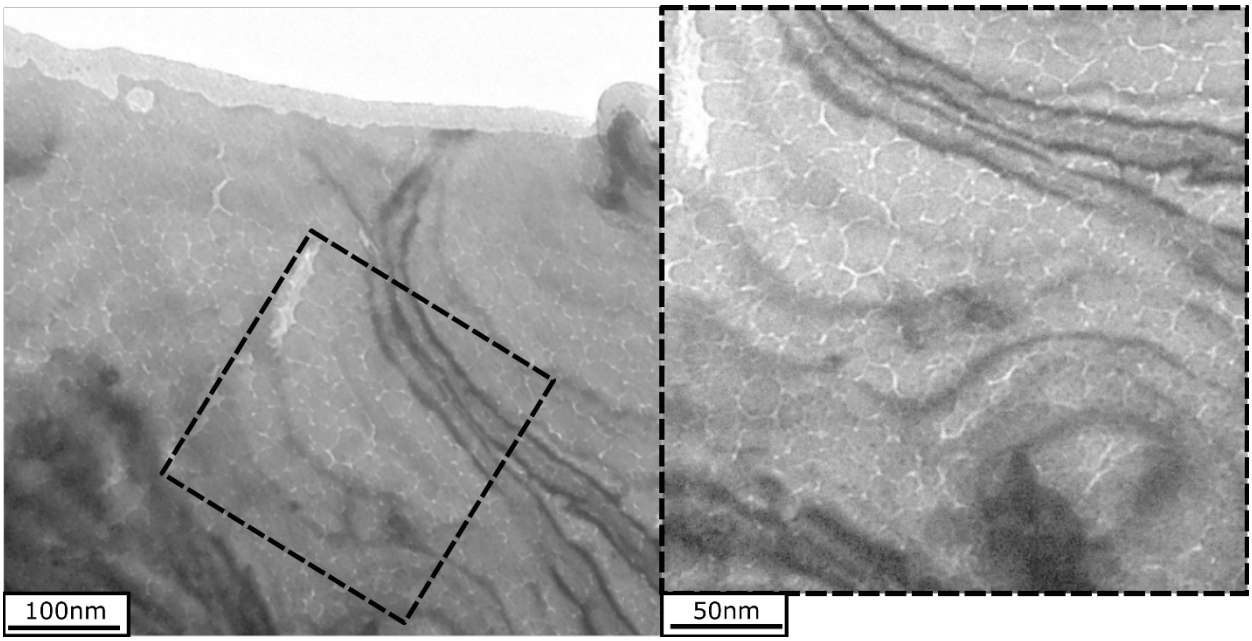

Figure 4.11: Final TEM images of sample 1 after 30 minutes testing at 920 °C. There is an appreciable development of a film at the coastline of the sample, with the interior of the sample containing many cracks, ostensibly the film penetrating within the sample and causing catastrophic mechanical failure. As the nominal sample temperature is 920 °C this film should not consist of Re_2O_7, as that oxide sublimates at 362 °C and would not be visible after forming. Further investigation was not performed on what the film was, as it was not in the scope of this work.

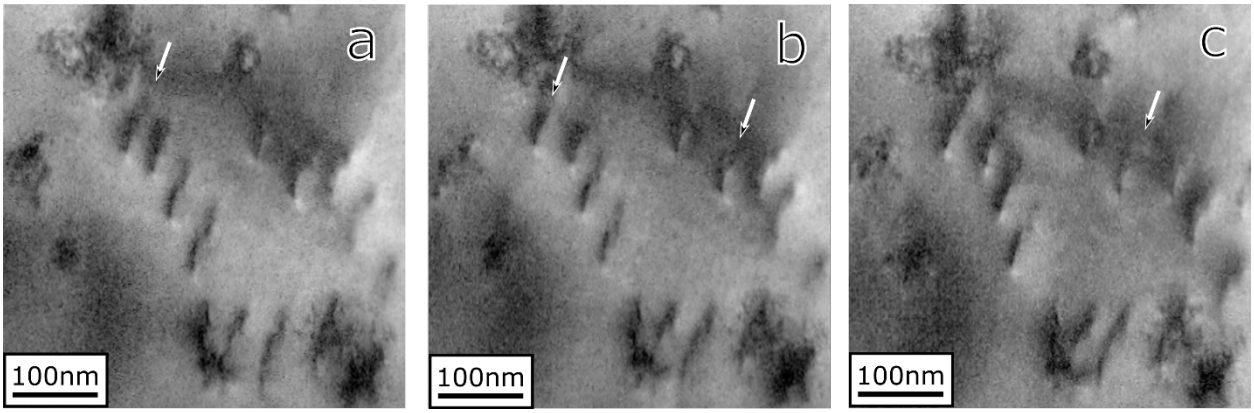

Figure 4.12: Still frames taken from a elevated temperature (920 °C) *in-situ* video of the dislocation motion of sample 2. The time is sequentially over a few seconds from a-c); the arrows show locations of small dislocation translations. The dislocations are more closely bundled here than in any other dislocation video. This is likely due to the sample geometry of this foil as well as the test being well developed, having much tie to generate additional dislocations. Other than the apparent increase dislocation density seen in this sample, no effects have been noticed through increasing the temperature of the sample.

4.3. Conclusions of *In-Situ* Testing

In-situ straining has been performed on rhenium both at room temperature and at elevated temperature. The samples used all had a foil texture, suppressing possible $\{11\bar{2}1\}\langle11\bar{2}6\rangle$ twinning, while exaggerating basal or prismatic dislocation activity. Two main samples were successfully tested, with both confirming the observation that <a> type $\langle11\bar{2}0\rangle$ basal dislocations were the dominant mechanism during tensile straining. No <c+a> type $\{10\bar{1}1\}\langle11\bar{2}3\rangle$ dislocations were observed *in-situ*, likely due the relatively low absolute stresses imposed upon the sample during the *in-situ* test. Dislocation motion was observed with video, with the general dislocation motion consisting of a "jerky" crawl of loosely aligned dislocations. The starting and stopping motion of dislocations is indicative of an "unlocking" mechanism for dislocation motion to become activated, as detailed by Clouet in Ti. The only appreciable effect that elevating temperature to 920°C had on dislocation motion was to possibly increase the number of active dislocations, something that also occurs naturally near the end of a test.

Chapter 5

Development of Re Replacement Alloys

As discussed in the introductory chapter, the dominant theory behind the rationale for the excellent mechanical properties in rhenium surround behavior of the unique $\{11\bar{2}1\}\langle 11\bar{2}6\rangle$ twins. Previously this work has shown the dominance of these twins during all types of deformation in Rhenium. The current theory referenced for this study predicts that the d-band filling of transition metals in between W and Re is most energetically stable for the topologically close-packed (TCP) structures (as well as other intermetallic structures). As the twin boundary has an atomic structure that closely resembles the icosahedral coordination polyhedral found in TCP phases, an alloy containing a similar energetic structure as a TCP transition metal structure would also be more likely to form the important $\{11\bar{2}1\}\langle 11\bar{2}6\rangle$ twin (9) (10). With this in mind, the focus for developing Re-free high temperature alloys which could approximate Re behavior involves the formation of a chemically complex (also known as multi-component) or high entropy alloy (HEA) single phase HCP alloy of transition refractory metals, while stoichiometrically approaching a d-band filling of roughly 4.6 electrons per atom. This provides the same crystal structure as Re while simultaneously increasing the energetic favorability of the structures most closely resembling the $\{11\bar{2}1\}\langle 11\bar{2}6\rangle$ twin boundary. HEAs refer to chemically complex alloys that have near equal proportions of 5 or more elements. The term high entropy alloy is just a moniker and they do not tend to actually have high entropy in a thermodynamic sense (84)

In any alloy development process, many alloys are created that will not be replacement candidates. In order to quickly determine which alloys are candidates for macroscopic testing, the spherical nanoindentation technique detailed in section 1.3.5 was used. This technique has some key features that make it well suited for determining these test alloys' mechanical properties. Since the indentation tip can have a diameter as small as a few hundred nanometers, the indentation process is highly localized, with plastic deformation taking place exclusively within a localized region roughly twice the diameter of the indentation tip (66). This allows for indentations to be made on multi-phase alloys while being able to separate the mechanical response of the two phases. Additionally, since indentation requires only a stable substrate and a well-polished planar sample surface, tests can be run with high throughput and high data collection rates on each unique alloy. There are drawbacks involved in data analysis as well as the validity of the data collected as a measurement of ductility and work hardening, however the comparative nature of the tests and the use of this this indentation technique to screen for an alloy candidate, indentation stress strain is valid for the needs of this study.

5.1. Creation of Alloys and Testing Procedure

Alloys were created with powder metallurgy techniques common in the processing of refractory metals. Each metal constituent powder was mechanically mixed to the correct wt% of alloy composition and then ball milled for 30 minutes. The resulting thoroughly mixed and refined powder was then pressed into pellets using 30,000 psi of force to be sintered at 1850 °C for 8 hours. The pellets were then arc melted, flipped, and re-melted again. Slag from on the

ingot surface was removed and the ingot was finally annealed at 1850 °C. The resulting ingots are roughly 0.5-1 cm^3 in volume. The final fully annealed and homogenized samples are then sectioned using a Struers M0D15 diamond cut-off wheel upon a Struers Accutom-50 precision saw (due to the initially assumed, and later observed, extreme hardness of these alloys, a Diamond Saw the proper cutting implement for sectioning). SiC sandpaper grit from 500 up to 4000 was used to first make a smooth planar surface on the top of the sample surface and on the bottom as a substrate base. Final polishing was done using Buehler MasterMet II non-crystallizing diamond suspension on a Buehler MasterPol polishing cloth. The resulting surface is suitable for indentation, optical imaging, and EBSD. However without knowledge of the crystal structure, gained through x-ray diffraction (XRD) techniques, the use of EBSD was an untenable solution for indexing the crystal as the software has no reference to index the EBSPs.

5.1.1. Motivational Basis for Alloy Choice

In order to develop candidate replacement alloys using a systematically improving iterative alloy choice method, we relied upon phase diagram simulations to determine a proper initial composition that gives a single-phase HCP alloy with a 4.6 $\frac{electron}{atom}$ d-band filling. With the collaboration of the group of Professor Axel van de Walle at Brown University, who employed first-principles thermodynamic calculations along with the Pandat™ software by CompuTherm LLC, ternary and quaternary phase diagram systems were produced using the CALPHAD framework (85) (86). Pandat™ software relies on thermodynamic data (such as free energies and entropies for the different constituent parts) that are not experimentally available for many chemical elements and complex systems used in this study. As such, thermodynamic information must be computed from first principles for each unique chemically complex system by each individual researcher for the software to produce a phase diagram. The resulting phase diagrams are approximate and can be greatly refined with experimental results. Verifying the phase diagram predictions confirms the validity of the calculated phase diagram and improves the accuracy of future chemically complex diagrams containing new species.

As the main requisite property of Re in mechanical applications involves maintaining a high strength and modulus over a large range of temperatures (17), a Re-free Ru-based system will provide costs savings as well as excellent high-temperature properties. With these conditions in mind, we selected the Ru-Ta-W system with Ru as the base metal as the first system to test. All three elements' high melting temperatures (2334 ºC for Ru, 3017 ºC for Ta, and 3422 ºC for W) (20) gave a ternary HCP alloy potentially favorable high temperature mechanical behavior. As pure ruthenium forms an HCP crystal structure and considering the high solubility of both Ta and W into Ru (roughly 20% and 40% respectively), the Ru-Ta-W system has great potential to contain an HCP single phase alloy. The potential of this HCP single phase alloy is due to a d-band filling similar to Re which should increase the favorably of $\{11\bar{2}1\}\langle11\bar{2}6\rangle$ type twins. Figures 5.1a) and 5.1b) show calculated binary phase diagrams for Ru-W, Ru-Mo and Ru-Ta. These figures include the large single-phase HCP regions that supplied the rationale for trying these elements in a ternary system (15). Figure 5.1d) shows the initial Ru-Ta-W phase diagram with inset an Re-equivalence line showing proper composition that provides the requisite 4.6 $\frac{electron}{atom}$ d-band filling for $\{11\bar{2}1\}\langle11\bar{2}6\rangle$ twin favorability. Alloys with compositions of 55-7-38 and 50-10-40 in wt% were created to form a Ru-Ta-W HCP alloy which intersects the Re-equivalent line. Initial optical investigations of these alloys showed that they contained an

obvious two-phase dendritic structure. Figure 5.1e) shows the improvement to the ternary phase diagram made by including a missing intermetallic compound (a Ga_3Pt_5 phase with space group number 65: Cmmm) that was left out of the initial calculations.

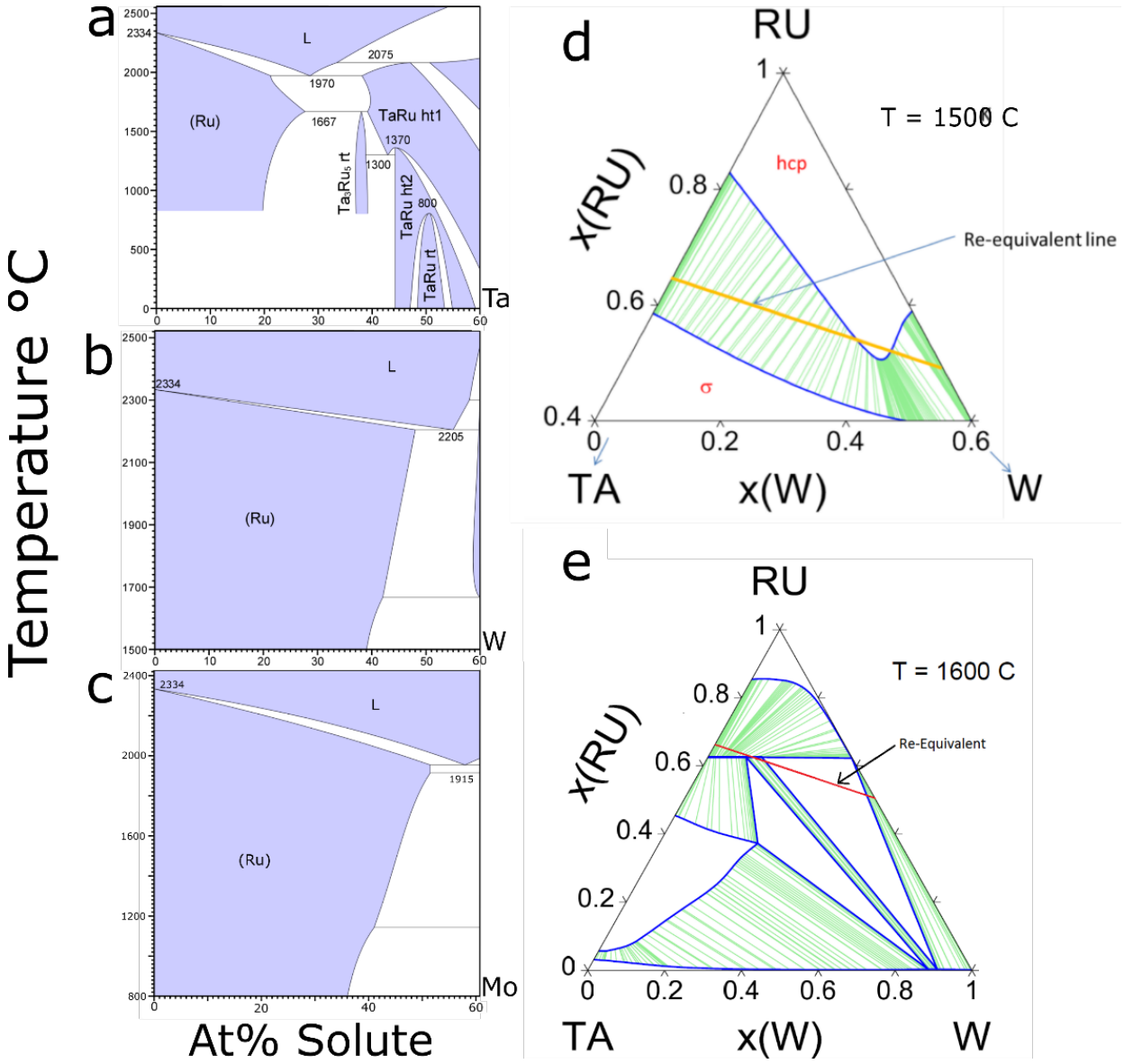

Figure 5.1: The binary phase diagrams of a) the Ru-Ta system and b) the Ru-W system and Ru-Mo system c) (15). Note the solubility of Ta into Ru is ~20 at% and the W and Mo binaries are almost identical with 40 at% solubility. d) Initial Ru-Ta-W ternary phase diagram and e) improved Ru-Ta-W phase diagram after initial alloys were investigated. (16) Where the Re-equivalent line intercepts the HCP single phase region was the initial investigation regime for alloy development.

Later compositions included a significant percentage of molybdenum (Mo, melting temperature of 2673 ºC) which replaced much of the W content. Since Mo has a very high melting temperature and high similar solubility than W into Ru, it was assumed that replacing W

with Mo would increase the configurational entropy in the system, thus increasing the solubility of all solutes into the HCP single phase (87). Additional rationales behind the addition of Mo were much the same as for W. For instance, the addition of Re into both W and Mo greatly increases the mechanical properties of ductility and creep properties while simultaneously lowering the ductile to brittle transition temperature (22) (88). As Mo is directly above W in the periodic table, it should behave electronically similar within the alloy (89). A common strategy for forming high entropy and chemically complex alloys is to replace one solute component for another that operates similarly (89). As was seen with the initial formation of ternary phase diagram for the Ru-Ta-W system, the intermetallic compositions contained within the Ru-Ta-W-Mo quaternary diagram were previously unknown. To start the investigation, a large range of compositions was chosen to push the content of Ru lower while increasing the Mo and W content. This allowed for us to simultaneously probe for the HCP single-phase boundary and test a large range of alloy compositions within the Ru-Mo-W and the Ru-Ta-W-Mo systems. Additionally, the effects of Mo on the size of single phase HCP region were investigated by creating two Ru-Mo-W alloys.

5.1.2. Indentation Stress-Strain Method with Berkovich Indentation

The fundamentals of indentation were explained at length during the introduction in section 1.3.5. The standard procedures for nanoindentation are consistent across tip geometries, with the Oliver-Pharr method (13) (64) of tip area function determination able to be carried out as a first step regardless of method. In order to prepare for indentation stress-strain using a spherical tip, a proper determination of the indentation modulus and hardness for each sample is measured. The method of determining indentation modulus uses a Berkovich tip with a quasi-static load function and a constant loading rate (and thus decreasing displacement rate) and a hold segment at the maximum load. This allows for any room temperature creep to occur. The initial unloading segment after the load hold is then used to determine indentation modulus. The maximum load is used to determine hardness. An example of the load displacement response for Re using Berkovich indentation is shown in Figure 5.2a). It should be noted that Berkovich indentation provides a much better data for measurements of indentation hardness as well as indentation modulus. This is due to the sharpness of the tip causing plastic deformation from the onset, making nano-hardness measurements possible as spherical or flat punch indenter would have to overcome an initial purely elastic regime. Additionally, the use of the quasi-static indentation method (one without an applied displacement amplitude, or CSM) has been shown to induce less deformation due to a constant oscillating displacement driving force. (90)

In order to fully use the indentation stress strain method during a real experiment, the experimental procedure requires a few features to collect the data required for analysis. The standard method requires having the spherical indentation tip approach the sample surface while having already activated the continuous stiffness measurement (CSM) protocol. Applying a differential force to the indenter tip causes the displacement to oscillate 2nm in air during the approach. As the tip approaches the sample in air, the system does not have to apply much load to the indentation tip in order to provide a 2nm displacement. As a result, the smallest applied load will induce a huge displacement amplitude. When the tip contacts the sample surface, the load control feedback loop is not responsive enough to increase the load in order to apply a 2nm displacement amplitude during the initial contact. This minimum in displacement oscillation can be used to quickly automate a method for finding the sample surface during post-indentation

analysis. When the tip contacts the sample surface, the displacement amplitude will be at a minimum before the load is increased to compensate for the greatly increased stiffness of sample compared to air. The analysis can be completed with sufficiently accurate knowledge of the initial indentation zero point, displacement, and load.

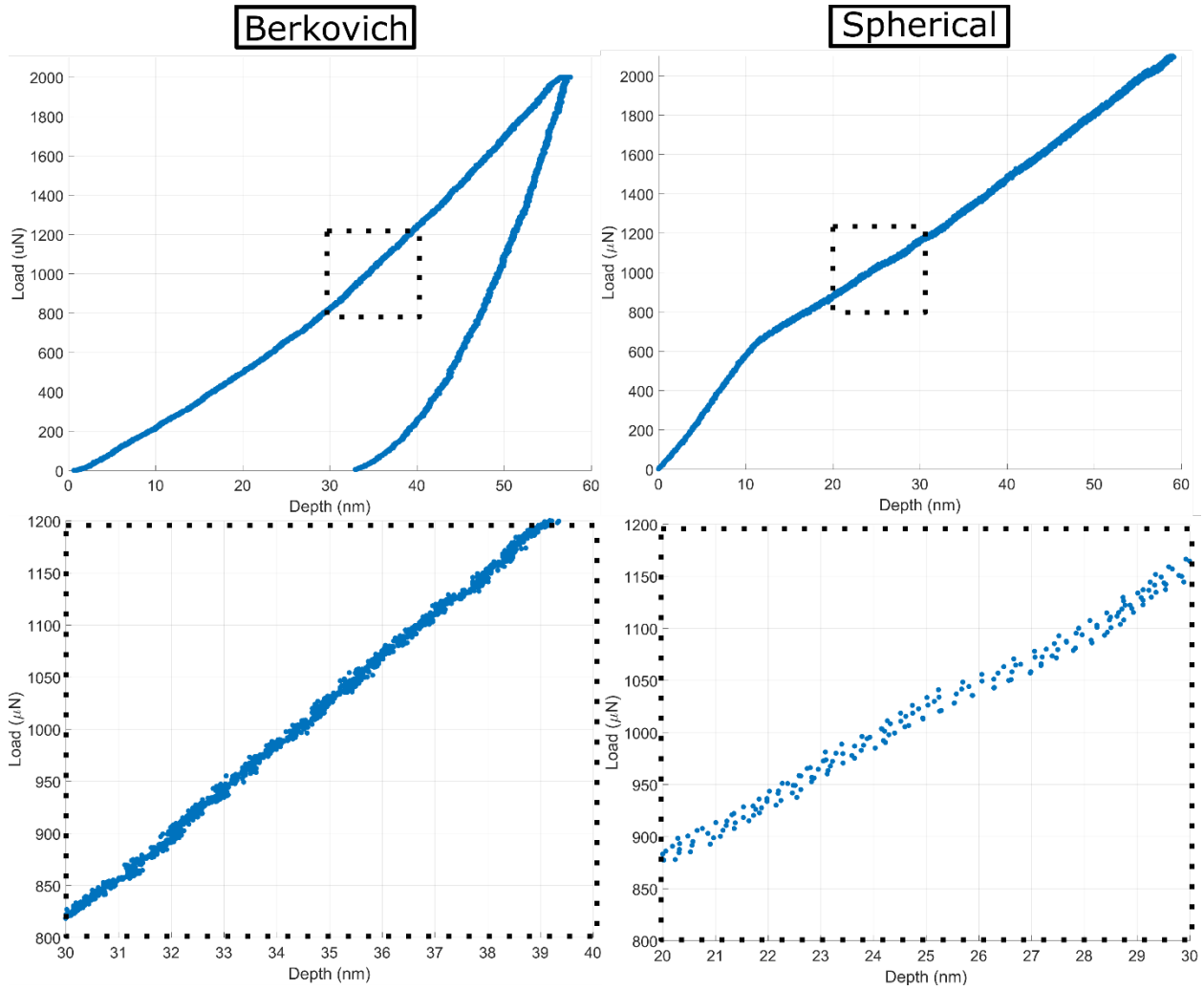

Figure 5.2: Comparison of load displacement curve for a Berkovich tip and for a spherical tip with enlarged images showing the individual data points of the curve. Note the sharp change in load-displacement response for the spherical tip after the initial loading, resulting in a "knee" of the graph. This results from the indentation procedure's transition from purely elastic loading to elastic-plastic deformation. As the Berkovich tip is sharp, plastic deformation occurs immediately during the initial indentation, and no elastic-plastic transition occurs. Also note the different shape of the collected data, the spherical indentation data uses the CSM method applying an oscillation to the load, clearly notable in the shape of the data.

Each sample was indented using Berkovich indentation to set a reference value for the indentation modulus. After the reference value is set, the samples were spherically indented using the indentation stress-strain method to give an idea of a compression-like plastic

deformation behavior after initial sample yielding. Since the indentation modulus was known, the proper value of contact area for this indentation tip can be adjusted to provide the previously measured Berkovich indentation modulus during the initial slope of the indentation stress-strain curve for each sample tested. With this value of contact area, the representative curves can be correctly analyzed and then cross-referenced in order to determine which of the alloy compositions have the best suitable values (see section 1.3.5). To determine the suitability of each alloy we selected the following properties: modulus, indentation yield strength, indentation work hardening (the slope of the indentation stress-strain curve after yielding), and general behavior of indents (large displacement bursts or load drops vs. smooth continuous deformation).

5.1.3. Powder XRD and Rietveld Analysis

Determination of alloy structure was accomplished with aid of a D8-Discover X-Ray diffractometer with a Co source operated at 40mA 35kV. This XRD system uses area detector that is able to collect 30° sections of the diffraction pattern, allowing for powder diffraction type measurements that would be much more difficult with more conventional detector systems. Through use of the area detector, samples with larger grains can also be indexed as each individual grain is more likely to show up as a spot pattern on the area detector. This geometry of this XRD is limited to between 10° and 45° for the mobile incident beam and the area detector. With the option of moving both the detector and the incident beam angle, angles for 2θ from 5° to 105° are achievable within the captured area diffraction patterns. While this range is smaller than for some higher precision x-ray diffractometers, the area detector compensates for this shortcoming with the ability to capture more x-ray counts within a single test run. The frames from the area detector are stitched together and integrated with the accompanying Bruker^{TM} software to provide a single 2θ vs intensity profile that is more typically used in XRD analysis.

Having acquired an XRD profile, the crystallographic information contained within the crystal structure present in the sample through the use of Bragg's law, allowing for the determination of present phases. Using the set of 2θ values, the lattice spacing from each intensity peak can be calculated. With that knowledge the structure factor, and thus lattice constants and crystal structure, can be determined. The process of structure determination has long been an automated process with many commercial and freely available software available for this. We used MDI-Jade software version 4.2.0 to index the XRD profiles. The general procedure involves identifying constituent elements and their chemically close neighboring elements and matching a known crystal structure's intensity vs 2θ plot to that of the collected XRD spectra. We achieved a strong match to the XRD spectra of alloys within all of the chemically complex alloy systems using the large databases consisting of many different simulated structures and materials found in commercial powder diffraction file (PDF) databases.

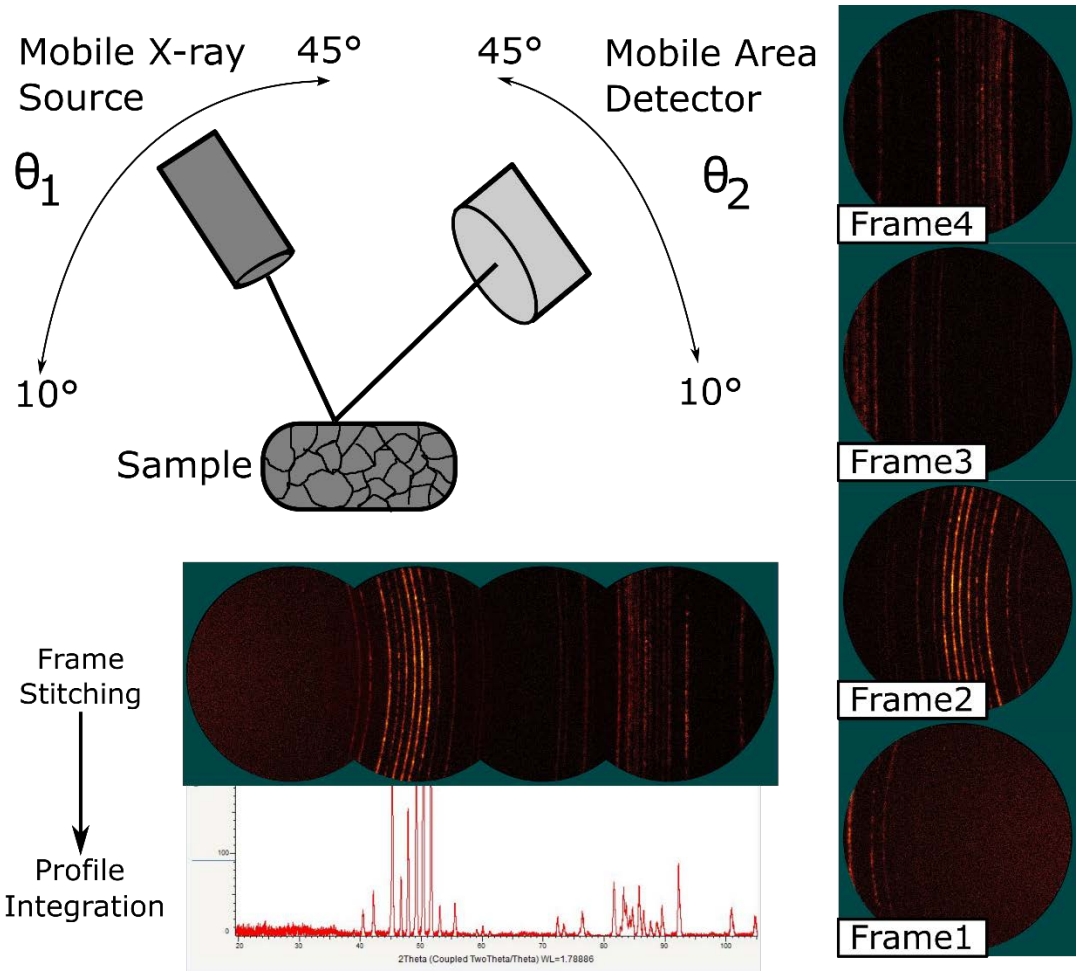

Figure 5.3: Geometry of D8-Discover XRD. Frames are at angles of 15,25,35,45° sequentially for both θ_1 and θ_2 allowing for a total 2θ range from 15° to 105°. The frames are then stitched together and integrated in order to form a standard intensity vs 2θ plot. Through the use of the area detector larger grained polycrystalline samples can be used, with the spots showing. However, this can lead to lower intensity for low-symmetry orientations.

5.2. Determination of Candidate Alloy using Indentation Stress Strain

After thorough mechanical polishing using standard procedure, sample surfaces were not always sufficiently detailed to determine if the alloys were single phase through optical microscopy for each alloy composition tested. Initial optical investigation conclusively showed that samples 1-1 and 1-2 contained two distinct phases, a “dark” phase and a “bright” phase, that did not disappear after annealing at 1600°C, 1700°C and 1850°C for 8hours sequentially. Figure 5.4 shows microstructural progression for both alloys 1-1 and 1-2 during subsequent annealing steps. It can be quickly seen that the annealing has grown the initially dendritic structure to be more uniform, with each ligament in the microstructure growing substantially. The alloys consisting of Ru-Ta-W only showed the lowest solubility of solute atoms into the HCP single phase, when compared to Ru-Mo-W and Ru-Ta-Mo-W. This can immediately be seen through the area fraction of the two phases under optical microscopy as measured using ImageJ image

analysis software to be 23.3% “dark” phase for Sample 1-1 and 47.4% “dark” phase for sample 1-2. It was initially assumed that the “bright” phase is the HCP Ru phase saturated with Ta and W, XRD measurements were performed to corroborate this and also determine the structure of the “dark” phase.

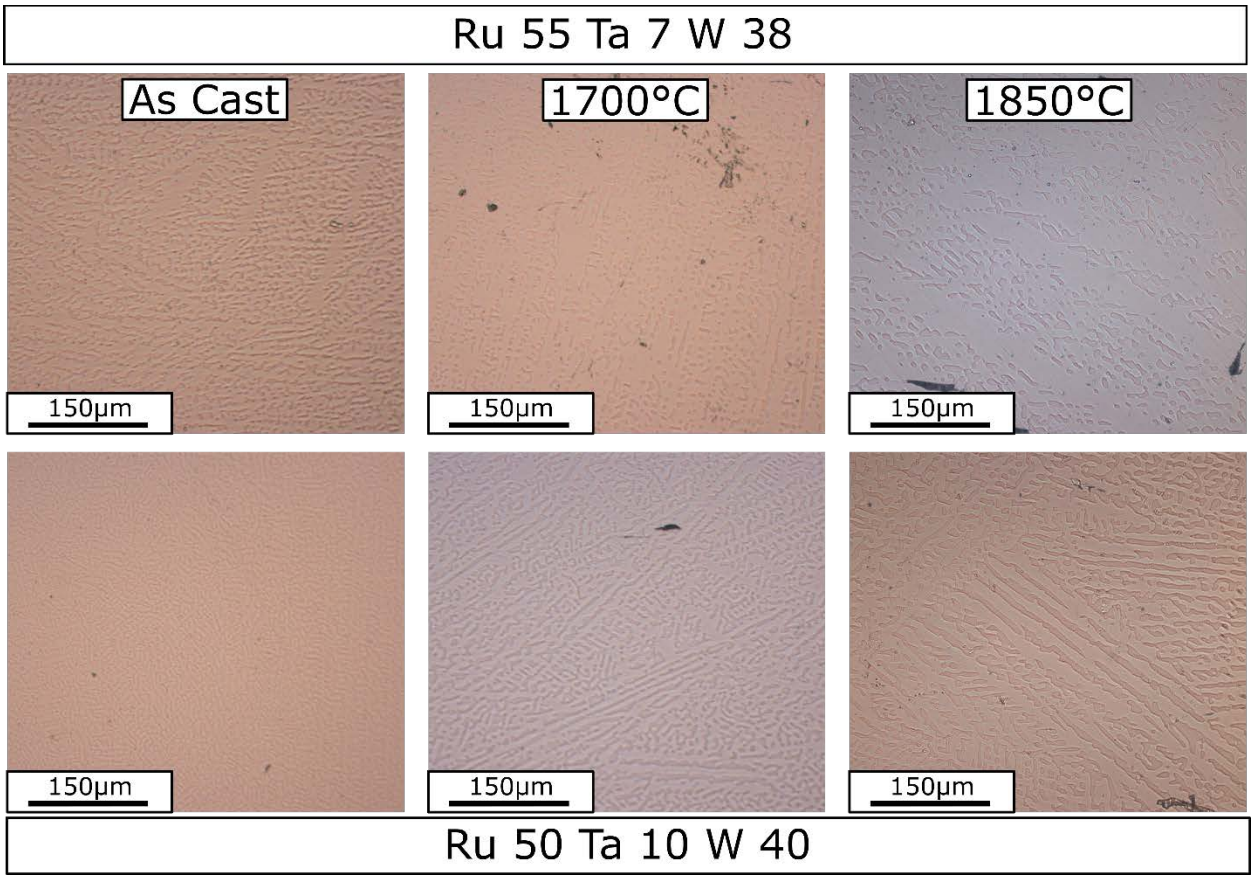

Figure 5.4: Optical micrographs showing the progression of the visible microstructure after annealing at a) 1600°C, b) 1700°C and c) 1850°C for 8 hours. Note the greatly increased size of the individual ligaments of the intermixing phases by the final anneal. Each subsequent anneal showed increase in ligament size.

5.2.1. Alloy Structures

Due to the casting of all alloys using powder metallurgy and arc melting in vacuum, the resulting ingots of material do not suffer from large solidification gradients as would be seen in typical casting methods at large scales. Due to arc-melting in vacuum, ingots come from casting with an oxide-free surface that is highly lustrous showing a generally small grain size (~100µm for the single-phase alloys). This combination allows for the ingots to be directly investigated in the XRD without further processing or polishing. The x-ray spectra were taken using a 300 second exposure time for each frame directly from the flat bottom of the ingots. The samples were translated over a large area during the spectra collection, in order to sample as many grains as possible during investigation. With the ingots having a randomized as-cast polycrystalline structure, some of the diffraction peaks have a much lower intensity than would be expected.

Despite this there was little difficulty in determining the structures present in the alloys, as the there was always sufficient information in order to index all available peaks. A full accounting of the alloy compositions as well as the final determination of the present crystal structure and compositions can be found in Table 5.1.

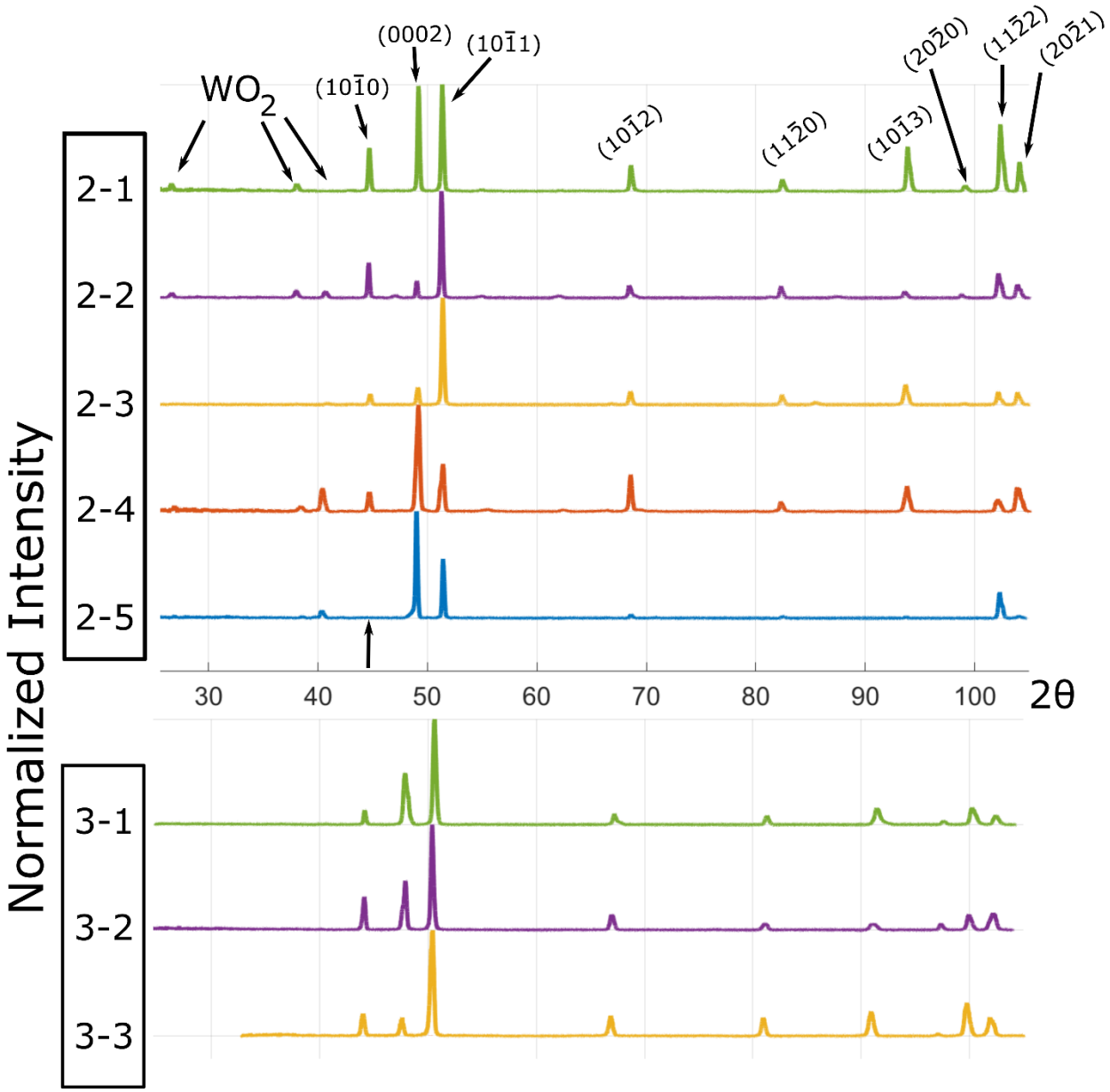

Figure 5.5: XRD spectra for Series 2 of Ru-Ta-W alloys probing the single-phase solubility limit of Ta and W into HCP Ru as well as the Series 3 alloys 3-1, 3-2 and 3-3, all containing single phase HCP structures. Series 3 alloys did not show any oxide spots as they were investigated immediately after casting with no anneal step. No secondary phase appears as the compositions change with any alloy. With the addition of Mo and W there is a much larger shift in the lattice spacing than with pure Ta and W. Note that Series 3 was not annealed, and as such the samples are not affected with any WO_2 peaks. The missing peaks in alloy 2-5 are due to the randomized nature of the individual grains inside each ingot.

The simplest indexing was performed on the second series of alloys testing the solubility of Ta and W into Ru. Samples 2-1 through 2-5 were all shown to be single phase HCP samples, as shown by Figure 5.5. This was slightly surprising since the goal of the series 2 alloy compositions was to determine the HCP phase boundary from the updated calculated ternary phase diagram. Alloys 2-1,4,5 were all chosen to be solidly within the HCP single phase region, with alloys 2-2 and 2-3 inside of the two-phase region with some orthorhombic phase precipitating out. As this did not happen, the solubility of Ta and W into Ru is much larger than expected, indicating that a single-phase Re-replacement alloy with the proper d-band electron to atom ratio is far more feasible than the initial two-phase series 1 alloys had suggested.

Alloys 3-1,2 were created to investigate the solubility limit of W and Mo into HCP Ru in the Ru-Mo-W ternary system. Here the compositions chosen were similar to that of Series 1, with W and Mo in relatively equivalent proportions. As was expected, the solubility of Mo and W in combination into Ru is much higher than for the Ru-Ta-W system, with no precipitation of other phases with Ru concentrations as low as 55 wt%. Additionally, by swapping 5% Mo with Ta in alloy 3-3 there was no change in solubility or in the position of peaks in the XRD spectra shown in Figure 5.5. The overall change in the XRD peak positions in Figure 5.5 indicate a solid solution of HCP Ru becoming increasingly saturated with the solute atoms, expanding the lattice. The initial lattice constants for the Ru based HCP structure that is seen in alloy 2-1 have: a = 2.7195Å and c = 4.3008Å, making the $\frac{c}{a} = 1.5815$, consistent with an expanded Ru lattice (Ruthenium having a base lattice constant of a = 2.7059 Å, c = 4.2815Å , $\frac{c}{a} = 1.582$). Conversely the addition of large amounts of Molybdenum have greatly shifted the characteristic HCP peaks in alloys 3-3, 3-4 and 3-5 to that consistent with the lattice constants of a = 2.7660 Å and c = 4.4586Å, making $\frac{c}{a} = 1.612$. In fact, the PDF that best fit to the Series 3 alloys was that of Re expanded by 1.2%, showing that the addition of Mo has not only greatly increased the solubility of solutes into Ru, but it has also changed the lattice constant to be virtually identical to that of pure Re, at $\frac{c}{a} = 1.615$.

For alloys 1-1,2 and 3-4,5 the identification went much the same, with the XRD spectra seen in Figure 5.6. Knowing the lattice constants for the HCP phases in the Ru-Ta-W system and the Ru-Ta-Mo-W system allowed for a relatively easy identification of the secondary phase seen previously in optical microscopy. Using a large search field, the PDF that best matched to this secondary phase was that of Niobium Tantalum Rhenium ($Ta_{37}Nb_9Re_{54}$) with the lattice constants of a = 9.6137 Å and c = 5.0074 Å, with the structure P42/mnm. It can be quite readily seen in Figure 5.6 that for the Ru-Ta-W system, the amounts of tetragonal and HCP phase are roughly equivalent, while in Ru-Ta-Mo-W system having a composition of 50 Ru - 5 Ta - 20 W - 25 Mo, in wt.%, is right on the edge of room temperature solubility into HCP Ru, whereas reducing the content of Mo by 5%, alloy 3-3, shows no secondary phase formation as cast. When annealing both alloys 3-4 and 3-5 for 8 hours at 1850 all secondary phase peaks disappear from the lattice. This leads to great progress of creating chemically complex alloys with the minimum possible Ru content (the most expensive element used), while still having an HCP single phase with nearly identical $\frac{c}{a}$ ratio to Re at 1.602Å.

In total, it has been shown that Mo addition greatly increases the solute solubility of HCP Ruthenium allowing for between 55 wt.% of the total composition to be non-Ru and still retain the HCP structure after annealing. It seems that Ta addition seems to be a solubility limiting factor when developing future chemically complex or high-entropy alloys, and as such it may be

feasible to substitute some portion of tantalum for niobium, in hopes of achieving a similar effect as seen through the replacement of tungsten with molybdenum.

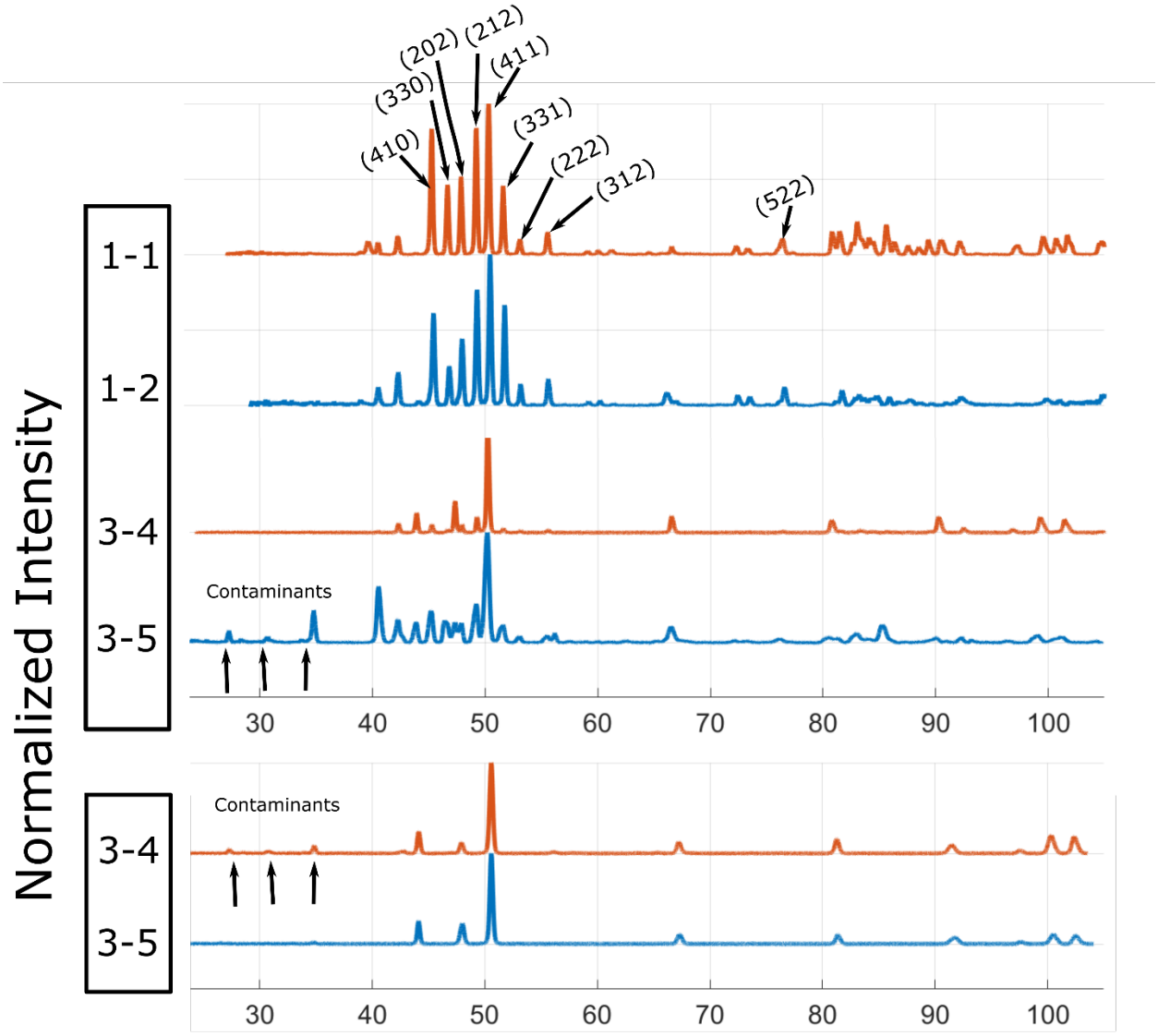

Figure 5.6: XRD spectra for samples containing 2-phase alloys. For both types the second phase was identified as a Tetragonal structure P42/mnm, with the primary phase being the same HCP structures seen in Figure 5.5. Here only the peaks for the Tetragonal phase are indexed. It can be seen that the Series 1 alloys have much more secondary phase than the Series 3 alloys, however the Series 1 alloys have been annealed at 1850 °C and the Series 3 have not in the initial Spectra. Alloy 3-5 contains nominally 45% Ru in total, yet shows only limited amounts of secondary phase. After annealing at 1850° for 8 hours, all secondary phase in alloys 3-4 and 3-5 have disappeared and the HCP phase has stabilized (bottom).

An approximate value for the solute content within the HCP phase of the two-phase series 1 alloys can be made with two simple approximations. Based on the single-phase diagrams in

Figure 5.1a) and b) it was assumed that twice as much W as Ta will be soluble into Ru, based on the size of the single-phase regions. Using optical micrographs to measure the relative areas of each phase within the alloys gives a tie line along which one can use a lever rule assuming that single phase HCP will contain 2:1 W:Ta within it. However, since the ratio of W:Ta is 4:1 within the overall alloy composition of alloy 1-2, a simple lever rule can be calculated as Ru vs solute content with the solutes in a 4:1 W:Ta ratio. When the Ru content is solved for in HCP alloy 1-2, the total Ru content within alloy 1-2 is 59.8 wt%, resulting in a total composition of approximately 60-8-32 Ru-Ta-W, in wt% (which is 73.12 at. % Ru, 21.44 at.% W and 5.45 at.% Ta) While this is an approximate answer, for this part of the alloy selection and screening process it provides a suitable starting composition from which one could make macroscopic alloys for tension testing.

Sample #	wt.% Ru	wt.% Ta	wt.% W	wt.% Mo	a (Å)	c (Å)	Structure
1-1	~40 ~60	~12 ~8	~48 ~32	0	9.6137 2.6774	5.0074 4.2918	23.3% Tet. 76.7% HCP
1-2	~40 ~60	~12 ~8	~48 ~32	0	9.6137 2.6853	5.0074 4.2975	47.4% Tet. 52.6% HCP
2-1	90	6	4	0	2.7195	4.3008	HCP
2-2	80	12	8	0	2.7206	4.3123	HCP
2-3	80	4	16	0	2.7131	4.3066	HCP
2-4	85	3	12	0	2.7166	4.3016	HCP
2-5	80	1.2	18.8	0	2.7206	4.3057	HCP
3-1	60	0	20	20	2.7511	4.4666	HCP
3-2	55	0	20	25	2.7534	4.4104	HCP
3-3	55	5	20	20	2.7576	4.4339	HCP
3-4	50	5	20	25	2.7522	4.4017	HCP (Annealed)
3-5	45	10	20	25	2.7505	4.4052	HCP (Annealed)

Table 5.1: Table of the chemically complex alloys tested and the determined crystal structures. Mo appears to have a favorable effect on solubility when replaced with W. All three of the tested systems, Ru-Ta-W, Ru-Mo-W and Ru-Ta-Mo-W systems have a much larger solubility limit of the HCP phase than calculated using the CALPHAD method to simulate phase diagrams.

5.2.2. Indentation Response of Alloys

Initial indentation was performed on an as-cast samples of pure rhenium and pure ruthenium using Berkovich indentation. Unlike with the spherical stress strain indentation method, Berkovich indentation uses a non-axisymmetric sharp triangular indentation tip with the indentation face inclination of 65°. The use of this tip allows for the proper determination of projected area. The indentation immediately enters the elastic-plastic regime of deformation, allowing for both hardness and modulus measurements at very shallow indentation depths, something not feasible with Spherical indentation as seen in Figure 5.2. As there is no data involving indentation modulus or hardness for pure rhenium and pure ruthenium as small indentation depths, initial Berkovich indentation was performed on Re and Ru in order to provide a basis for comparison between values obtained via traditional indentation modulus and

hardness values and the indentation stress strain curves. Additionally, the indentation modulus response is measured during Berkovich indentation from the unloading segment and should be independent of indentation depth, any discrepancy seen between samples is either an artifact of the individual sample preparation, mounting, testing method or due to some property of the sample influencing the load upon unloading, such as detwinning in Re. All procedural discrepancies between samples should be negligible as all samples are prepared and tested using the same methodology. Indentation was performed without accounting for grain boundaries or grain orientations as an average hardness and modulus value was important for future invesitgation.

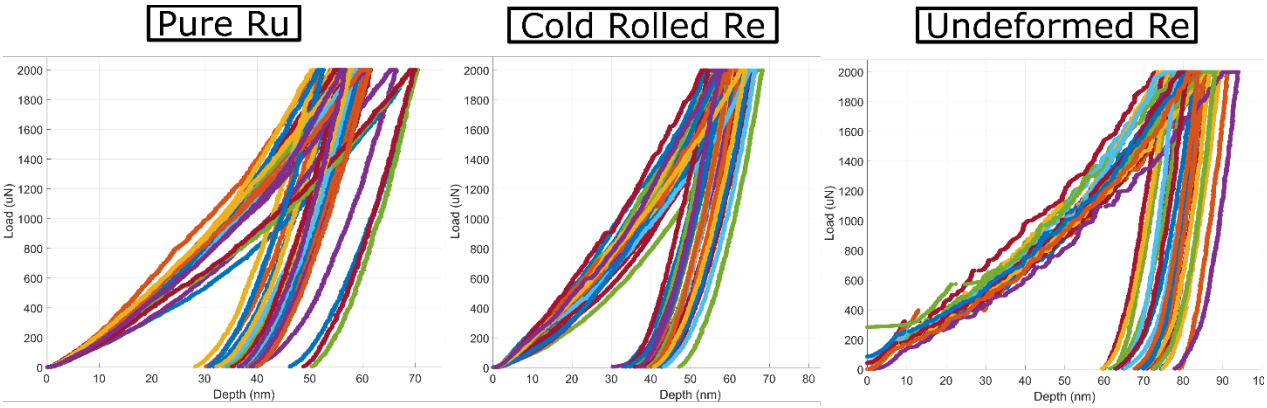

Figure 5.7: Indentation response of pure Ru, cold rolled Re and an undeformed small grained Re sample using Berkovich indentation. Note that the spread for both the Ru sample and the undeformed Re sample is very large, while cold rolled Re has less varience. In Ru this is due to the prolific cracking seen, and in the undeformed Re this is due to orientation and the extent of twinning seen in each individual indent. The extensive pop-ins seen in the undeformed Re sample that are not seen in cold worked Re are mainly due to the formation of deformation twins that are pre-existing in cold-worked structures.

During initial indentation, it was quickly noted that Berkovich indentation of Ru and pure undeformed Re resulted in a very large variation of hardness and the general shape of the indentation curve. For the case of Ru, the large variances in indentation hardness and modulus corresponded to irregular asymmetric projected area indentation profiles, that were indicative of cracking around the indentation tip. It was determined not to be a normal sink-in or pile-up behavior, as sink-in and pile-up occurs as a symmetrically continuous deformation around the indentation tip, generally lacking any asymmetries. For the pure undeformed Re, the irregularities were due to grain orientation and the amount of twinning present around the indentation tip, as twins are orientation dependent and can deform much more quickly than dislocations, resulting in load-displacement pop-in. This can be seen in the later section detailing, the performed EBSD around the indentation tips. Additionally, as there are no barriers to dislocation motion in the form of twins, any dislocations generated will be able to freely flow and accommodate the plastic deformation around the indentation tip. This behavior was largely muted in the cold rolled Re indentation profiles as the cold working process in rhenium introduces many deformation twins, reducing the number formed during the indentation process while simultaneously hardening the sample by providing barriers to dislocation motion. A full

accounting of all the indentation hardness responses as well as indentation modulus using Berkovich indentation can be found in Table 5.2. While this data is extensive and gives insight into the different behaviors of the various alloys, this is used as a starting reference point before continuing with spherical indentation.

Sample	Ru wt.%	Ta wt.%	W wt.%	Mo wt.%	Ind. Modulus(GPa)	Ind. Hardness (GPa)
Re	0	0	0	0	451.9 ± 48.85	12.28 ± 2.982
CW-Re	0	0	0	0	400.0 ± 31.42	12.55 ± 1.156
Ru	100	0	0	0	375.9 ± 54.86	12.55 ± 2.167
2-1	90	6	4	0	406.9 ± 43.93	13.54 ± 2.183
2-2	80	12	8	0	419.7 ± 37.07	14.41 ± 1.388
2-3	80	4	16	0	370.2 ± 54.53	11.89 ± 3.018
2-4	85	3	12	0	411.4 ± 47.22	12.88 ± 1.904
2-5	80	1.2	18.8	0	370.6 ± 36.49	13.01 ± 2.168
1-2-HCP	~50	~10	~40	0	327.5 ± 19.32	12.35 ± 0.062
1-2-Tet.	~50	~10	~40	0	341.4 ± 14.52	19.16 ± 0.481
3-1	60	0	20	20	312.5 ± 24.13	11.87 ± 1.370
3-2	55	0	20	25	341.0 ± 16.45	11.89 ± 0.752
3-3	55	5	20	20	314.1 ± 16.27	12.16 ± 0.860
3-4	50	5	20	25	275.8 ± 16.35	10.67 ± 0.473
3-5-HCP	~45	~10	~20	~25	267.0 ± 23.24	11.01 ± 1.244
3-5-Tet.	~45	~10	~20	~25	314.0 ± 21.88	17.52 ± 1.694

Table 5.2: Berkovich indentation data for each sample. The modulus measured for the cold-worked Re sample is used as a control value in order provide the correct contact radius during indentation stress-strain analysis. Note how indentation hardness increases slightly between cold-worked and as cast samples, likely due to the twin separation being much larger than the roughly 200nm indentation tip size. The large variance in modulus is likely due to orientation effects coupled with enhanced detwinning present in the cold-worked sample. The tetragonal phases both have extreme hardness, with increased modulus values, making them unsuitable for further testing using the indentation stress-strain method.

Spherical indentation was performed on all samples without controlling for crystallographic orientation. Again, the crystal orientation was not measured as the goal of the indentation procedure was to find a pseudo-compression response that would elucidate the macroscopic plastic deformation behavior of each alloy. The indentation hardness and modulus values for Berkovich indentation on cold-worked rhenium had a much smaller variance, with much more regular deformation behavior. This was due to ample pre-existing deformation twins, which were not present in the annealed swaged Re sample.

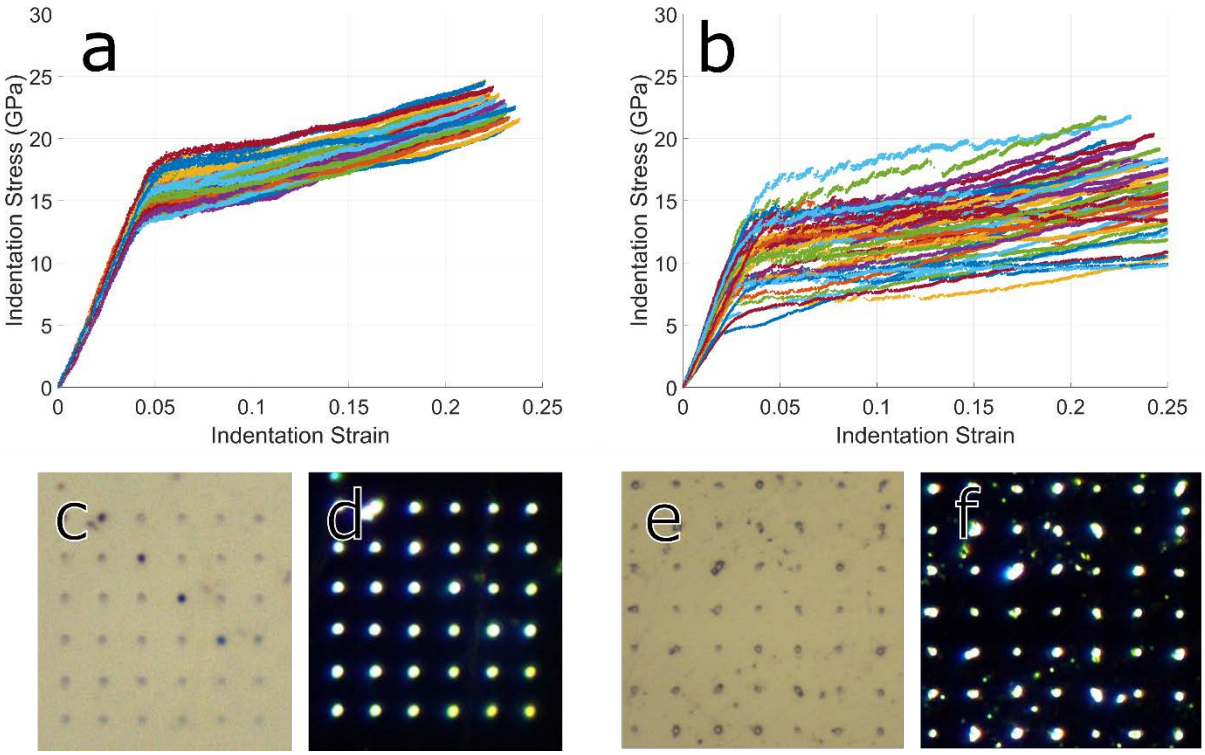

Figure 5.8: Indentation stress-strain curves for rhenium a) and ruthenium b). Note the large variance in yield stress for Ru. Ru cracks at different stresses for each randomly oriented indentation. The post yield deformation behavior is also largely dependent on the extent of cracking in Ru. Optical images of both Re c,d) and Ru e,f) using bright-field c,e) and dark-field d,f) optical microscopy. The indentation profile is best seen using the dark-field, as cracks can appear much the same as surface contamination.

The initial comparison of Re to Ru showed drastically different responses in yield stress, modulus, average indentation hardness, and work-hardening behavior. The average indentation hardness is measured by averaging the applied load divided by the calibrated contact area after yielding. The slope of the indentation stress-strain curve after yielding is taken to be the work-hardening rate. Figure 5.8 a) and b) show the many differences in the indentation stress-strain curves of Re and Ru. The large difference seen in the Ru sample in Figure 5.8b) is due the surface cracking that is extremely common in the very brittle Ru sample. While the smaller variance in Figure 5.8a) is due to interactions between the pre-existing twins and indentation tip for the cold-worked Re sample. It should also be noted in the optical images taken of the indentation sites, Figures 5.8c-f), that the indentation profiles seen for Re are almost perfectly symmetric, while Ru has consistently irregular shapes due to the extensive surface cracking. The extent of surface contamination and scratching can be seen in the optical images, partially accounting for the large spread in the Re indentation data. For the investigation of future alloys, optical images were taken to help in the ductility screening process, in order to determine the extent of surface cracking or expanded plastic deformation.

With the Ru and Re showing extremely different characteristic indentation behaviors, the first set of alloys indented were the Series 1 2-phase alloys. The indentation was performed both

by targeting the indentation sites to probe each phase individually and by placing a large grid of random indents and then later separating the two alloys by their disparate behavior. The second method was easily accomplished due to the unique characteristic between indentation curves of HCP and tetragonal phase seen in Figure 5.9. It can be seen that the behavior of the HCP Ta-W saturated phase is much improved over pure Ru, with a comparable yield strength as well as work hardening behavior with that of the pure Re. This shows that replacing as much Ru with other solute atoms as possible increases the ductility of subsequent alloy.

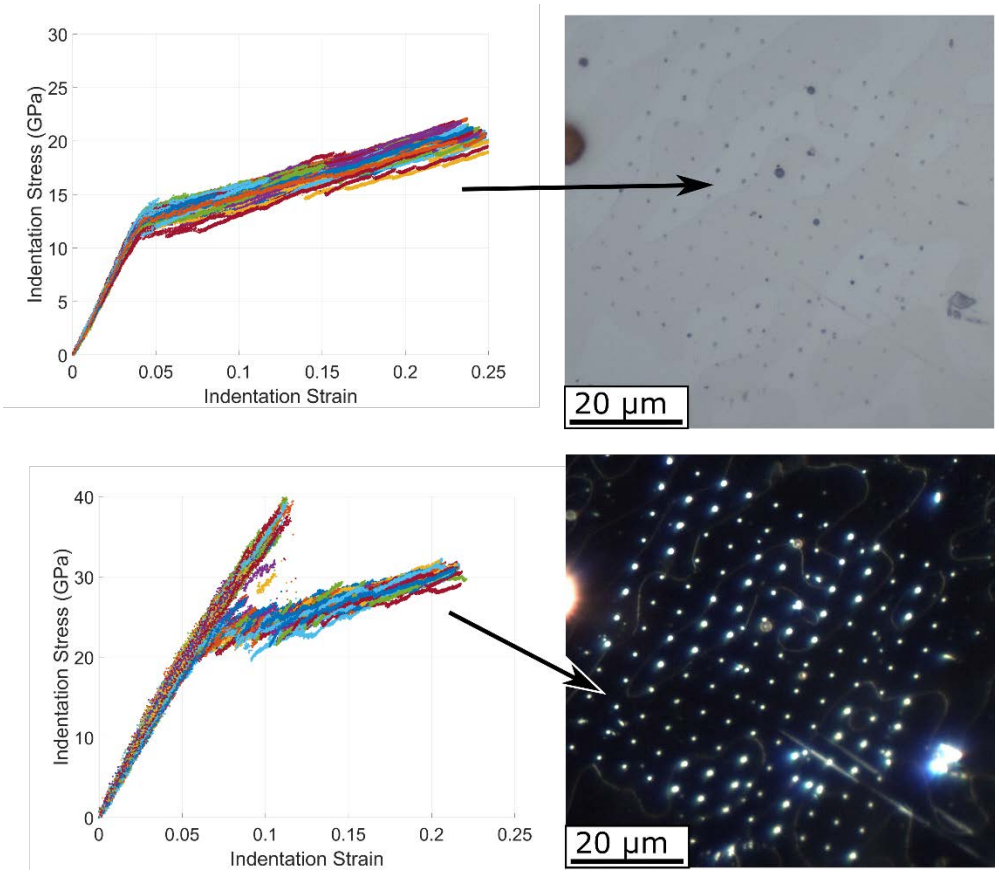

Figure 5.9: Indentation stress-strain curves for the series 1 two-phase alloys with optical micrographs showing arrows to the phases where the stress-strain curves are measured. Using optical microscopy, it can easily be seen that the two phases not only have different indentation profiles, the HCP phase being much deeper softer indents, but are easily distinguishable in the indentation stress strain data. The HCP phase has Re-like behavior, while the tetragonal phase is much harder than the initial Ru. The cracking is very consistent for the tetragonal phase, with some curves showing extremely high hardness before the initial crack. With a 100Hz data collection rate, the single data point between the load maximum and the large drop shows the extreme brittle yield of the undesired tetragonal phase.

As would be expected based on general properties of intermetallic phases (91), the tetragonal intermetallic σ phase is extremely brittle and hard. Cracking around the indents is difficult to observe with optical microscopy due to the extreme hardness of the sample producing such

shallow indentation depths. However, the brittleness can be seen by the irregular indentation stress-strain profiles showing some samples with extremely high yield stresses with a load drop taking place in the space of a single data point at 100Hz collection rate. This catastrophically brittle yielding is not desirable for any structural material used in practical applications. With an initial lower bound yield stress of 20 GPa and upper bound of 40GPa, this is the hardest material tested, having the least favorability for future development into macroscopic samples. As is the case in most alloys, σ phase intermetallic compounds should be avoided to achieve the best possible mechanical behavior. To reiterate, the goal in rhenium replacement is to get an HCP single phase Ru-based alloy while alloy out the maximum expensive Ru possible without precipitating out undesired secondary phases, which negatively impact mechanical properties.

The initial purpose of investigating series 2 of the Ru-Ta-W alloys was to probe the predictive validity of the improved ternary alloy diagram seen in Figure 5.1e). This series of alloys were shown to be solidly within the HCP single phase regime of the ternary phase diagram, allowing for indentation testing to determine the effects of each solute element on the overall indentation response of HCP Ru based alloys. With an understanding of how each substitutional solute affects the solid solution, future designer-alloys can be tailored to each specific property required. As seen in Table 5.1, the compositions of the series 2 alloys are all between 80-90% Ru with different contents of Ta and W, from a low of 1.8 wt.% Ta (alloy 2-5) to a high of 12 wt.% Ta (Alloy 2-2). All of the indentation stress-strain curves for each Series 2 alloy can be seen in Figure 5.10 with the addition of the HCP phase from alloy 1-2. Any difference between alloy 1-2 and 1-1 HCP phases was within the experimental variance. The HCP phase from the series 1 alloys provides the limit to the Ta and W content in Ru, showing a comparison of the partially alloyed material to that of the fully saturated solid solution.

Immediately through the addition of 10% solute content in Figure 5.10a), it can be seen that the extreme variance due to cracking in indentation yield strength seen in pure Ru has been largely suppressed. There remains substantial variance of yielding, indicating that there is still some remnant cracking and non-uniform deformation, however after the after yielding work hardening behavior has improved considerably, resulting in a consistent slope and continuity. Alloys 2-2, Figure 5.10b), shows the same consistent work hardening and large variance in yield stress as in alloy 2-1. In alloy 2-2, the post yield stress-strain curves all trend toward the same stresses and work hardening rates after 0.15 indentation strain. Again, this is likely due to enhanced cracking for some orientations becoming less pronounced after the contact area increases sufficiently. Alloys 2-3,4 shows a nice comparison of the change in mechanical response with increasing solute addition. With only 15% solute content, the stress-strain curves in Figure 5.10d) have large strain bursts and drops very consistent with sudden extreme cracking around the indentation tip. By increasing the W content by 4 wt.%, Figure 5.10c), the variance of load-displacement data is much reduced, with the largest strain bursts all removed.

While the initial addition of Ta and W into the Ru-based solid solution had greatly increased ductility, seen Figure 5.10a), it can be seen that when comparing the curves in Figure 5.10e) and d) to those of Figure 5.10c) the ratio of Ta to W must be carefully chosen. The indentation stress-strain curves all best approach Re when the ratio of Ta:W is 1:4, as is the case in Figure 5.10c) and e), making the target alloy for macroscopic Tension in the Ru-Ta-W system one containing roughly 60% Ru with 8% Ta and 32%W. As would be predicted by the initial models, this alloy has a d-band filling of 5.28 $\frac{electron}{atom}$, making it very close to the d-band filling of Rhenium at 5$\frac{electron}{atom}$. While this is approaching the goal of between 4.6-5 $\frac{electron}{atom}$,

improvements upon this value can be obtained through the addition of Mo to the system.

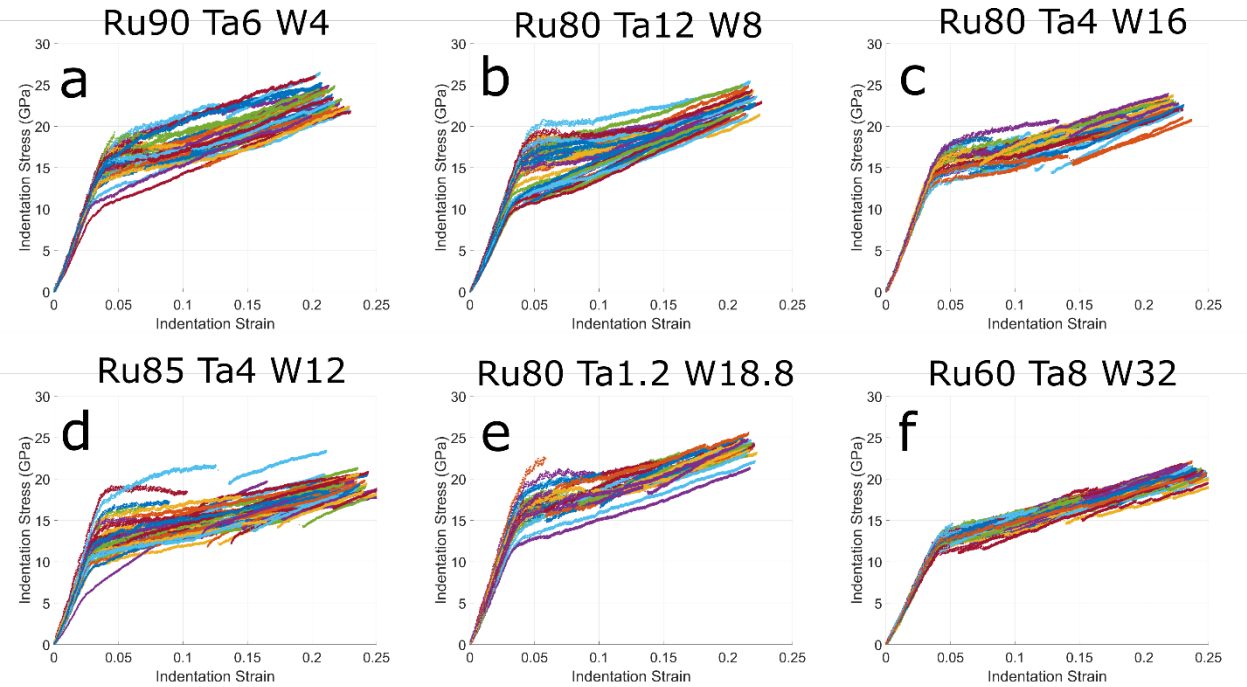

Figure 5.10: Indentation stress-strain curves for the Series 2 alloys a-e) with the HCP phase from Series 1 f). The composition for the HCP phase is approximate as calculated earlier, however the ratio of W to Ta should be 4:1, and as such it bears much of the same behavior as seen in Figure c).

The initial two alloys in series 3, 3-1 and 3-2, were to test the single-phase solubility of a Ru-Mo-W ternary single phase HCP alloy with roughly equivalent contents of W and Mo. For all of the series 3 alloys, the same W content was chosen to reduce the number of variables. Having already seen in series 2 that a larger W content is more favorable for mechanical properties than Ta, it was assumed, and shown experimentally in the XRD results, that Mo will behave largely like W within the alloys in terms of solubility. When compared to the Series 2 alloys, the Ru-Mo-W alloys 3-1 and 3-2 have much better deformation behavior in terms of consistent yield stresses, with minimal strain bursts. While alloy 3-1 shows some strain bursts with coupled stress drops, through increasing Mo content a further 5% the strain bursts are eliminated. Most striking in the Series 3 alloys is the transition from alloy 3-2 to 3-3 through the replacement of 5% Mo with Ta. The resulting decrease in yield strength spread and further reduction in strain burst events with extremely consistent work hardening behavior most closely resembles that of the pure cold-worked Re sample. This is unsurprising as a sample with Ru 55 - Ta 5 - W 20 -Mo 20 wt.% (Ru 61.2 - Ta 3.1 - W 12.2 - Mo 23.5 at.%), has a d-band filling of 5.19 $\frac{electron}{atom}$, the closest to Re of any alloy tested to this point.

As the Ru content lowers further for alloys 3-4 and 3-5 we can see that the improvements made with alloy 3-3 decrease slightly producing a larger variance. This of course could always be a product of different grain, boundary, and orientation effects, as both samples 3-4 and 3-5 have a secondary phase which commonly precipitate at grain boundaries refining grain size (92). Additionally, having a secondary phase contained within the structure gives the possibility of having phase boundary interactions in addition to grain boundary during indentation. This effect

is exacerbated in alloy 3-5, stress-strain curves seen in Figure 5.11e), with a very large variation in yield stresses as well and increased strain bursts over alloy 3-4. For the best mechanical behaviors of as-cast alloys, a composition between that of 3-3 and 3-4 would most likely produce the most favorable results. For instance, the creation of a Ru 52 - Ta 6 - W 20 - Mo 22 wt.% (Ru 58.1 - Ta 3.7 - W 12.3 - Mo 25.9 at.%), alloy would likely remain single phase HCP, while reducing the d-band filling to 5.12 $\frac{electron}{atom}$ without the need for high-temperature annealing. This would be lowest d-band filling out of any chemically complex alloy tested, and it would test the theory that a d-band filling between 4.6 $\frac{electron}{atom}$ and 5 $\frac{electron}{atom}$ would increase the favorability of $\{11\bar{2}1\}\langle 11\bar{2}6\rangle$ type twins, producing a Re-replacement alloy.

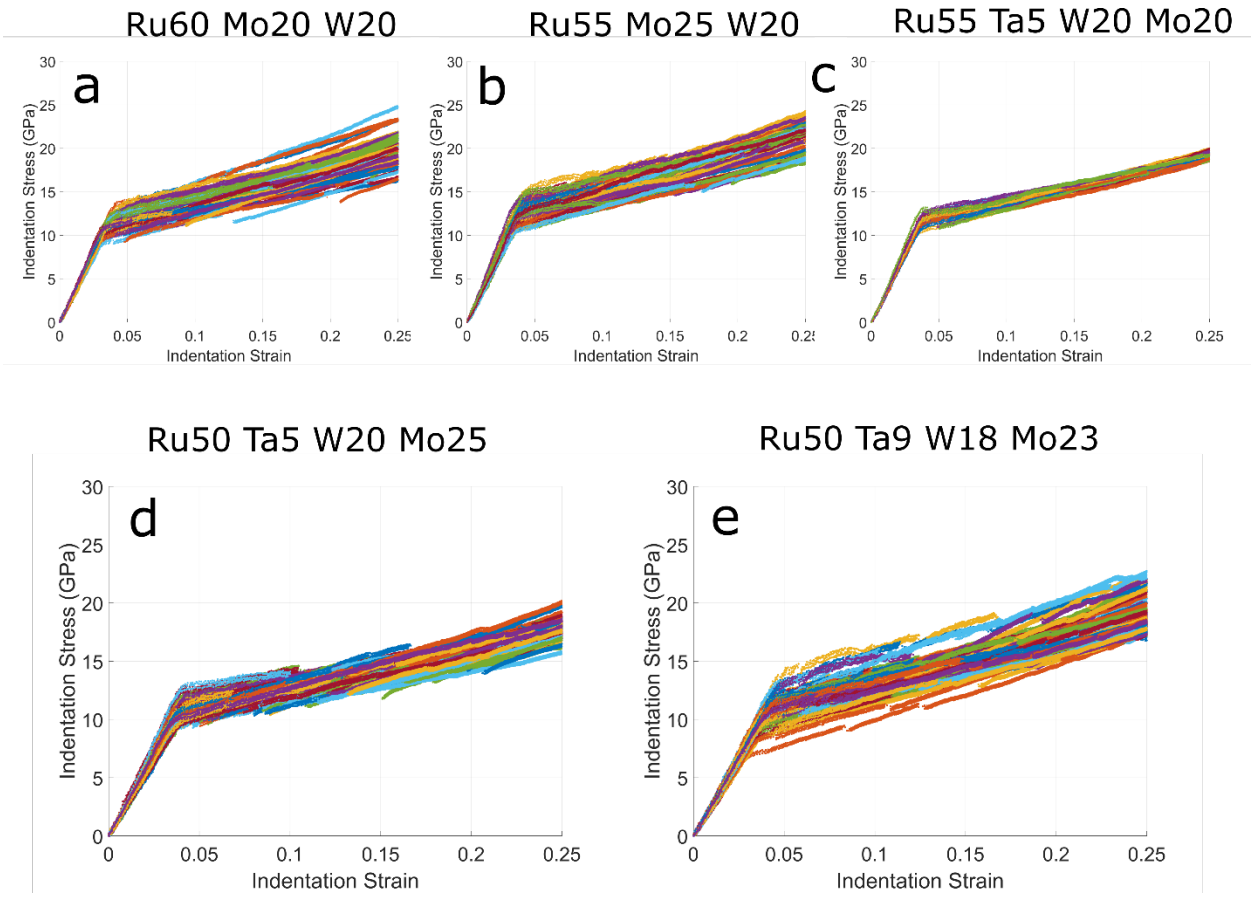

Figure 5.11: Indentation stress-strain curves for the Series 3 alloys, all phases are HCP with the solute content in e) an approximation based on the macroscopic solute content made within the original alloys. Alloy d) is almost completely single phase per XRD making an alloy with slightly more ruthenium content viable for macroscopic testing. Not that the addition of Ta between b) and c) has greatly reduced the spread in the alloy.

The full accounting of all the indentation stress-strain data can be found in Table 5.2. The modulus values are not copied from the Berkovich indentation data, instead they are taken from the initial slopes of the indentation stress-strain curves for each sample. The contact radius was calibrated using the modulus from Berkovich indentation of the cold-worked pure Re sample and

then applied to all samples. This was accomplished by changing the contact radius within the calculations until the modulus measured on the indentation stress-strain curve matched with the modulus measured from the unloading curve of Berkovich indentation. Using this method, it can be seen that in general the measured indentation modulus for each of the alloys is appreciably higher than during the unloading of a Berkovich quasi-static indent. However, for Ruthenium this modulus value of 401.93 GPa is much closer to the actual value of modulus, 414 GPa, as measured through conventional macroscopic tests (20). This is due to the fact that the spherical indentation technique does not immediately induce elastic-plastic deformation as is done with a sharp indentation tip. As such there can be no cracking during the elastic portion of the deformation curve, making the assumed contact area much closer to the real value.

Sample	Ind. Modulus(GPa)	Ind. Hardness(GPa)	Yield Stress(GPa)	Work Hardening(GPa)
CW-Re	397.65 ± 29.79	14.53 ± 0.84	14.65 ± 1.58	36.29 ± 10.72
Ru	401.93 ± 75.29	8.503 ± 2.22	10.01 ± 2.41	23.73 ± 12.43
2-1	461.67 ± 35.19	15.11 ± 1.36	14.83 ± 1.94	43.19 ± 16.02
2-2	439.40 ± 43.83	14.70 ± 1.18	14.09 ± 2.95	44.64 ± 17.75
2-3	451.33 ± 28.67	14.23 ± 0.75	14.95 ± 1.29	32.10 ± 9.545
2-4	452.07 ± 49.78	11.15 ± 1.02	11.86 ± 2.20	34.28 ± 16.39
2-5	444.64 ± 44.10	15.75 ± 0.95	15.86 ± 1.98	39.48 ± 17.06
1-2-HCP	328.30 ± 21.47	12.67 ± 0.63	12.67 ± 0.73	40.43 ± 8.464
3-1	353.65 ± 28.05	11.61 ± 1.13	11.12 ± 0.85	39.43 ± 7.085
3-2	364.85 ± 28.18	12.80 ± 1.06	12.47 ± 1.03	43.41 ± 7.377
3-3	348.49 ± 22.86	11.28 ± 0.26	11.84 ± 0.67	34.69 ± 4.805
3-4	286.17 ± 32.15	10.46 ± 0.47	10.72 ± 0.70	32.41 ± 7.260
3-5-HCP	260.96 ± 26.51	11.06 ± 0.93	10.78 ± 1.09	37.66 ± 7.866

Table 5.3: Tabulation of relevant quantities using spherical indentation. While ductility is not directly measurable with this procedure, the work hardening behavior in conjunction with yield stress can provide insight into the macroscopic properties. From this list, the alloys most promising are the fully saturated 1-2 HCP phase, alloy 3-2 and the saturated HCP phase from the unannealed alloy 3-5.

5.2.3. Indent Microscopy of Pure Re and Select Alloys

EBSD is a microscopy technique that can only probe the top surface of a sample. There exists a large interaction volume of material within the bulk of the sample that produces extensive secondary radiation, x-rays backscattered, secondary and auger elections, upon interaction with the incident electrons that serves to lower spatial resolution considerably. Despite this it is still possible to gain an understanding of the crystallographic changes induced through deformation of samples during indentation. While the bottom of an indentation pit shields much of the signal from reaching the EBSD detector, much of the deformation takes place around the indentation tip, allowing for EBSD maps to be formed on the surrounding surfaces. In the case of the sharp tip Berkovich indentation, the resulting EBSD patters are extremely interpretable with both local misorientations as well as much twinning visible at the surface.

In order to determine the types of twining present under the indentation surfaces in pure

undeformed Re, indentations were performed to a maximum nominal load of 1000 μN, which resulted in an indentation depth of 250nm, on the pure as delivered Re sample. This would provide a wide enough indentation profile in order easily be able to investigate the different types of twins present under and surrounding the indentation tip. For this set of "deep" (when compared to the 50nm deep indents used to measure modulus and hardness) of indents, the orientation of the indented grains was random and there were some indents occurring on grain boundaries. An overview of indentation locations and surface quality using SEM is seen in Figure 5.12a). It should be noted that some indents occurred on pre-existing twins or surface scratches and voids, Figure 5.12b), as well as having some surface contamination stamped into the indent. Finally, through most indents regardless of the crystal orientation showed significant pile-up around indents (an effect which increases the contact area between sample and indenter tip, thus artificially increasing the measured modulus or hardness), the amount of pile-up was highly orientation dependent, as seen in the difference between indents in Figure 5.12b) and c). All of these factors are likely to be present in all samples analyzed previously using indentation stress-strain, and are the main reason for the difference in reproducibility seen between indentation tests and macroscopic samples.

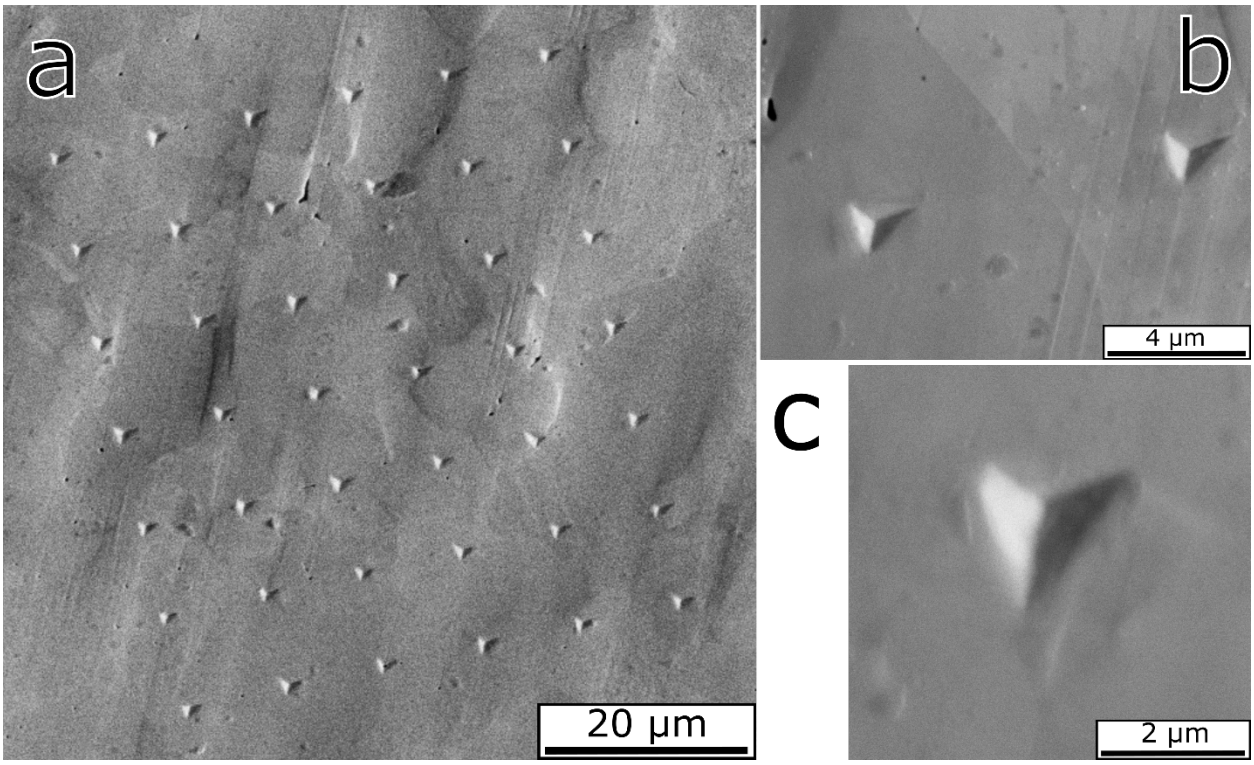

Figure 5.12: Overview SEM image showing "deep" indents that were investigated using EBSD a). Indents in two neighboring grains can be seen in b), with the rightmost indent having been performed on top of some pre-existing twins. On the far left in the image a void can be seen in the sample. Finally, a close-up image of an indent c) where pile-up can be seen on both sides of the indent, and the indent appears to have symmetrical pile-up.

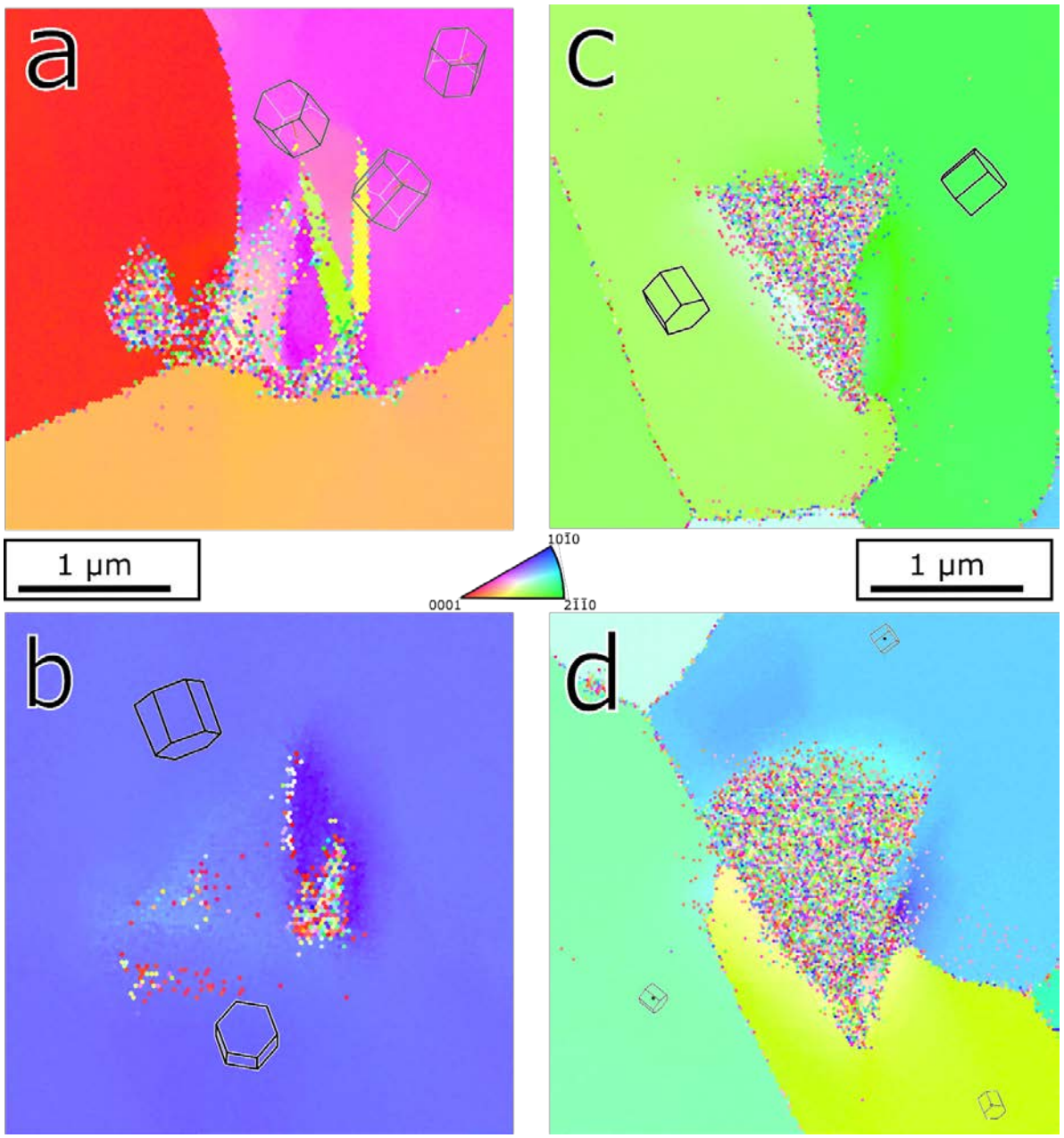

Figure 5.13: Characteristic EBSD maps for Berkovich indents of choice grain orientations taken at the same length scale. For a) it must be noted that the IPF map is oriented as an IPF-Y map (all other maps are the standard IPF-Z maps), such that the color chart in the center dictates the orientation relative to the image vertically. This was done so that the different twin types, $\{11\bar{2}1\}\langle 11\bar{2}6\rangle$ left and $\{11\bar{2}2\}\langle 11\bar{2}3\rangle$ right, could more easily be recognized. In b) the twin present, $\{10\bar{1}2\}\langle 10\bar{1}1\rangle$ type twin, is mainly below the surface, but small portions were able to be indexed using EBSD. For all twins and grains an HCP lattice is inset. Note that for all of the indents involving grain boundaries, no twins are seen interacting with the grain boundaries, instead it appears that the indentation response is purely orientation dependent. Additionally, TEM lift-outs were produced out of the indents from indent 6, c), and indent 13, d), in order to investigate the sub-surface structure.

Using the SEM overview in Figure 5.12a), a few indents were chosen in order to gain insight into the different behaviors seen in various crystal orientations as well as twinning effects along grain boundaries. Through the EBSD investigation of different indented grain orientations it was immediately seen that all twin variants reported in the literature for Re (the most prominent $\{11\bar{2}1\}\langle 11\bar{2}6\rangle$ type twin, the secondary $\{11\bar{2}2\}\langle 11\bar{2}3\rangle$ type twin and the ubiquitous $\{10\bar{1}2\}\langle 10\bar{1}1\rangle$ type twin seen in all HCP metals) were also observed in Berkovich indent. Figure 5.13 shows a series of select EBSD maps that detail the different crystal orientations that show the different twin types as well as select orientations that do not show any twinning. The indent in Figure 5.13a) is unique in that it shows both $\{11\bar{2}1\}\langle 11\bar{2}6\rangle$ and $\{11\bar{2}2\}\langle 11\bar{2}3\rangle$ within a single indent. This behavior shows the difficulty in interpreting the mechanical response for Berkovich indentation, where the stress states below the sharp indention tip involve tensile, compressive and shear states (25) (93). Another large driving factor for the deformation underneath the Berkovich indenter tips is the fact that the indenter has sharp edges. As an example, note how in Figure 5.13a) both twins are much thicker near the bottom right edge of the indent, indicating they nucleated as the sharp edge was carving through the sample surface.

In order to investigate the sub surface structure of the indents chosen from the "deep" Berkovich set, a pair of focused ion beam (FIB) prepared lift-out samples were prepared from two indents that were not seen to have surface twinning, indents 6 and 13 in Figure 5.13 c and d) respectively. As is standard with FIB lift-out preparation, a thick layer of platinum was deposited on the indent surface, shielding the underlying rhenium from accumulated extensive radiation damage from incident Ga^+ ions. Figure 5.14 shows TEM images taken from the two indents. While the EBSD images in Figure 5.14c and d) show very similar crystallography underlying the indents, both consisting of indents upon grain boundaries with similar orientations. The microstructure shown by TEM images in Figure 5.14 show extremely different structures. One key different between the two samples is the depth at which the data is taken. Indent 6 was milled for a longer period of time, such that there is no longer any platinum visible along the indentation surface, taking the TEM images from deep underneath the indent. Indent 13 still show the protective platinum cap intact, allowing for images to be collected directly at the indent surface. Regardless of the surface difference, indent 13 was never shown to contain any twinning.

The first difference seen between the two indents is in the diffraction patterns seen in Figures 5.14a and c). These DPs show that while the surfaces surrounding the indents are similar, below the surface the operative deformation mechanism differ wildly. In the case of indent 6, the diffraction pattern is smeared and dotted with spots of a multitude of orientations. The superposition of multiple diffraction patterns shows itself within the DF images in Figure 5.14b), where the microstructure of the indent consists of multitudes of smaller twinned zones in a variety of orientations. This is consistent with the behavior of twins seen in the macroscopic compression samples at elevated strains in Chapter 2, where twins were formed from many smaller twins aggregating together to form a larger twinned regime. Most peculiarly seen in Indent 13, Figures 5.14c,d), is that unlike Indent 6 the microstructure underneath the indent surface is completely devoid of any twins. While the diffraction spots seen in Figure 5.14c) are defuse with a large halo, an effect most likely due to thickness and some contamination of Ga^+ ions. The imaging direction is clearly a [0001] zone along the c-axis. A higher magnification image of the indent surface in Figure 5.14d) shows extensive contrast from a large number of dislocations entangling and clustering near the surface. These two indents elucidate the

deficiency of using Berkovich indentation in order to characterize crystallographic response to mechanical deformation. While the EBSD maps in Figure 5.13c) and d) show relatively similar orientations of the indented grains, with both indents lying on a grain boundary of comparable misorientation. With the complicated nature of stress states below a Berkovich tip, it is extremely difficult to predict the mechanical behavior of a very ductile metal that deforms through twinning, like rhenium, before indentation has been completed.

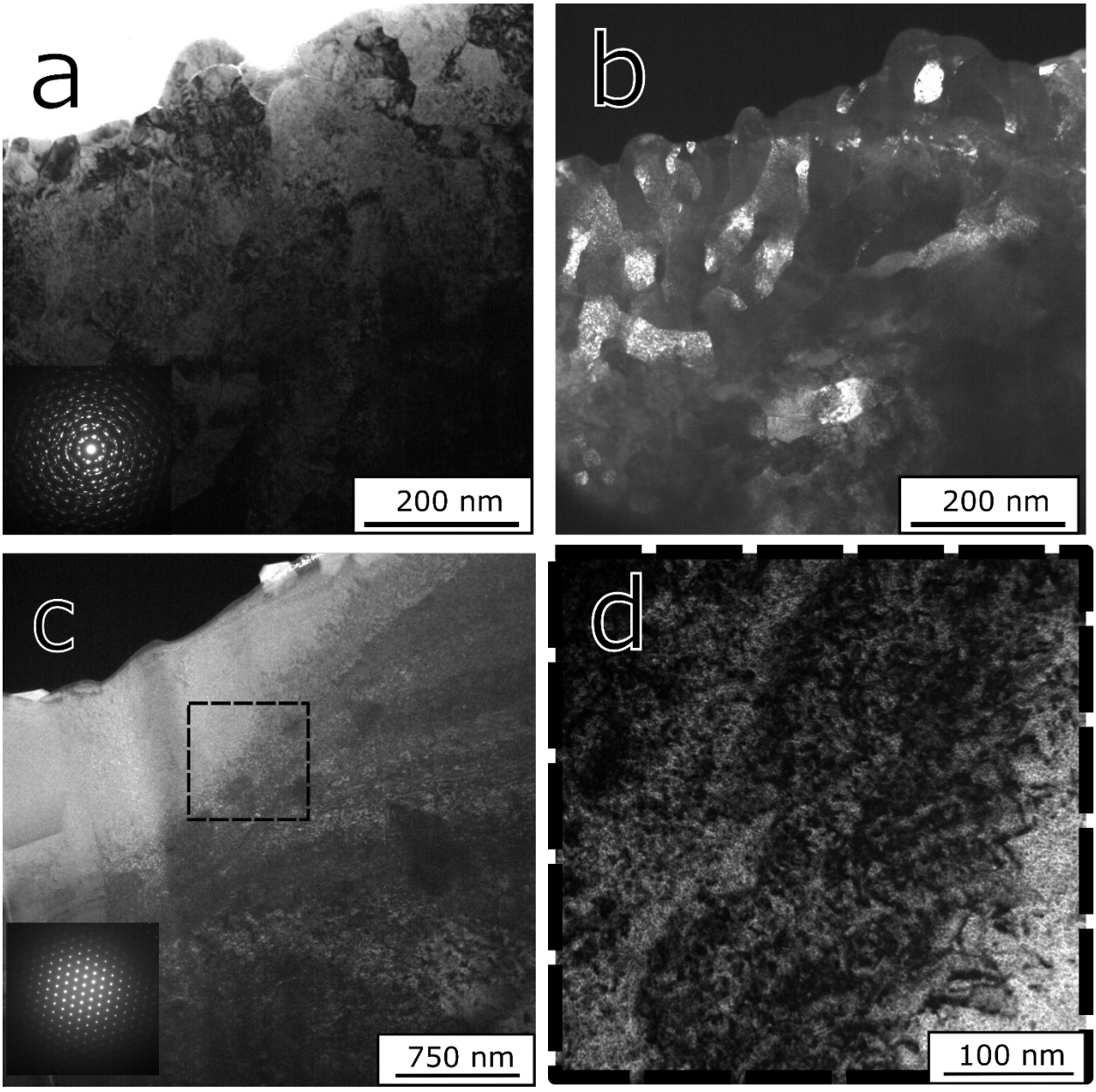

Figure 5.14: TEM lift-outs produced using focused ion beam gallium ion milling from indent 6 a,b) and 13 c,d), seen previously through EBSD in Figure 5.14 c and d) and respectively. The BF image from indent 3 shows a cellular structure lacking ample dislocations, with the DF image in b) showing that the indent consists of an aggregate twin structure similar to what was seen in the 5% strain sample during compression testing. The DF image in c) shows the indent as well as the grain boundary at the

bottom of the indent. d) shows a heavily dislocated region below the indent surface with no twinning present.

With what we have seen from Berkovich indentation as an initial reference, it can already be seen that plastic deformation as well as crystallographic response is best described through spherical indentation with the accompanying indentation stress-strain curves, instead of Berkovich indentation, because well-defined analytical solutions are available for stress states underneath the indentation tip. The same methods used for characterizing the crystal structures induced through Berkovich indentation can be used with equal efficacy on spherical indentation, with the caveat that this more closely represents the types of deformation structures one would see in macroscopic compression. The indentation stress-strain procedure was fully analysed, as stated previously in this chapter, with the accompanying the strain-bursts and stress-drops seen in the indentation stress strain curves induced through twinning and dislocation motion. Through examining a large selections of spherical indentation sites, Figure 5.15, it is clear that surface deformation twins are much less common than was observed using Berkovich indentation. When looking at spherical indents in the Ru based chemically complex alloys, it was important to observe a large number of indents investigated, with many crystal orientations, in order to fully ascertain the presence of deformation twinning using surface based EBSD.

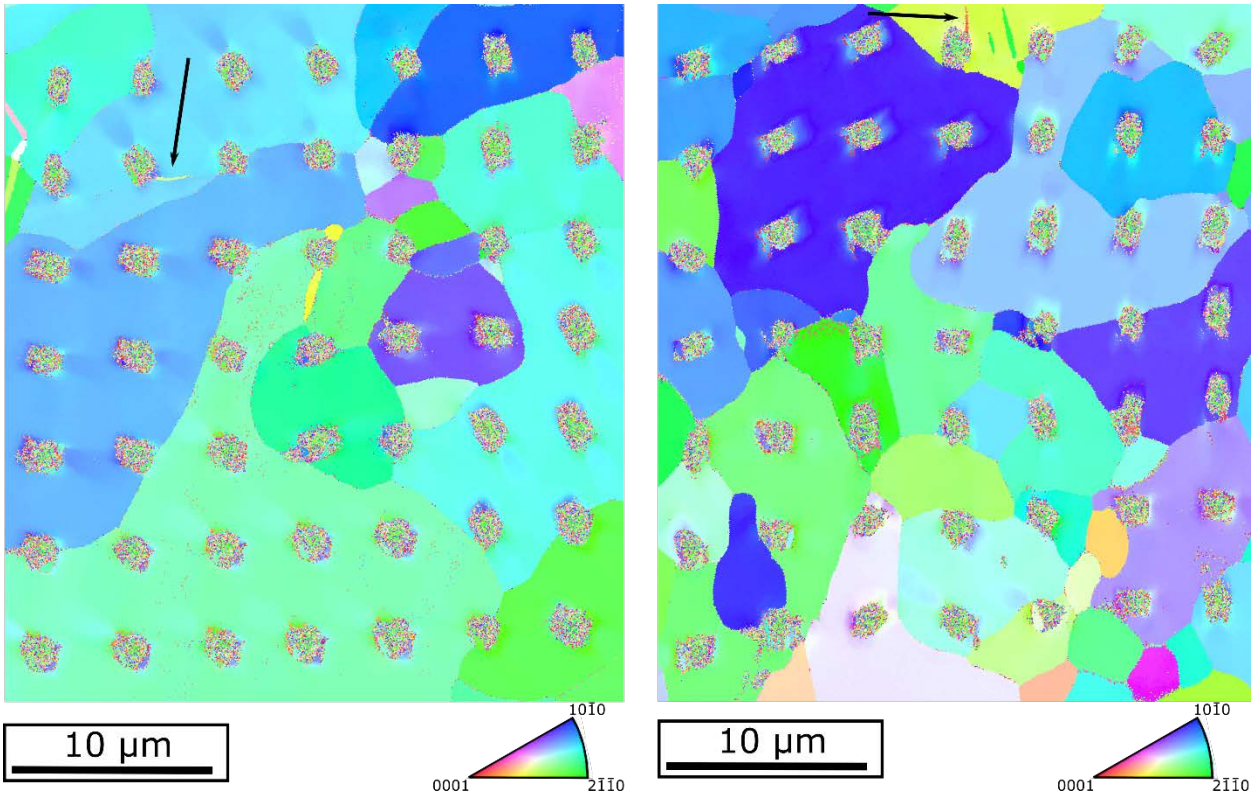

Figure 5.15: Two large sets of EBSD maps for spherical indents of a swaged and annealed Re rod sample, with the indent direction being parallel to the swaged rod direction. Note that the largely prismatic texture has resulted in very few sites with noticeable surface twinning, which are marked with arrows. While the stress state for spherical indentation is less complicated than for Berkovich indentation, the amount of surface twinning seen is less extensive for similar orientations than for Berkovich indentation.

Multiple EBSD scans were performed on the Ru-Ta-W alloy 1-2 using selected phases of Ru, Re, and an iron based intermetallic σ phase, with the lattice constants corrected based on previous XRD data, used to determine the crystal structure present in the two-phase alloys. It can be quickly seen that for adjacent ligaments within the 2-phase region of alloy 1-2, large portions of single orientation tetragonal phase are accompanied by single phase HCP regions. Indents were located in both tetragonal and HCP regions. It can be seen for the Ru-Ta-W sample, that the general surface quality and indexing is poor, with large regions of secondary crystal as well as misorientation bands. For Figure 5.16, a large amount of micro-grained regions were indexed and investigated for a distinct crystallographic relationship between the apparent matrix and micro-grain. These micro-grains, while appearing to be consistent with deformation twins occurring during polishing, have no distinct crystallographic relationship to the larger grains within which they are embedded, precluding them from being deformation twins. With the knowledge that large regions of HCP phase contain large grains with imbedded micro-grains, when evaluating the twinning effect of indentation, great care must be taken in order to not assume micro-grains surrounding or underneath an indent are due to deformation twinning.

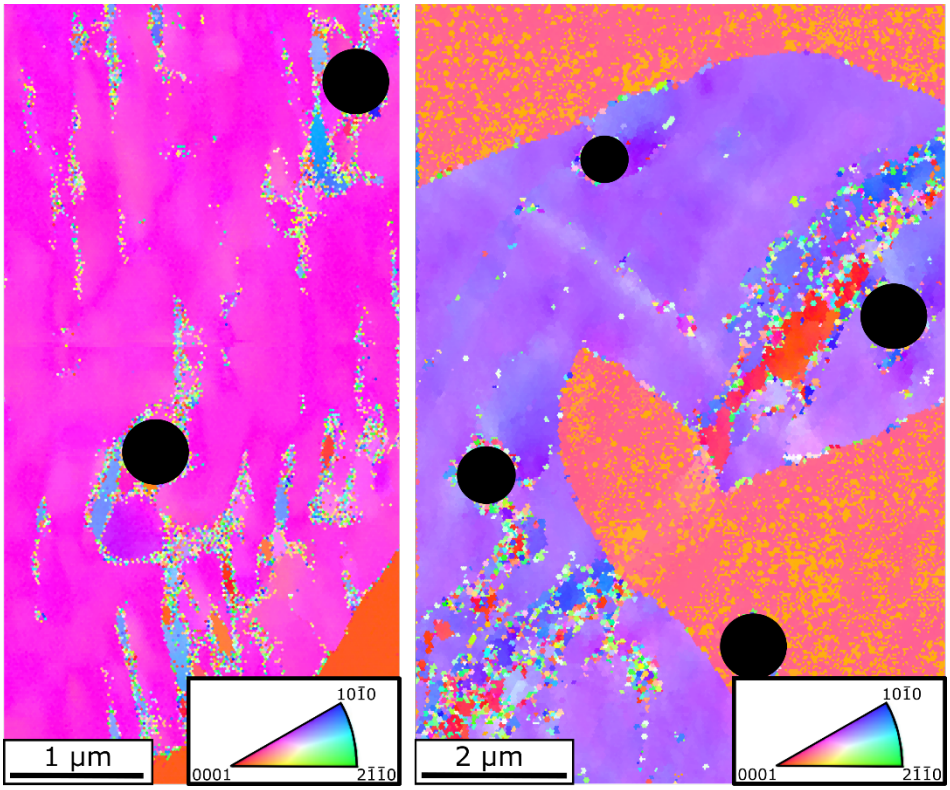

Figure 5.16: Overview EBSD maps for indentation in the Ru-Ta-W alloy 1-2. Note that in the two large regions, despite the heavy surface contamination (resulting in poor indexing), the HCP single phase can be distinctly contrasted with the tetragonal phase despite signal noise. It should be noted that small micro-grained areas are not all due to deformation twining, as the "matrix" does not have any crystallographic relationship to the micro-grains. Black circles mark the location of indents, as it can be difficult to determine the indent positions purely from the EBSD map.

Another set of indents analyzed using EBSD had a nearly pyramidal orientation normal to the surface, seen Figure 5.17a,b). With this orientation any applied compressive stress applied along the plane normal direction the formation of a tensile twin along the c-axis direction should reduce the local strain surrounding the indent, however much of the plastic deformation can be accommodated through dislocation plasticity and it is not generally not easily predictable when an indent will twin. As was seen previously in the indents with Rhenium in Figure 5.15, only a few indents out of the large set of indents performed on Re would show any trace of the indent at the surface level. This same behavior is also seen in the HCP phase of alloy 1-2, where multiple indents seen in Figure 5.17a) show no distinct sign of twins around the indents, however there is much plastic deformation, seen as crystal misorientations, surrounding the indent.

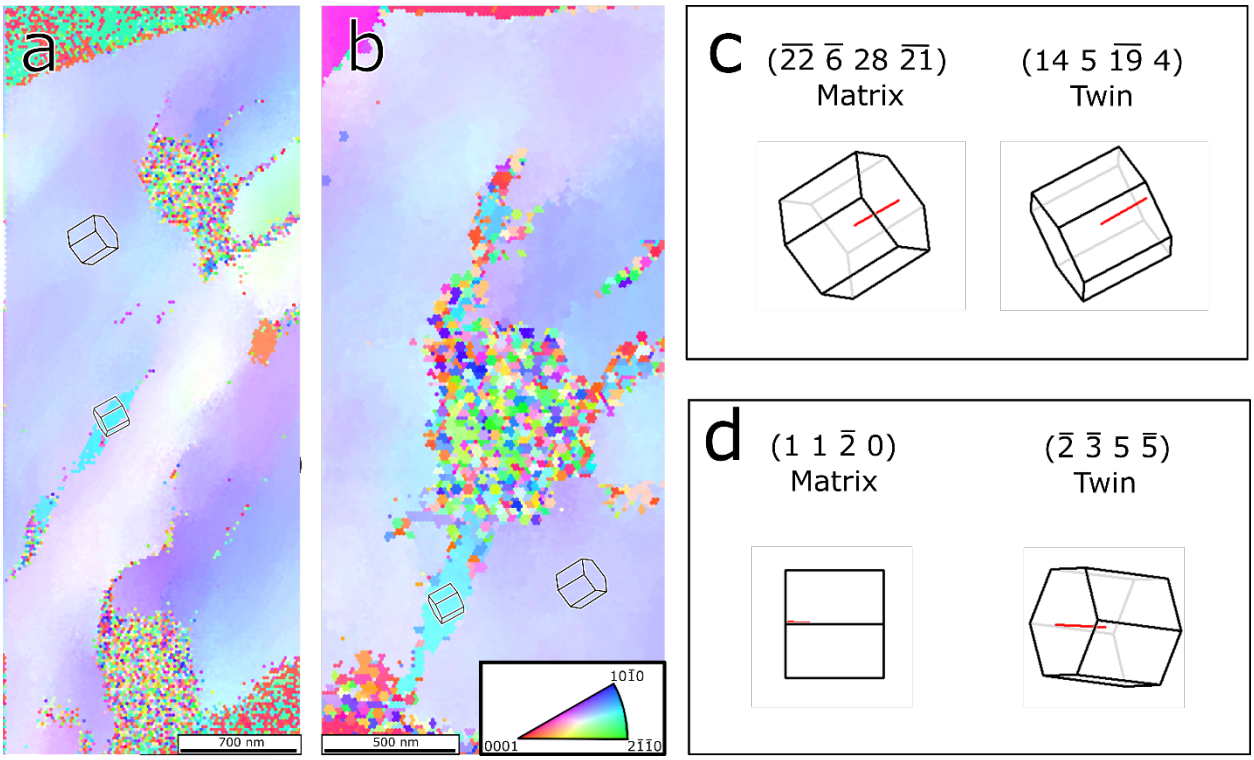

Figure 5.17: a) EBSD map showing two indents with heavy plastic deformation surrounding the indentation tip, but no twinning. b) EBSD of indent showing $\{11\bar{2}1\}\langle11\bar{2}6\rangle$ type twin transmitting across the indent. c) Matrix and twin crystal orientations given directly from the EBSD software. Crystallographic direction indexes given by the software are oriented out of plane. d) Re-oriented matrix-twin crystal relationship to view the matrix along a $\langle10\bar{1}0\rangle$ direction to best see the resulting twinning plane, to be given as $\{\bar{2}\bar{3}55\bar{5}\}$. The unique index of this plane is due to dislocation plasticity that has caused small misorientations moving the twin plane from the ideal orientation of $\{11\bar{2}1\}\langle11\bar{2}6\rangle$.

For the indent seen in Figure 5.17b), the inset crystal orientation wireframes show that there is a secondary crystal orientation extending from the indent toward the top and bottom of the EBSD map. Figure 5.17c) shows the plane index for the matrix and crystal as they appear within the sample. Looking for twin symmetry using the relationship between twin and matrix is not easily interpretable. The large amount of dislocation plasticity as well as the random nature of

the initial crystal's orientation provides very obscure plane indexes that do not obviously describe the crystallographic relationship between matrix and twin. Using the EBSD analysis software, one can rotate the crystal toward the orientation along which will best describe the twin matrix relationship. In the case of the $\{11\bar{2}1\}\langle 11\bar{2}6\rangle$ twin, the rotation axis around which the twin relationship can be easily seen is one of the $\langle 11\bar{2}0\rangle$ directions. Figure 5.17d) shows the orientation of relationship between twin and matrix, with the twin having the normal plane of $(\bar{2}\bar{3}5\bar{5})$ which is a non-standard twinning plane. However due to the large amount of plastic deformation surrounding the indent tip, as well as the tendency for EBSD software to give high-value non-standard indexes, it can be readily assumed based upon this that the relationship between twin and matrix is that of the $\{11\bar{2}1\}\langle 11\bar{2}6\rangle$ twin, as this is the closest possible twin plane within the HCP system.

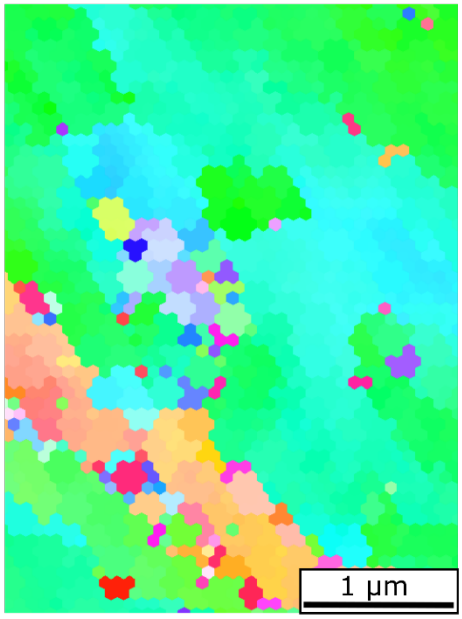

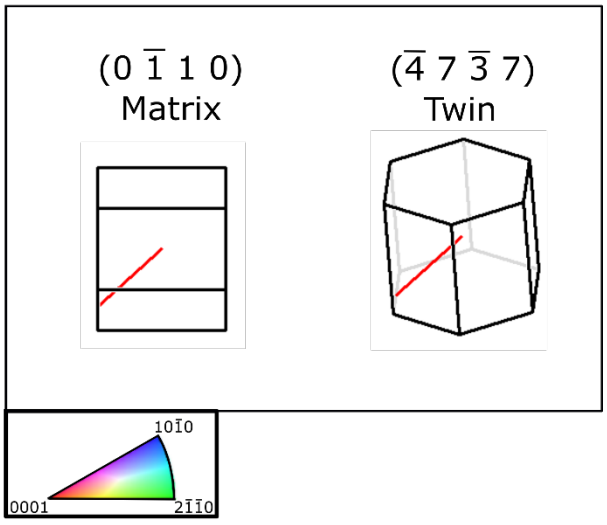

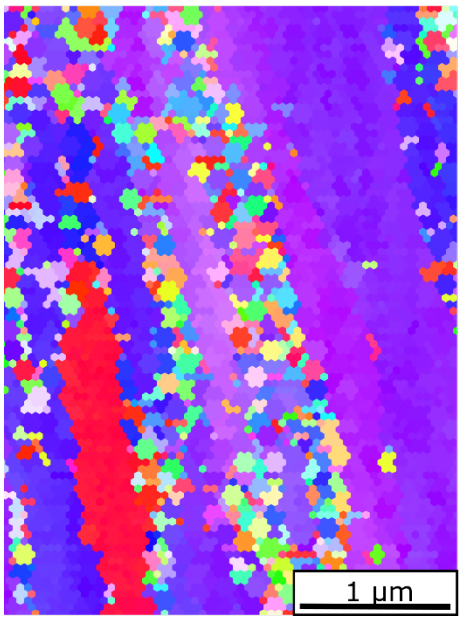

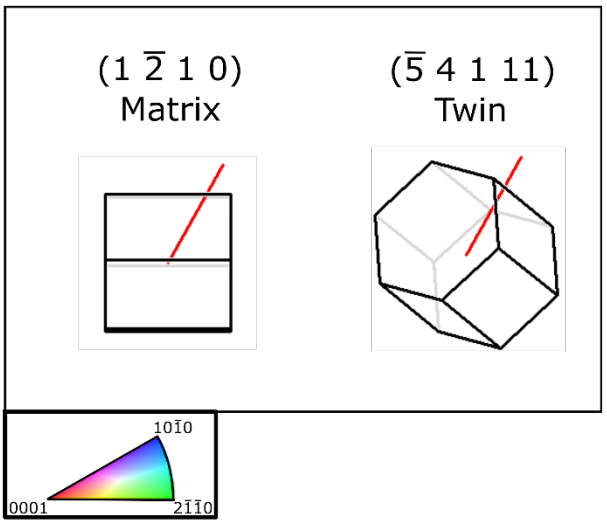

Figure 5.18: Two EBSD maps of alloy 3-2 (top) and alloy 3-4 (bottom). Surface quality for EBSD acquisition was poor, however glancing angle FIB milling was used in order to remove the unindexable top layer of the samples. Alloy 3-2 shows $\{11\bar{2}2\}\langle 11\bar{2}3\rangle$ type twining, and alloy 3-4 shows $\{10\bar{1}2\}\langle 10\bar{1}1\rangle$ type twinning as active twin planes for these two orientations.

EBSD scans were also performed on the Mo containing chemically complex alloys. The alloys chosen for further investigation were alloy 3-2 and the unannealed alloy 3-4. Both alloys had extremely low EBSD signal, similar to metals which form an extensive oxide layer. Since alloy 3-4 showed signs of having WO_2 within the XRD scans, the low quality of the surface for EBSD is likely due to some oxide formation, or a reaction of Mo or W with a solvent used during polishing. In order to successfully EBSD the surface of the indents, glancing angle FIB preparation was used in order remove the surface obfuscating the EBSD signal. An angle of 4° from parallel was chosen and roughly 10nm of material was removed from the surface of alloy 3-4 and nominally 60nm was removed from the surface of alloy 3-2. With the obfuscating layer removed, large scale EBSD patterns were taken of the surface, with Figure 5.18 showing the IPF maps surrounding single indents. The crystal orientations seen next to the IPF maps show the relationship of the twin and matrix that best shows the twinning relationship. This shows that alloy 3-2 has the $\{11\bar{2}2\}\langle 11\bar{2}3\rangle$ type twin and alloy 3-4 has the $\{10\bar{1}2\}\langle 10\bar{1}1\rangle$ twin activated near and around the indentation site.

This set of EBSD data is a very promising observation for the future of Re replacement alloy development, as the initial theory describing a d-band filling of Re being an important component in formation of $\{11\bar{2}1\}\langle 11\bar{2}6\rangle$ twins. While not every twin system was seen in each alloy, the sum of the alloys have shown all the twinning systems observed in pure Re during Berkovich indentation. It should be noted that of the sparse amount of research performed on pure Ru, it has been reported (albeit through a personal communication in the cited reference) that twinning occurs in Ru on the $\{11\bar{2}1\}$, $\{11\bar{2}2\}$, $\{10\bar{1}2\}$, and occasionally $\{10\bar{1}2\}$ planes (94). With this in mind, future investigations will be needed to determine if $\{11\bar{2}1\}\langle 11\bar{2}6\rangle$ twins become more or less favorable during macroscopic tension testing using the chemically complex alloys when compared to pure Ruthenium.

5.3. Conclusions and Future Developments

The effects of alloying ruthenium with tungsten, tantalum, and molybdenum were investigated, using powder x-ray diffraction to determine crystal structures and the mechanical properties of all alloys developed investigated using a spherical indentation stress-strain method. It was shown that for the three chemically complex alloy systems (Ru-Ta-W, Ru-W-Mo, and Ru-Ta-W-Mo), an HCP phase could be formed with a significantly high solubility limit for tantalum, tungsten and molybdenum. In general, it was seen that tantalum would lower solute solubility of the HCP single phase, while molybdenum would show improved solute solubility, with tungsten generally used as a balance when increasing solute content. The 4-component chemically complex Ru 51.2 -Ta 6.4-W 12.5 - Mo 30.0 (compositions in at.%) alloy was shown to be near the solubility limit of the HCP phase, proving to be the composition with the lowest Ru content and having completely HCP single phase after annealing at 1850 °C.

Screening for the changes in mechanical properties has been performed using indentation stress-strain analysis. Each alloy system has shown great mechanical property improvements

over pure Ru, which is extremely hard and brittle with extensive cracking around the indentation tip. Both Berkovich and spherical indentation was performed on all alloys, with indents in pure Re and Ru used as a basis for comparison Tungsten was shown to provide a consistent alloy basis between the three alloying systems, with systems containing low tungsten content behaving much more poorly than systems with low tantalum. In general, low level additions of tantalum were seen to improve the mechanical properties significantly, however significant additions of tantalum generally lead to the formation of additional phases and reduced mechanical response. With molybdenum seen greatly increasing the solubility of all solute elements within the HCP alloys, the addition of Mo into any system usually accompanied a much larger concentration of solute atoms, further improving the mechanical properties of any alloy by reducing Ru content.

It was concluded empirically through stress strain curve analysis based on the compositions tested, that a ratio of 4:1 W:Ta or 2:2:1 W:Mo:Ta had the best balance between the improvements made through additional solute content and improvements through tantalum addition. Three select alloys were chosen for future developments into the uniaxial tensile behavior at macroscopic industrial scales. Based on the alloys tested here the Ru 73.1 -Ta 5.5 - W 21.4 , Ru 59.6 -W 11.9 -Mo 28.5 , and Ru 51.2 -Ta 6.4-W 12.5 - Mo 30.0 (all compositions in at.%) are best candidate alloys for improved macroscopic properties. Further developments could also be achieved with the addition of iron or rhenium as a fifth alloying element, either of which could simultaneously improve strength and ductility while increasing solute solubility in an HCP matrix, solidly enhancing the chemical complexity of these alloys to reach high-entropy states.

EBSD scans of the HCP alloys showed that the alloys at the solubility limit of Ta and W into Ru had significant twinning present around the indentation tips. The twins seen were shown to be of the $\{11\bar{2}1\}\langle 11\bar{2}6\rangle$ type family most commonly seen in pure Re. The observation of these twins is extremely promising for the future of alloy development theory, as the predicted cause of this twin in Re was d-band filling, a variable for which the alloy development was based upon.

Chapter 6

Conclusions

6.1. Research Summaries

Rhenium is an extraordinarily unique material; with an acute rarity that is severely unfortunate. Were Re to be much more abundant much more knowledge would be available about this wonderous material. Knowledge which is currently sorely lacking. The work done here provides insights into the complex microstructure evolution of Re. The compression and tension asymmetries were analyses using multiple advanced microscopy techniques. Due to the rarity of Re, great strides have been made into the creation of a much cheaper replacement alloy from the far more abundant transition metals Ru, Ta, W, and Mo. However, despite the improvements made in understanding both Re and developing high performance transition metal alloys that can mimic the properties of pure Re, much more work must be performed on this area of metallurgy.

6.1.1. Macroscopic Compression of Rhenium

The evolution of the rhenium microstructure during uniaxial compression has been described. Sample texture was shown to be a large determinant of the operative deformation mechanism for all samples tested, with grains having c-axis near parallel to the compression axis showing no twinning. The post-compression microstructure was shown to consist of $\{11\bar{2}1\}\langle 11\bar{2}6\rangle$ twins, with basal, prismatic and some pyramidal slip bands only recognizable during the initial deformation. Slip bands were quickly overshadowed by twinning. Due to the sample texture and large amount of strain accommodation by $\{11\bar{2}1\}\langle 11\bar{2}6\rangle$ twins, twinning becomes the dominant deformation mode, with nearly half of the available twins activating. The ability for twins to accommodate strain was further improved by the unique propensity for twins in Rhenium to bypass twin and grain boundaries, increasing the number of active twins per grain.

TEM investigations of the twin structure and dislocation-twin interactions has confirmed the EBSD result of relatively low dislocation activity for all strained samples. Low strain samples showed atomically thin twins and larger twins aggregated from many smaller twins, unpopulated with dislocations. As strain increased, the matrix surrounding twins were populated by <a> type dislocations impeded from transmitting through the twin boundaries, as is common in TWIP steels. As twinning saturated the crystal, twins were seen to be regularly spaced apart without an extensive matrix dislocation population, showing that twins boundaries are not mobile but resulted in new twin formation instead of twin growth. The aggregate twin nature and lack of twin growth at the smallest length scales is explained by high twin boundary stability of $\{11\bar{2}1\}\langle 11\bar{2}6\rangle$ twins coupled with an anomalously low twin boundary energy.

6.1.2. Macroscopic Tension of Rhenium

Tension tests were performed systematically on Re to understand effect of microstructure on the high work hardening rate. Re tension samples were strained to systematically chosen total strain amounts and sectioned in order to understand the microstructure present in at each point of

the deformation profile. Through the use of multiple microscopy techniques, a full understanding of the typical microstructures in rhenium as a function of strain has been achieved. The use of EBSD has shown that the overall undeformed microstructure had a large grains size distribution, with a very $\{11\bar{2}1\}\langle 11\bar{2}6\rangle$ twin unfavorable microstructure under tension. Twin area fraction plateaued once one third of the failure strain was achieved. After twin saturation, all changes to the deformed microstructure was seen as increased interior grain misorientations. Grains showing extensive large twins had large misorientations in between the twins due to basal slip activity, as determined by the Schmidt factor favorably seen in the EBSD maps and later confirmed using TEM imaging. Finally, EBSD had shown that prismatic and pyramidal slip activated appreciably only at strain values above half of the failure strain.

Conventional TEM "G dot B" analysis was performed to understand the dislocation structures as well as the planes upon which dislocation slip operated. <a> type $\vec{b} = [11\bar{2}0]$ screw dislocations operated on the basal planes in loosely aligned slip bands. Only <a> type dislocations were seen at low strains generally between twin boundaries. At failure stresses, <a> type $\vec{b} = [11\bar{2}0]$ basal screw dislocations were again observed in dislocation slip bands. <c+a> type $\vec{b} = [11\bar{2}3]$ pyramidal screw dislocations which formed tangled dislocation nets interfering with <a> type glide was observed. HAADF STEM imaging was used in order to view twin boundaries without dynamical contrast as well as dislocations passing through twin boundaries. The morphology of tension induced $\{11\bar{2}1\}\langle 11\bar{2}6\rangle$ twins was more representative of classical twin structures involving well defined twin boundaries surrounding a region of crystal with a single new orientation. This did not represent the $\{11\bar{2}1\}\langle 11\bar{2}6\rangle$ type twins seen in compression which consisted of twin aggregates. This compression-tension asymmetry is likely due to the twin favorability of the microstructure forcing the creation of many more twins during compression. Twin transmission with $\{11\bar{2}1\}\langle 11\bar{2}6\rangle$ changing twin plane between parent and matrix orientations was observed. Multiple twin systems with twins growing out of twin boundaries was observed, with the TEM observations confirming the observations made using purely EBSD maps for analysis.

6.1.3. In-Situ Tension of Rhenium

In-situ straining was performed on rhenium both at room temperature and at 920°C. The samples used all had a foil texture which consisted of basal planes lying parallel to the loading direction. This texture suppressed possible $\{11\bar{2}1\}\langle 11\bar{2}6\rangle$ twinning, while exaggerating basal or prismatic dislocation activity. Two main samples were successfully tested, with both confirming the observation that <a> type $\langle 11\bar{2}0\rangle$ basal dislocations were the dominant mechanism during tensile straining. Samples were all tested both at room temperature and elevated temperature in order to find any differences in behavior based on temperature. Dislocation motion was observed with video, with the general dislocation motion consisting of a semi "jerky" crawl of loosely aligned dislocations. The starting and stopping motion of dislocations is indicative of an "unlocking" mechanism for dislocation motion to become activated, as detailed by Clouet in Ti in contrast to the smooth motion of Zr. However as the dislocation motion was not completely "jerky" as in Ti, The energy barrier for Re dislocation motion must be significantly smaller than that in Ti.The only appreciable effect that elevating temperature to 920°C had on dislocation motion was to possibly increase the number of active dislocations, something that would also occurs naturally near the end of a test. As more and more sources are activated and more

dislocations are required to accommodate strain, dislocation would naturally increase. As such tests at 920°C to observe significant differences in behavior between room temperature and elevated temperatures was insufficient to draw extensive conclusions.

6.1.4. Rhenium Replacement Alloy Development

The effects of alloying ruthenium with tungsten, tantalum, and molybdenum were investigated, using powder x-ray diffraction to determine crystal structures. A novel indentation stress-strain method was developed as a method for mechanical property screening, using indents on pure Re and Ru as a basis for comparison. It was shown that for the three chemically complex alloy systems (Ru-Ta-W, Ru-W-Mo, and Ru-Ta-W-Mo), an HCP phase could be formed with a significantly high solubility limit for tantalum, tungsten and molybdenum. In general, it was seen that increasing tantalum would reduce solute solubility, while molybdenum would show improved solute solubility. Tungsten was generally used as a balance when increasing solute content, behaving interchangeably with Mo. The 4-component chemically complex Ru 51.2 -Ta 6.4-W 12.5 - Mo 30.0 (compositions in at.%) alloy was shown to be near the solubility limit of the HCP phase, proving to be the composition with the lowest Ru content and having completely HCP single phase after annealing at 1850 °C.

Screening for the changes in mechanical properties was performed using indentation stress-strain analysis. Each alloy system has shown great mechanical property improvements over pure Ru. Through initial indentation tests, Ru was seen to be extremely hard and brittle with extensive cracking around the indentation tip. Both Berkovich and spherical indentation was performed on all alloys, with indents in pure Re and Ru used as a basis for comparison Tungsten was shown to provide a consistent improvement to Ru alloy behavior throughout all three alloying systems, with systems containing low tungsten content behaving much more poorly than systems with low tantalum. In general, low level addition of tantalum were seen to improve the mechanical properties significantly, however significant additions of tantalum generally lead to the formation of additional phases and reduced mechanical response. With molybdenum seen greatly increasing the solubility of all solute elements within the HCP alloys, the addition of Mo into any system usually accompanied a much larger concentration of solute atoms, further improving the mechanical properties of any alloy by reducing Ru content. It was concluded empirically through indentation stress-strain curve analysis based on the compositions tested, that a ratio of 4:1 W:Ta or 2:2:1 W:Mo:Ta had the best balance between the improvements made through additional solute content and improvements through tantalum addition.

EBSD scan were performed on all of the alloy systems with compositions near the solubility limit. Indents within the Ru-Ta-W system had the unique $\{11\bar{2}1\}\langle 11\bar{2}6\rangle$ twins seen near the indent tip. The Ru-Mo-W system showed $\{11\bar{2}2\}\langle 11\bar{2}3\rangle$ type twins underneath the indents. Finally, the Ru-Ta-W-Mo system showed $\{10\bar{1}2\}\langle 10\bar{1}1\rangle$ twins beneath the indent surface. This makes all of the twin variants that were observed in this work when indenting Re also observable in the designed chemically complex alloys. The observation of these twins is extremely promising for the future of alloy development theory, as the predicted cause of this twin in Re was d-band filling, a variable for which the alloy development was based upon.

6.2. Future Work

Much progress has been made in understanding the mechanisms that control the deformation of Re, however many avenues of detailed investigation have been left open. Further research is required into the twin transmission mechanisms seen in the large Re grains, using both in-situ and high-resolution TEM (HRTEM) techniques. Confirming the experimentally predicted twin boundary structure using HRTEM or HRSTEM will further validate the theoretical rationale for alloy development. The asymmetries seen in the $\{11\bar{2}1\}\langle 11\bar{2}6\rangle$ twins formed in compression compared to those formed in tension leave much room for further analysis. Additionally, the effect of twin boundary stability and dislocation density along the twin boundaries on the work hardening rates requires further investigation in samples deformed in tension. Microstructural analysis of the creep properties of Re and the effects on the microstructure could provide further insights into the roll $\{11\bar{2}1\}\langle 11\bar{2}6\rangle$ twins play in accommodating deformation. As rhenium is mainly used at high temperatures, the microstructural analysis preformed here should be repeated, with temperature being the operative variable while straining samples to fracture.

Future in-situ experiments should focus on the mechanisms which control the formation of twins, ideally viewing the formation of a $\{11\bar{2}1\}\langle 11\bar{2}6\rangle$ at high resolution would be ideal. As texture played a key role in the formation of twin in Re, new experiments with samples machined from bulk arc-melted samples would remove the heavy texture, however at great cost in materials and machining. This would allow for more observable grains with orientations which favor twin formation, and at high strains flow of <c+a> dislocations, which were not yet observed *in-situ*. Finally, a new sample stage would have to be created, likely involving large currents passing through the sample for joule heating, in order to test an *in-situ* sample at temperatures high enough to have significant effects on deformation behavior.

Three chemically complex alloys were chosen to be used for future experiments involving macroscopic uniaxial tension. Based on the alloys tested here the Ru 62 - Ta 8 - W 32, Ru 55 - W 20 - Mo 25, and Ru 45 - Ta 10 - W 20 - Mo 25 (all compositions in at.%) are best candidate alloys to be tested using macroscopic uniaxial tension. Further developments could also be achieved with the addition of iron or rhenium as a fifth alloying element, either of which could simultaneously improve strength and ductility while increasing solute solubility in an HCP matrix, solidly enhancing the chemical complexity of these alloys to reach high-entropy states. Using uniaxial tension, as was done in Chapter 3, allows for the opportunity to investigate the deformation microstructure of the chemically complex alloys using advanced EBSD and TEM techniques performed throughout this work. As with pure rhenium itself, once the alloy with optimum performance has been measured, high temperature testing will be required to determine how closely the chemically complex alloy replicates Re.

References

1. *Twinning and the ductility of magnesium alloys: Part I. 'Tension' twins.* **Barnett, MR.** 1, 2007, Materials Science and Engineering: A, Vol. 464, pp. 1-7.
2. *Twinning and the ductility of magnesium alloys: Part II. 'Contraction' twins.* **Barnett, MR.** 1, 2007, Materials Science and Engineering: A, Vol. 464, pp. 8-16.
3. *The crystallography and deformation modes of hexagonal close-packed metals.* **Partridge, PG.** 1, 1967, Metallurgical reviews, Vol. 12, pp. 169-194.
4. *Twin boundary interactions with grain boundaries investigated in pure rhenium.* **Kacher, Josh and Minor, Andrew M.** 2014, Acta Materialia, Vol. 81, pp. 1-8.
5. *Deformation twinning in rhenium single crystals.* **Jeffery, RA and Smith, E.** 126, 1966, Philosophical Magazine, Vol. 13, pp. 1163-1168.
6. *Deformation Twinning of Rhenium.* **Peter, K and Lagerlof, D and Xiao, S-Q and Bryskin, B and Carlen, J-C.** 1993, Twinning in Advanced Materials, pp. 475-482.
7. *Deformation Mechanisms and Work Hardening in Rhenium.* **Churchman, AT.** 2, 1960, TRANSACTIONS OF THE AMERICAN INSTITUTE OF MINING AND METALLURGICAL ENGINEERS, Vol. 218, pp. 262-270.
8. *Physical and mechanical properties of rhenium.* **Sims, Chester T and Craighead, Charles M and Jaffee, Robert I.** 1, 1955, JOM, Vol. 7, pp. 168-179.
9. *Electronic origins of anomalous twin boundary energies in hexagonal close packed transition metals.* **de Jong, Maarten and Kacher, J and Sluiter, MHF and Qi, L and Olmsted, DL and Van de Walle, A and Morris Jr, JW and Minor, AM and Asta, M.** 6, 2015, Physical review letters, Vol. 115.
10. *Ab initio study of metastability in refractory metal based systems.* **Berne, C and Pasturel, A and Sluiter, M and Vinet, B.** 8, 1999, Physical review letters, Vol. 83, p. 1621.
11. **Reimer, Ludwig.** *Scanning electron microscopy: physics of image formation and microanalysis.* s.l. : IOP Publishing, 2000.
12. **Schwartz, Adam J and Kumar, Mukul and Adams, Brent L and Field, David P.** *Electron backscatter diffraction in materials science.* s.l. : Springer, 2009.
13. *On the generality of the relationship among contact stiffness, contact area, and elastic modulus during indentation.* **Pharr, GM and Oliver, WC and Brotzen, FR.** 3, 1992, Journal of materials research, Vol. 7, pp. 613-617.
14. *Mathematica Diffraction Code.* **Poschmann, Max.** s.l. : Personal Communications, 2017.
15. *Vol. 3: Alloy Phase Diagrams.* **Handbook, ASM.** 1992, Vol. 9.
16. *Ternary Phase Diagrams.* **Walle, Axel van de.** s.l. : Perosonal Communications, 2017.
17. *High temperature thruster technology for spacecraft propulsion.* **Schneider, Steven J.** s.l. : Acta Astronautica, 1992, Vol. 28, pp. 115-125.
18. *Evaluation of properties and special features for high-temperature applications of rhenium.* **Bryskin, Boris D.** s.l. : Proceedings of the ninth symposium on space nuclear power systems, 1992.
19. *Advances in the extraction, processing and application of refractory metals.* **Wittenauer, Jerry and Liddell, KNona.** 7, 1991, JOM, Vol. 43, pp. 6-7.
20. *Volume 2.* **Handbook, Aerospace Structural Metals.** 2005, Properties and Selection: Nonferrous Alloys and Special-Purpous Materials, Vol. 1.

21. *Nonferrous alloys.* **Klopp, WD.** s.l. : Aerospace Structural Metals Handbook, Code, 1984, Vol. 4214, pp. 1-18.
22. *Rhenium-a unique rare metal.* **Carlen, Jan-C and Bryskin, Boris D.** 6, s.l. : Taylor & Francis, 1994, Vol. 9.
23. *Rhenium Metal Powder Quote.* **Aldrich, Sigma.** s.l. : Personal Correspondence, 2017.
24. **Kelly, Anthony A and Knowles, Kevin M.** *Crystallography and crystal defects.* 2nd. s.l. : John Wiley \& Sons, 2012.
25. *Indentation modulus of elastically anisotropic half spaces.* **Vlassak, Joost J and Nix, WD.** 1045-1056, 1993, Philosophical Magazine A, Vol. 67, p. 5.
26. *Measuring the elastic properties of anisotropic materials by means of indentation experiments.* **Vlassak, Joost J and Nix, WD.** 8, 1994, Journal of the Mechanics and Physics of Solids, Vol. 42, pp. 1223-1245.
27. *Therapeutic efficiency of rhenium-188-HEDP in human prostate cancer skeletal metastases.* **Liepe, K and Kropp, J and Runge, R and Kotzerke, J.** 4, s.l. : British journal of cancer, 2003, Vol. 89. 625-629.
28. *Powder processing and the fabrication of rhenium.* **Bryskin, Boris D and Danek, Frank C.** 7, 1991, JOM, Vol. 43, pp. 24-26.
29. *The properties and applications of rhenium produced by CVD.* **Sherman, Andrew J and Tuffias, Robert H and Kaplan, Richard B.** 7, 1991, JOM, Vol. 43, pp. 20-23.
30. *Magnesium: properties-applications-potential.* **Mordike, BL and Ebert, T.** 1, s.l. : Materials Science and Engineering: A, 2001, Vol. 302. 37-45.
31. *Vereinfachung kristallographischer Rechnungen in hexagonalen Gittern durch konsequente Benutzung des vierachsigen hexagonalen Koordinatensystems.* **Neumann, P.** 1, 1966, physica status solidi (b), Vol. 17.
32. *Kink formation and concomitant twin nucleation in Mg--Y.* **Wang, L and Sabisch, J and Lilleodden, ET.** s.l. : Scripta Materialia, 2016, Vol. 111. 68-71.
33. *Orientation dependent deformation by slip and twinning in magnesium during single crystal indentation.* **Zambaldi, Claudio and Zehnder, Christoffer and Raabe, Dierk.** s.l. : Acta Materialia, 2015, Vol. 91. 267-288.
34. *Basal and non-basal dislocation slip in Mg--Y.* **Sandlöbes, Stefanie and Friak, Martin and Neugebauer, Jörg and Raabe, Dierk.** s.l. : Materials Science and Engineering: A, 2013, Vol. 576. 61-68.
35. **Read, William Thornton.** *Dislocations in crystals.* s.l. : McGraw-Hill, 1953.
36. *CXXVIII. Stable dislocations in the common crystal lattices.* **Frank, FC and Nicholas, JF.** 358, 1953, The London, Edinburgh, and Dublin Philosophical Magazine and Journal of Science, Vol. 44, pp. 1213-1235.
37. *Deformation twinning.* **Christian, John Wyrill and Mahajan, Subhash.** 1, 1995, Progress in materials science, Vol. 39, pp. 1-157.
38. *A study of the stress state associated with twin nucleation and propagation in anisotropic materials.* **Lebensohn, RA and Tom{\'e}, CN.** 1, s.l. : Philosophical Magazine A, 1993, Vol. 67. 187-206.
39. *Volume 1.* **Handbook, Aerospace Structural Metals.** 2005, Properties and Selection: Irons, Steels, and High Performance Alloys, Vol. 1.
40. **Sarkar, Bibudhendra.** *Heavy metals in the environment.* s.l. : CRC Press, 2002.

41. **Sims, CT and Wyler, EN and Gaines, GB and Rosenbaum, DM.** *A SURVEY OF THE LITERATURE ON RHENIUM. Period Covered: June 1952 to January 1956.* s.l. : Battelle Memorial Inst., Columbus, Ohio, 1956.
42. *Microstructures and textures of pure magnesium deformed in plane-strain compression.* **Nave, Mark Denis and Barnett, Matthew Robert.** 9, s.l. : Scripta Materialia, 2004, Vol. 51. 881-885.
43. *Formation of zigzag-shaped {112} <111> Beta mechanical twins in Ti--24.5 Nb--0.7 Ta--2 Zr--1.4 O alloy.* **Yang, Y and Li, GP and Wang, H and Wu, SQ and Zhang, LC and Li, YL and Yang, K.** 5, s.l. : Scripta Materialia, 2012, Vol. 66. 211-214.
44. *Effect of deformation twinning on microstructure and texture evolution during cold rolling of CP-titanium.* **Chun, YB and Yu, SH and Semiatin, SL and Hwang, SK.** 1, s.l. : Materials Science and Engineering: A, 2005, Vol. 398. 209-219.
45. **Williams, David B and Carter, C Barry and Veyssiere, P.** *Transmission electron microscopy: a textbook for materials science.* s.l. : Springer, 1998.
46. *Compatibility of deformation in two-phase Ti-Al alloys: Dependence on microstructure and orientation relationships.* **Luster, J and Morris, MA.** 7, s.l. : Metallurgical and Materials Transactions A, 1995, Vol. 26. 1745-1756.
47. *Nucleation of paired twins at grain boundaries in titanium.* **Wang, L and Eisenlohr, P and Yang, Y and Bieler, TR and Crimp, MA.** 8, s.l. : Scripta Materialia, 2012, Vol. 63. 827-830.
48. *Comprehensive first-principles study of stable stacking faults in hcp metals.* **Yin, Binglun and Wu, Zhaoxuan and Curtin, WA.** 2017, Acta Materialia, Vol. 123, pp. 223-234.
49. *First-principles study of the structural and elastic properties of rhenium-based transition-metal alloys.* **de Jong, Maarten and Olmsted, David L and van de Walle, Axel and Asta, Mark.** 22, 2012, Physical Review B, Vol. 86.
50. *High manganese austenitic twinning induced plasticity steels: A review of the microstructure properties relationships.* **Bouaziz, Olivier and Allain, S and Scott, CP and Cugy, P and Barbier, D.** 4, 2011, Current opinion in solid state and materials science, Vol. 15, pp. 141-168.
51. *Tensile deformation behavior of mechanically stabilized Fe-Mn austenite.* **Tomota, Y and Strum, M and Morris, JW.** 6, s.l. : Metallurgical and Materials Transactions A, 1988, Vol. 19. 1563-1568.
52. *Martensitische Umwandlung in austenitischen mangan-kohlenstoff-stählen.* **Schumann, VH.** 10, s.l. : Neue Hütte, 1972, Vol. 17. 605-609.
53. *Microstructural dependence of Fe-high Mn tensile behavior.* **Tomota, Y and Strum, M and Morris, JW.** 3, s.l. : Metallurgical and Materials Transactions A, 1986, Vol. 17. 537-547.
54. *Stretch-Flangeability of High Mn TWIP steel.* **Chen, Lei and Kim, J-K and Kim, S-K and Kim, G-S and Chin, K-G and De Cooman, BC.** 7, s.l. : steel research international, 2010, Vol. 81. 552-568.
55. **Solutions, Correlated.** Vic-2D Reference Manual. *Correlated Solutions.* [Online] Correlated Solutions, 2009. [Cited: 11 05, 2017.] http://www.correlatedsolutions.com/installs/Vic-2D-2009-Manual.pdf.
56. **Walker, Perrin and Tarn, William H.** *CRC handbook of metal etchants.* s.l. : CRC press, 1990.
57. **Davim, Joao Paulo.** *Machining of complex sculptured surfaces.* s.l. : Springer, 2012.
58. *Quantification of surface damage of tool steels after EDM.* **Lee, LC and Lim, LC and Narayanan, V and Venkatesh, VC.** 4, s.l. : International Journal of Machine Tools and Manufacture, 1988, Vol. 28. 356-372.

59. *Strains, planes, and EBSD in materials science.* **Wilkinson, Angus J and Britton, T Ben.** 9, s.l. : Materials Today, 2012, Vol. 15, pp. 366-376.
60. *Elements of X-ray Diffraction.* **Cullity, Bernard Dennis and Weymouth, John W.** 6, 1957, American Journal of Physics, Vol. 25, pp. 394-395.
61. *Transmission electron microscopy of metals.* **Thomas, Gareth.** s.l. : Wiley, 1962.
62. **Fultz, Brent and Howe, James M.** *Transmission electron microscopy and diffractometry of materials.* s.l. : Springer Science \& Business Media, 2012.
63. *Imaging single atoms using secondary electrons with an aberration-corrected electron microscope.* **Zhu, Yimei and Inada, H and Nakamura, K and Wall, J.** 10, s.l. : Nature materials, 2009, Vol. 8, pp. 808-812.
64. *Measurement of hardness and elastic modulus by instrumented indentation: Advances in understanding and refinements to methodology.* **Oliver, Warren C and Pharr, Georges M.** 1, s.l. : Journal of materials research, 2004, Vol. 19, pp. 3-20.
65. *Determination of the effective zero-point and the extraction of spherical nanoindentation stress--strain curves.* **Kalidindi, Surya R and Pathak, Siddhartha.** 14, s.l. : Acta Materialia, 2008, Vol. 56, pp. 3523-3532.
66. *Spherical nanoindentation stress--strain curves.* **Pathak, Siddhartha and Kalidindi, Surya R.** s.l. : Materials Science and Engineering: R: Reports, 2015, Vol. 91, pp. 1-36.
67. *Contact mechanics.* **Johnson, Kenneth Langstreth and Johnson, Kenneth Langstreth.** s.l. : Cambridge university press, 1987.
68. *Observation, analysis, and simulation of the hysteresis of silicon using ultra-micro-indentation with spherical indenters.* **Weppelmann, ER and Field, JS and Swain, MV.** 4, 1993, Journal of materials research, Vol. 8, pp. 830-840.
69. *Comparison of Stress-Strain Curves Obtained by Single-Thickness and Pack Methods.* **Paul, DA and Howell, FM and Grieshaber, HE.** 1941, National Advisory Committee for Aeronautics.
70. *Standard test methods of compression testing of metallic materials at room temperature.* **Standard, ASTM and others.** 1990, 1990 Annual Book of ASTM Standards, ASTM, West Conshohocken, PA, pp. 98-105.
71. *Refractory Metals: Tungsten, Tantalum, Columbium, and Rhenium.* **Pugh, John W.** s.l. : J. Metals, 1958, Vol. 10.
72. *Quantification of surface damage of tool steels after EDM.* **Lee, LC and Lim, LC and Narayanan, V and Venkatesh, VC.** 4, s.l. : International Journal of Machine Tools and Manufacture, 1988, Vol. 28. 359-372.
73. **Inc., Re Alloys.** Rhenium Bar Quote. s.l. : Personal Correspondence, 2016.
74. *Friction of Rhenium and Co-Re Alloys in Vacuum at High Temperatures.* **Semenov, AP and Pozdnyakov, VV and Katsura, AA.** s.l. : the Study and Use of Rhenium Alloys,(Nauka Publishers, Moscow, 1975),(American Publishing Co. 1978), 1975, pp. 230-235.
75. *New opportunities for 3D materials science of polycrystalline materials at the micrometre lengthscale by combined use of X-ray diffraction and X-ray imaging.* **Ludwig, Wolfgang and King, Andrew and Reischig, P and Herbig, Michael and Lauridsen, Erik Mejdal and Schmidt, S{\o}ren and Proudhon, Henry and Forest, Samuel and Cloetens, Peter and Du Roscoat, S Rolland and others.** 1, s.l. : Materials Science and Engineering: A, 2009, Vol. 524, pp. 69-76.

76. *Optimizing disk registration algorithms for nanobeam electron diffraction strain mapping.* **Pekin, Thomas C and Gammer, Christoph and Ciston, Jim and Minor, Andrew M and Ophus, Colin.** s.l. : Elsevier, 2017, Vol. 176.
77. *Strain mapping at nanometer resolution using advanced nano-beam electron diffraction.* **Ozdol, VB and Gammer, C and Jin, XG and Ercius, P and Ophus, C and Ciston, J and Minor, AM.** 25, s.l. : Applied Physics Letters, 2015, Vol. 106.
78. *Dislocation locking versus easy glide in titanium and zirconium.* **Clouet, Emmanuel and Caillard, Daniel and Chaari, Nermine and Onimus, Fabien and Rodney, David.** 9, 2015, Nature materials, Vol. 14, pp. 931-936.
79. *Achieving the ideal strength in annealed molybdenum nanopillars.* **Lowry, MB and Kiener, D and LeBlanc, MM and Chisholm, Claire and Florando, JN and Morris, JW and Minor, AM.** 15, s.l. : Acta Materialia, 2010, Vol. 58, pp. 5160-5167.
80. *Dislocation starvation and exhaustion hardening in Mo alloy nanofibers.* **Chisholm, Claire and Bei, Hongbin and Lowry, MB and Oh, Jason and Asif, SA Syed and Warren, OL and Shan, ZW and George, Easo P and Minor, Andrew M.** 5, s.l. : Acta Materialia, 2012, Vol. 60, pp. 2258-2264.
81. *Re Foil Sheet Quote.* **Inc., Re Alloys.** s.l. : Personal Correspondence, 2016.
82. *The structure of <c+a> type dislocation loops in magnesium.* **Geng, J and Chisholm, Matthew F and Mishra, RK and Kumar, KS.** 6, s.l. : Taylor & Francis, 2014, Vol. 94.
83. **Greenwood, Norman Neill and Earnshaw, Alan.** *Chemistry of the Elements.* s.l. : Elsevier, 2012.
84. *Relative effects of enthalpy and entropy on the phase stability of equiatomic high-entropy alloys.* **Otto, Frederik and Yang, Ying and Bei, Hongbin and George, Easo P.** 7, 2013, Acta Materialia, Vol. 61, pp. 2628-2638.
85. *An understanding of high entropy alloys from phase diagram calculations.* **Zhang, Fan and Zhang, Chuan and Chen, Shuang-Lin and Zhu, J and Cao, Wei-Sheng and Kattner, Ursula R.** s.l. : Calphad, 2014, Vol. 45, pp. 1-10.
86. *The CALPHAD method and its role in material and process development.* **Kattner, Ursula R.** 1, s.l. : Tecnologia em metalurgia, materiais e mineracao, 2016, Vol. 13.
87. *Microstructural development in equiatomic multicomponent alloys.* **Cantor, Brain and Chang, ITH and Knight, P and Vincent, AJB.** 2004, Materials Science and Engineering: A, Vol. 375, pp. 213-218.
88. *Tungsten alloys with rhenium, carbides and oxides: production and properties.* **Povarova, KB and Bannykh, OA and Zavarzina, EK and Bryskin, BD.** 1998. Proceedings of the Fourth International Conference on Tungsten Refractory Metals and Alloys.
89. *Multicomponent and high entropy alloys.* **Cantor, Brian.** 9, 2014, Entropy, Vol. 16, pp. 4749-4768.
90. **J.E.C, Sabisch.** Anisotropic Deformation Measurements in Mg-4Gd using Berkovich Indentation. s.l. : Unpublished Work, 2017.
91. *Elastic properties, hardness, and indentation fracture toughness of intermetallics relevant to electronic packaging.* **Ghosh, G.** 5, s.l. : Journal of materials research, 2004, Vol. 19, pp. 1439-1454.
92. *Grain boundary segregation.* **Seah, MP and Hondros, ED.** s.l. : The Royal Society Publishing, 173. Proceedings of the Royal Society of London A: Mathematical, Physical and Engineering Sciences. Vol. 335. 1601.

93. *Indentation induced dislocation nucleation: The initial yield point.* **Gerberich, WW and Nelson, JC and Lilleodden, ET and Anderson, P and Wyrobek, JT.** 9, s.l. : Materialia, 1996, Vol. 44, pp. 3585-3598.
94. *The fabrication and properties of ruthenium.* **Rhys, DW.** 4, s.l. : Journal of the Less Common Metals, 1959, Vol. 1, pp. 269-291.